

**Alpha capture reactions for abundance observations in
nuclear astrophysics**

Joseph William Frost-Schenk

Doctor of Philosophy

University of York

Physics

October 2020

Abstract

Heavy element production in the Universe is dependent upon α capture reactions. Their measurement can help to explain discrepancies in stellar models and observation. In this thesis two key alpha capture reactions have been investigated, $^{15}\text{N}(\alpha,\gamma)^{19}\text{F}$ and $^{17}\text{O}(\alpha,\text{n})^{20}\text{Ne}$. The latter through $^{20}\text{Ne}(\text{d,p})^{21}\text{Ne}$ for the study of the $^{17}\text{O}(\alpha,\text{n})^{20}\text{Ne} / ^{17}\text{O}(\alpha,\gamma)^{21}\text{Ne}$ reaction rate ratio.

^{19}F can be observed in galactic absorption spectra, its abundance is not however well understood. The first directly measured direct capture measurement of $^{15}\text{N}(\alpha,\gamma)$ has been conducted in inverse kinematics using the DRAGON recoil separator. A measurement of the 1.323 MeV $^{15}\text{N}+\alpha$ resonance was made extracting a resonance strength of 0.92 ± 0.11 eV.

In massive stars heavy elements are formed through the s-process, the rate of which is dependent on the neutron flux. The $^{16}\text{O}(\text{n},\gamma)$ reaction is known to occur at a significant rate. Hence, the neutron poisoning effectiveness of ^{16}O is dependent upon the reaction rate ratio of $^{17}\text{O}(\alpha,\text{n})^{20}\text{Ne}$ and $^{17}\text{O}(\alpha,\gamma)^{21}\text{Ne}$.

The $^{20}\text{Ne}(\text{d,p})$ transfer reaction has been used as a mechanism for populating states with large neutron widths in ^{21}Ne ; those important for $^{17}\text{O}(\alpha,\text{n})^{20}\text{Ne}$. The measurement was conducted using TUNLs split-pole spectrograph to populate states inside the Gamow window.

Significant reductions of state energy uncertainties inside the Gamow window have occurred. Transferred angular momenta were found by comparison with states of known J^π as well as comparison with outputs from FRESKO. Partial widths were extracted using a weakly bound extrapolation. Reaction rates were calculated using the RatesMC reaction rate code. Presented is a revision to the $^{17}\text{O}(\alpha,\text{n})^{20}\text{Ne}$ and $^{17}\text{O}(\alpha,\gamma)^{21}\text{Ne}$ reaction rate ratio. A decrease in the previously accepted effectiveness of ^{16}O as a neutron poison is found, suggesting an increased neutron flux within massive stars.

Contents

Abstract	ii
List of Tables	viii
List of Figures	ix
Acknowledgements	xviii
Declaration	xx
1 Introduction and Background Theory	21
1.1 Nucleosynthesis	21
1.1.1 CNO cycle	22
1.1.2 S-process	22
1.2 Astrophysical environments	24
1.2.1 AGB stars	24
1.2.2 Massive stars	25
2 Theoretical Considerations	29
2.1 Reaction theory	29
2.1.1 Reaction cross-section	29
2.1.2 Gamow window	30
2.1.3 S-factor	31
2.1.4 Resonance strength	31
2.1.5 Reaction rate	32
2.2 Nuclear theory	33
2.2.1 Spectroscopic factors and partial widths	34
2.2.2 Wigner limit	36

2.2.3	Optical model	36
3	$^{15}\text{N}(\alpha,\gamma)^{19}\text{F}$ Previous Measurements	38
4	$^{15}\text{N}(\alpha,\gamma)^{19}\text{F}$ Experimental Technique	45
4.1	Beam production	45
4.2	DRAGON	46
4.2.1	Charge state selection	48
4.2.2	Target chamber and gas cell	49
4.2.3	BGO array	49
4.2.4	Surface barrier detectors	50
4.2.5	Recoil detection: DSSSD	51
4.2.6	Timing	53
4.2.7	Tuning DRAGON and beam energy	53
5	$^{15}\text{N}(\alpha,\gamma)^{19}\text{F}$ Data Analysis	55
5.1	Normalisation	55
5.2	Recoil extraction and particle identification	57
5.2.1	RF period	57
5.2.2	Separator time of flight	57
5.2.3	Surface barrier trigger latch	58
5.2.4	BGO threshold	60
5.2.5	DSSSD energy cut	64
5.2.6	Combining cuts	66
5.2.7	Low count statistics and the central confidence interval	67
5.3	Efficiencies	69
6	$^{15}\text{N}(\alpha,\gamma)^{19}\text{F}$ Results	72
7	$^{15}\text{N}(\alpha,\gamma)^{19}\text{F}$ Discussion	74
8	$^{20}\text{Ne}(\text{d,p})^{21}\text{Ne}$ Previous Measurements	79
9	$^{20}\text{Ne}(\text{d,p})^{21}\text{Ne}$ Experimental Technique	88
9.1	Beam production	88
9.2	Split-pole spectrograph	89
9.3	Focal plane detector	91

9.4	Target content	93
10	$^{20}\text{Ne}(\text{d,p})^{21}\text{Ne}$ Data Analysis	94
10.1	Beam normalisation	94
10.2	Target content	95
10.3	Contaminant removal	98
10.4	Narrow state width extraction	102
10.5	Peak fitting method development	103
10.6	Calibration	106
10.7	State fitting and parameter extraction	111
10.8	State energies	119
10.9	FRESCO	126
10.10	Spin parity assignment and spectroscopic factors based on FRESCO	129
10.11	Spin parity assignment using known states	143
10.12	Neutron partial widths	147
10.13	Reaction rate	149
11	$^{20}\text{Ne}(\text{d,p})^{21}\text{Ne}$ Results	151
12	$^{20}\text{Ne}(\text{d,p})^{21}\text{Ne}$ Discussion	155
12.1	^{21}Ne state properties	155
12.2	Reaction rate	165
12.3	Further work	170
13	Conclusions	173
	Appendix A	175
	Bibliography	186

List of Tables

2.1	Transferred angular momentum in the transfer reaction $^{20}\text{Ne}(d,p)$, Δl , total angular momentum and parity of possible ^{21}Ne states.	34
3.1	Results from 2017 Di Leva et al. [27] measurement using ERNA for two key resonances.	44
5.1	Beam energies with corresponding gas target pressures.	56
5.2	Calculated N_{beam} values using the R-factor method, the simple scaling method and the percentage difference. $N_{beam}\sigma$ is the standard deviation between each runs cup readings for the given beam energy, i.e. a measure of fluctuation between Faraday cup readings, not the total uncertainty. *resonance beam energy.	57
5.3	^{19}F counts extracted for each beam energy. *resonance beam energy	67
5.4	Uncertainty method comparison for various values of N; using central confidence interval for 2σ , 1σ and \sqrt{N}	68
5.5	Uncertainties for all beam energies for BGO detection efficiency and livetime of the DAQ, data acquisition system. *resonance beam energy.	69
5.6	Calculated and measured charge state fraction for the selected ^{19}F tune through DRAGON. *resonance beam energy.	70
6.1	Cross-sections measured for $^{15}\text{N}(\alpha,\gamma)^{19}\text{F}$ along with their asymmetric uncertainties with a central confidence interval equivalent to 1σ at 68.27%. *resonance beam energy.	72
6.2	S-Factors for $^{15}\text{N}(\alpha,\gamma)^{19}\text{F}$ along with their uncertainties.	73
8.1	Energies in CoM, respective ^{21}Ne energies, resonance strengths and previous values from Best et al. in 2011 [72]. *May contain two other resonances. Table adapted from Taggart et al. [24].	84

10.1	Number of beam particles onto the target at each angle.	94
10.2	Target neon content by layers and also the total thickness of each layer. No uncertainties are presented on these thicknesses, as they are a modelling construct only. The neon fraction errors are not presented as the errors on individual layers were not investigated, but the uncertainty on the total neon content was found.	95
10.3	Peak widths for narrow states, derived predominantly from the width of the 6.609 MeV peak.	104
10.4	The four calibration peaks, note their proximity to the Gamow window. . . .	109
10.5	Peak centroids at all angles for two selected chosen binning settings at each angle for the 6.609 MeV energy ^{21}Ne state.	110
10.6	χ^2 values for the key calibrations, note the particularly significant decrease in the quadratic calibration fit χ^2 with removal of 5.334 MeV state.	111
10.7	Optical model parameters used in FRESKO input. R-Match was assumed to be 11 fm, thought is given to the radius of the transfer in section 10.12. . . .	128
10.8	Transferred angular momentum, Δl , and the number of radial nodes.	129
11.1	Δl along with the extracted partial widths for both the neutron channel and α channel. $^*\Gamma_\alpha$ from Best et al. [65]. ** Partial width assumed equal to the total width from Cohn and Fowler [100] as the neutron partial width expected to dominate. *** The resonance energy of this state is shown as 631 keV as the state energy extracted of 7.981(1) MeV cannot be confirmed to be solely from this state and not partly its higher in energy doublet counterpart. T This alpha width is informed by Taggart et al. [24] and Denker et al. [66]. D Resonance strength from the thesis of Denker [66]. c The energy of these states is assumed from literature as these are calibration states.	152
11.2	The total reaction rate for $^{17}\text{O}(\alpha,n)^{20}\text{Ne}$ extracted using the Monte Carlo reaction rate code [98].	154
12.1	^{21}Ne state energies, spins and parities measured here and those from previous accepted literature. * This state energy likely has contribution from peaks in an unresolvable doublet. c The energy of these states is assumed from literature as these are calibration states, any difference in energy from literature is from the calibration fit.	156

12.2 ^{21}Ne state energies, spins and parities measured here and those from previous accepted literature. ^aState measurement could not be confirmed as being measured here and this energy is from NNDC, [30] including the measurement of Thummerer et al. ^bIn literature these states are represented as the 7.980(10) MeV and the 7.9821(6) MeV states respectively [102], detector resolution here was insufficient to separate these peaks. ^cThe energy of these states is assumed from literature as these are calibration states, any difference in energy from literature is from the calibration fit. ^{*}Measured by Best et al. [65], however their results could be reproduced by other transferred l values. 157

List of Figures

1.1	The four CNO cycles. Note that while the catalysts may vary in each version of the cycle, the outcome in each is identical.	22
1.2	S-process path shown on an extract of the nuclear chart, notice its path close to the line of stability. Furthermore inset top left is a plot of nuclear abundance relative to silicon and showing the iron abundance peak and the abundance peaks formed by the s and r-processes. Figure from Kappeler et al. [4]. . . .	23
1.3	Production factors for nuclei formed inside a massive star, figure from Frischknecht et al. [25]. Triangles represent a model without rotation, here nuclei formed by the s-process are insufficiently produced. Circles and diamonds represent a model that includes rotation. Stars represent a model in which the $^{17}\text{O}(\alpha,\gamma)$ rate is reduced by a factor of 10 and has the same rotation as the diamonds. v_{ini} represents the initial velocity at the stars surface, and v_{crit} the critical surface rotation velocity which is the surface velocity where the gravity at the equator equals the force required to stop the loss of matter from the stars surface [25].	28
2.1	An example of angular momentum and spin coupling, diagram from Krane [28].	33
3.1	^{19}F states where the Gamow window at 200 MK is highlighted, figure from Lennarz [38].	39
3.2	Part of the energy spectrum showing the 4.378 MeV state at 15° in the centre of mass frame from Oliviera et al. [47].	41
3.3	Resonances of 5.337 MeV and 5.501 MeV and corresponding cross-sections. Figure adapted directly from Wilmes et al. [16].	42
3.4	Sample ΔE -E spectrum showing ion identification. Figure from Di Leva et al. [27]	43

4.1	A three dimensional representation of ISAC–1 from Ball et al. [51]. DRAGON is located centrally within ISAC-1.	46
4.2	A schematic of DRAGON from Hutcheon et al. [54] with minor adaptations. Examples of ion trajectories are shown. MD and ED stand for magnetic and electric dipoles respectively.	47
4.3	Diagram of gas target adapted from Hutcheon et al. [57]. The beam entered from the right and leaves to the left. The gas was pumped in from below. . .	50
4.4	Schematic diagram of the DRAGON BGO detectors. Left: A cut-away 3D schematic of the DRAGON BGO detectors from Hutcheon et al. [54]. Right: 2D cutaway from Hutcheon et al. [57]. Note the dashed lines represent the outline of the gas target system, as seen in figure 4.3, relative to the location of the BGO detector array.	51
4.5	Figure from Tengblad et al. [58]. a) shows the detector in ΔE -E arrangement b) Shows the ΔE component as presented by Tengblad et al. [58]. Note the pick-up strips covering part of the detector surface, note that DRAGON uses a $300\ \mu\text{m}$ thick version.	52
5.1	RF peak fitted giving a centroid of $86.89(2)$ ns, matching the frequency of the RFQ.	58
5.2	Separator time of flight for the $1323\ \text{keV}$ CoM measurement energy, note the asymmetrical fashion of the peak and the apparent double gaussian.	59
5.3	Separator time of flight for the $957\ \text{keV}$ centre of mass measurement energy, note the lack of significant identifiable peak.	60
5.4	The separator time of flight spectrum for the $957\ \text{keV}$ centre of mass measurement energy using the surface barrier trigger latch, fitted. Note only the centroid is used from this low statistic fit.	61
5.5	DSSSD spectrum for the $957\ \text{keV}$ centre of mass measurement energy.	61
5.6	DSSSD spectrum for the $957\ \text{keV}$ centre of mass measurement energy with surface barrier detector trigger.	62
5.7	BGO spectrum with separator time of flight cut applied for the grouped runs at the $1323\ \text{keV}$ CoM measurement energy.	62
5.8	BGO spectrum with separator time of flight cut applied for the grouped runs at the $957\ \text{keV}$ centre of mass measurement energy with $1\ \text{MeV}$ BGO threshold applied.	63

5.9	Individual BGO detector hit energies for the 1323 keV CoM measurement energy. Note the comparable energy distributions for all channels except for channel 23.	63
5.10	BGO hit patterns for the highest direct capture energy of 1720 keV in the centre of mass frame.	64
5.11	BGO hit patterns for the resonance beam energy of 1323 keV in the centre of mass frame.	65
5.12	DSSSD spectrum for a beam energy of 1323 keV in the centre of mass frame, with BGO and separator time of flight cuts included.	66
5.13	DSSSD spectrum for a beam energy of 1323 keV in the centre of mass frame, showing the effect of each cut.	67
7.1	From left to right resonance strengths for: work completed and presented here; other DRAGON runs analysed by A. Lennarz et al.; Aitken et al. [39]; Dixon and Storey [43], their average including the scaled measurements and corrected absolute measurement, their raw absolute measurement, their absolute measurement with correction applied; Wilmes et al. [16]; and far right, Di Leva et al. [27].	75
7.2	The resonance contained within the DRAGON gas target for run 7086. Using the 1323 keV centroid and the widths from both Wilmes [16] and Di Leva [27].	77
7.3	Higher energy run of 7065 and the two centroids 1323 keV and 1331.4 keV both with the Di Leva et al. [27] width of 2.51 keV.	78
8.1	^{21}Ne states across the Gamow window with state energies as accepted by literature [30]. The Gamow window can be seen shaded green.	80
8.2	Neutron yield for each component, note $n_{total} = n_0 + n_1$. Figure from Best et al. [65]	81
8.3	R-Matrix fit of the two neutron decay channels. Figure from Best et al. [65]	81
8.4	Effects on element abundance of Best rates and the previous rates. Note CF88, represents the comparison point of (α, γ) from the work of Caughlan et al. [70] scaled by the factor of 1000 from Descouvemont et al. [71] described by Best et al. [65] for the (α, γ) . The (α, n) comparison point is from a compilation, NACRE [69] using unpublished data. Figure from Best et al. [65]	82
8.5	Current predictions of heavy element production due to the s-process compared with the work of Best et al. [65] in fast rotating massive stars. Figure from Taggart et al. [24] with minor adaptation.	84

8.6	Measured differential cross-section values for the 6.606 MeV state and the fitted DWBA $l=2$ output. Figure from Howard et al. [73].	85
8.7	Spectra of ^{21}Ne , note the population of the 6.605 MeV peak, later measured as 6.609 MeV. Figure from Stanford and Quin et al. [75]	86
8.8	Measured differential cross-section values for the 6.61 MeV state and the DWBA outputs. Figure from Stanford and Quin et al. [75].	86
9.1	Schematic of deuteron acceleration in Van de Graff accelerator from the Thesis of A. H. Couture [77].	89
9.2	Schematic of trajectories through the split pole spectrograph from Marshall et al. [78].	90
9.3	A cutaway perpendicular to the beam and looking down the anode wires. Figure from Marshall et al. [78] with minor adaptation. Red arrow represents reactant particle path, passing through 2 position sections.	91
9.4	Schematic of one of the position section assemblies. Figure from Marshall et al. [78].	92
10.1	Elastic measurement spectra at 25° after the 20° measurement overlaid with Focal Plane Plotter calculation to identify peak species.	96
10.2	Elastic measurement ^{20}Ne peak at 25° after 38° measurement. Showing a fitted Gaussian peak.	97
10.3	Counts in neon peak per unit beam particle during 25° elastic run against the total beam particles on target through whole experiment since initial RBS measurement of target.	97
10.4	Energy deposited in the dE component of the detector against the focal plane position, both in an arbitrary channel number, for the 40.1° measurement. The shaded region represents the gated region. Figure extracted from Jam [85].	99
10.5	Energy deposited in the dE component of the detector against the remaining energy deposited in the E component of the detector. Both energies plotted in an arbitrary channel number, for the 40.1° measurement. The shaded region represents the dE-E gate region.	100
10.6	Position spectra for the anti-gated particles from the dE-E gate as seen in figure 10.5. Note the removal of what will later be shown as counts from the three carbon peaks formed through the $^{12}\text{C}(d,p)$ reaction.	101

10.7	The particles present in the anti-gate of both the dE position gate and also the dE-E gate, displayed on a dE against E plot. Axis are in arbitrary channel numbers.	101
10.8	Fitted 6.609 MeV state at 21.2° showing good separation and flat, linear background.	102
10.9	Fitted 6.609 MeV state at 40.1° showing composite fit with a linear background.	103
10.10	Carbon target 40.1° spectra fitted with a cubic function and two Gaussians, replicating the oxygen peak.	104
10.11	Neon spectra fitted (red) on scaled carbon background, comprised of a scaled version of the carbon fit, scaled gaussian and cubic function background (green) and cubic function and gaussian of oxygen (orange), 38° spectra shown. . . .	105
10.12	Neon background subtracted 38° neon spectra.	106
10.13	Rough calibration using the Focal Plane Plotter at 38°.	108
10.14	Energies for all fitted ²¹ Ne states except 6.609 MeV.	112
10.15	Fitting of ²¹ Ne states across the Gamow window for the 40.1° spectra. All state energies are in MeV and are those calculated across all angles using mean weighted average, where states were only seen at 40.1° the energies from the 40.1° spectra have been adopted.	114
10.16	Fitting of ²¹ Ne states across the Gamow window for the 26.4° spectra. All state energies are in MeV and are those calculated across all angles using mean weighted average. Note the significant background centred around channel 1200 from the p(d,p)d reaction.	115
10.17	Fitting of ²¹ Ne states across the Gamow window for the 21.2° spectra. All state energies are in MeV and are those calculated across all angles using mean weighted average. Note the tail of the p(d,p)d reaction tail around the 7.420 MeV energy state peak.	116
10.18	Fitting of ²¹ Ne states across the Gamow window for the 15.9° spectra. All state energies are in MeV and are those calculated across all angles using mean weighted average.	117
10.19	Fitting of ²¹ Ne states across the Gamow window for the 10.6° spectra. All state energies are in MeV and are those calculated across all angles using mean weighted average.	118
10.20	Fitting of ²¹ Ne states across the Gamow window for the 26.4° spectra. Note the distinct p(d,p)d background.	119

10.21	Energy with measurement angle, showing negligible fluctuation in state energy for the known 7.420 MeV calibration state of ^{21}Ne	120
10.22	Extract of 21.2° spectra showing the 7.619 MeV and 7.601 MeV energy peak with centroids at 1563 ± 1 channels and 1579 ± 4 channels respectively.	122
10.23	Extract of 40.1° spectra showing the 7.619 MeV and 7.601 MeV peak with centroids at 1349 ± 1 channels and 1365 ± 1 channels respectively, note the increased prominence when compared with the 21.2° of the 7.601 MeV energy state.	123
10.24	Extract of 40.1° spectra showing the fit of the 7.749 MeV energy state in ^{21}Ne .	123
10.25	Fluctuations in energy and the originally suspected potential doublet witnessed at 40.1° . It seems however there is are contaminant state(s) in this region as well as the 7.820 MeV energy ^{21}Ne state.	124
10.26	Energy drift with angle change of the 7.961 MeV energy state, implying these peaks are not from ^{21}Ne	125
10.27	Minor energy drift with angle change of the 8.069 MeV energy calibration state.	126
10.28	Minor energy drift with angle change of the 8.189 MeV energy calibration state.	127
10.29	Experimental differential cross-sections for 5.549 MeV compared with FRESCO outputs. Each sub-plot has a different value of transferred angular momentum. It is clear the 5.549 MeV energy state was formed through an $l=2$ transfer.	131
10.30	Experimental differential cross-sections for 6.609 MeV compared with FRESCO outputs. Each sub-plot has a different value of transferred angular momentum and different C^2S scaling factor.	132
10.31	Experimental differential cross-sections for 7.420 MeV compared with FRESCO outputs. Each sub-plot has a different value of transferred angular momentum and different C^2S scaling factor.	133
10.32	Experimental differential cross-sections for 7.559 MeV compared with FRESCO outputs. Each sub-plot has a different value of transferred angular momentum and different C^2S scaling factor.	134
10.33	Experimental differential cross-sections for 7.601 MeV compared with the FRESCO outputs. Each sub-plot has a different value of transferred angular momentum.	135
10.34	Experimental differential cross-sections for 7.619 MeV compared with FRESCO outputs. Each sub-plot has a different value of transferred angular momentum and different C^2S scaling factor.	136

10.35	Experimental differential cross-sections for 7.820 MeV compared with FRESCO outputs. Each sub-plot has a different value of transferred angular momentum and different C ² S scaling factor.	138
10.36	Experimental differential cross-sections for 7.981 MeV compared with FRESCO outputs. Each sub-plot has a different value of transferred angular momentum and different C ² S scaling factor.	139
10.37	Experimental differential cross-sections for 8.068 MeV compared with FRESCO outputs. Each sub-plot has a different value of transferred angular momentum and different C ² S scaling factor.	140
10.38	Experimental differential cross-sections for 8.146 MeV compared with FRESCO outputs. Each sub-plot has a different value of transferred angular momentum and different C ² S scaling factor.	141
10.39	Experimental differential cross-sections for 8.189 MeV compared with FRESCO outputs. Each sub-plot has a different value of transferred angular momentum and different C ² S scaling factor.	142
10.40	Experimental differential cross-sections for the 8.189 MeV, 8.146 MeV, 8.068 MeV, 7.820 MeV, 7.559 MeV and 6.609 MeV energy states taken in ratio with the differential cross-sections of the known l=1 transfer of the 7.619 MeV energy state.	144
10.41	Experimental differential cross-sections for the 8.146 MeV, 8.068 MeV, 7.820 MeV, 7.619 MeV, 7.559 MeV and 6.609 MeV energy states taken in ratio with the differential cross-sections of the 8.189 MeV energy state.	145
10.42	Experimental differential cross-sections for the 8.189 MeV, 8.146 MeV, 8.068 MeV, 7.820 MeV, 7.619 MeV, 7.559 MeV and 6.609 MeV energy states taken in ratio with the differential cross-sections of the 5.549 MeV energy state.	146
10.43	The partial width as a function of interaction radius for the 7.619 MeV energy state with a 100 keV binding energy for an l=1 transfer.	147
10.44	The Asymptotic Normalisation Coefficient as a function of interaction radius for the 7.619 MeV energy state with a 100 keV binding energy for an l=1 transfer in ²⁰ Ne+n.	148
10.45	The partial width as a function of binding energy for the 7.619 MeV energy state for an l=1 transfer.	149
11.1	Total reaction rate from the narrow resonance equation as a function of temperature. At 0.2 GK the rate is $7(4) \times 10^{-13} \text{cm}^3 \text{s}^{-1} \text{mol}^{-1}$	153

11.2	Fractional contribution to the reaction rate using the narrow resonance formula to calculate the rates. Note how at astrophysically important temperatures the 7.749 MeV dominates the rate. The fractional rate plot should only be considered complete up to 0.3 GK.	154
12.1	Residuals of energies for each measured state. Weighted average across all angles. Uncertainties represent the combination of uncertainties from this work and also the literature uncertainties.	158
12.2	A comparison of the differential cross-section measurements for the 6.609 MeV energy state from Howard et al. [73] compared with those measured in this work. Note how the peak is at more forward angles in the data measured here. Hence the different assignment of transferred l from previous literature. . . .	159
12.3	The effect on the reaction rate uncertainty of the 7.749 MeV energy state with its new reduced uncertainty. Black: the literature [88] rate at 7.750 MeV taken in ratio with the rates at ± 10 keV. Red: the reaction rate from the narrow resonance formula at 7.749 MeV taken in ratio with the rates at ± 1 keV. Where these curves cross is where the upper and lower limits have equal rate. Note the significant fractional uncertainty reduction in reaction rate achieved. . .	162
12.4	Fractional contribution of each state to the $^{17}\text{O}(\alpha, n)$ reaction rate, calculated using the Monte Carlo code. Note the agreement between this method and the narrow resonance assumption rate calculation. Higher energy resonances may not be included at higher temperatures above >0.3 GK, however from an astrophysics perspective at 0.2 GK all known states are accounted for.	166
12.5	Fractional contribution to the $^{17}\text{O}(\alpha, \gamma)$ reaction rate, calculated using the Monte Carlo code. Higher energy resonances may not be included at temperatures above >0.3 GK, however from an astrophysics perspective, at 0.2 GK, all known states are accounted for.	167
12.6	The effect of the measurement here on the $^{17}\text{O}(\alpha, n)$ total median reaction rate relative to Best et al. [65]. The dashed lines represent the upper and lower uncertainties on the rate extracted here. Note the good agreement between the Monte Carlo mean and the narrow resonance formula method.	168

12.7	The ratio of the $^{17}\text{O}(\alpha, n)^{20}\text{Ne}/^{17}\text{O}(\alpha, \gamma)^{21}\text{Ne}$ as a function of temperature. The dashed lines represent the upper and lower uncertainties on the Monte Carlo rate ratio, the median of which is the solid black line, the red line represents the narrow resonance formula rate calculation, the blue line the ratio from Best et al. [65] and the finely dashed red line represents the narrow resonance ratio if the 308 keV resonance was a $5/2+$	169
12.8	The Monte Carlo ratio of the $^{17}\text{O}(\alpha, n)^{20}\text{Ne}/^{17}\text{O}(\alpha, \gamma)^{21}\text{Ne}$ reaction rate as a ratio with $^{17}\text{O}(\alpha, n)^{20}\text{Ne}/^{17}\text{O}(\alpha, \gamma)^{21}\text{Ne}$ of Best et al. [65]. The dashed lines represent the upper and lower uncertainties on the ratio.	170
12.9	The effect of the measurement here on the $^{17}\text{O}(\alpha, \gamma)$ total median reaction rate relative to Best et al. [65]. The dashed lines represent the upper and lower uncertainties on the Monte Carlo method rate extracted here. Note the difference between the Monte Carlo method median and the rate of Best et al. [65].	171
12.10	Yields from the s-process for a $25 M_{sun}$ star. Note the effect on reducing the $^{17}\text{O}(\alpha, \gamma)^{21}\text{Ne}$ by a factor of 10 (increasing the $^{17}\text{O}(\alpha, n)^{20}\text{Ne}/^{17}\text{O}(\alpha, \gamma)^{21}\text{Ne}$ ratio). Figure from Taggart et al. [24] with minor adaptation.	171
12.11	The effect on the reaction rate by changing the transferred l in $^{17}\text{O}+\alpha$ from 0 to 1. This results in a 71% decrease in reaction rate for this resonance at 0.2 GK.	172

Acknowledgements

I came to study Nuclear Astrophysics to seek out a challenge that would stretch my abilities and broaden my knowledge. It certainly has not disappointed. I would like to thank those people that made the last four years possible, there are too many to mention you all by name. I apologise if I missed you out, you certainly know who you are.

A special mention must go to Alison Laird and Christian Diget, my supervisors. They have guided me from the level of knowledge and ability I arrived with, to what I hope is a good, fruitful thesis. I must make a special thanks for the evenings and weekends donated by Alison during the write up period, for countless Skype calls and discussions away from her family. Thank you. And to Christian for making me feel such a central part of York, I will cherish these memories with fondness, and for the countless hours of on-call advice. Words cannot describe what an honour it has been to work so closely with two such knowledgeable, brilliant minds for the last four years, it has been a real privilege. Thank you.

My thanks also to those who without their advice the completion of the projects within this thesis would not be possible.

Thanks to Annika Lennarz for her willingness to help and advise on the ^{15}N data and DRAGON analysis, the discussions we have had as well as her exceptional levels of patience on many occasions. The awesome team at TRIUMF and more specifically those at DRAGON who immediately involved me heavily during my trips there.

Richard Longland for his knowledge and patience explaining all things TUNL split-pole related and his help and dedication to the experiment. The hours of discussion during the analysis have been extremely valuable. Thanks also to the wider community at the TUNL split-pole spectrograph who were exceptional whenever I needed information on the setup or some discussion. You made me feel like a member of your team that you had known for years. Thank you.

Of course I cannot forget Phil Adsley, who has been my personal tour guide through the wall that was FRESCO. His endless hours of discussion including late into the night on several occasions have been beyond exceptionally useful. I am truly grateful for his efforts

and time. Thank you!

Thanks to Cameron Angus for his efforts and discussion on the literature, I wish you the very best for your PhD and I hope elements of my work presented here are useful. A special thanks must also be given to Simon Fox who tutored an (almost) completely code illiterate 1st year, with calm and patience. Your advice and time was greatly valued.

As everyone involved knows, the sudden passing of my father during my PhD made my studies significantly harder and as such at times I could not always engage with all the activities, that looking back, I would have loved to. A special thank you to Ana, Alison, Christian and Simon for their understanding and encouragement during these exceptionally dark times.

I would like to thank Ana for her support in dealing with my ups and downs during this PhD, especially during the writing up period, you really have put up with a lot.

Lastly but not least, my parents, grandparents, family and friends. An extra special thanks to my mother and father. You have always been there, supported me through school and University, encouraged me and pushed me to do more.

My father shared all he knew with regards to building, construction and mechanics and it is this that sparked my initial interest in Physics. For this I am so unbelievably grateful, else I would not have embarked on such a conquest described in the coming pages. Although my father isn't here to see me finish this epic journey that is a PhD in Nuclear Astrophysics he was there at the start and he wanted me to finish this. Well here it is dad, ready to go.

I hope this exciting road does not end here, but is the beginning of something brilliant. Thank you to you all for your patience, encouragement and support.

Declaration

I, Joseph William Frost-Schenk, declare that this thesis is a presentation of original work and I am the sole author. This work has not previously been presented for an award at this, or any other, University. All sources are acknowledged as References.

Chapter 1

Introduction and Background Theory

Nuclear Astrophysics aims to explain the origin and behaviour of nuclei in the Universe. The field of nuclear astrophysics bridges a substantial gap between, on one hand; Astronomy and Astrophysics and on the other; Nuclear physics.

Efforts to measure stellar properties have been ongoing for thousands of years from Babylonian astronomy and early Greek astronomy [1]. Potentially one of the most famous discoveries in astronomy was that of Galileo Galilei in January 1610, when he discovered and witnessed the motion of Jupiters “stars”. Recent technological advancements have allowed Astronomy to progress rapidly, today producing more detailed data than ever before on regions of the Universe previously unexplored. Through the study of cosmological phenomena, today it is widely accepted that the Universe was created in the big bang.

The subatomic particle make-up was a disputed topic, until in 1911 Rutherford published a paper [2] describing an experimentally validated model. Atoms were proved to have a dense core, today known as the nucleus. In this thesis it is the nuclei, consisting of positively charged protons and neutral neutrons that form the basis for the studies of element production.

By comparing observations of stellar abundances to models, discrepancies may be identified to obtain knowledge on the most significant reactions to measure from an astrophysical perspective. This thesis shall focus on two important α -capture reactions.

1.1 Nucleosynthesis

Nucleosynthesis is the creation of nuclei, which are produced through several mechanisms. In this thesis particular interest is paid to the formation of heavier nuclei inside stellar systems.

The burning of Hydrogen to form Helium is the first building block for heavier element

formation in stars. The simultaneous collision of 4 protons, or equivalently 4 ^1H nuclei would not occur frequently enough to produce sufficient energy to explain the luminosity of stars [3]. It can however, in part, be explained by the proton-proton chain and the CNO, carbon-nitrogen-oxygen cycle.

1.1.1 CNO cycle

The CNO cycle is a catalytic process to fuse hydrogen into helium. A star with Carbon, Nitrogen or Oxygen present can burn hydrogen through the CNO process. Due to its catalytic nature the star requires little of the CNO catalysts to conduct hydrogen burning at a significant level, as ultimately, the amount of CNO material will remain unchanged. This process is particularly important inside AGB, asymptotic giant branch stars.

The four CNO cycles can be seen in figure 1.1. Note how all cycles fuse 4 protons into a ^4He nucleus. Each cycle in the CNO consist of one (p,α) reaction, three proton captures and two β^+ decays.

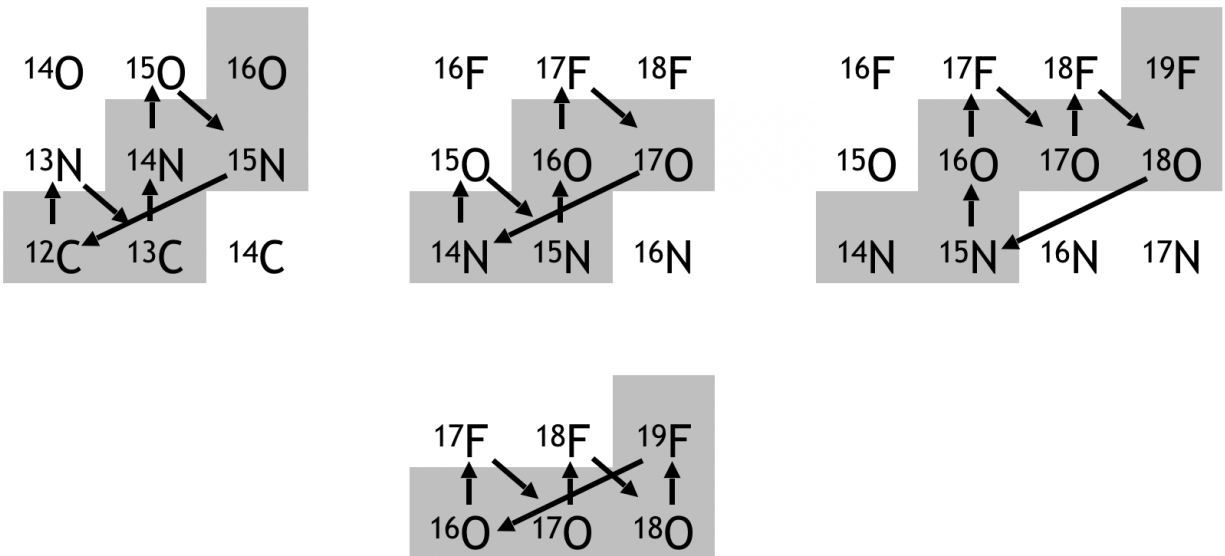


Figure 1.1: The four CNO cycles. Note that while the catalysts may vary in each version of the cycle, the outcome in each is identical.

1.1.2 S-process

Charged particle reactions are limited in what masses they can produce due to the increase in Coulomb repulsion with increasing proton number of the reactants. The heaviest elements

formed by fusing charged nuclei are found in the iron region. The s-process, also known as the slow neutron capture process, allows heavier element production due to the absence of the Coulomb barrier. The s-process produces n -nuclei close to the valley of stability. The neutron captures occur at a comparatively slow rate relative to the β^- decay, meaning that many of the nuclei produced by the s-process are stable. A sample of this process can be seen in figure 1.2. Nuclei further from the valley of stability on the neutron rich side are formed through the r-process, rapid neutron capture process, whereby the environment dictates that the neutron capture rate is fast relative to the β decay rate.

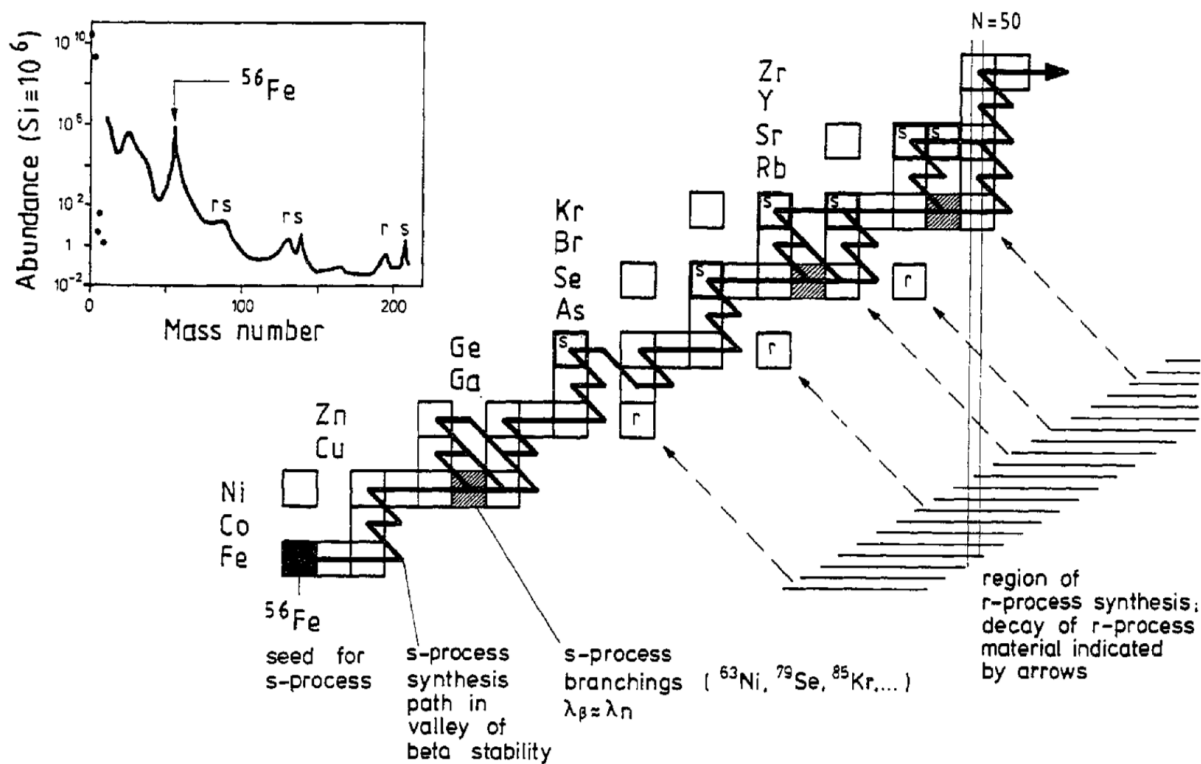


Figure 1.2: S-process path shown on an extract of the nuclear chart, notice its path close to the line of stability. Furthermore inset top left is a plot of nuclear abundance relative to silicon and showing the iron abundance peak and the abundance peaks formed by the s and r-processes. Figure from Kappeler et al. [4].

In the s-process the competition between beta decay and neutron capture reactions are approximately balanced and when the branching ratio allows so the pathway may β -decay or neutron capture. This leads to a split in the s-process path, this can be seen multiple times in figure 1.2. Note the abundance plot and how the s-process peaks at three distinct points. These represent the nuclei with neutron numbers of 50, 82 and 126, these are those with full neutron shells, more commonly referred to as magic numbers.

The s-process is divided into three categories: the weak s-process, the main s-process and the strong s-process. The weak and main s-process occur in stars of mass, $M > 8 M_{sun}$, $1.3 M_{sun} \leq M \leq 8 M_{sun}$ respectively. The strong s-process occurs in AGB stars with low metallicity. The weak s-process is most important for the massive stars that are studied here and is responsible for producing nuclei from iron to strontium [5]. The s-process rate is dependant upon both the availability of seed nuclei and neutron flux in the environment. The $^{20}\text{Ne}(d,p)$ measurement in this thesis aims to help explain neutron abundance in massive stars. An explanation of its importance to the neutron flux can be seen in section 1.2.2.

1.2 Astrophysical environments

1.2.1 AGB stars

Those AGB stars, discussed here for the purposes of ^{19}F production typically have a mass $M_{sun} \leq M \leq 7 M_{sun}$. These are considered low and intermediate mass AGB stars [6]. An AGB star has a core of ^{12}C and ^{16}O formed through helium burning. This C-O core is surrounded by a helium shell which is then covered in a hydrogen shell. As the C-O core increases in size, during helium burning so the outwards radiative pressure becomes insufficient to obtain the stars physical size so it contracts and the hydrogen shell begins burning. The He burning restarts as the star shrinks and this causes an increase in outwards pressure, so the star expands and the process starts again with helium burning. The expansion and contraction continues in a cyclic fashion.

^{19}F can be observed in stars of varying metallicity, such as $[\text{Fe}/\text{H}] = -1.27$ to -2.06 [7]. Its importance is due to being one of the observables in galactic absorption spectra [8]. Spectral lines provide information on the content of ^{19}F across galactic material, the abundance of which cannot be explained, and its exact origins are poorly understood [7]. Federman et al. [8] presented the first measurement using FUSE, Far Ultraviolet Spectroscopic Explorer to measure the Fluorine abundance. Abia et al. [6] studied the fluorine abundances inside AGB stars, the content of which is not completely understood either. By Lucatello et al. [7] it has further been noted that upper limits of fluorine for low-mass ($2M_{sun}$), low metallicity AGB models are not in agreement. It is important to obtain further information on ^{19}F creation at relevant temperatures, for AGB stars this occurs between the temperatures of 20 MK [9] upto 200 MK [10].

Further understanding of the abundance of ^{19}F may also enable more accurate modelling of core-collapse supernovae, novae and Wolf-Rayet stars. Wolf-Rayet stars are very massive

stars that are rich in CNO material [7] and typically have a mass of 25-30 M_{sun} . Many Wolf-Rayet stars are stars that have passed through the red supergiant phase [11]. Fluorine may also be produced in White Dwarf mergers [12]. Note however ^{19}F has only been proven, and witnessed to be produced in AGB stars. There has been disagreement with theory and observation [13] [14] on the abundance.

The abundance of any element depends on its production and destruction/decay rate. For ^{19}F , which is stable, its destruction depends largely on the proton and alpha capture rates. In AGB stars ^{19}F destruction depends on the reaction rates of $^{19}\text{F}(\alpha, p)^{22}\text{Ne}$ [14], $^{19}\text{F}(p, \alpha)^{16}\text{O}$ and $^{19}\text{F}(n, \gamma)^{20}\text{F}(\beta)^{20}\text{Ne}$ [15]. The production of ^{19}F can be dependent upon ^{14}N from the CNO cycle; providing temperatures are high enough, around 100 MK; so $^{14}\text{N}(\alpha, \gamma)^{18}\text{F}(\beta^+ \nu)^{18}\text{N}(p, \gamma)^{19}\text{F}$ [9]. It can also be formed through $^{15}\text{N}(\alpha, \gamma)^{19}\text{F}$ [16] via direct capture or through the 364 keV resonance [10]. The CNO cycle provides ^{13}C which can then react via $^{13}\text{C}(\alpha, n)^{16}\text{O}$. The neutrons this produces then react via $^{14}\text{N}(n, p)^{14}\text{C}$. This $^{13}\text{C}(\alpha, n)^{16}\text{O}$ reaction can be considered to be absorbing α particles, but more importantly, producing protons, inside the helium burning shell so that $^{14}\text{N}(\alpha, \gamma)^{18}\text{F}(\beta^+)^{18}\text{O}(p, \alpha)^{15}\text{N}(\alpha, \gamma)^{19}\text{F}$ can occur [17], where the $^{15}\text{N}(\alpha, \gamma)^{19}\text{F}$ reaction rate can ultimately change the abundance of ^{19}F .

The $^{15}\text{N}(\alpha, \gamma)^{19}\text{F}$ reaction occurs in the He burning region [17] during the thermal pulses. This reaction may proceed through a resonance or direct capture. The direct capture reaction has never been directly measured before until this work, so it contributes significantly to the uncertainty of ^{19}F abundance.

1.2.2 Massive stars

Massive stars can be considered the main source of heavy element production in the Universe [18]. For this reason alone studies offer an important and exciting opportunity to explain element production in the Universe and also its make-up. As explained by Zinnecker and Yorke [18] the elements produced in massive stars are ejected into the Universe through, amongst other things, expanding hydrogen regions and supernovae explosions.

Massive stars are so named as they are more massive than main sequence stars. Their exact formation mechanism is a point of research in itself, they are thought to be formed through two key mechanisms [19].

- Either they form in a similar process as a main sequence star, where material collapses under its own gravity. The collapse causes an increase in pressure in turn causing rapid temperature increase and so burning begins inside the core of the newly formed stellar

object. Molecules break down and become nuclei as the material begins to contract. Note that in this formation method the initial mass of the mass collapse is correlated with the final mass of the star.

- The competing theory is that several smaller stellar bodies in a cluster compete for matter, eventually those smaller stellar objects accrete the material from smaller stars due to their weaker gravitational fields. The mass of the massive star formed this way has no dependence upon the initial mass as the accretion process is ongoing. However when a star reaches $\sim 10M_{sun}$ the outward radiation pressure halts further mass gain. Accretion induced collisions in a dense young stellar cluster were shown by Bonnell et al. [20] to bypass this issue to allow formation of more massive stars.

Initially, as with main sequence stars a massive star is largely hydrogen and so the nucleosynthesis occurs through hydrogen burning, via the CNO cycle. The inward pressure of the outer layers due to the high mass of the star causes fusion beyond carbon to occur. The heaviest nuclei are found in the core of the massive star, which towards the end of its burning phase will be predominantly iron. At this point the star will exhibit an onion like structure with lighter nuclei towards the outside of the star.

The formation of heavier elements beyond iron in massive stars through the s-process is heavily reliant upon the abundance of neutrons. These neutrons come largely from $^{22}\text{Ne}(\alpha, n)^{25}\text{Mg}$. Where the ^{22}Ne is made from converted CNO material, especially ^{14}N [21]. It must be noted that CNO material is catalytically used in Hydrogen burning, as such it must be present in the initial composition of the star.

$^{22}\text{Ne}(\alpha, n)^{25}\text{Mg}$ is also in competition with other α -capture reactions, such as $^{22}\text{Ne}(\alpha, \gamma)^{25}\text{Mg}$, the latter not yielding a neutron for the s-process [22] [23]. The removal of α particles from the system effectively inhibits the s-process.

There is competition between ^{56}Fe for neutrons and other lighter nuclei. ^{56}Fe is the starting point for the s-process and is frequently referred to as the s-process seed. Here we shall investigate one of these key competing neutron absorption reactions.

From helium burning ^{12}C is created and in-turn this may proceed via $^{12}\text{C}(\alpha, \gamma)^{16}\text{O}$, forming ^{16}O . ^{16}O can react via $^{16}\text{O}(n, \gamma)^{17}\text{O}$, hence absorbing a neutron. The reaction at this point has removed one available neutron from the system that is no longer free for the s-process. ^{17}O may proceed via $^{17}\text{O}(\alpha, \gamma)^{21}\text{Ne}$ or $^{17}\text{O}(\alpha, n)^{20}\text{Ne}$. With the latter returning the neutron absorbed by ^{16}O back into the star, hence no neutron has been “lost” from the star. If a capture of a neutron occurs onto an isotope at a significant rate and it is not later returned to the star then that isotope can be described as a neutron poison. The ratio at which these two

reactions, $^{17}\text{O}(\alpha,\gamma)^{21}\text{Ne}$ and $^{17}\text{O}(\alpha,n)^{20}\text{Ne}$ occur directly affects the number of free neutrons for the s-process, and hence to what extent ^{16}O is a neutron poison.

There are two key reasons for a nucleus being a significant neutron poison. Firstly, the neutron capture cross-section must be high enough. As discussed later the spectroscopic factor for the ^{17}O ground state as $^{16}\text{O}+n$ is large and this is suggestive that the ^{17}O nucleus resembles closely that of $^{16}\text{O}+n$. Those states where the capture is likely may have a larger spectroscopic factor. The second reason for a nucleus being a notable neutron poison is that it must exist in significant quantities. As discussed by Taggart et al. [24] ^{16}O is produced in significant quantities inside the star and, as discussed earlier, it only relies on the production of ^{12}C and ^4He . Pignatari et al. [5] further detail the large abundance of ^{16}O present in this stellar environment.

The existence of ^{16}O does not depend on the initial metallicity of the star because its formation depends solely on the occurrence of the He burning phase. With decreasing heavy s-process seed nuclei flux within a star, so the efficiency of ^{16}O as a neutron poison increases due to the lack of competing neutron absorption reactions.

The ratio of $^{17}\text{O}(\alpha,\gamma)^{21}\text{Ne}$ and $^{17}\text{O}(\alpha,n)^{20}\text{Ne}$ will still ultimately dictate to what extent ^{16}O is a neutron poison. Figure 1.3 shows the effect of simply changing the $^{17}\text{O}(\alpha,\gamma)$ rate by a factor of 10, or equivalently changing the ratio of $^{17}\text{O}(\alpha,\gamma)^{21}\text{Ne}$ and $^{17}\text{O}(\alpha,n)^{20}\text{Ne}$ by a factor of 10.

Note that without the inclusion of rotation induced mixing the production ratio of s-process nuclei is far under predicted. The difference between a rotation inclusive model, circles and diamonds, compared to the model with varied $^{17}\text{O}(\alpha,n)^{20}\text{Ne}$ ratio is somewhat extraordinary. A well defined definition of this ratio could help explain s-process production and ultimately heavy element formation in massive stars. The mixing of the Hydrogen and Helium burning layers allows production of ^{22}Ne . Hence, rotation increases the rate of the s-process, especially at low Z [25].

It must be noted that production of the neutron poison ^{16}O does not depend on the initial metallicity of the star as it is produced during the helium burning phase through $^{12}\text{C}(\alpha,\gamma)$. So, in a star with reduced metallicity the neutron capture efficiency of ^{16}O increases due to reduced competition from the s-process and its seed nuclei. The importance of the $^{17}\text{O}(\alpha,n)^{20}\text{Ne} / ^{17}\text{O}(\alpha,\gamma)^{21}\text{Ne}$ ratio is highlighted by Rayet and Hashimoto [26].

During the work presented in this thesis the intermediate nucleus, ^{21}Ne was studied. It was populated through a neutron transfer using the reaction $^{20}\text{Ne}(d,p)^{21}\text{Ne}$. This work contributes to the understanding of the $^{17}\text{O}(\alpha,n)^{20}\text{Ne}$ reaction rate and hence the $^{17}\text{O}(\alpha,n)^{20}\text{Ne} / ^{17}\text{O}(\alpha,\gamma)^{21}\text{Ne}$ ratio. Performing the $^{20}\text{Ne}(d,p)^{21}\text{Ne}$ reaction populated states in ^{21}Ne , in-

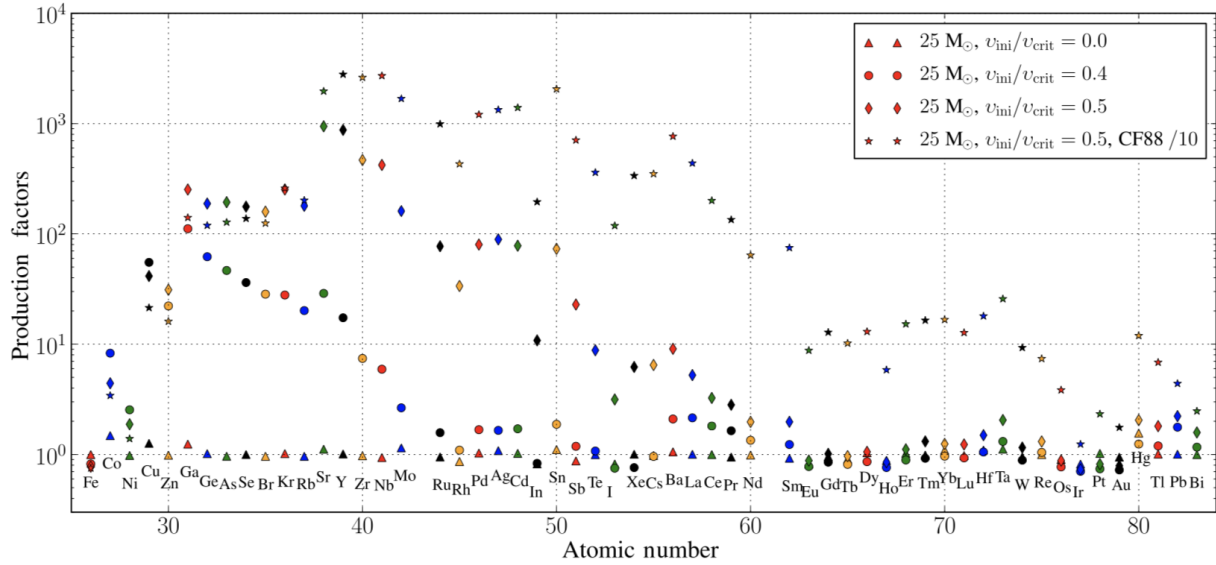


Figure 1.3: Production factors for nuclei formed inside a massive star, figure from Frischknecht et al. [25]. Triangles represent a model without rotation, here nuclei formed by the s-process are insufficiently produced. Circles and diamonds represent a model that includes rotation. Stars represent a model in which the $^{17}\text{O}(\alpha, \gamma)$ rate is reduced by a factor of 10 and has the same rotation as the diamonds. v_{ini} represents the initial velocity at the stars surface, and v_{crit} the critical surface rotation velocity which is the surface velocity where the gravity at the equator equals the force required to stop the loss of matter from the stars surface [25].

cluding those with largest neutron widths, discussed in section 2. The reaction most strongly populated those intermediate ^{21}Ne states where the alpha capture reaction is most likely to proceed via $^{17}\text{O}(\alpha, n)^{20}\text{Ne}$.

Chapter 2

Theoretical Considerations

2.1 Reaction theory

2.1.1 Reaction cross-section

The reaction cross-section provides a measure of the likelihood of a reaction to occur and is fundamental in making measurements within nuclear physics. The formula to calculate the total reaction cross-section can be seen in eqn. 2.1.

$$\sigma = \frac{N_R}{\epsilon N_B N_T} \quad (2.1)$$

where N_R refers to the number of outgoing resultant particles, recoils, from a given reaction per unit time, N_B the number of beam particles per unit time, N_T the number of target particles per area² and ϵ is the total efficiency, including all experimental efficiencies. Where the values for number of recoil and beam particles must be measured over the same time period.

The cross-section of a narrow resonance is described by the Breit Wigner cross-section as seen in eqn. 2.2 [27].

$$\sigma_{BW}(E) = \frac{\lambda^2}{4\pi} \frac{(2J+1)}{(2J_t+1)(2J_p+1)} \frac{\Gamma_\alpha(E)\Gamma_\gamma(E)}{(E_r - E)^2 + (\frac{\Gamma(E)}{2})^2} \quad (2.2)$$

where λ is the de Broglie wavelength of the resonance; J , J_t , J_p are the total angular momenta of the resonance and that of the target and projectile respectively; $\Gamma_{ent}(E)$ and $\Gamma_{exit}(E)$ are the partial widths of the entrance and exit channels respectively; and E_r and E are the resonance energy and particle energy respectively.

It must be noted that, except in specific circumstances reactions are seldom isotropic which leads to a dependence on the angle for the reaction cross-section, the differential cross-section. When calculating transferred angular momenta for reactions one must consider the differential cross-section which is the cross-section per unit solid angle as described in eqn. 2.3 and is comparable to eqn. 2.1.

$$\frac{d\sigma}{d\Omega} = \frac{N_R(\Omega)}{\epsilon N_B N_T} \frac{1}{d\Omega} \quad (2.3)$$

where $d\Omega$ refers to the solid angle coverage and $N_R(\Omega)$ indicates the dependence of N_R on the angle relative to the beam. The differential cross-section varies with angle θ , where θ is the angle of the outgoing resultant particles trajectory compared to the ingoing trajectory. The function with which the differential cross-sections vary depend primarily on the transferred angular momentum and hence the populated state. Using the differential cross-section, predictions can be made about the transfer of angular momentum during a reaction.

2.1.2 Gamow window

To measure nuclear reactions at astrophysically relevant reaction energies the energy range which is most relevant for the stellar environment must be calculated. The Gamow window is the energy range at which most nuclear reactions will occur for a given stellar temperature. It is the product of the Maxwell Boltzmann distribution of particle energies and the probability of tunnelling through the Coulomb barrier. The centroid and width of the Gamow window are calculated in keV by using equations 2.4 and 2.5 respectively.

$$E_G = 1.22 \times (Z_1^2 Z_2^2 \mu T_6^2)^{\frac{1}{3}} \quad (2.4)$$

$$\Delta E_G = 0.749 \times (Z_1^2 Z_2^2 \mu T_6^5)^{\frac{1}{6}} \quad (2.5)$$

where Z_1 and Z_2 are the reactants atomic numbers; T_6 the environment temperature in MK and μ is the reduced mass, given by eqn.2.6.

$$\mu = \frac{m_1 m_2}{m_1 + m_2} \quad (2.6)$$

where m_1 and m_2 are the two reactants masses. The calculation of the Gamow window allows the determination of the energy range of resonances for a given reaction that, from an astrophysics perspective, is most important.

2.1.3 S-factor

The cross-section, σ , as in eqn. 2.1, can be rescaled so that Coulomb repulsion is excluded, this is called the S-factor. It can be defined as in eqn. 2.7 [3].

$$S(E) = Ee^{2\pi\eta}\sigma(E) \quad (2.7)$$

where η is the Sommerfeld parameter defined as in eqn. 2.8 and contains the Coulomb repulsion component.

$$2\pi\eta = 0.98951013Z_1Z_2\sqrt{\frac{\mu}{E}} \quad (2.8)$$

where Z_1 and Z_2 are the charges of the two incident particles, μ is the reduced mass and E is the energy with which they collide in MeV.

2.1.4 Resonance strength

The resonance energies that are most important from an astrophysics perspective are found inside the Gamow window. To understand which of this subset of resonances dominate their reaction rates must be found. Reaction rates are determined using the resonance strength, $\omega\gamma$. For $^{17}\text{O}(\alpha,n)^{20}\text{Ne}$ the reaction rate can be seen in eqn. 2.9 and the equivalent for $^{17}\text{O}(\alpha,\gamma)^{21}\text{Ne}$ in eqn. 2.10.

$$\omega\gamma_{(\alpha,n)} = \frac{2J_{21\text{Ne}} + 1}{(2J_{17\text{O}} + 1)(2J_{\alpha} + 1)} \frac{\Gamma_{\alpha}\Gamma_n}{\Gamma_{total}} \quad (2.9)$$

$$\omega\gamma_{(\alpha,\gamma)} = \frac{2J_{21\text{Ne}} + 1}{(2J_{17\text{O}} + 1)(2J_{\alpha} + 1)} \frac{\Gamma_{\alpha}\Gamma_{\gamma}}{\Gamma_{total}} \quad (2.10)$$

where $J_{21\text{Ne}}$, $J_{17\text{O}}$ and J_{α} are the total angular momenta of: the populated state in ^{21}Ne , ^{17}O and α respectively. Γ_{total} represents the total width and is the sum of each channels partial width. Partial widths are the contribution a given channel makes towards the total width and is representative of the probability a state may be formed or proceed through a given channel.

The astrophysically important ratio of $\omega\gamma$ for $^{17}\text{O}(\alpha,\gamma)^{21}\text{Ne}$ and $\omega\gamma$ for $^{17}\text{O}(\alpha,n)^{20}\text{Ne}$ requires both equations 2.9 and 2.10. Should a partial width, Γ_x , in either of these cases be much larger than the others so the denominator, Γ_{total} , tends to equal to that of the much larger partial width and so γ reduces to a single partial width on the numerator, cancelling the denominator. In the case of $\omega\gamma_{(\alpha,n)}$ the discovery that a state has Γ_n much larger than

Γ_α so eqn. 2.9 can be reduced to eqn. 2.11.

$$\omega\gamma_{(\alpha,n)} = \omega\Gamma_\alpha \quad (2.11)$$

In the case of a thick target as with the $^{15}\text{N}(\alpha,\gamma)^{19}\text{F}$ experiment, where an entire resonance is contained within a target so the resonance strength can be found using eqn. 2.12 as seen in Taggart et al. [24].

$$\omega\gamma = \frac{2\zeta}{\lambda^2} Y_{max} \quad (2.12)$$

where λ is the DeBroglie wavelength and Y_{max} is given by eqn. 2.13,

$$Y_{max} = \frac{N_R}{\epsilon_{total} N_B} \quad (2.13)$$

where ϵ_{total} is the total efficiency. In eqn. 2.12 ζ refers to the stopping power and this is given by eqn. 2.14. The target stopping power is calculated using the reciprocal target density and the rate of beam energy loss.

$$\zeta = -\frac{V}{N_T} \frac{dE}{dx} \quad (2.14)$$

2.1.5 Reaction rate

The total reaction rate is given by eqn. 2.15.

$$\langle\sigma v\rangle = \left(\frac{8}{\pi\mu}\right)^{\frac{1}{2}} \frac{1}{(k_b T)^{\frac{3}{2}}} \int_0^\infty \sigma(E) E e^{\frac{-E}{k_b T}} dE \quad (2.15)$$

where σ is the cross-section given by eqn. 2.2 and the integral over all energies. If the resonances are narrow such that the penetrabilities and particle energies change negligibly over the resonance width so eqn. 2.15 can be simplified to the narrow resonance reaction rate formula as seen in eqn. 2.16.

$$\langle\sigma v\rangle = \frac{2\pi}{(\mu k_b T)}^{\frac{3}{2}} \hbar^2 (\omega\gamma) e^{\frac{-E_r}{k_b T}} \quad (2.16)$$

where k_b is the Boltzmann constant, T the temperature, \hbar the reduced Planck's constant, $\omega\gamma$ is the resonance strength and E_r the resonance energy.

2.2 Nuclear theory

Key nuclear quantum numbers include principal quantum number, n , total angular momentum, j , and orbital angular momentum quantum number, l , the nucleon spin, s and the parity of a state, π . Angular momentum quantum number l , is the quantum mechanical equivalent to classical angular momentum given by $r \times p$. l may assume only integer values and orbitals can be labelled by their angular momentum as s, p, d... for corresponding $l=0,1,2...$ respectively. The coupling of angular momentum, l , and spin, s forms j , the coupling of these two to form the latter can be seen in figure 2.1.

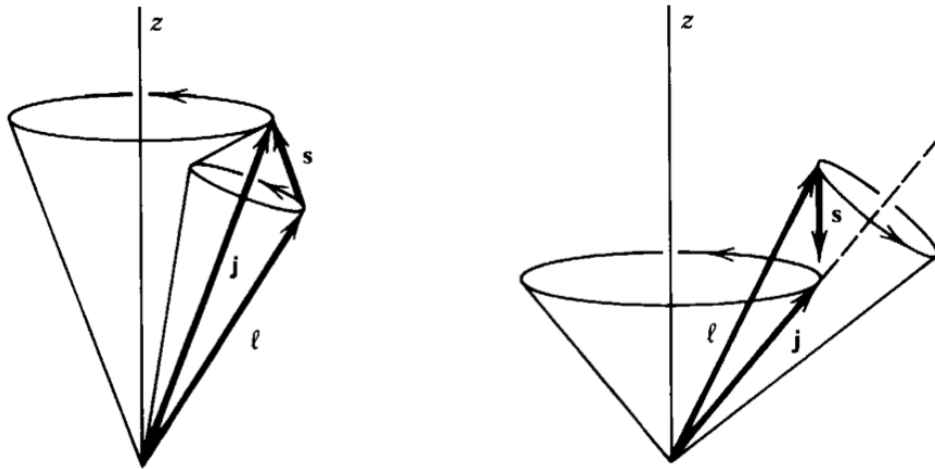


Figure 2.1: An example of angular momentum and spin coupling, diagram from Krane [28].

The coupling of the l and s to form j and their vector addition defines specific values that are allowed for the total angular momentum. An alpha particle has a ground state of 0^+ due to its two neutron, two proton arrangement. The pairing of the protons and the pairing of the neutrons means there is no net spin, s . The plus denotes the positive parity of the arrangement. Parity refers to the nature of its wavefunction, for a given function, $f(x)$, $f(x) = f(-x)$ refers to positive parity and negative parity $f(-x) = -f(x)$, or more specifically in quantum mechanics we refer to the wavefunctions and so $f(x) \rightarrow \psi(x)$. Parity of a given state, π can be found using eqn. 2.17.

$$\pi = (-1)^l \quad (2.17)$$

where l is the angular momentum of a given state. It must be noted that the parity of a collection of wavefunctions, such as the ${}^4\text{He}$ case, is related to the product of the individual

wavefunctions. Hence for any nucleus, such as ^{20}Ne , that has an even number of protons and an even number of neutrons the ground state will always have $j = 0$ and positive parity.

The 0^+ of ^{20}Ne makes the prediction of possible state angular momenta in ^{21}Ne somewhat simple. If the transferred angular momentum in $^{20}\text{Ne}(d,p)$, Δl is even (or 0) so the parity of the composite ^{21}Ne nucleus is positive and if Δl is odd so the composite nucleus parity is negative. For a Δl of 0 the resultant state in ^{21}Ne must be $j=1/2^+$, where the $1/2$ comes from the neutron spin. Other options to populate states can be seen in table. 2.1.

Transferred angular momentum, Δl	Available states in ^{21}Ne	^{21}Ne state parity
0	$\frac{1}{2}$	+
1	$\frac{1}{2}, \frac{3}{2}$	-
2	$\frac{3}{2}, \frac{5}{2}$	+
3	$\frac{5}{2}, \frac{7}{2}$	-
4	$\frac{7}{2}, \frac{9}{2}$	+
5	$\frac{9}{2}, \frac{11}{2}$	-
6	$\frac{11}{2}, \frac{13}{2}$	+

Table 2.1: Transferred angular momentum in the transfer reaction $^{20}\text{Ne}(d,p)$, Δl , total angular momentum and parity of possible ^{21}Ne states.

2.2.1 Spectroscopic factors and partial widths

In this work typically C^2S is discussed, which is the Spectroscopic factor, S , in product with the Clebsch-Gordon coefficient squared, C^2 . The Clebsch-Gordon coefficient arises from the coupling of the isospin [29] and relates to how momentum can be coupled to form the desired state momentum. C^2S can be considered the probability of nucleons arranging themselves

like a given final state or equivalently the single particle state, as such it can be written as in eqn. 2.18 [3].

$$\Gamma = C^2 S \Gamma_{sp} \quad (2.18)$$

Or more colloquially, how much the final state behaves like its constituent nuclei. So in the important case in this work, $^{20}\text{Ne}(d,p)^{21}\text{Ne}$, how much ^{21}Ne behaves like $^{20}\text{Ne}+n$. Predictions for the spectroscopic factor are somewhat difficult. It should be noted that for the ^{21}Ne ground state the spectroscopic factor for $^{20}\text{Ne}(d,p)$ is 0.11 [30]. Due to the 0^+ nature of ^{20}Ne and hence its even-even arrangement the spectroscopic factor of 0.11 for $^{20}\text{Ne}(d,p)$ is much smaller than that which would be intuitively predicted, this is potentially suggestive of a deformed nucleus. The first ^{21}Ne excited state spectroscopic factor is 3.7 [30]. This implies that relative to the ground state the first excited state of ^{21}Ne represents a $^{20}\text{Ne}+n$ nucleus arrangement more closely. However the equivalent spectroscopic factor for the addition of the neutron to the 0^+ ground state of ^{16}O , making ^{17}O , is 0.9 [31], implying that ^{17}O nucleus ground state represents a nucleus that resembles closely that of $^{16}\text{O}+n$. The latter is not so surprising given the closed shell nature of the ^{16}O nucleus.

By obtaining the experimental differential cross-sections and scaling the single particle width, the value of C^2S is obtained. The neutron widths for each state can be extracted using eqn. 2.19 [32].

$$\Gamma_n = 2 \frac{\hbar^2}{\mu r} P C^2 S \theta_{sp}^2(r) \quad (2.19)$$

where r is the reaction radius, P the penetrability factor and $\theta_{sp}^2(r)$ the square of the single particle radial wavefunction at radius, r . The penetrability of the Coulomb and centrifugal barrier can be seen in eqn. 2.20 [32].

$$P = \frac{kr}{F^2 + G^2} \quad (2.20)$$

where k denotes the channels wavenumber, r the interaction radius, F and G are Coulomb wavefunctions, representing the regular and irregular components. It can be seen as in Iliadis [3] that despite the lack of Coulomb barrier an $l=0$ transfer for a neutron has an energy dependence of approximately $E^{\frac{1}{2}}$, derived from $E^{l+\frac{1}{2}}$.

2.2.2 Wigner limit

The Wigner limit is the maximum possible value a reduced partial width γ^2 may take and is given by eqn. 2.21 [33].

$$\gamma_\lambda^2 \leq \frac{3}{2} \frac{3\hbar^2}{2\mu a^2} \quad (2.21)$$

where γ represents a reduced partial width which relates to a partial width by eqn. 2.22.

$$\Gamma = 2P\gamma^2 \quad (2.22)$$

2.2.3 Optical model

To extract a C^2S , spectroscopic factor, and hence find a partial width for a given state a comparison between the measured differential cross-section of a state and a calculation of the differential cross-section for the case where ^{21}Ne wavefunction is comprised entirely of a ^{20}Ne wavefunction and a neutron wavefunction, also known as the single particle wavefunction, is required. To calculate this we can use the optical model.

The optical model treats the beam particle as an incoming planar wave and the target nucleus as a spherical, partially opaque object. Using typical notation, as in Krane [28], the scattering can be represented as a potential, $U(r)$, of two components, a real part, $V(r)$ that represents the elastic scattering component and an imaginary part that represents the absorption, $W(r)$. These components can then further be broken down, comparably as in Koning and Delaroche [34], or where some of the potentials in this work are extracted from, as in Varner et al. [35]. The potentials consist of a volume potential, a surface potential and a spin-orbit potential. These were extracted from literature based on appropriate interaction energies. The potentials were used in the input file for the DWBA, Distorted Wave Born Approximation code FRESKO [36].

The overlaps take into account the overlap of the wavefunctions between key clusters such as the overlap of the neutron and proton in the deuteron and the overlap between the neutron and ^{20}Ne in forming ^{21}Ne . Where the angular momentum transferred, and possible ^{21}Ne states can be defined as in table. 2.1.

Also important to note is the number of radial nodes in the wavefunction. In FRESKO we include the centroid as a node, including, counter-intuitively the centre of the s, or $l=0$ orbital, which very strictly speaking does not contain a node at $r=0$.

Considering the shell model structure, the number of wavefunction nodes is dependant

upon the principal quantum number and must be calculated for the resulting ^{21}Ne nucleus considering the transferred angular momenta values of the neutron.

Elaboration on the values used in the FRESCO calculation for the optical potentials, radius of interaction and other key parameters are discussed later in section 10.9. In order to calculate the single particle differential cross-sections FRESCO uses the DWBA. This assumes the core, previously described here as an optically opaque object, causes a perturbation to the wavefunction of the incoming particle.

Chapter 3

$^{15}\text{N}(\alpha,\gamma)^{19}\text{F}$ Previous Measurements

Measured reaction cross-sections already existed for $^{15}\text{N}(\alpha,\gamma)^{19}\text{F}$, however, prior to this work the direct capture cross-section had never been directly measured and a 40 % uncertainty has been adopted [37]. There were also unresolved discrepancies between measurements of the 1.323 MeV resonance with regards to both its width and its energy. The ^{19}F level scheme can be seen in figure 3.1 from Lennarz [38], where the α separation energy is 4.0138 MeV. This allows identification of the Gamow window, shaded in figure 3.1 and hence which states are most likely to be populated inside the stellar environment. In this work measurement inside the Gamow window did not occur. Instead the measurement addressed the 1.323 MeV resonance discrepancies and direct capture cross-sections were extracted.

There are several previous measurements of the $^{15}\text{N}(\alpha,\gamma)^{19}\text{F}$ reaction. In 1969 Aitken et al. [39] measured 13 new resonances in $^{15}\text{N} + \alpha$, including a measurement of the 1.323 MeV resonance, measured as the $E_\alpha = 1.681$ MeV. The target was a solid tantalum backed titanium nitride target using a beam of ^4He with currents upto 100 μA . Carbon build-up would have been significant due to this beam current. The build-up of carbon was reduced using a liquid nitrogen cooling system. $\omega\gamma$ was found to be 1.30 ± 0.20 eV for the 1.323 MeV energy resonance. Aitken et al. [39] used the $^{14}\text{N}(\alpha,\gamma)^{18}\text{F}$ 1.532 MeV energy resonance from Price [40, 41] applying the Snover correction [42], which yielded an $\omega\gamma$ of 1.24 ± 0.10 eV for the comparison $^{14}\text{N} + \alpha$ resonance. The comparison point used here was later shown to be unreliable as Dixon and Storey [43] used an $\omega\gamma$ of 1.34 ± 0.11 eV for the same energy $^{14}\text{N} + \alpha$ comparison resonance in 1971. The reliability of the relative comparison resonance brings into question this measurement.

In 1971 Dixon and Storey measured the $^{15}\text{N}(^7\text{Li},\text{t})^{19}\text{F}$ reaction [43]. Three measurements of the 1.323 MeV energy $^{15}\text{N} + \alpha$ resonance were conducted. These consisted of a comparison of $^{14}\text{N}(\alpha,\gamma)^{18}\text{F}$ and $^{15}\text{N}(\alpha,\gamma)^{19}\text{F}$, a comparison of the relative strength of $^{15}\text{N}(\text{p},\alpha\gamma)^{12}\text{C}$ and

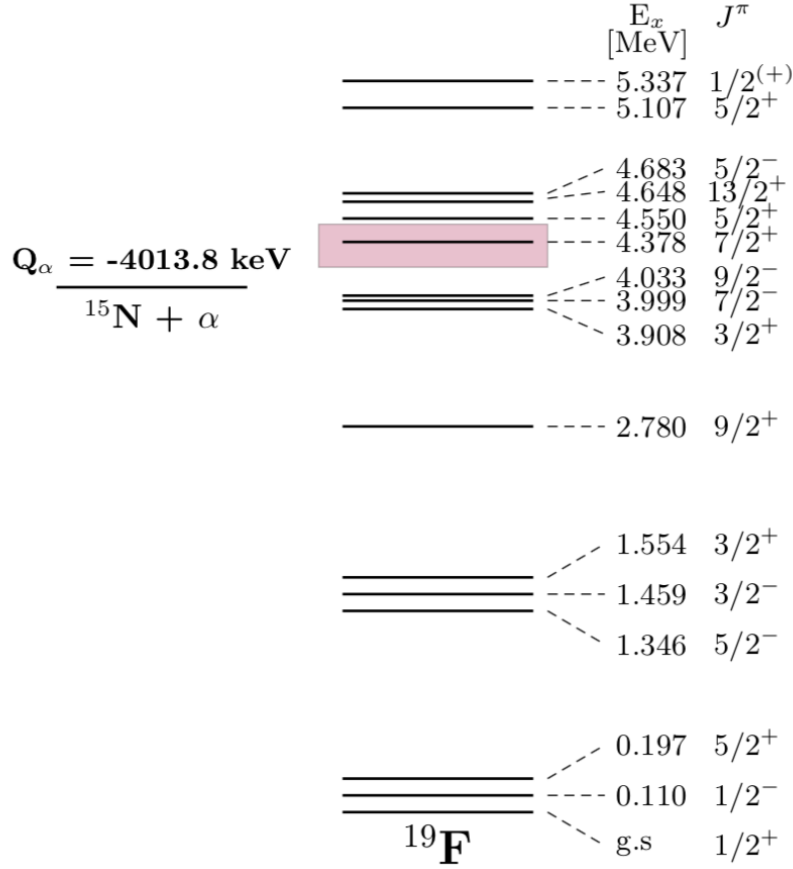


Figure 3.1: ^{19}F states where the Gamow window at 200 MK is highlighted, figure from Lennarz [38].

the third was an absolute measurement of the resonance strength.

A titanium nitride solid target with cooling ring was used and a helium beam of energy 1.68 MeV whose integral was found using a current integrator, accurate to 2%. The γ -ray germanium detector had a resolution of 2.8 keV at 1.332 MeV and was calibrated using the $^{23}\text{Na}(p,\gamma)^{24}\text{Mg}$ reaction at $E_p=1416$ keV, as it produces three γ energies with known ratios. The stopping power in the nitride target is difficult to predict but required to calculate the resonance strength as seen in equations 2.12 and 2.14. Dixon and Storey note that at the α energies used it was preferable according to earlier literature to adopt proton stopping powers and then from these calculate the alpha stopping powers. They note that Chu and Powers [44] had measured the stopping powers of α particles in titanium from 0.4-2 MeV, which were utilised, and higher energies used the proton stopping power adjustment. This method and other data at 9-10 MeV allowed stopping powers with 5% accuracy to be calculated.

The target was found to have a $^{15}\text{N}/^{14}\text{N}$ ratio of 0.35 ± 0.02 and was found to be 30 keV deep. They found the ratio of the $\omega\gamma(^{19}\text{F } E_\alpha=1.68 \text{ MeV})/\omega\gamma(^{18}\text{F } E_\alpha=1.53 \text{ MeV}) = 1.21\pm 0.11$. Dixon et al. used a measurement of the ^{18}F resonance strength from Parker et al. [45] as $1.60\pm 0.13 \text{ eV}$. They corrected this using the Chu and Powers [44] stopping power measurement, resulting in a corrected value of $1.34\pm 0.11 \text{ eV}$. This is the comparison point that differs from the Aitken work [39]. Using this first comparison method they find the resonance strength of the $E_\alpha=1.53 \text{ MeV}$ resonance, 1.323 MeV resonance as $1.62\pm 0.20 \text{ eV}$.

The second method compared the $^{15}\text{N}+\alpha$ 1.323 MeV energy resonance strength with the $^{15}\text{N}(\text{p},\alpha\gamma)^{12}\text{C}$ resonance at $E_p=0.898 \text{ MeV}$. The target had to be thicker due to the reduced energy losses of protons and the beam current used was restricted to $0.1 \mu\text{A}$ so the detectors did not have to be moved between the $^{15}\text{N}(\alpha,\gamma)^{19}\text{F}$ and the $^{15}\text{N}(\text{p},\alpha\gamma)^{12}\text{C}$ measurement. Note that Dixon and Storey were unable to ascertain whether their comparison point of the $^{15}\text{N}(\text{p},\alpha\gamma)^{12}\text{C}$ reaction resonance strength at $E_p = 0.898 \text{ MeV}$ was in the lab or centre of mass frame, they assumed the latter. The resonance strength used was from Gorodetzky et al. [46] as $480\pm 48 \text{ eV}$. Three targets were used and the average $\omega\gamma$ obtained for the 1.323 MeV energy resonance was $1.72\pm 0.20 \text{ eV}$, with a spread in target yield of 20% and resonance strengths of 10%. Note the uncertainty in the comparison point and the potentially incorrect frame of reference.

Efficiency calibrations of the detectors were made using a ^{60}Co source for the absolute measurement. Due to the dependency of the resonance strength on the stopping powers the target composition must be known accurately. Assuming a 1:1 ratio of N:Ti in the target so the resonance strength was found to be 1.03, 1.12 and 1.19 eV for each target. It is noted that with a lower ratio of ^{15}N to Ti so the resonance strength would increase. Due to the disagreement between the relative measurements and the absolute measurements the target content was scrutinised further. The make-up of the target was tested using several previously measured comparison reactions. $^{14}\text{N}(\alpha,\gamma)^{18}\text{F}$ was used to search for the $E_\alpha=1.53 \text{ MeV}$ resonance which was not found so the amount of ^{14}N was assumed negligible compared to the amount of ^{15}N . The levels of oxygen, titanium and carbon were checked, though the authors note the target sustained substantial carbon deposition. The ^{15}N was found to comprise 0.79 ± 0.13 of the target. This target correction, based on the resonance strength measurements of others, changes the absolute $\omega\gamma$ from 1.19 eV to $1.5\pm 0.3 \text{ eV}$.

In 1996 Oliveira et al. [47] published the results of an experiment where they performed a transfer reaction using the reaction $^{15}\text{N}(^7\text{Li,t})^{19}\text{F}$ at Orsay. Detection was via a split-pole spectrometer, used to detect the forward tritons. Differential cross-section distributions were extracted for states in ^{19}F . Oliveira et al. state that the selection of an enriched ^{15}N gas target

was due to early, solid target experiments being problematic due to carbon contamination.

Beam current was monitored using a Faraday cup behind the nickel exit window. Further monitoring occurred using the off-axis Si detector, which detected elastically scattered beam particles. The particles produced could exit via a mylar window into the split-pole spectrograph. The experiment had an approximate resolution of 100 keV so resolving some of the ^{19}F states such as those at 4.033 MeV, 3.999 MeV and 3.908 MeV wasn't possible.

The calibration was based on other ^{19}F levels and was deemed straightforward by Oliveira et al. due to spectra with minimal background and a broad range of ^{19}F states upto 5 MeV. The 4.378 MeV energy state was seen in each spectrum but was weakly populated. Resonances with energies of 0.536 MeV and 0.542 MeV were treated as a single resonance, two levels at 0.634 MeV as well as 0.669 MeV were also seen, these were also treated as a single resonance. A weak peak was seen corresponding to the 1.093 MeV $^{15}\text{N}+\alpha$ resonance. Oliveira et al. also find the spin parity of the 4.378 MeV energy state to be $7/2+$ using a comparison of differential cross-sections with PTOLEMY and DWUCK 5 calculations. The fit of the 4.378 MeV is shown below in figure 3.2 at 15° in the centre of mass frame. Note how despite experimental resolution the peak is resolvable from the neighbouring peaks. A resonance strength, $\omega\gamma$, of $6_{-3}^{+6} \times 10^{-9}$ eV was extracted for this 0.364 MeV resonance.

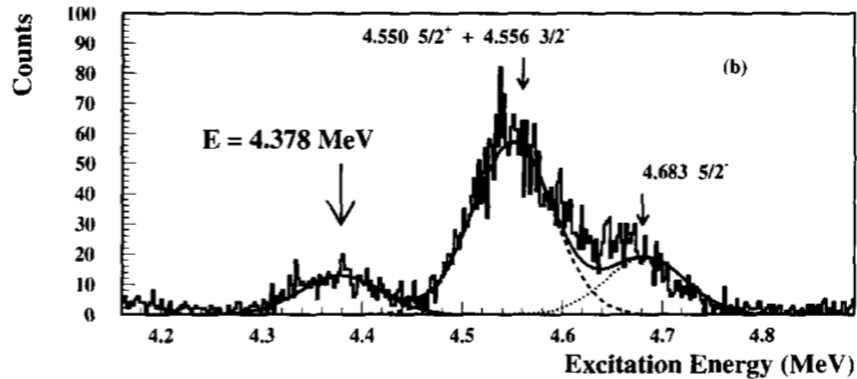


Figure 3.2: Part of the energy spectrum showing the 4.378 MeV state at 15° in the centre of mass frame from Oliviera et al. [47].

Due to the resolution of the detector it was not possible to resolve the 4.550 MeV and 4.556 MeV or the 4.648 MeV and 4.683 MeV states, 4.378 MeV and 5.107 MeV were also measured, an extract of the spectra can be seen in figure 3.2. The 1.323 MeV resonance was not measured here.

In 2002 Wilmes et al. [16] measured the $^{15}\text{N}(\alpha,\gamma)^{19}\text{F}$ reaction. A ^{15}N enriched gas target was used, utilising the Rhinoceros target setup [48] and Dynamitron accelerator at

Stuttgart supplying a He^+ beam. The target was a differentially pumped gas target with the ion beam passing axially, perpendicular to the gas inlet jets. Target pressures were typically at ~ 0.75 Torr. The beam was monitored using surface barrier detectors, detecting elastically scattered beam from the target. γ -rays were detected using two high purity germanium detectors. The efficiency of detection was predicted using a Geant simulation with known and proven reliability from previous measurement comparison.

Amongst the measurement of 14 resonances was the 1.323 MeV energy $^{15}\text{N}+\alpha$ resonance. The parity of the populated 5.337 MeV state in ^{19}F was confirmed as positive and the spin parity assigned as $\frac{1}{2}^+$. The resonance strength, $\omega\gamma$ was found to be 1.69 ± 0.14 eV and the width, Γ found to be 1.3 ± 0.5 keV with the γ partial width, Γ_γ found to be 1.69 ± 0.14 eV, thus as stated by Wilmes et al. $\Gamma_\alpha \approx \Gamma$ for this resonance. The measured 5.337 MeV energy ^{19}F state can be seen in figure 3.3.

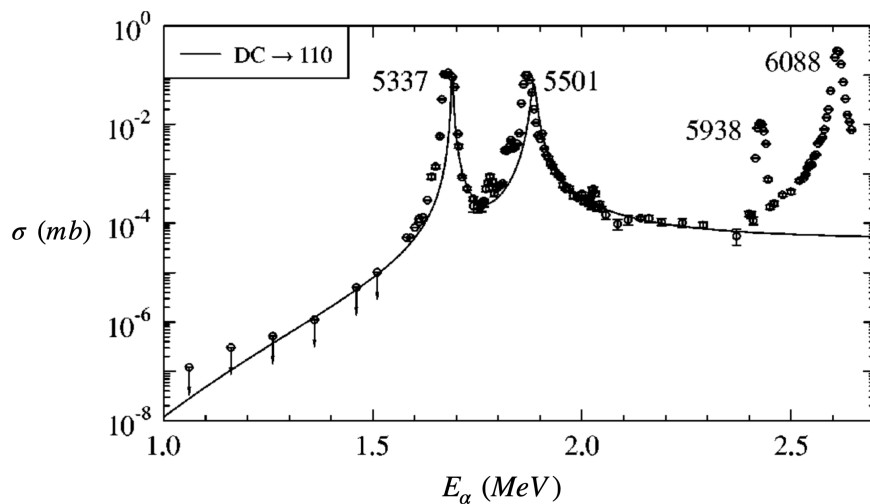


Figure 3.3: Resonances of 5.337 MeV and 5.501 MeV and corresponding cross-sections. Figure adapted directly from Wilmes et al. [16].

The direct capture was also calculated around the 5.537 MeV ^{19}F state as seen in figure 3.3. It was noted that when off resonance the tails of the 5.337 MeV and the 5.501 MeV dominate the region and as such the tails produce an energy dependent cross-section. Due to the resonance tails a true direct capture in this energy region is hard to measure.

Di Leva et al. [27] used ERNA, the European Recoil separator for Nuclear Astrophysics in 2017 to measure the $^{15}\text{N}(\alpha,\gamma)^{19}\text{F}$ reaction. The previously measured resonances at 1.323 MeV and 1.487 MeV were measured. They extracted the Γ_α and Γ_γ , finding agreement for the 1.487 MeV resonance widths with previous measurements. The 1.323 MeV measurement yielded significant characteristic differences to previous measurements. Di Leva et al. found

the resonance to have an energy of 1.3314 ± 0.0016 MeV, not the previous value of 1.323 MeV. This previous value of 1.323 MeV for the resonance energy can be seen in Tilley et al. [49] as $E_x = 5.337 \pm 0.002$ MeV.

Similarly to this DRAGON measurement the ERNA measurement was conducted in inverse kinematics with a ^4He windowless gas target and a ^{15}N beam. The beam energy was checked using a 90° analysing magnet. This beam bending also removed significant beam contamination, including those of similar mass-charge ratio to Fluorine recoils.

The gas cell of ERNA is differentially pumped with an effective length of 300 mm. With this length of gas cell the angular acceptance was poor, so the gas cell was sectioned, reducing the effective length of the gas cell, containing $(0.54 \pm 0.03) \times 10^{18}$ atoms/cm². An Argon gas post target component was used to ensure that the recoils reached a charge state equilibrium, regardless of reaction coordinates within the target. This Argon gas component's effective thickness was measured using a $^{19}\text{F}^{2+}$ beam. The Helium gas target pressure was 4 mbar, equivalently ≈ 3 Torr, which gave a total target thickness of $(0.54 \pm 0.03) \times 10^{18}$ atoms/cm².

The charge state fraction for ^{19}F ions were characterised and the separation of ^{19}F ions and ^{15}N beam examined. Di Leva et al. [27] gives an example of a ΔE -E spectrum equivalent, as seen in figure 3.4. The ^{19}F ions could be effectively separated from the beam.

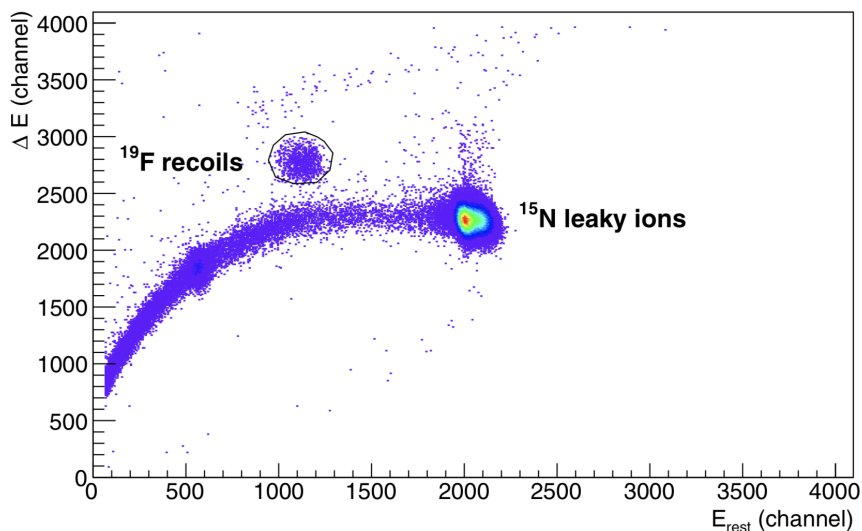


Figure 3.4: Sample ΔE -E spectrum showing ion identification. Figure from Di Leva et al. [27]

Di Leva et al. [27] described the reaction yield as in eqn. 3.1.

$$Y_i = N_p \Phi_q T_{RMS} \eta \int_{E_{15N-T_t}}^{E_{15N}} \frac{\sigma(E)}{\epsilon(E)} dE \quad (3.1)$$

where N_p is the number of ^{15}N ions onto the target; Φ_q is the ^{19}F charge state fraction probability, with charge state $q+$; T_{RMS} is the separator recoil transmission in charge state $q+$; η is the detection efficiency; the integral is over the entire target, with the limits being the energy at the front and back of the target; $\epsilon(E)$ is the stopping power of the ^{15}N ions in the ^4He gas target. With the extraction of all these properties the cross-section $\sigma(E)$ can be found. The stopping power over the target changes negligibly and as such Di Leva et al. took an average value of $77.2 \text{ keV cm}^2/10^{18}$ atoms.

The Breit-Wigner cross section was calculated using the Breit-Wigner formula as in eqn. 2.2 [27]. The result of the Di Leva et al. [27] measurement can be seen in table 3.1. Di Leva et al. conclude that the Γ_α values found increased the contribution to the reaction rate by approximately 15% at astrophysically relevant energies.

	1323 keV resonance	1487 keV resonance
E_r keV	1331.4 ± 1.6	1486.1 ± 1.9
Γ_γ	1.62 ± 0.09	2.2 ± 0.2
Γ_α	2.51 ± 0.10	6.0 ± 0.3

Table 3.1: Results from 2017 Di Leva et al. [27] measurement using ERNA for two key resonances.

In summary two contradicting measurements exist for the 1.323 MeV energy $^{15}\text{N}+\alpha$ resonance, with ambiguity in both its energy and its strength. Note also how minimal information is available on the direct capture cross-sections of $^{15}\text{N}(\alpha,\gamma)^{19}\text{F}$ as it is yet to be measured outside significant resonance tails.

Chapter 4

$^{15}\text{N}(\alpha,\gamma)^{19}\text{F}$ Experimental Technique

4.1 Beam production

DRAGON, Detector of Recoils And Gammas Of Nuclear reactions is located in the Isotope Separation And Accelerator hall I, ISAC-I facility at TRIUMF. The production of the stable ^{15}N beam was conducted using the OffLine Ion Source, OLIS [50]. To produce the beam a ^{15}N enriched gas bottle supplied the ^{15}N which was injected into a plasma chamber, where magnetic fields confined the plasma. The plasma chamber was split into high and low electron energy regions. Electrodes extracted the positively charged beam [50]. OLIS was located just upstream of the Radio Frequency Quadropole, RFQ, which upon extraction from OLIS was the next point of beam acceleration. The layout of ISAC-1 is depicted in figure 4.1.

The RFQ raised the beam energy and requires charge/mass $\geq 1/30$. This allowed energy boosting on nuclei with 2 keV/u by 75 times, upto 150 keV/u [52]. The RF buncher operated at 11.66 MHz, which equates to a period of approximately 86 ns.

After the RFQ the beam then passed into a 105 MHz Drift-Tube Linac; DTL, where the level of acceleration is variable and the A/q of the beam is between 3 and 6. By using alternate polarity across the drift tubes so the ions were attracted to the end of the drift tube arrangement, as such the ions gained energy through the series of drift tube charge cycles. This has the potential to raise the beam energy to between 0.15 MeV/u and 1.8 MeV/u [53].

Throughout the beam delivery process quadrupoles allowed the beam to be focused axially and the dipoles allowed steering of the charged ions to allow path manipulation through the facility. It must be noted in this case all ions that were still within the beam were those with the same or similar mass/charge ratio. Hence few of these contaminants were present at the beam destination, into the target of DRAGON. Typical beam intensities were 10^{11} to 10^{12}

ISAC-I and ISAC-II Facility

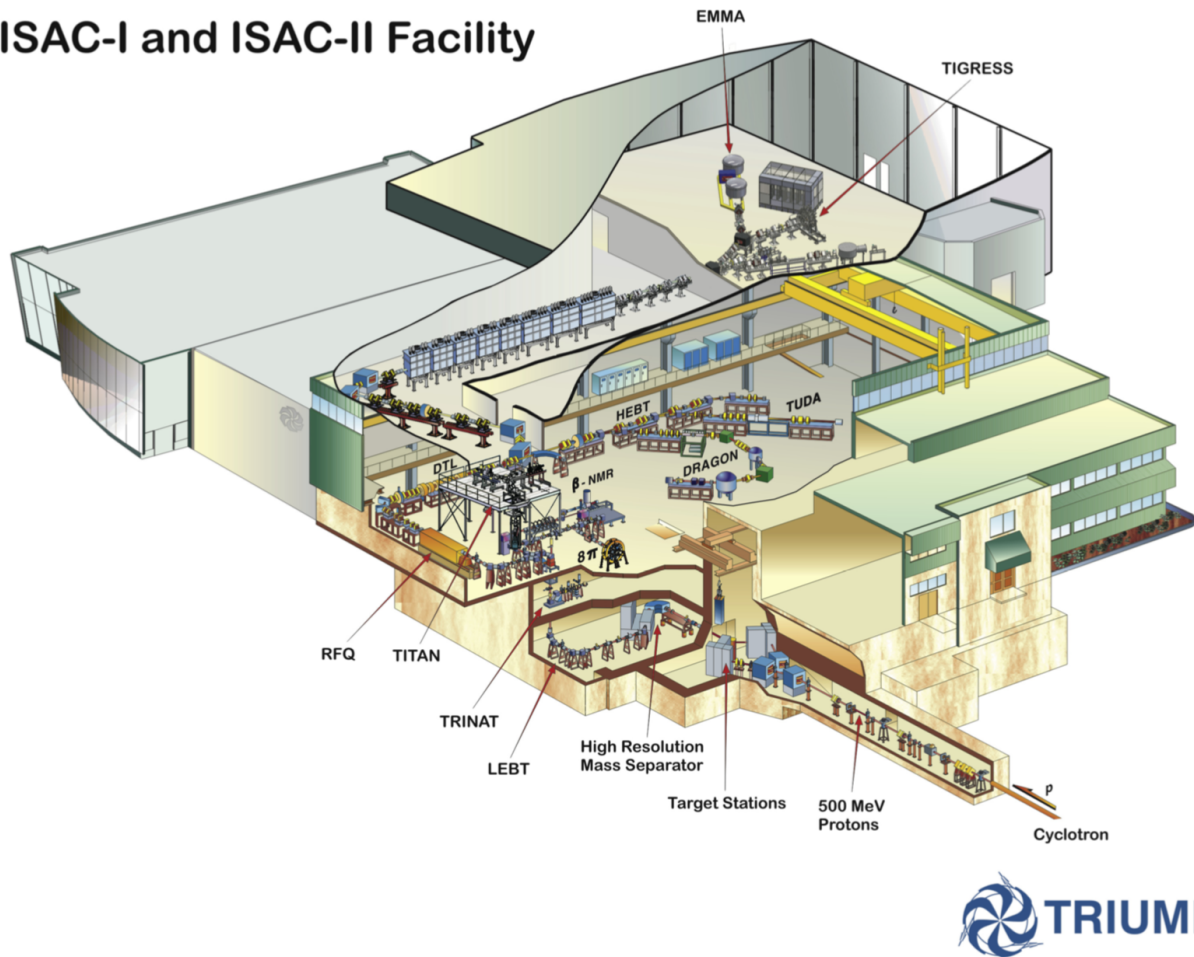


Figure 4.1: A three dimensional representation of ISAC-1 from Ball et al. [51]. DRAGON is located centrally within ISAC-1.

particles per second.

4.2 DRAGON

DRAGON is a recoil separator and separates particles on mass/charge ratio. During the experiment it separated out ions using 2 electric dipoles and 2 magnetic dipoles achieving high levels of beam suppression. This allowed separation of non select recoil ions. A schematic of DRAGON can be seen in figure 4.2 with the paths of select ions traversing the recoil separator depicted.

For electric and magnetic dipoles the separation occurred through eqn. 4.1. Eqn. 4.2 shows the Lorentz force on a particle traversing an electromagnetic field. The force applied

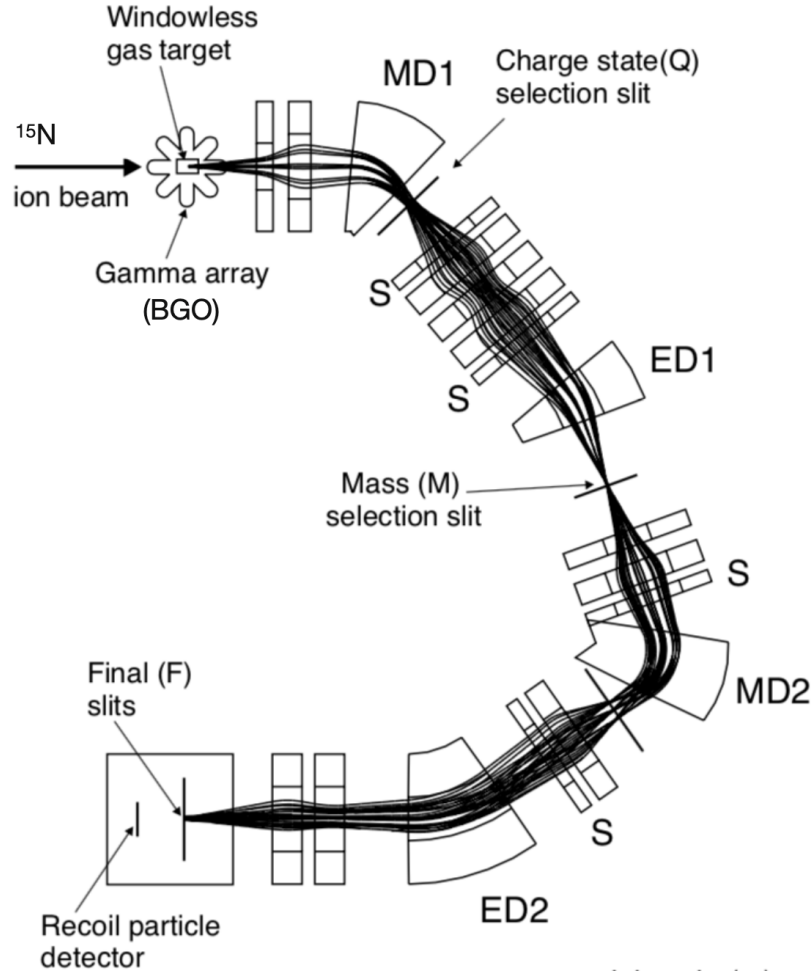


Figure 4.2: A schematic of DRAGON from Hutcheon et al. [54] with minor adaptations. Examples of ion trajectories are shown. MD and ED stand for magnetic and electric dipoles respectively.

was related to the particle path by eqn. 4.3.

$$\mathbf{F} = Q\mathbf{E} \quad (4.1)$$

where \mathbf{F} is the force applied to the particle, \mathbf{E} the Electric field strength and Q the charge of the beam particle.

$$\mathbf{F} = Q(\mathbf{E} + \mathbf{v} \times \mathbf{B}) \quad (4.2)$$

where \mathbf{v} is the velocity of the beam particle and \mathbf{B} is the magnetic field strength.

$$\mathbf{F} = \frac{m\mathbf{v}^2}{\mathbf{r}} \quad (4.3)$$

where \mathbf{r} is the particle trajectory arc radius.

The magnetic fields were measured using an NMR probe. Upon achievement of the desired field strength the fields were locked and hence consistent through a run, with drifts on the order of 0.01 G. Field strengths were selected by directing the particles down the centre of a pair of slits. Hence with negligible unexpected charge selected recoil losses, i.e. effectively all selected recoils of a given mass-charge ratio passed through DRAGON as seen in figure 4.2.

DRAGON was designed with the first magnetic dipole upstream of the first electric dipole to allow selection on charge states exiting the gas target through the first magnetic dipole, hence reducing the chance of ions striking other dipoles [54]. The undesired particles with charge states not selected are stopped on the slits, represented by the single lines perpendicular to the particles traversing dragon in figure 4.2. The first slits, the charge state selection slits, are located directly after MD1 and the mass selection slits after ED1. As explained in Hutcheon et al. [54] the order of the magnetic and electric dipoles was chosen as the particles require 3 charge state changes with residual gas in the separator rather than the two as in the second configuration considered. The second considered order was: magnetic dipole, two electric dipoles then magnetic dipole. Note that MD1 and MD2 bend the ions through 50° and 75° respectively [54], hence requiring increased bending of particles downstream in the separator than upstream.

The arrangement of the quadrupoles and sextupoles allowed effective focusing of ions. The quadrupoles allowed focusing of the ions into an achromatic arrangement with sextupoles used to correct for aberration [54]. The aberration correction discussed here is akin to the correction required in telescopic systems.

The arrangement described above is also discussed by Hutcheon et al. [55] in the context of its rejecting power of beam particles. Hutcheon et al. [55] explain it is expected in α -capture reactions the beam suppression is in the order of 10^{12} to 10^{13} for beam energies between 0.75 MeV/u upto 1.25 MeV/u. This level of rejection efficiency allows DRAGON to perform experiments involving relatively low cross-sections by utilising higher beam intensities than would be possible with a less efficient separator.

4.2.1 Charge state selection

The charge state of the recoils was selected based on three main criteria. The recoil separator must be able to bend the selected charge state of the recoils adequately to reach the DSSSD,

double sided silicon strip detector. Secondly, the beam and any main contaminants should have a significantly different mass to charge ratio to the recoils to avoid significant beam transmission through to the DSSSD and hence increasing DAQ busy time. Thirdly, the charge state selected for the recoils should be a significant fraction of the charge state distribution. Here all selected charge states represented a fraction greater than 35% of the total charge. The charge states were selected based on the work of Liu [56]. For the analysis and extraction of cross-sections and the resonance strength measured charge state fractions of ^{19}F in He gas were used.

4.2.2 Target chamber and gas cell

The target chamber contained a differentially pumped windowless gas cell. The dimensions of which consisted of a 0.6 cm diameter entrance aperture and a 0.8 cm exit, with physical length of 11 cm. Because the gas cell is differentially pumped the ends of the gas have a decreasing pressure, hence the effective length was a better measure of the target length. The length of the target at central gas pressure can be found to be 12.3 ± 0.4 cm [54]. The contents of the gas cell were contained in a thin walled aluminium box, thin to minimise the energy loss of reaction γ -rays. The design of the gas cell allowed the γ -ray detector array to have good spacial coverage of around 80% [54], these can be seen depicted in figure 4.4. The target gas was circulated using a series of Roots blower pumps and cooled via an LN2 cooled zeolite trap and passed back into the gas cell. This maintained gas pressure consistency to 1% [54]. A schematic of the target gas cell can be seen in figure 4.3.

The pressure within the gas target was set to contain the resonance of interest ensuring the energy loss over the target provided enough energy loss such that the it encompassed both tails of the resonance sufficiently.

4.2.3 BGO array

The Bismuth Germanate, BGO array consisted of 30 hexagonal detectors, arranged in a closely packed configuration as depicted in figure 4.4. These were located around the gas cell to detect γ -rays as seen in figure 4.4. Hutcheon et al. [54] found that for γ -rays with energy between 1 and 10 MeV they have a detection efficiency of 45% to 60%. This is largely due to BGO having a high proton number and hence good photon absorption qualities. Each of the 30 detectors consisted of a BGO crystal of diameter 55.8 mm and width 76 mm coupled to a 51 mm diameter photomultiplier tube [54].

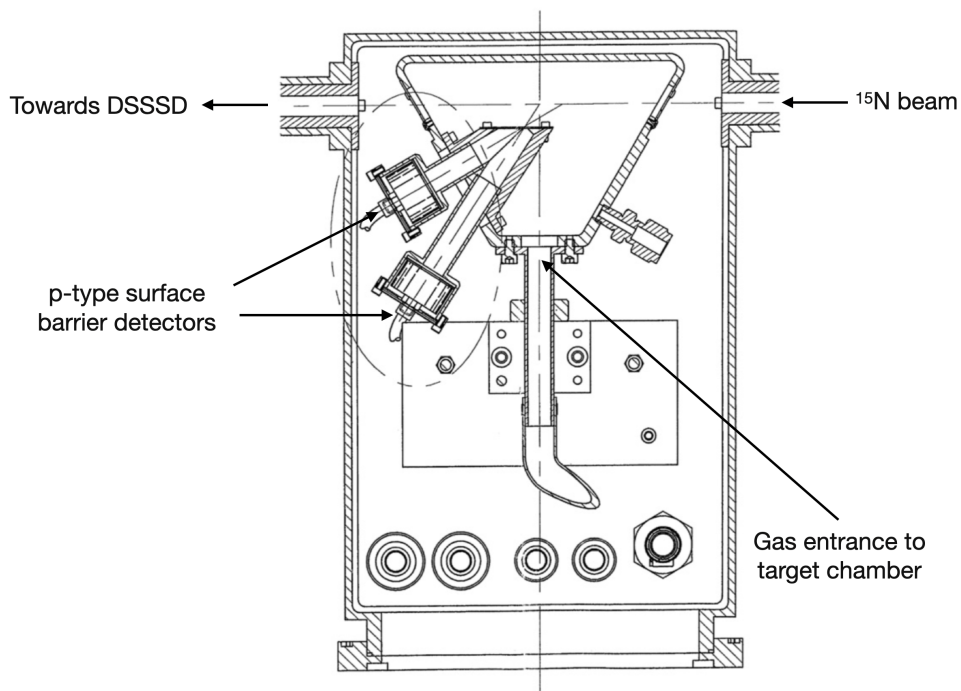


Figure 4.3: Diagram of gas target adapted from Hutcheon et al. [57]. The beam entered from the right and leaves to the left. The gas was pumped in from below.

Each BGO detector had a photomultiplier tube, PMT. When the BGO, a scintillator, emits photons, due to the interaction with an incident γ -particle, photons are then passed to a photo-cathode. From here electrons were released, these photo-electrons then struck dynodes, which were biased so that the photo-electron triggers a cascade of secondary electrons, or equivalently an avalanche. These electrons were then collected on the anode and registered as a signal.

4.2.4 Surface barrier detectors

The silicon p-n type surface barrier detectors can be seen circled in the top left of figure 4.3. These monitored elastically scattered beam particles, which allowed relative beam intensity monitoring. Solely using a Faraday cup before and after a run would have introduced large uncertainties in the beam current during a measurement where cup measurements are not possible. Using the elastic scattering rate onto these detectors alongside the absolute Faraday cup readings allowed a scaling of the elastic scattered particles to beam current. Then these detectors were used to monitor the beam current, checking for intensity fluctuations during a run.

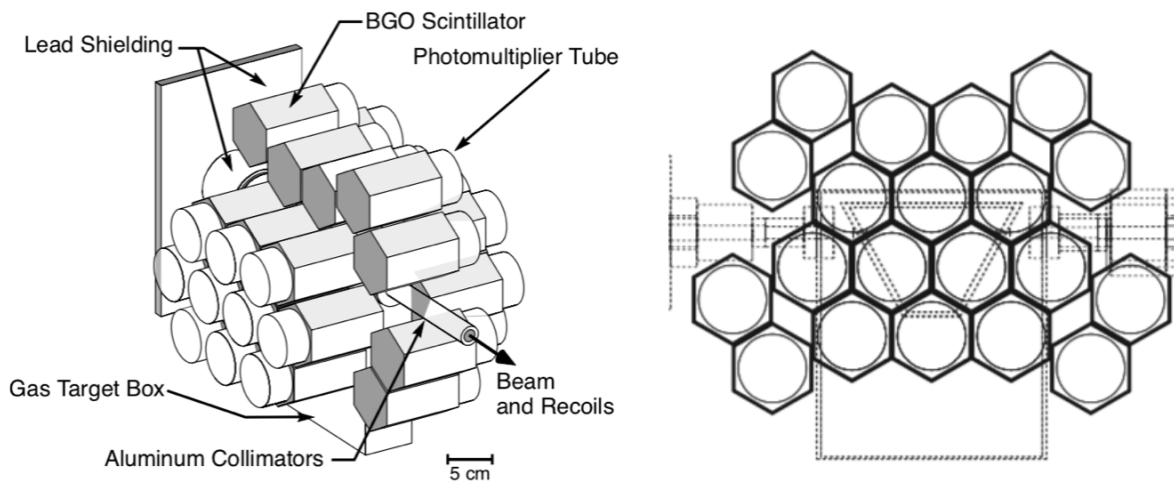


Figure 4.4: Schematic diagram of the DRAGON BGO detectors. Left: A cut-away 3D schematic of the DRAGON BGO detectors from Hutcheon et al. [54]. Right: 2D cutaway from Hutcheon et al. [57]. Note the dashed lines represent the outline of the gas target system, as seen in figure 4.3, relative to the location of the BGO detector array.

The make-up of a surface barrier detector comprises of n-type silicon, with excess electrons and with p-type silicon, with a lack of electrons or, equivalently, an excess of holes. These layers are separated by a depletion layer, or barrier. Upon contact with particles of sufficient energy the electrons traverse the depletion region and as such a current is induced in the circuit. This current is registered as a count, the stronger the signal produced the greater the energy of the incident particle.

4.2.5 Recoil detection: DSSSD

The DSSSD, Double Sided Silicon Strip Detector was a gridded type detector, from here referred to as a DSSSD. The DSSSD formed the sole direct detection mechanism for recoils in this DRAGON run.

The DSSSD was located at the focal plane at the downstream end of DRAGON and was positioned perpendicular to the path of recoils that traverse DRAGON. This orientation maximised the detection area available and hence the geometric efficiency. The gridded DSSSD meant the pick-up regions were effectively comprised of 16 strips on the front and 16 on the back. Those on the back were perpendicular to both the beam and the front strips. The combination of the perpendicular strips allowed the determination of recoil position on

the 49.5 mm by 49.5 mm DSSSD with thickness $300\ \mu\text{m}$. The DSSSD is of “Tengblad” [58] or equivalently, Micron W1(G) type and can be seen in fig.4.5. This style of detector allows the contact layer to be replaced with a grid covering a minimal area of the detector, hence reducing the dead layer thickness [58]. It should be noted the typical bias voltage for this detector is 60 V with a leakage current in the region of 400 nA.

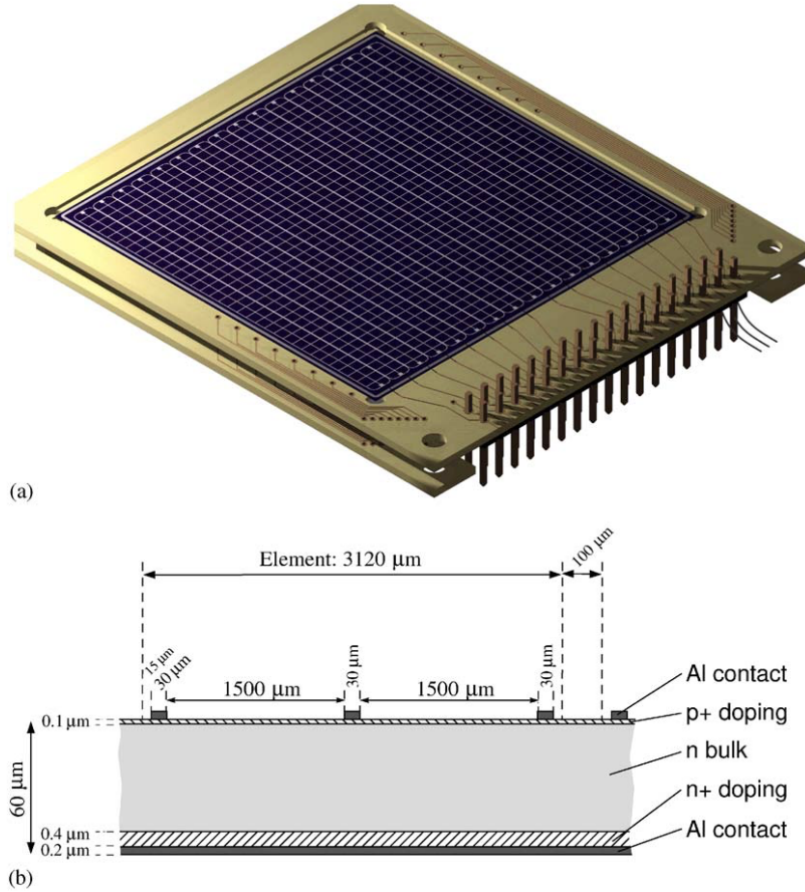


Figure 4.5: Figure from Tengblad et al. [58]. a) shows the detector in ΔE -E arrangement b) Shows the ΔE component as presented by Tengblad et al. [58]. Note the pick-up strips covering part of the detector surface, note that DRAGON uses a $300\ \mu\text{m}$ thick version.

Particles striking the 3% pick-up region covered by the electrical pick-ups could still be detected, but they left a reduced total energy in the detector strips. This 3% pick-up region produces a secondary peak of recoils in the DSSSD, this can also be seen in Yorkston et al. [59]. These regions were required to separate the strips to allow for position sensitivity. Furthermore this position sensitivity allowed the tune of DRAGON to be checked such that recoils were striking the center of the DSSSD, if this was not the case the tune was adjusted.

4.2.6 Timing

The separator time of flight was the time taken for a particle to travel from the target through the full length of DRAGON onto the DSSSD. This was measured from the γ -detectors to the DSSSD. The separator time of flight is used for particle identification. The separator time of flight cut was based on the beam RF period, directly linked to the frequency of the RFQ.

It should be noted the micro channel plate detectors are normally also used to aid identification of the recoils. These were not used during this measurement due to excessive noise from their circuit, ranging in frequency but on the order of ~ 60 Hz. The origin of this noise was not known. The lack of micro channel plate detectors had no impact on the analysis in this case as the beam and recoil species were separable using other methods.

4.2.7 Tuning DRAGON and beam energy

The ion beam, in this case $^{15}\text{N}^{3+}$, on the order of 10^{12} particles per second, was first tuned through DRAGON's gas target. This process was completed for each beam energy of 4541(1) keV, 4544(1) keV, 5742(1) keV, 5709(1) keV, 6284(2) keV and 8166(43) keV in the lab frame. The transmission through the target was measured; firstly by measuring the collected charge on the Faraday cup upstream of DRAGON, using FC4 and then charge collected on the other side of the gas target, on FC1. Target transmission was then found by comparing FC1 and FC4. The ratio of which yielded a target beam transmission value. This was typically in the region of 90% and was measured for each energy. Beam may have been lost due to scattering through the gas target and some beam particles will not have been axially aligned.

By adjusting the strengths of the fields of MD1, ED1, MD2 and ED2 in order beam species were progressed through DRAGON towards the DSSSD. This gave a tune for ^{15}N to use for scaling to the ^{19}F ions. Each charge slit pair was used to aid with beam progress through DRAGON. The beam was then attenuated before checking the detector response and beam position on the DSSSD. The attenuation was to avoid ion damage of the silicon detector. The tune was then scaled to recoils, meaning the tune was adjusted for the ^{19}F in the chosen charge state, here, 3^+ or 4^+ . It must be noted that the recoils pattern of the DSSSD was checked on-line where there were sufficient recoils to do so.

The beam was accelerated to the required energy and checked upstream of DRAGON on the PRAGUE magnet. MD1 in conjunction with the NMR probe were used to check the beam energy more precisely. The beam was tuned through the gas cell without gas and was bent using MD1, through a field measured by the NMR probe, and passed centrally through

the charge slits. The strength of the magnetic field created by MD1 allowed the calculation of the energy of the beam into DRAGON using eqn. 4.4, as in Hutcheon et al. [57].

$$\frac{E_{beam}}{A} = c_{mag} \left(\frac{qB}{A} \right)^2 \quad (4.4)$$

where c_{mag} is a constant of value 48.23 MeV T^{-2} , E the kinetic energy of the beam particle and A its mass in atomic mass units. Similarly the exit energy of the beam after the gas target was found by repeating the process with the helium gas in the gas cell at the pressure for the run. This energy loss measurement was repeated whenever the pressure in the gas cell or beam energy was changed. The calculation of these two beam energy values; with gas in and gas out of the target; allowed the energy loss across the gas cell to be calculated using eqn. 4.5.

$$\Delta E = E_{beam\text{in}} - E_{beam\text{out}} \quad (4.5)$$

Whilst the energy loss through the gas cell was not completely linear, at the beam energies used here with their energy loss, the assumption can be made that the energy loss through the gas cell is linear and therefore $E_{beam\text{centre}}$ was found using eqn. 4.6.

$$E_{beam\text{centre}} = \frac{E_{beam\text{in}} + E_{beam\text{out}}}{2} \quad (4.6)$$

or equivalently can be found using eqn. 4.7.

$$E_{beam\text{centre}} = E_{beam\text{in}} + \frac{\Delta E}{2} \quad (4.7)$$

The beam spread/spatial profile also allowed troubleshooting of the beam when tuning. If the beam was significantly spread it was rectification using the quadrupoles. If significant beam was detected on one slit so the dipoles were adjusted to obtain axial alignment.

Chapter 5

$^{15}\text{N}(\alpha,\gamma)^{19}\text{F}$ Data Analysis

5.1 Normalisation

In order to extract a meaningful cross-section the number of beam particles for each run, and therefore the number of beam particles for each group of runs must be determined. The most simple method for finding N_{beam} for a run is to scale FC4 readings to account for run time and the target transmission. For example:

$$N_{beam} = \epsilon_t N_{FC4} \Delta t \quad (5.1)$$

where ϵ_t is the target transmission efficiency, N_{FC4} is the average number of beam particles that arrived on FC4 per second in the 120 second period; and Δt is the length of time of the run. It is important to note that N_{FC4} is a calculated value found by dividing the current per second on FC4 by qe , where q is the beam charge state.

This method is not suitable for the final analysis but acted as a useful comparison point by which to compare the R-factor method, described later. The scaling method is not suitable as it assumes that the first 120 seconds of a run are representative of an entire run and that the mean charge collection per second over an entire run is identical to the first 120 seconds. The R-factor method was used due to it containing information from over the entire run, and as such a more reliable representation of the beam particles through the target during runs. This is necessary to account for variations in beam current during a run.

For the R-factor method the surface barrier detectors were utilised. A relationship between the FC4 readings and the surface barrier detectors was established. It was assumed that the FC4 reading and surface barrier detectors scale with each other as the surface barrier detectors recorded elastically scattered beam particles, rather than total beam particles that

traversed the target.

The absolute normalisation factor between beam current and elastically scattered beam is given by eqn. 5.2.

$$R = \frac{I \Delta t}{qe N_p} \frac{P}{E_{beam}^2} \quad (5.2)$$

where the energy of the beam is assumed to be E_{centre} and can be found as in eqn. 4.7. P is the average pressure of the gas target, I is the beam current as measured on FC4 and N_p the number of scattered particles during time Δt . The pressures used during the experiment can be seen in table 5.1. The larger uncertainty on the highest direct capture energy was caused by the failure of the NMR probe.

Energy in CoM (keV)	Energy CoM uncertainty (keV)	Pressure (Torr)	σ in Pressure (Torr)
956.4	0.2	6.11	0.02
957.1	0.2	6.11	0.05
1202.5	0.3	6.06	0.05
1209.5	0.3	4.12	0.06
1323.6	0.3	7.23	0.06
1720	9	6.78	0.02

Table 5.1: Beam energies with corresponding gas target pressures.

The R-factor is then used to calculate the number of beam particles, N_{beam} as seen in equations 5.3 and 5.4.

$$N_{beam} = \frac{N_{scattered} R_{scaled}}{P} \quad (5.3)$$

where

$$R_{scaled} = R E_{centre}^2 \quad (5.4)$$

It can be seen in table 5.2 that the beam intensity is relatively stable, with agreement within errors from averaging the FC4 current integration method and the R-factor method.

Energy CoM (keV)	N_{beam} from R-Factor Method	N_{beam} Uncertainty from R-Factor Method	N_{beam} from Scaling Method	$N_{beam}\sigma$ from Scaling Method	$\delta\%$
956.4(2)	9.65E+15	3.0E+14	9.74E+15	2E+13	0.9
957.1(2)	1.39E+17	6.7E+15	1.3446E+17	7E+13	3.0
1202.5(3)	3.39E+16	5.6E+15	3.40E+16	7E+14	0.4
1209.5(3)	3.01E+16	1.9E+15	2.936E+16	8E+13	2.5
1323.6(3)*	5.70E+14	1.9E+13	5.63E+14	3E+12	1.3
1720(9)	5.81E+15	5.8E+13	5.83E+15	1E+13	0.3

Table 5.2: Calculated N_{beam} values using the R-factor method, the simple scaling method and the percentage difference. $N_{beam}\sigma$ is the standard deviation between each runs cup readings for the given beam energy, i.e. a measure of fluctuation between Faraday cup readings, not the total uncertainty. *resonance beam energy.

5.2 Recoil extraction and particle identification

The number of ^{19}F nuclei reaching the DSSSD for each target centroid beam energy must be found. Those nuclei reaching the detector of undesired species must be removed, this includes ^{15}N nuclei, colloquially referred to as “leaky beam”. DRAGON is an effective recoil separator and as such the quantity of leaky beam is minimal, but nevertheless its removal is important. The process for removing the contaminants at the DSSSD comprises of, a separator time of flight cut, a DSSSD energy cut, a BGO threshold and a surface barrier trigger, all discussed here.

5.2.1 RF period

The RF period peak can be fitted as seen in figure 5.1 and yields a result of 86.89(2) ns for this case of the resonance and similarly for other beam energies. This peak represents the time between the leading edges of two adjacent beam bunches, or equally, the time period of the beam.

5.2.2 Separator time of flight

The separator time of flight cut uses the time period of the beam, found to be 86.89 ns. To obtain an effective cut the time taken for the beam to traverse through DRAGON, from

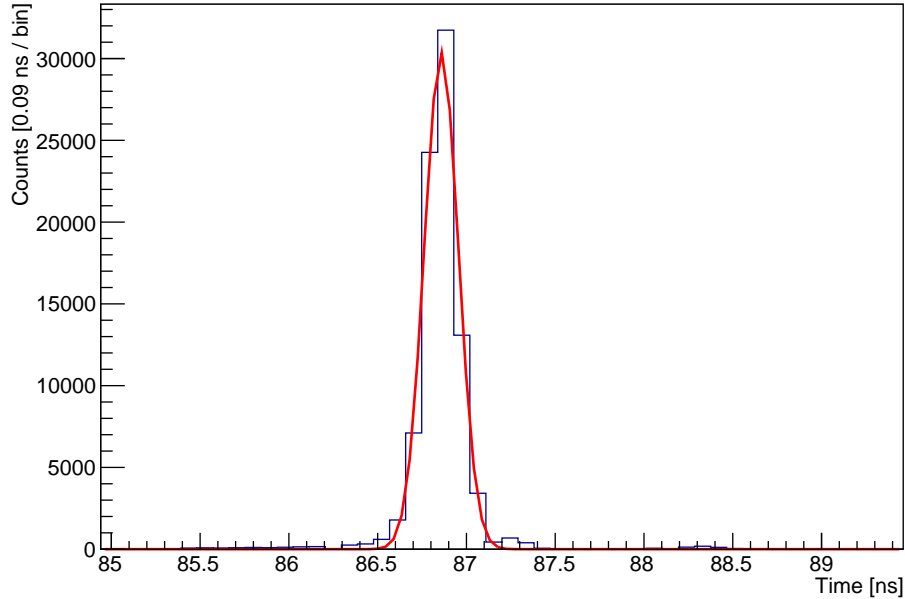


Figure 5.1: RF peak fitted giving a centroid of 86.89(2) ns, matching the frequency of the RFQ.

the target chamber through to the DSSSD was found. Fitting the separator time of flight allows extraction of a mean flight time through DRAGON. As an example figure 5.2 shows the separator time of flight for the 1323 keV CoM measurement energy.

A cut is made based on the separator time of flight spectrum fit outcome and the radio frequency period peak fit. A separator time of flight cut is made based on lower separator time of flight centroid - $1.5 \times \text{RF}$ period and the higher separator time of flight centroid + $1.5 \times \text{RF}$ period. This is a very conservative cut to ensure particles travelling through the separator with similar velocity are not discounted at this stage. This cut was to ensure there are no particles travelling through the separator that have significantly dissimilar velocity, such that they could not possibly be ^{19}F .

5.2.3 Surface barrier trigger latch

In the case of the lowest direct capture beam energy, 957 keV/u, the separator time of flight was not trivial to fit, due to significant background in the separator time of flight spectrum as seen in figure 5.3. A filter was made by ignoring those events where the surface barriers triggered the DAQ and only using those events where the DSSSD triggered the DAQ. This method proved to be effective in reducing background in this spectrum as seen in figure 5.4.

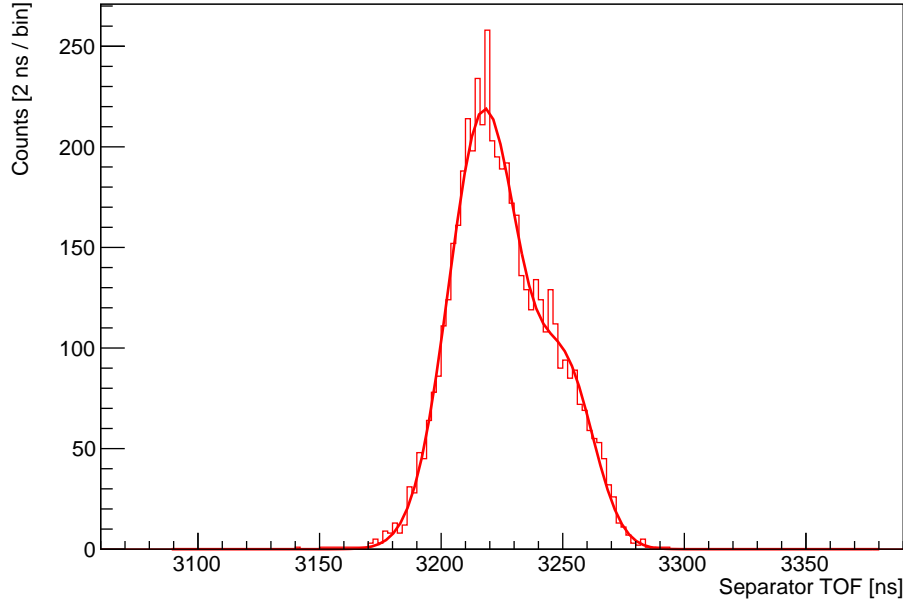


Figure 5.2: Separator time of flight for the 1323 keV CoM measurement energy, note the asymmetrical fashion of the peak and the apparent double gaussian.

This cleaner spectrum can then be fitted as in figure 5.4. The time of flight peak location was approximated by comparison with other beam energies. After the surface barrier trigger latch was applied the fitted peak was also the only significant peak seen in the separator time of flight spectrum. From this fit only the peak centroid was extracted. The apparent fluctuation across bins is due to the statistical fluctuation from such low count statistics, rebinning yields little variation in centroid.

Removal of such a large number of counts was considered with care as to ensure no ^{19}F recoils were lost. By comparing the DSSSD spectrum with no cuts and the DSSSD spectrum with the surface barrier detector trigger latch allowed identification of what the energy of the particles removed in the DSSSD. Figure 5.5 shows how the DSSSD spectrum was prior to applying the surface barrier detector trigger and figure 5.6 after. Note how from before and after the trigger latch was applied i.e. from figure 5.5 to figure 5.6, primarily the counts with DSSSD energy of 0 keV/u were removed. This comparison assures that no valid ^{19}F recoil counts were lost during the surface barrier trigger latch implementation.

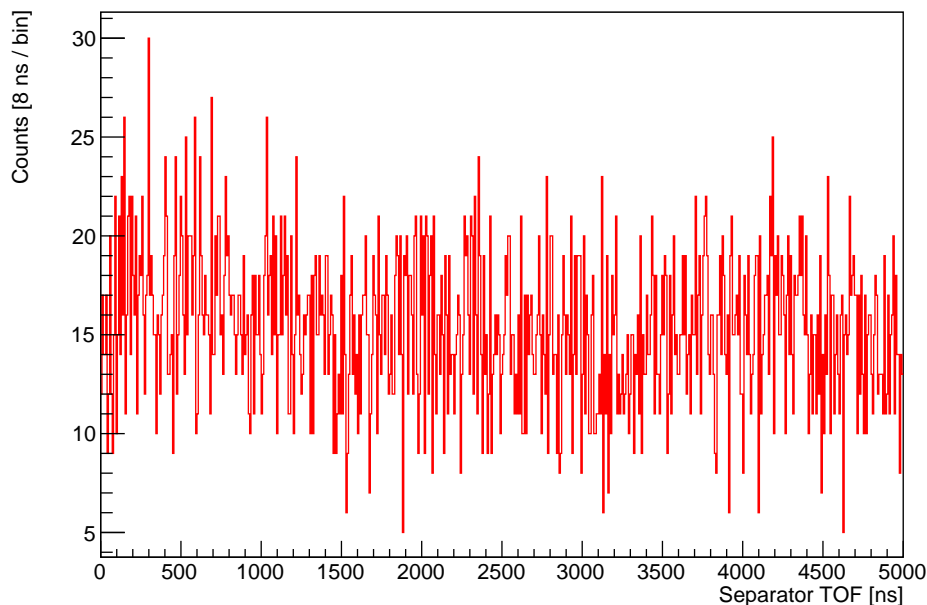


Figure 5.3: Separator time of flight for the 957 keV centre of mass measurement energy, note the lack of significant identifiable peak.

5.2.4 BGO threshold

A BGO threshold was applied during the analysis stage to ensure removal of any low energy background in the detector. Figure 5.7 shows the BGO spectrum after applying the separator time of flight cut without a threshold applied. There were not any low energy counts whose removal could be justified, hence in the unique case of the 1323 keV CoM measurement energy no further BGO threshold was applied beyond the experimental threshold.

In the cases of other beam energies a conservative threshold of 1 MeV was applied. At all energies except for the 1720 keV CoM measurement energy runs the BGO threshold removed no counts. For the measurement at an energy in the centre of mass frame of 1720 keV only an isolated, single count was removed. An example of the cut spectrum for the 957 keV CoM measurement energy can be seen in figure 5.8.

Unfortunately channel 23, corresponding to a detector at ~ 3 cm was removed from the analysis as its energy spectrum did not match that of other channels. The plot seen in figure 5.9 shows each channel along with energy of γ -rays detected. Note how all runs were comparable whereas channel 23 appears to have significantly higher energies and the distribution somewhat random.

As an aside it can be useful to view the BGO hit patterns to check for symmetry, especially

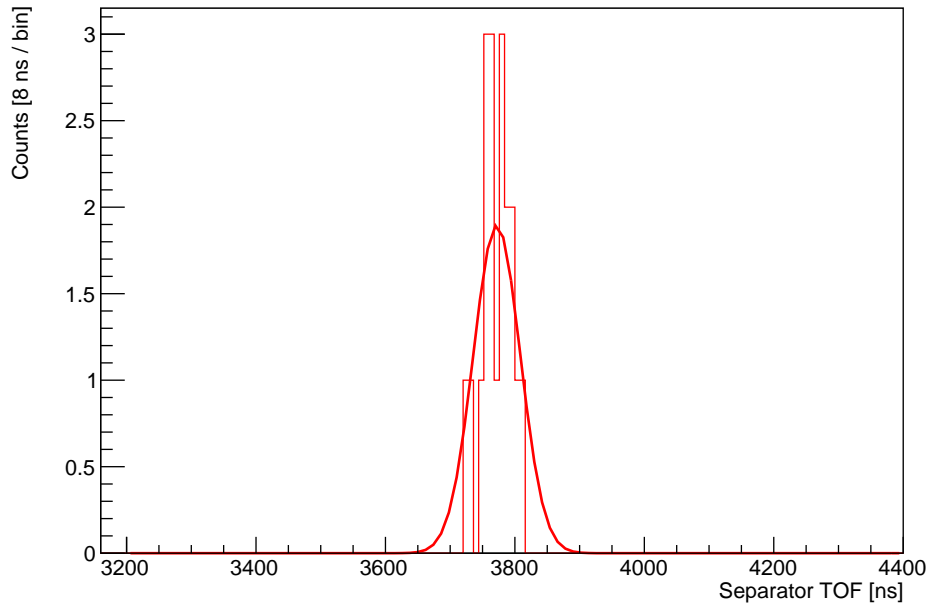


Figure 5.4: The separator time of flight spectrum for the 957 keV centre of mass measurement energy using the surface barrier trigger latch, fitted. Note only the centroid is used from this low statistic fit.

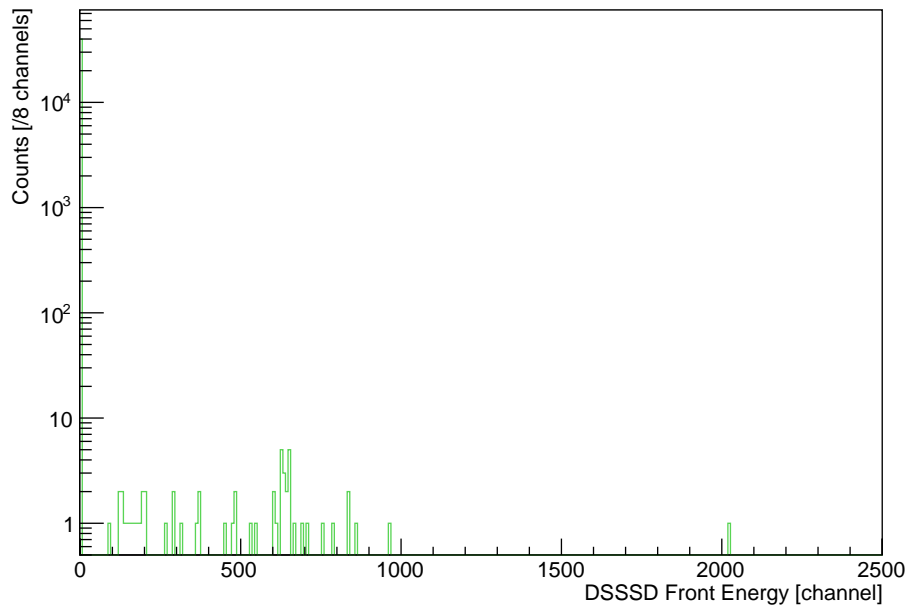


Figure 5.5: DSSSD spectrum for the 957 keV centre of mass measurement energy.

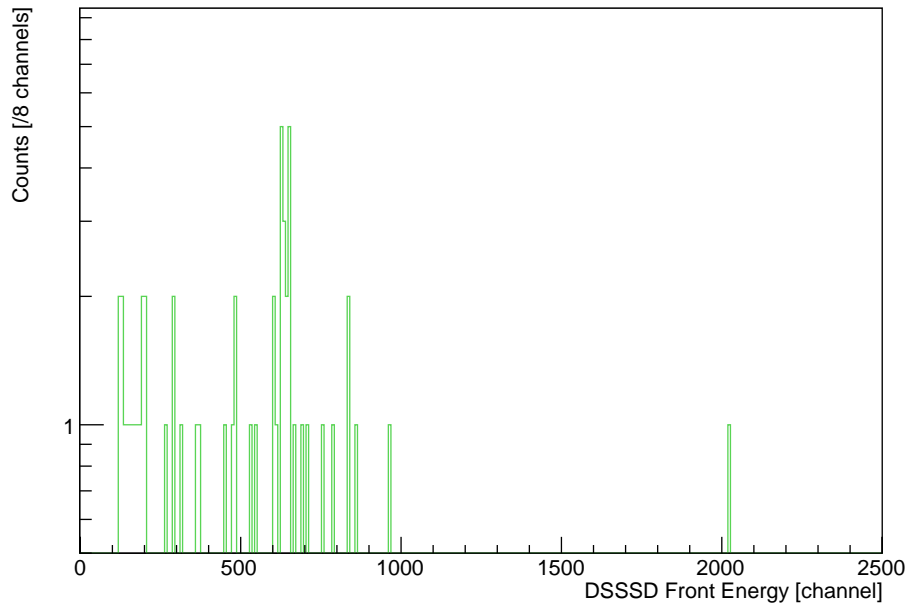


Figure 5.6: DSSSD spectrum for the 957 keV centre of mass measurement energy with surface barrier detector trigger.

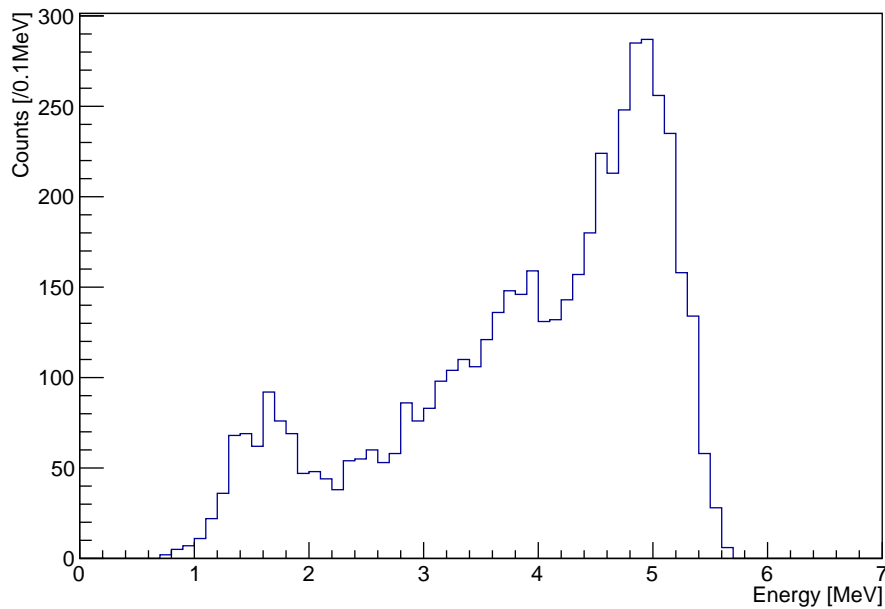


Figure 5.7: BGO spectrum with separator time of flight cut applied for the grouped runs at the 1323 keV CoM measurement energy.

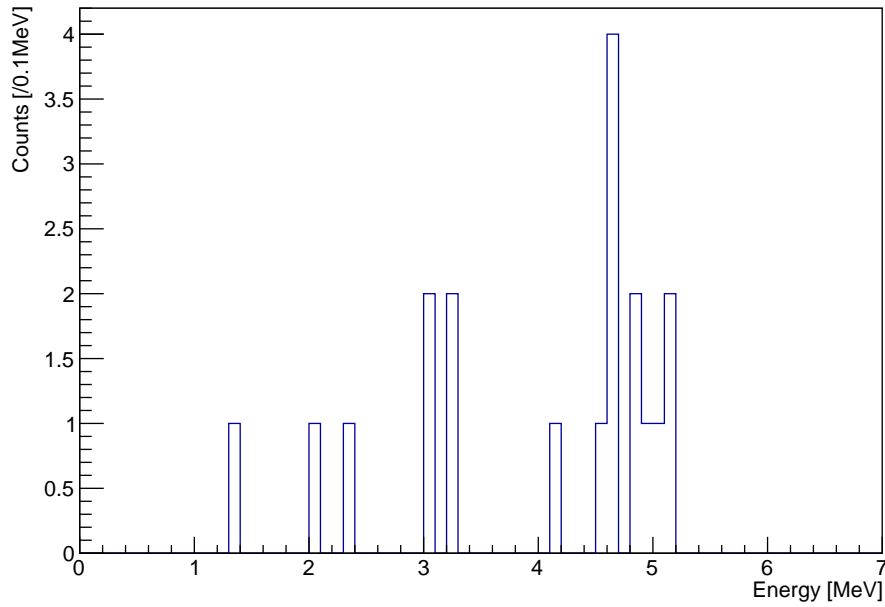


Figure 5.8: BGO spectrum with separator time of flight cut applied for the grouped runs at the 957 keV centre of mass measurement energy with 1 MeV BGO threshold applied.

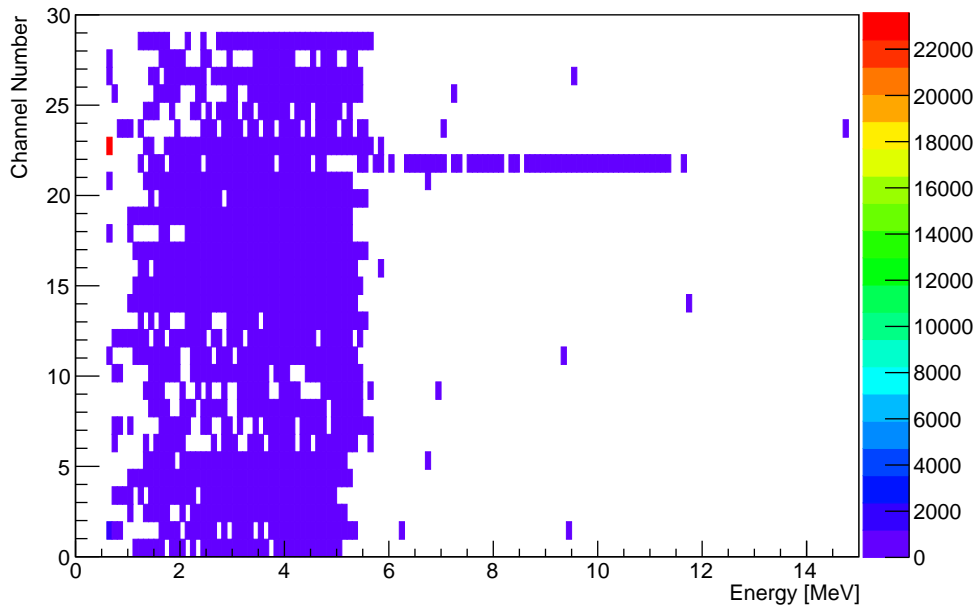


Figure 5.9: Individual BGO detector hit energies for the 1323 keV CoM measurement energy. Note the comparable energy distributions for all channels except for channel 23.

in the case of the 1323 keV CoM resonance energy measurement. In figures 5.10 and 5.11 two examples of hit patterns can be seen. The fluctuation witnessed in the 1720 keV centre of mass beam energy BGO hit pattern appears within statistical fluctuation of symmetric and the resonance energy hit pattern of the BGO array appears symmetric. The centering here suggests the resonance is centred well inside the target. Note the intensity at ~ 3 cm is lower than would be expected due to the removal of channel 23 as explained earlier.

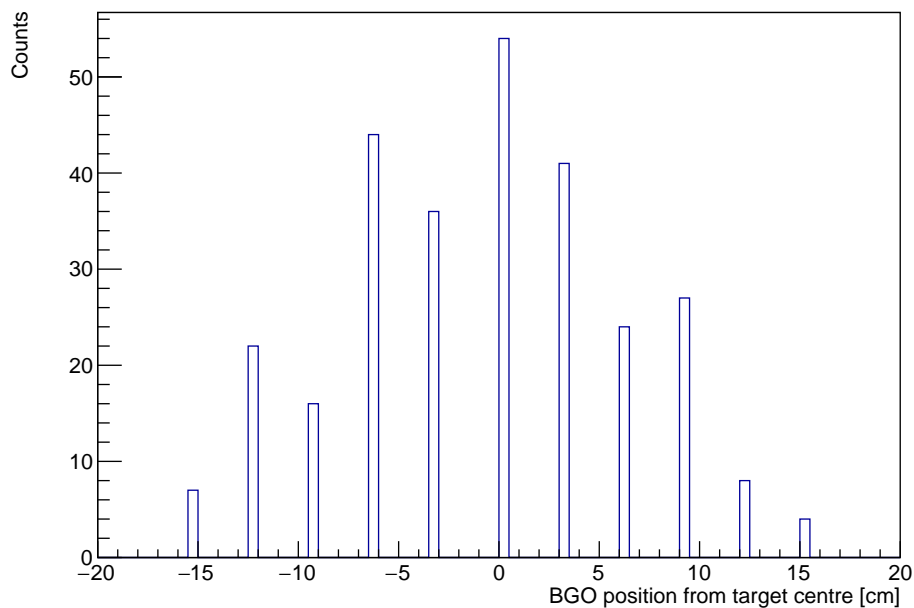


Figure 5.10: BGO hit patterns for the highest direct capture energy of 1720 keV in the centre of mass frame.

5.2.5 DSSSD energy cut

As discussed in section 4.2.5 the DSSSD is gridded. Particles that travel through the segmentation pick-up regions in the front detector will have reduced energy relative to those that travel, desirably, directly through the detector, due to losing energy travelling through the pick-up material. Hence the DSSSD fits must be made considering both the main peak and also those counts that traverse through the surface covered by the gridded region. As such the two Gaussian peaks fitted allowed for a 3.5σ variation off peak, hence cut at pick-up particle energy centroid - $3.5\sigma_{gridded-strip}$ and main particle energy centroid + $3.5\sigma_{main}$, where $\sigma_{gridded-strip}$ and σ_{main} are the standard deviation of the gridded energy and main peak

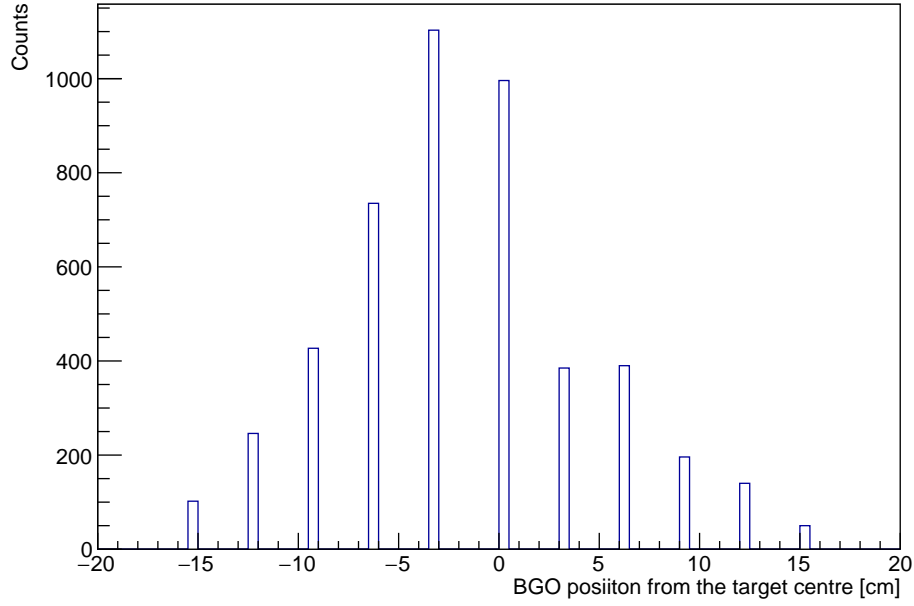


Figure 5.11: BGO hit patterns for the resonance beam energy of 1323 keV in the centre of mass frame.

respectively. The identification of the gridded peak was checked using the definition of the gridded region in equations 5.5 and 5.6.

$$N_{main} \approx 97\% \quad (5.5)$$

$$N_{gridded} \approx 3\% \quad (5.6)$$

where $N_{gridded}$ and N_{main} are the number of recoils in the gridded peak and the main peak respectively. Using the fitted double gaussian these peak integrals were found to be of 96.4% and 3.6% for N_{main} and $N_{gridded}$ respectively, for the resonance measurement. These percentages of area are useful in certifying the peak identified is the peak of the gridded region. Figure 5.12 shows the main peak and the gridded region peak fitted for a beam energy of 1323 keV in the centre of mass frame. It also shows those counts removed by the DSSSD cut.

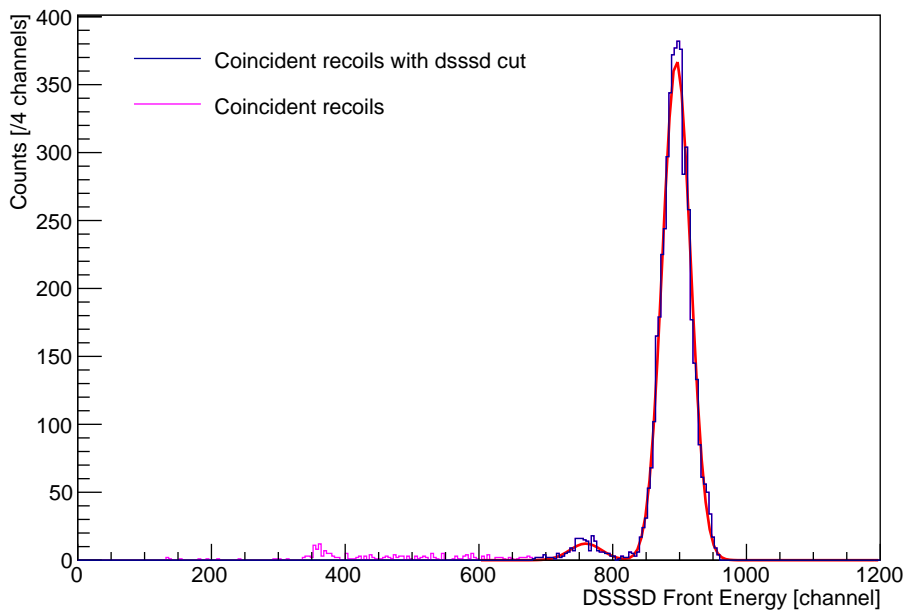


Figure 5.12: DSSSD spectrum for a beam energy of 1323 keV in the centre of mass frame, with BGO and separator time of flight cuts included.

5.2.6 Combining cuts

The final number of ^{19}F recoils was extracted using a combination of all the aforementioned cuts. The cuts on the resonance data can be seen in figure 5.13. The singles, blue, represents all particles detected by the DSSSD, including ^{19}F , leaky beam and any other background counts. The red represents all coincidence events with the BGO cut. Few counts are removed when separator time of flight (TOF) is included. Finally the DSSSD cut removes those counts with energies significantly different from the gridded region events and the main ^{19}F events.

Table 5.3 shows a summary of the number of extracted recoils in each case. It was decided that the 956 keV CoM measurement energy measurement would be removed due to only comprising of 2 counts and as such high statistical fluctuation, as seen in table 5.4, rendering the measurement, relative to the 957 keV CoM measurement, unreliable. Despite being close in beam energy the two measurements were not combined due to the large error on 2 counts relative to the 18 counts at the 957 keV CoM measurement energy.

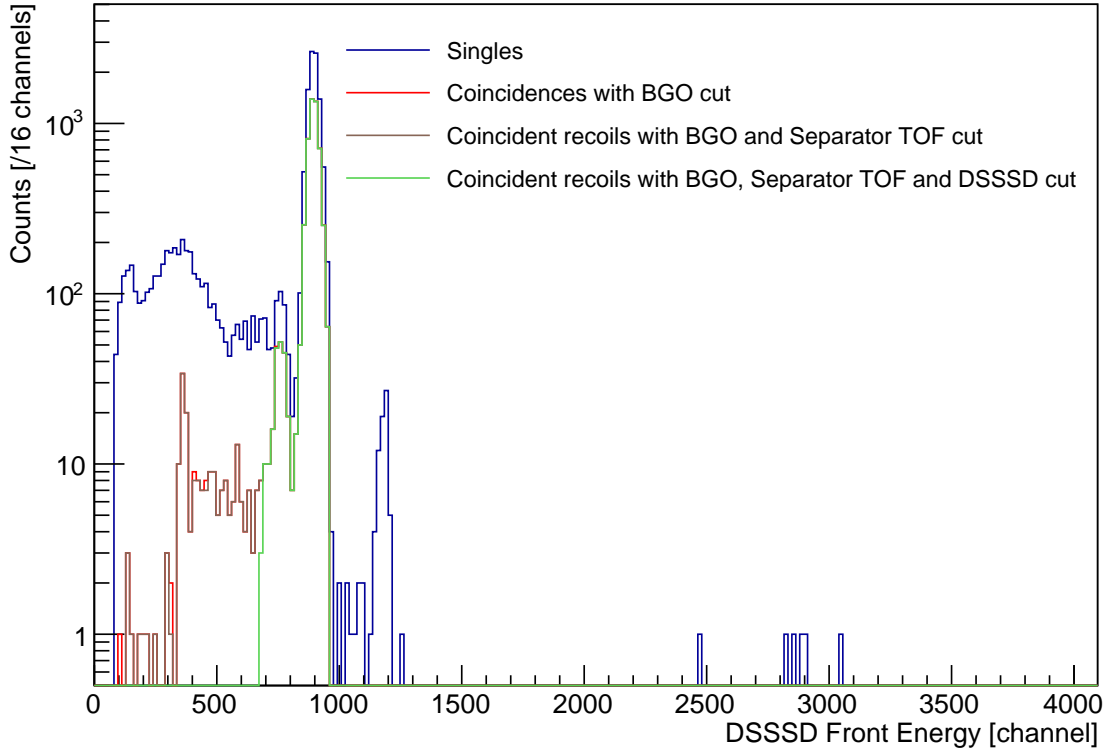


Figure 5.13: DSSSD spectrum for a beam energy of 1323 keV in the centre of mass frame, showing the effect of each cut.

Beam Energy keV/u Lab Frame	Beam Energy keV CoM	Number of recoils extracted
302.71	956.4	2
302.91	957.1	18
380.61	1202.5	209
382.81	1209.5	125
418.94*	1323.6	5009
544.40	1720	282

Table 5.3: ^{19}F counts extracted for each beam energy. *resonance beam energy

5.2.7 Low count statistics and the central confidence interval

For low number of recoils such as for the lower direct capture energies, especially at the beam energy of 303 keV/u it is not acceptable to use \sqrt{N} as the statistical uncertainties

become asymmetric. At low N , particularly $N < 100$ the poisson distribution may not be approximated by a normal distribution. To investigate the difference between the \sqrt{N} and the central confidence interval, CCI, the statistical uncertainty in the recoils was found for 68.27%, or 1σ . 2σ is included as a comparison point with the 1σ central confidence interval. Note, as expected, that 2σ contains less than double the 1σ central confidence interval across all N tested here.

The results may appear different to the results displayed in some literature such as Feldman and Cousins [60], however those are for the confidence interval, which is solely a one sided interval. The literature confidence interval results cannot be compared with the \sqrt{N} method due to the central confidence interval nature of \sqrt{N} . The results of the calculation completed here can be seen in table 5.4. So the central confidence interval values are the plus and minus values from N at which there is a 68.27% or 95% probability that the actual N lies between the two. In the case of $N=2$ with a 95% central confidence interval there is a 95% probability that the actual value lies between 0.24 and 7.22.

N	+ error with 95% CCI	- error with 95% CCI	+ error with 68.27% CCI	- error with 68.27% CCI	\sqrt{N}	% difference upper limit	% difference lower limit
2	5.22	1.76	2.64	1.29	1.41	46.43	9.63
18	10.45	7.33	5.32	4.20	4.24	20.25	-1.02
125	23.93	20.95	12.21	11.17	11.18	8.43	-0.09
209	30.34	27.38	15.48	14.45	14.46	6.61	-0.05
282	34.91	31.96	17.81	16.78	16.79	5.71	-0.08
5009	140.67	137.76	71.78	70.77	70.77	1.40	-0.01

Table 5.4: Uncertainty method comparison for various values of N ; using central confidence interval for 2σ , 1σ and \sqrt{N} .

It can be seen that as N becomes large so the validity of using \sqrt{N} in place of the central confidence interval is increased, i.e the percentage difference between counts assuming a normal distribution in place of a poisson distribution decreases. Using table 5.4 it is also apparent that even with 5009 counts an asymmetric nature is still present, as the upper bound differs from \sqrt{N} by 1.40%, whereas in the lower limit there is no significant difference. As expected when N is small, larger error in the uncertainty is induced by using \sqrt{N} , certainly for $N=2$ and $N=18$ the root N method yields a misleading and invalid statistical uncertainty value.

5.3 Efficiencies

With the attainment of the number of recoils as in table 5.4 it is necessary to find what portion of the number of produced ^{19}F recoils have been detected. Each detection point, component of the equipment, has an associated efficiency, the amount of ^{19}F that is successfully processed relative to the ^{19}F produced. This section will cover the attainment of each of the necessary efficiencies.

The BGO array efficiency was measured using a Geant simulation, this was carried out by a collaborator, A. Lennarz. Where the appropriate decay schemes were selected that best represented and contributed to the BGO spectra. The BGO array had one detector that failed in channel 23. The cause of this was undiagnosed and so the Geant simulation was adapted to remove the single failed detector as well as the detector in channel 23 that had a dissimilar energy spectrum and so the geant simulation was used to produce a new γ -ray detection efficiency. In principle removal of detectors only reduced the coverage of the detectors and hence the BGO array geometric efficiency. The geant simulation yielded BGO array detector efficiencies as seen in table 5.5. It should be noted a simple arithmetic mean of the decay branch efficiencies was taken, this was shown to be within 2% of a reference measurement, well within the assumed 10% BGO efficiency uncertainty typically assumed on this setup.

Beam Energy keV/u	BGO efficiency	BGO efficiency uncertainty	Livetime	Livetime uncertainty
302.91	0.52	0.05	0.70581	4×10^{-5}
380.61	0.54	0.05	0.70811	4×10^{-5}
382.81	0.54	0.05	0.71508	4×10^{-5}
418.94*	0.59	0.06	0.72927	4×10^{-5}
544.40	0.57	0.06	0.73311	4×10^{-5}

Table 5.5: Uncertainties for all beam energies for BGO detection efficiency and livetime of the DAQ, data acquisition system. *resonance beam energy.

Livetime refers to the fraction of time the data acquisition system is able to record incoming signals, at times this system will be busy processing signals. These “lost” signals were accounted for using the livetime efficiencies as seen in table 5.5. Livetimes were calculate by comparing the DAQ busytime with the runtime. The busytime and runtime are automatically collected for each individual run.

The DSSSD detection efficiency is 0.962 ± 0.004 [61], this is assumed to be the same across all beam energies tested here. Furthermore it was assumed that the detector was isotropically efficient across all detector segments. Transmission of recoils through DRAGON is particularly effective and transmission rates are effectively 100% [54].

The charge state fraction of ^{19}F ions can be calculated using equation 5.7 from the thesis of W.Liu [56].

$$\bar{q} = Z_p \times (1 - \exp(-\frac{A}{Z_p^\gamma} \sqrt{\frac{E}{E'}} + B)) \quad (5.7)$$

with \bar{q} being the average equilibrium charge state; E the projectile energy and $E' = 0.067635$ MeV/u; Z_p is the atomic number of helium, 2; A, B and γ are fit parameters from the thesis of W.Liu and have values of 1.1326, 0.3449 and 0.44515 respectively for a Helium gas target. Equation 5.7 will yield an average charge state however to obtain charge state fractions the width of the gaussian peak was required, which was also explored in W.Liu in equation 5.8, from Liu [56].

$$d = d_1 Z_p^w \quad (5.8)$$

where appropriate values of d_1 and w were found by Liu to be 0.23675 and 0.54772 respectively. With this known distribution so the charge state fraction for a given charge state can be calculated. The results of which are shown in Table 5.6.

Beam Energy (keV/u)	^{19}F Q (+)	Calculated CSF	Calculated CSF Uncertainty	Measured CSF	Measured CSF Uncertainty
302.91	3	0.483	0.024	0.435	0.044
380.61	3	0.476	0.024	0.433	0.043
382.81	3	0.473	0.024	0.433	0.043
418.94*	4	0.413	0.021	0.383	0.045
544.40	4	0.501	0.025	0.454	0.038

Table 5.6: Calculated and measured charge state fraction for the selected ^{19}F tune through DRAGON. *resonance beam energy.

The calculated charge states are marginally outside the error boundaries of the measured charge states. It must be noted that the calculated value CSFs error consist of a 5% error. It is possible that this is an underestimated uncertainty on the theoretical values as in the thesis of Liu [56]. The CSFs used for efficiency calculations and ultimately to yield a cross-section

are the experimental values.

It must be noted that after the main experiment the charge state fractions were measured for ^{19}F as discussed in the thesis of Lovely [62]. Whilst this part of the experiment and analysis was not conducted by myself, DRAGON was again used to measure the CSF. As described by Lovely, ^{19}F was passed into the DRAGON gas target through ^4He and then bent using MD1. The strength of the field on MD1 was varied to allow measurement of the fraction of particles at a given charge state. The work of Lovely [62] did produce some revised parameters to those of Liu [56].

The total efficiency can be found by combining the CSF, Livetime, BGO efficiency and DSSSD efficiency. This represents the fraction of actual recoils that are detected.

Chapter 6

$^{15}\text{N}(\alpha,\gamma)^{19}\text{F}$ Results

Cross-sections were extracted using the number of recoils, number of target particles, number of beam particles, total efficiency and calculated using eqn. 2.1. Table 6.1 shows the measured cross-sections with asymmetric uncertainties for a 68.27% central confidence interval at the given beam energies.

Beam Energy (keV) CoM	Beam Energy Uncertainty (keV)	σ (Barn)	σ uncertainty (-) (Barn)	σ uncertainty (+) (Barn)
957.1	0.2	3.51×10^{-10}	9.8×10^{-11}	1.17×10^{-10}
1202.5	0.3	1.60×10^{-8}	3.7×10^{-9}	3.7×10^{-9}
1209.5	0.3	1.57×10^{-8}	2.9×10^{-9}	2.9×10^{-9}
1323.6*	0.3	1.96×10^{-5}	2.9×10^{-6}	2.9×10^{-6}
1720	9	9.9×10^{-8}	1.6×10^{-8}	1.6×10^{-8}

Table 6.1: Cross-sections measured for $^{15}\text{N}(\alpha,\gamma)^{19}\text{F}$ along with their asymmetric uncertainties with a central confidence interval equivalent to 1σ at 68.27%. *resonance beam energy.

The large error on the highest energy direct capture energy was due to issues with the NMR probe and as such the field through which the beam passed was not known to the same level of accuracy as in other runs, as such this beam error carries a larger error. As expected relative to the direct capture measurements the resonance has a higher cross-section by several orders of magnitude. From the cross-sections S-factors were calculated as seen earlier in eqn. 2.7 and are shown in table 6.2.

The 1323 keV energy resonance strength was found using eqn. 2.12 using the thick target assumption. The resonance strength was found to be 0.92 ± 0.11 eV using a beam energy of

Beam Energy (keV) CoM	Beam Energy Uncertainty (keV)	S-Factor (MeVb)	S-Factor uncertainty (-) (MeVb)	S-Factor uncertainty (+) (MeVb)
957.1	0.2	28.7	8.0	9.6
1202.5	0.3	108.9	25.2	25.3
1209.5	0.3	100.6	18.3	18.7
1323.6*	0.3	51172	7671	7672
1720	9	24.3	3.8	3.9

Table 6.2: S-Factors for $^{15}\text{N}(\alpha,\gamma)^{19}\text{F}$ along with their uncertainties.

1323.6(3) keV. At this beam energy the resonance was contained with the target, between an energy of 1300 keV and 1347 keV.

Chapter 7

$^{15}\text{N}(\alpha, \gamma)^{19}\text{F}$ Discussion

The direct capture cross-section of $^{15}\text{N}+\alpha$ was measured directly for the first time at energies of 956.4(2) keV, 957.1(2) keV, 1202.5(3) keV, 1209.5(3) keV and 1720(9) keV in the centre of mass frame. It was decided due to obtaining two different target centroid energies at ~ 957 keV that the 956.4(2) keV energy measurement with two counts was removed due to large statistical uncertainty compared with the group of runs at 957.1(2) keV with 18 counts. The resulting direct capture cross-sections were $3.51_{-0.98}^{+1.17} \times 10^{-10}\text{b}$, $1.60 \pm 0.37 \times 10^{-8}\text{b}$, $1.57 \pm 0.29 \times 10^{-8}\text{b}$ and $9.9 \pm 1.6 \times 10^{-8}\text{b}$ for centre of mass energies of 957.1(2) keV, 1202.5(3) keV, 1209.5(3) keV and 1720(9) keV, with S-factors of $28.7_{-8.0}^{+9.6}\text{MeVb}$, $108.9_{-25.2}^{+25.3}\text{MeVb}$, $100.6_{-18.3}^{+18.7}\text{MeVb}$ and $24.3_{-3.8}^{+3.9}\text{MeVb}$ respectively.

$\omega\gamma$ for the 1323 keV energy resonance was found to be $0.92 \pm 0.11\text{eV}$. This value can be seen relative to previous literature values and the average of all DRAGON runs of the 1323 keV energy $^{15}\text{N}+\alpha$ resonance in figure 7.1. It can be seen that the DRAGON measurement analysed here yields a lower resonance strength than literature. Here each resonance relative to the DRAGON measurement will be discussed.

Aitken et al. [39] conducted a relative measurement with which the DRAGON measurements agree. Its reliance upon the $^{14}\text{N}+\alpha$ 1.532 MeV energy resonance comparison point from Price [40] [41] using the Snover correction [42] must be questioned. The disagreement between the $^{14}\text{N}+\alpha$ resonance strength in the work of Aitken et al. [39] and that of Dixon and Storey [43], $1.24 \pm 0.10\text{eV}$ and $1.34 \pm 0.11\text{eV}$ respectively, calls into question the validity the use of this resonance as a comparison point. The comparison resonance had been measured as $1.60 \pm 0.13\text{eV}$ by Parker [45] and corrected by both Aitken et al. and Dixon and Storey due to the proposed corrections by Chu and Powers [44] to the stopping powers.

The comparison method used by Aitken was chosen as the quantity of ^{15}N in the solid target need not be known, just the ratio of ^{15}N and ^{14}N . Therefore the scaling with such a

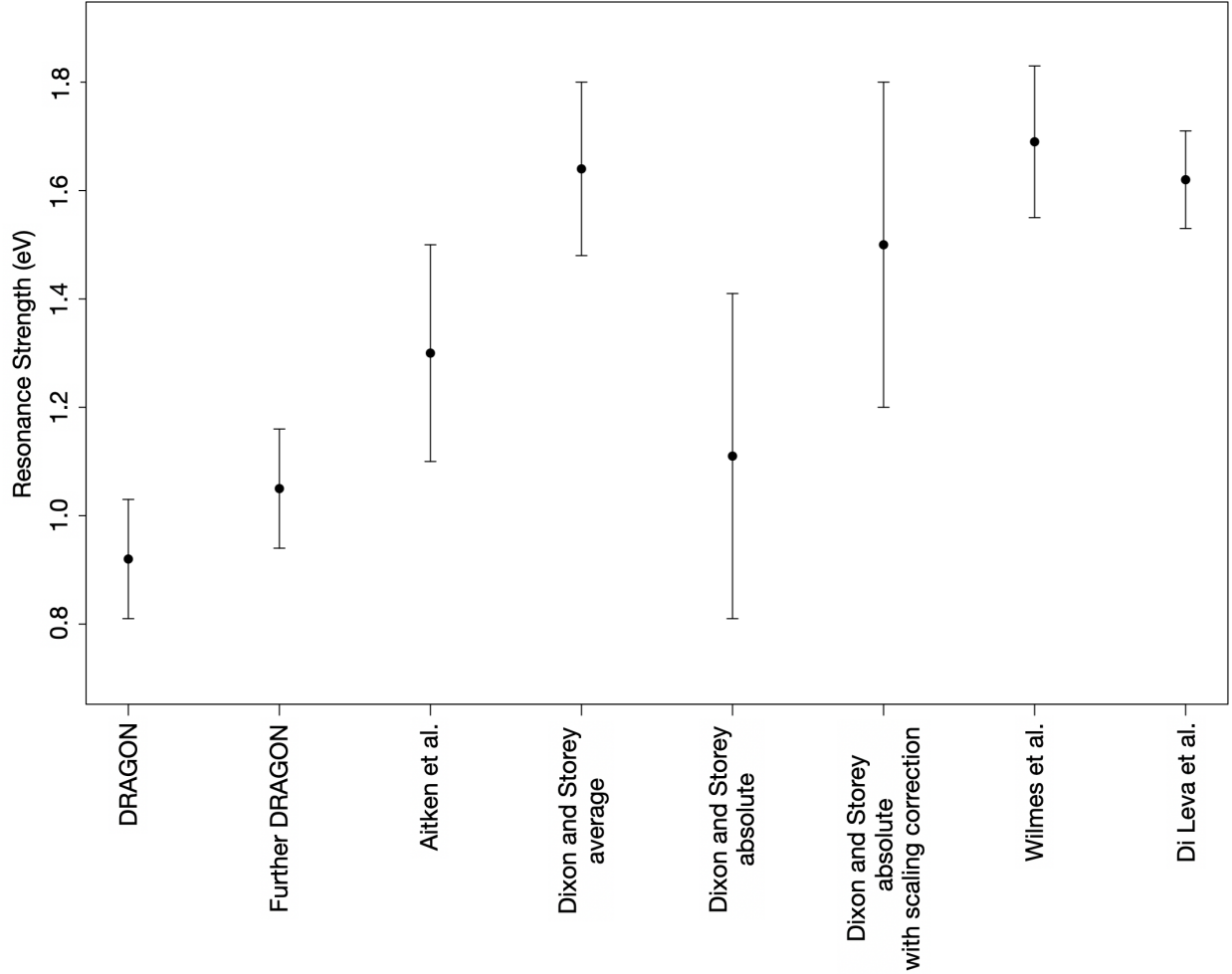


Figure 7.1: From left to right resonance strengths for: work completed and presented here; other DRAGON runs analysed by A. Lennarz et al.; Aitken et al. [39]; Dixon and Storey [43], their average including the scaled measurements and corrected absolute measurement, their raw absolute measurement, their absolute measurement with correction applied; Wilmes et al. [16]; and far right, Di Leva et al. [27].

resonance strength as $^{14}\text{N}+\alpha$ removes dependence on understanding of the absolute nitrogen content within the target.

Dixon and Storey [43] conducted three measurements, the first one using the same scaling comparison of $^{14}\text{N}(\alpha,\gamma)$ as used by Aitken et al. [39]. The second measurement by Dixon and Storey used the $^{15}\text{N}(\text{p},\alpha\gamma)^{12}\text{C}$ reaction, utilising the strong $E_p = 0.898\text{ MeV}$ energy $^{15}\text{N}+\text{p}$ resonance, which at the time was believed to have a strength of $480\pm 48\text{ eV}$, although Dixon and Storey note there is uncertainty around the Gorodetzky [46] reference frame for this resonance strength. This $^{15}\text{N}+\text{p}$ resonance was later remeasured by Zijderhand and Van Der

Leun [63] and in 2010 this resonance was measured again to be at 897 keV with a resonance strength of 362 ± 20 eV by Marta et al. [64]. Using the $^{15}\text{N}(\text{p},\alpha\gamma)^{12}\text{C}$ resonance strength of 362 eV from Marta et al. this rate would be corrected to 1.3 eV, hence aligning much better with the DRAGON measurement.

The third method for resonance extraction by Dixon and Storey was a direct measurement. Measured three times at 1.03, 1.12 and 1.19 eV respectively these measures would also show agreement with the DRAGON measurement. However the authors believed this to be incorrect due to the disagreement with the relative measurements at the time and applied a correction to their target content. The resonances stated before assumed that the ratio of Ti to Ni in the target was equal. The target analysis was extensive comparing resonance strengths to extract target content, it must be noted this method has significant dependence on other previous measurements. Dixon and Storey concluded the resonance to have a strength of 1.64 ± 0.16 eV. The correction to the $^{15}\text{N}(\text{p},\alpha\gamma)^{12}\text{C}$ resonance strength brought the measurement inline with the DRAGON measurement and the absolute measurement had further dependencies on other resonance reaction rates. The average of the Dixon and Storey measurement as they presented it can be seen in figure 7.1 as well as the first absolute measurement and their corrected target measurement.

In 2002 Wilmes et al. [16] measured the 1323 keV energy $^{15}\text{N}+\alpha$ resonance to have a strength of 1.69 ± 0.14 eV, which was in agreement with the average Dixon and Storey [43] measurement when they applied their correction. In the Wilmes et al. measurement the gamma ray HPGe detectors efficiencies were calculated using geant simulations and these were checked using $^{27}\text{Al}(\text{p},\gamma)^{28}\text{Si}$. It seems unlikely that efficiencies of detectors were the reason for the higher resonance strength when compared with the DRAGON result presented here. The reaction is noted by Wilmes et al. to be isotropic due to the $1/2^-$ spin parity of the ^{15}N and the $1/2^+$ of ^{19}F . The uncertainties presented by Wilmes et al. are relatively small and the final uncertainty less than 10%. Furthermore, their branching ratios to the $1/2^+$ 5.337 MeV energy state in ^{19}F are all in agreement with previous literature [49]. The difference between the Wilmes et al. [16] measurement and the measurement conducted here remains unexplained.

Di Leva et al. [27] measured the previously measured 1323 keV energy resonance at an energy of 1.3314(16) MeV with a Γ_α of 2.51 ± 0.10 keV compared to the width from Wilmes et al. of 1.3 ± 0.5 keV [16].

Due to the disagreement between this DRAGON measurement and the Wilmes et al. [16] measurement for the resonance strength the containment of the resonance within the target was also checked for the literature energy value of 1323 keV for both the Wilmes and Di Leva

widths, both were contained well within the target and can be seen in figure 7.2.

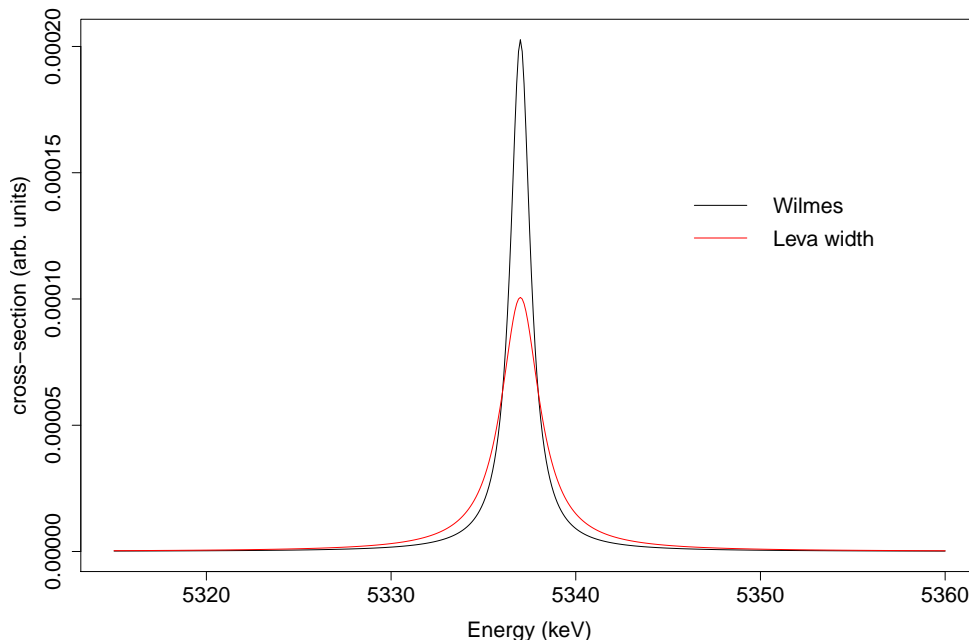


Figure 7.2: The resonance contained within the DRAGON gas target for run 7086. Using the 1323 keV centroid and the widths from both Wilmes [16] and Di Leva [27].

The resonance energy found by Di Leva et al. [27] was tested using DRAGON. By pushing the 1323 keV resonance largely out of the target and remeasuring at a higher energy with target energy range from 1.325 MeV to 1.358 MeV in the CoM frame, this analysis was done by A.Lennarz on run number 7065. This increased beam energy yielded a resonance strength of 0.29 ± 0.03 eV. The fraction within the target of the resonance for each beam energy can be seen in figure 7.3. This concludes the new resonance energy proposed by Di Leva et al. [27] is likely incorrect when compared with the DRAGON data, where the original energy is supported.

Given the resonance energy discrepancy from the Di Leva et al. [27] measurement and the discrepancies with the comparison resonance strengths, and in some cases, supersession, for the Aitken et al. [39] and the Dixon and Storey measurements [43] a current resonance strength could be found using the weighted average of the further DRAGON measurement and the Wilmes et al. [16] measurement. However the discrepancy between these two measurements should be further investigated.

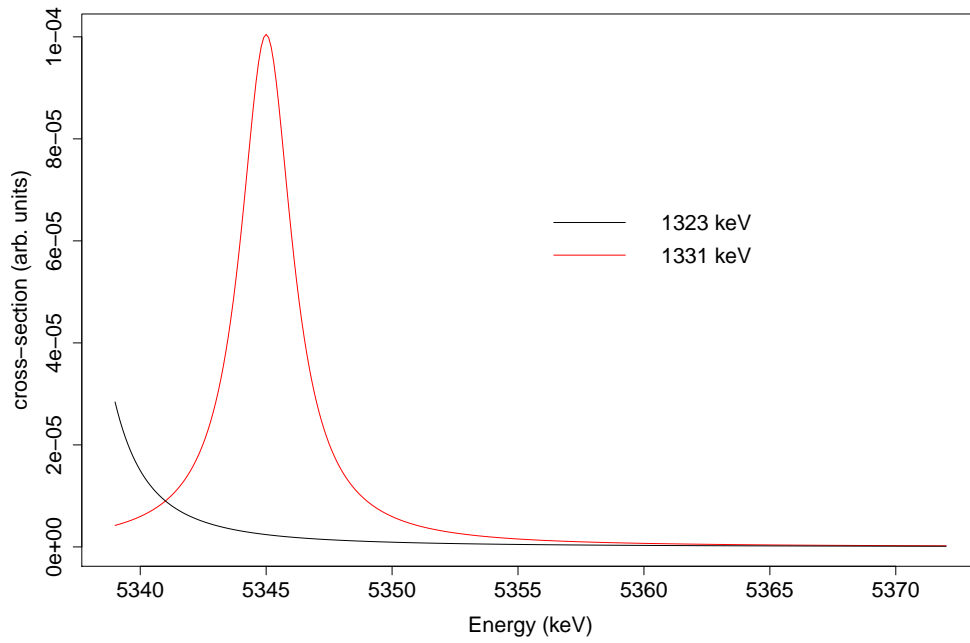


Figure 7.3: Higher energy run of 7065 and the two centroids 1323 keV and 1331.4 keV both with the Di Leva et al. [27] width of 2.51 keV.

Chapter 8

$^{20}\text{Ne}(d,p)^{21}\text{Ne}$ Previous Measurements

Multiple measurements have occurred aiming to measure the $^{17}\text{O}(\alpha,n)^{20}\text{Ne} / ^{17}\text{O}(\alpha,\gamma)^{21}\text{Ne}$ reaction rate ratio to measure the effectiveness of ^{16}O as a neutron poison. Few have however successfully made measurements inside the Gamow window. The work of this thesis focuses on the $^{17}\text{O}(\alpha,n)^{20}\text{Ne}$ reaction, or more specifically extracting properties of states with large neutron widths in the Gamow window for $^{17}\text{O}+\alpha$.

The ^{21}Ne level scheme as accepted by literature [30] before the measurement conducted here can be seen in figure 8.1 where the neutron separation energy is 6.76116(4) MeV and $Q_\alpha=7.34793(4)$ MeV. The energy region of interest, informed by the Gamow window, is at 7.645-7.835 MeV for a temperature of 200 MK and 7.728-7.995 MeV for a temperature of 300 MK in ^{21}Ne . Given the massive star environment of 200-300 MK the adopted energy region of interest in ^{21}Ne is 7.645-7.995 MeV and can be seen shaded green in figure 8.1. It must be noted that states near the outside of this range could contribute to the reaction rate, hence here we measured above and below the Gamow window also. In figure 8.1 the notation used by NNDC [30] is adopted where unconfirmed J^π are shown in parenthesis.

In 2013 Best et al. [65] conducted a measurement of $^{17}\text{O}(\alpha,n)^{20}\text{Ne}$ at the University of Notre Dame. The experiment consisted of an α beam onto a solid Ta_2O_5 target, made using Ta backing and passing ^{17}O enriched H_2O across it. Unlike a previous measurement in the thesis of Denker [66] Best et al. notes they improved their reliability by reducing the background from $^{18}\text{O}(\alpha,n)^{21}\text{Ne}$ by having a target containing only 0.4% ^{18}O .

Detection was via two layers of axially aligned ^3He neutron detectors which utilised the $^3\text{He}(n,p)$ reaction with a Q-value of 764 keV. Their final physical location was decided by placing the detector in the location of maximum neutron flux before the measurement. It must be noted that there was no information collectable on the neutron energies due to the moderator absorbing much of the energy of the neutrons. In reality the inability to

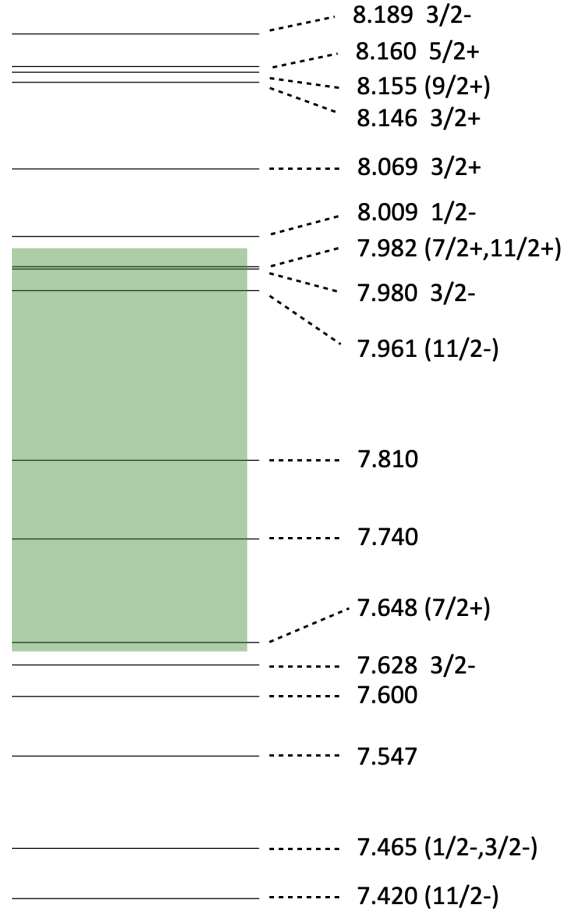


Figure 8.1: ^{21}Ne states across the Gamow window with state energies as accepted by literature [30]. The Gamow window can be seen shaded green.

obtain neutron energies likely had little impact on the experiment output as the experiment scanned across beam energies with a 2 keV uncertainty, hence having neutron energies would have only made identifying background neutrons from other reactions easier. Background reactions were considered, especially the $^{13}\text{C}(\alpha,n)^{16}\text{O}$ reaction. The efficiency of the neutron detectors was found using the reaction $^{51}\text{V}(p,n)^{51}\text{Cr}$, utilising a vanadium target to detect the isotropically distributed neutrons. The efficiencies found from this experiment were supported by simulation.

In the experiment of Best et al. [65] the ^{21}Ne intermediate nucleus may decay via two neutron channels; n_0 or $n_1\gamma$, whose branching ratios are known. Alongside these two reactions of interest there was also measurable background as seen in figure 8.2.

Having subtracted the background neutrons an R-Matrix calculation was run using Azure

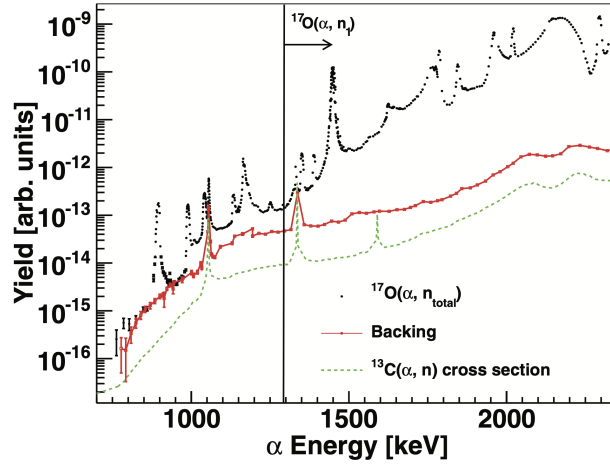


Figure 8.2: Neutron yield for each component, note $n_{total} = n_0 + n_1$. Figure from Best et al. [65]

[67]. Cross-sections and resonance energies were extracted. The fit of the R-Matrix code to the experimental data for the two neutron reaction channels can be seen in figure 8.3. The extracted state energies have a 2 keV uncertainty derived from the uncertainty in the beam energies. The numerous measurements over each resonance that were made justify this uncertainty.

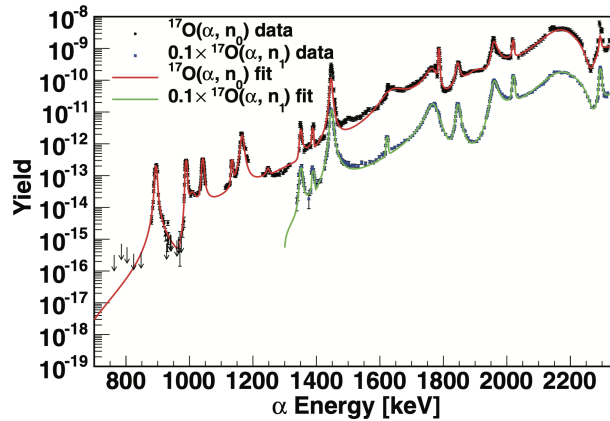


Figure 8.3: R-Matrix fit of the two neutron decay channels. Figure from Best et al. [65]

Combination of all uncertainties for both channels and their combination ultimately led to the total rate uncertainty giving an S-factor uncertainty of 18%. Best et al. measured down to the top of the Gamow window, with their lowest measured state at 8.069 MeV.

DWUCK4 [68] was used to evaluate widths inside the Gamow window. Spectroscopic

factors of 0.01 were assumed as no experimental partial widths were available. Assumptions were also made that if a state has a given neutron width then the (α,γ) channel was likely to be highly suppressed.

Figure 8.4 shows the effect of the new Best et al. [65] rates compared with using the NACRE [69] and Caughlan et al. [70] rates with a correction applied from Descouvemont [71, 65]. The difference in the $(\alpha,\gamma)/(\alpha,n)$ ratio is less than a factor of 2. This does cause the s-process yields to vary dramatically, as seen in figure 8.4. From Best et al. it is clear there is a need for measurement of the properties of the lower lying Gamow window states.

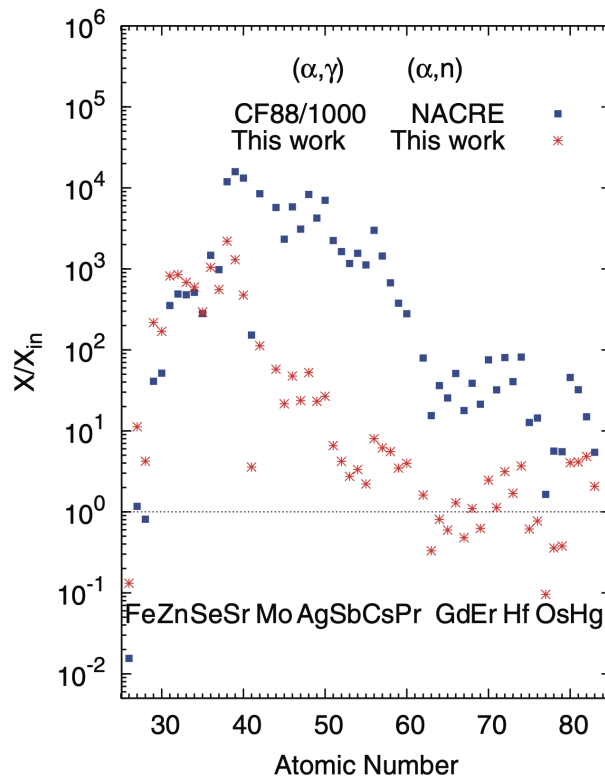


Figure 8.4: Effects on element abundance of Best rates and the previous rates. Note CF88, represents the comparison point of (α,γ) from the work of Caughlan et al. [70] scaled by the factor of 1000 from Descouvemont et al. [71] described by Best et al. [65] for the (α,γ) . The (α,n) comparison point is from a compilation, NACRE [69] using unpublished data. Figure from Best et al. [65]

In 2011 Best et al. [72] made the first measurement of the reaction $^{17}\text{O}(\alpha,\gamma)^{21}\text{Ne}$. It used the same beam and target setup and was similar to that in the 2013 work of Best et al. [65]. The experiment was well shielded to isolate the 45° off-axis germanium detector from background radiation. It was noted that the content of ^{18}O in the target was around

0.4% and that $^{18}\text{O}(\alpha,n)$ is strongly populated. To remove this contamination $^{18}\text{O}(\alpha,n)$ was measured using the same setup and subtracted from the $^{17}\text{O}(\alpha,\gamma)$ data, hence effectively removing the contamination from the data.

The energy was stepped in intervals less than 10 keV to scan across states above the Gamow window. Interestingly the work of Best et al. [72] supports the reaction rate of Caughlan and Fowler [70], not the theoretical rate of Descouvemont [71]. Best et al. [72] are cautious with their initial reaction rate stating that they did only measure three resonances. States in ^{21}Ne with energies between 7.960 MeV to 8.645 MeV that were not seen were concluded as having a smaller (α,γ) strength than was detectable. Best et al. comment that these weaker resonances proceeding via $^{17}\text{O}(\alpha,\gamma)$ could also have contributions of around $\sim 10\%$ to the reaction rate. The conclusion of this publication, prior to the 2013 Best et al. paper [65] was that the (α,γ) channel appears competitive with that of the (α,n) channel. The main drawback of this 2011 Best et al. work was the narrow range over which the measurements were made and the limited resonances measured.

In 2019 Taggart et al. [24] conducted a direct measurement of $^{17}\text{O}(\alpha,\gamma)^{21}\text{Ne}$ in inverse kinematics using an ^{17}O beam and a helium gas target at DRAGON. The experimental setup of DRAGON is discussed earlier in this work in chapter 4 during the $^{15}\text{N}(\alpha,\gamma)$ experimental chapter. A beam of $^{17}\text{O}^{3+}$ was used and DRAGON tuned for ^{21}Ne . The ionisation chamber at the focal plane detector was used allowing an extraction of ΔE -E for each incident particle and the MCPs, micro channel plate detectors were included, which yielded effective particle identification.

Efficiencies were extracted similarly to in chapter 5 with charge state fractions extracted using the work of Liu et al. [56]. Measurements were taken at several energies with resonance strengths found for four resonances as seen in table 8.1. It must be noted that the 633 keV resonance measurement has potentially 3 resonances inside the target and as such this is actually a summation of all three.

The work here resulted in a reaction rate for $^{17}\text{O}(\alpha,\gamma)$ which is two to three orders of magnitude smaller than that of Caughlan et al. [70]. Inside the Gamow window the main difference between the Taggart et al. [24] measurement and the Best et al. [72] measurement lies in the prediction of the contribution of the 305 keV resonance, at 7.653 MeV in ^{21}Ne . The result of this measurement inside the Gamow window can be seen in figure 8.5. The red line was to illustrate the difference in the predictions of Best if the 305 keV resonance is weaker than was predicted and assumed in Best et al. [65].

In summary figure 8.5 from Taggart et al. [24] shows a dramatic change in the production of s-process nuclei due to the change in $^{17}\text{O}(\alpha,n)^{20}\text{Ne} / ^{17}\text{O}(\alpha,\gamma)^{21}\text{Ne}$ reaction rate ratio. This

$E_{COM}(\text{keV})$	^{21}Ne state energy (MeV)	$\omega\gamma$ (meV)	$\omega\gamma$ (meV) from Best et al. [72]
633	7.981*	$(4.0^{+3.1}_{-2.0}) \times 10^{-3}$	
721	8.069	$(8.7^{+7.0}_{-3.7}) \times 10^{-3}$	
810	8.159	5.4 ± 0.8	7.6 ± 0.9
1122	8.470	1.4 ± 0.3	1.2 ± 0.2

Table 8.1: Energies in CoM, respective ^{21}Ne energies, resonance strengths and previous values from Best et al. in 2011 [72]. *May contain two other resonances. Table adapted from Taggart et al. [24].

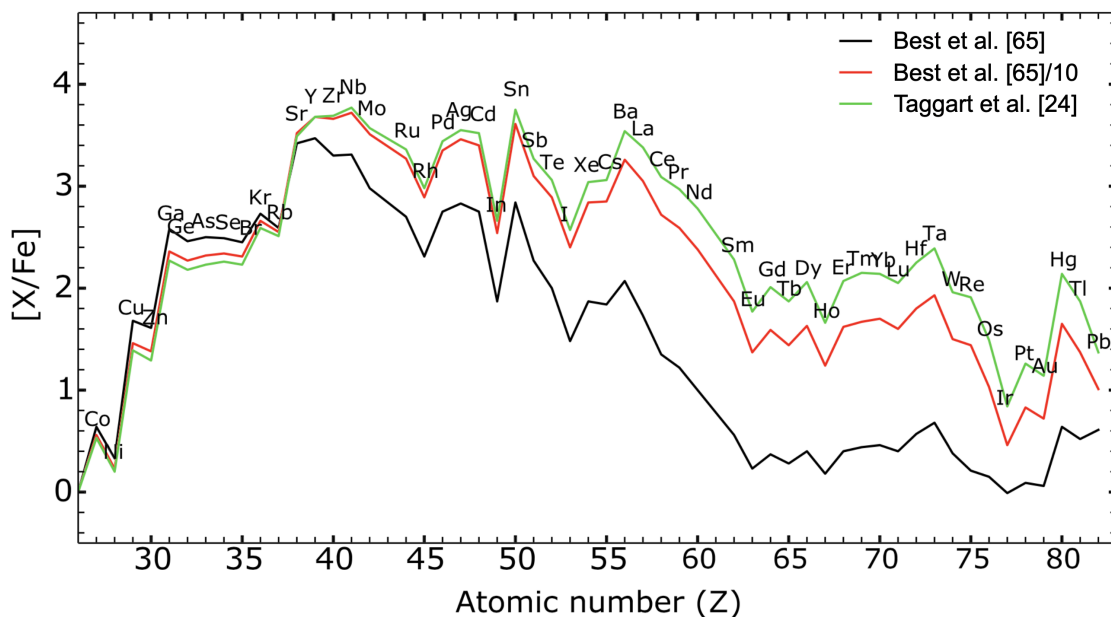


Figure 8.5: Current predictions of heavy element production due to the s-process compared with the work of Best et al. [65] in fast rotating massive stars. Figure from Taggart et al. [24] with minor adaptation.

calls for further measurement inside the Gamow window to obtain further knowledge of the ^{21}Ne states involved, including their partial widths and hence reaction rates.

Direct measurements across the entirety of the Gamow window have not been made using $^{17}\text{O}+\alpha$. However $^{20}\text{Ne}(d,p)$ as measured in this work populated states within the window, hence allowing extraction of neutron partial widths. This reaction method has been utilised before, in 1970 when Howard et al. [73] measured the $^{20}\text{Ne}(d,p)^{21}\text{Ne}$ reaction using a 16.4 MeV beam of deuterons onto a 200 Torr ^{20}Ne gas target contained with foil windows. Measurements were made from 10° up to 150° in the lab frame. The detector used was of

ΔE - E configuration and as such allowed particle identification.

Differential cross-sections were extracted and compared with DWBA differential cross-sections produced using the code JULIE, as referred to by Satchler [74]. Howard et al. [73] show the optical potentials used in their model. Howard et al. do not reach ^{21}Ne state energies that are within the Gamow window, they do however measure and analyse the 6.606 MeV state. The differential cross-section plot as in figure 8.6 shows the differential cross sections relative to the DWBA calculation.

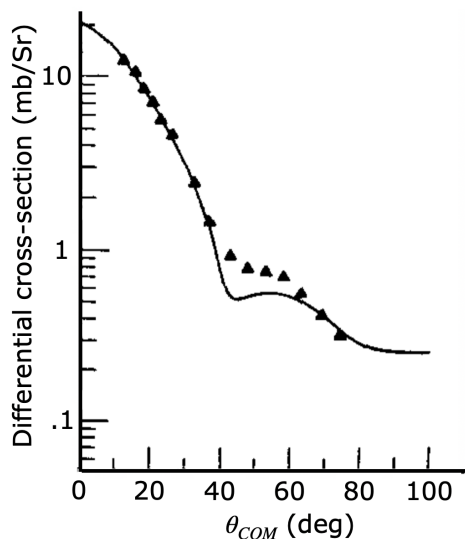


Figure 8.6: Measured differential cross-section values for the 6.606 MeV state and the fitted DWBA $l=2$ output. Figure from Howard et al. [73].

In 1980 Stanford and Quin [75] studied levels of ^{21}Ne using a polarized deuteron beam at 10 MeV into a 99% enriched gaseous ^{20}Ne target. Detection was through four detectors each behind collimating slits such that the solid angle was known, the detectors had a 100 keV resolution. Whilst Stanford and Quin did not populate states in the Gamow window they did measure states that are also seen in the measurement discussed here and as such offers a comparison point. Of particular interest is the 6.609 MeV state, identified then as the 6.605 MeV state and its prevalence as seen in figure 8.7 was used in this work to identify it as a suitable calibration state.

Stanford and Quin show some of their optical model parameters, used also in presented DWBA outputs for extraction of spectroscopic factors and transferred l values. The DWBA code used was DWUCK2 [76]. They show the DWBA output with their 6.61 MeV data, as seen in figure 8.8. Notice how the data appears to have the rough shape of an $l=2$ transfer, not however completely conclusive.

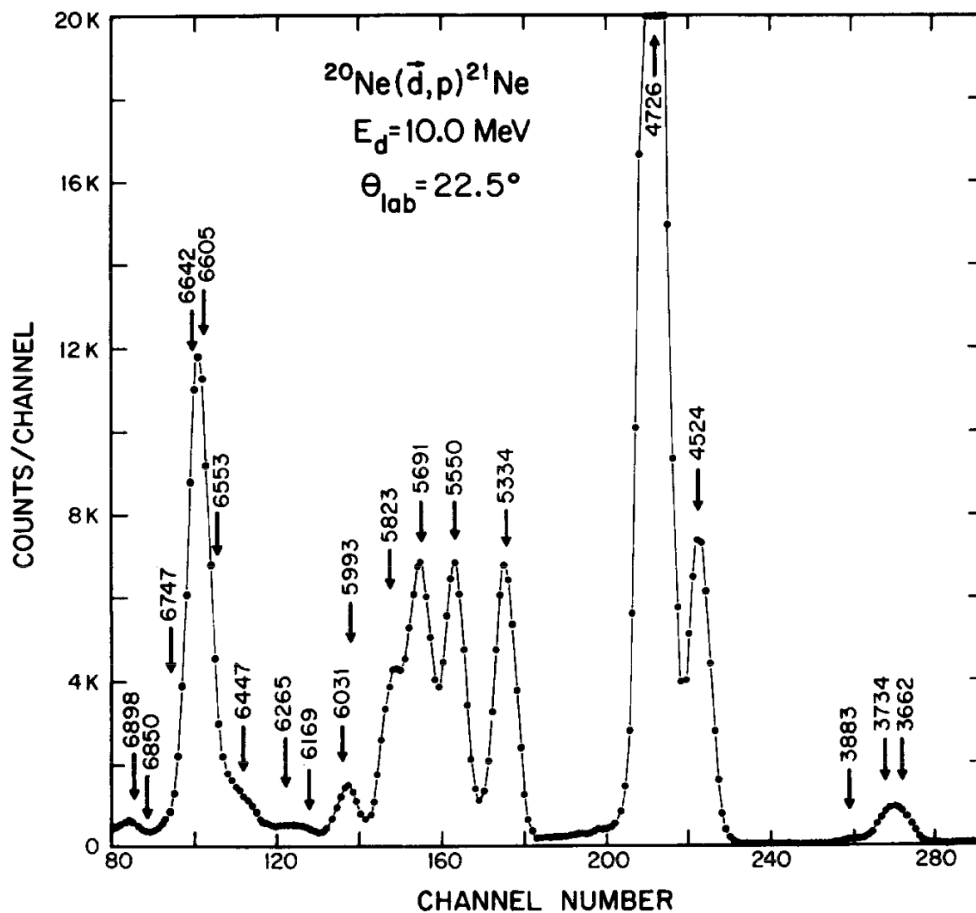


Figure 8.7: Spectra of ^{21}Ne , note the population of the 6.605 MeV peak, later measured as 6.609 MeV. Figure from Stanford and Quin et al. [75]

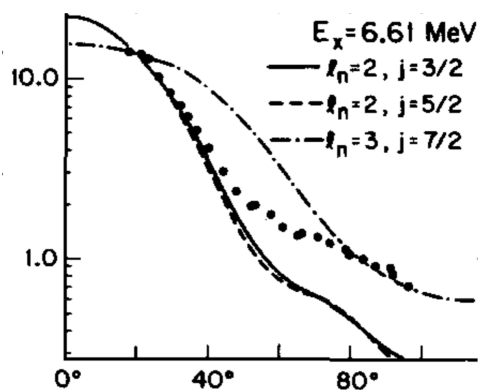


Figure 8.8: Measured differential cross-section values for the 6.61 MeV state and the DWBA outputs. Figure from Stanford and Quin et al. [75].

The previous work leaves significant opportunity for improvement of the rate by measurement of state properties of states that are within the Gamow window. Figure 8.5 shows the dramatic effect on heavy element production through the s-process with changes to the $^{17}\text{O}(\alpha,n)^{20}\text{Ne} / ^{17}\text{O}(\alpha,\gamma)^{21}\text{Ne}$ reaction rate. In the work presented here states in ^{21}Ne will be populated inside the Gamow window using $^{20}\text{Ne}(d,p)$.

Chapter 9

$^{20}\text{Ne}(\text{d},\text{p})^{21}\text{Ne}$ Experimental Technique

9.1 Beam production

The production of the deuteron beam occurred in a Direct Extraction Negative Ion Source (DENIS). This source could produce a beam of negative deuterons at a rate of $30\ \mu\text{A}$ with an energy of $50\ \text{keV}$ [77]. An electrical arc was made between a cathode and an anode using a $150\ \text{V}$ potential. The region between the anode and cathode was filled with deuterium and hydrogen gas, this was pumped to maintain pressure at around $0.01\ \text{Torr}$ [77].

Deuterons were accelerated to an energy of $13.984\ \text{MeV}$ using a terminal voltage of $6.992\ \text{MV}$ through the TUNL Cyclo-Graaff. This beam energy was chosen based on the ability to populate states in the Gamow window on the focal plane. This was the maximum energy possible without significant breakdown inside the accelerator. Figure 9.1 shows the method of acceleration of the deuterons. The chains consisted of electronically isolated pellets that are charged by driving the electrons from the pellet. As these pellets move through the centre of the accelerator the pellets become negatively charged. The initial acceleration of the $^2\text{H}^-$ ions occurred alongside the first chain, these $^2\text{H}^-$ ions then passed through a stripping foil, creating $^2\text{H}^+$ ions, which were then accelerated alongside the second chain. The accelerator was designed such that the high voltage is located centrally and the external terminals are grounds. Due to the charge of the beam ions acceleration occurs effectively twice. As such the potential difference felt by the beam ions was twice the voltage that is induced on the high voltage terminal.

The accelerated deuterons passed through two 90° magnets. This technique ensured

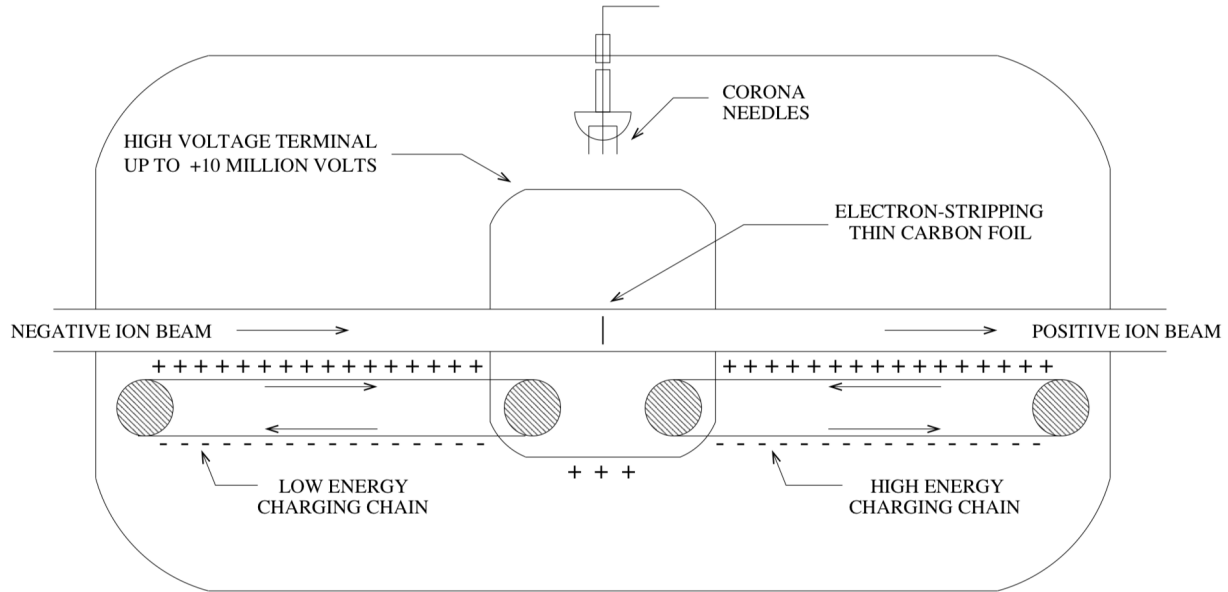


Figure 9.1: Schematic of deuteron acceleration in Van de Graaff accelerator from the Thesis of A. H. Couture [77].

the beam was as close to mono-energetic as possible and species with differing magnetic rigidity, or equivalently mass-charge ratio would have been removed from the beam. As such effectively mono-energetic deuterons arrived at the target chamber.

Typical beam intensities were 300-575 nA. However, with the detector at its most forward angle, 10.6° in CoM, 10° in the lab frame, the beam intensity was reduced significantly, to approximately 90 nA. This was due to significant beam passing through to the detector causing electrical break-down. The final beam on target for each measurement was extracted using the integral of charge on the target ladder.

9.2 Split-pole spectrograph

The reactants left the target and proceeded through the exit aperture which had a solid angular acceptance of (0.54 ± 0.01) mSr. The force on a charged particle passing through a magnetic field is described by eqn. 4.2, as in DRAGONs magnetic dipoles. As the particles passed through the dipoles they were separated by energy and on mass-charge ratio. Those particles with the highest mass/charge ratio travelled through the split pole following a path similar to that of the green line in figure 9.2. Considering particles with the same mass-charge ratio those with most energy would have followed a path similar to that of the green line with

the lowest energy particles reaching the focal plane detector at the opposite end, following the purple path.

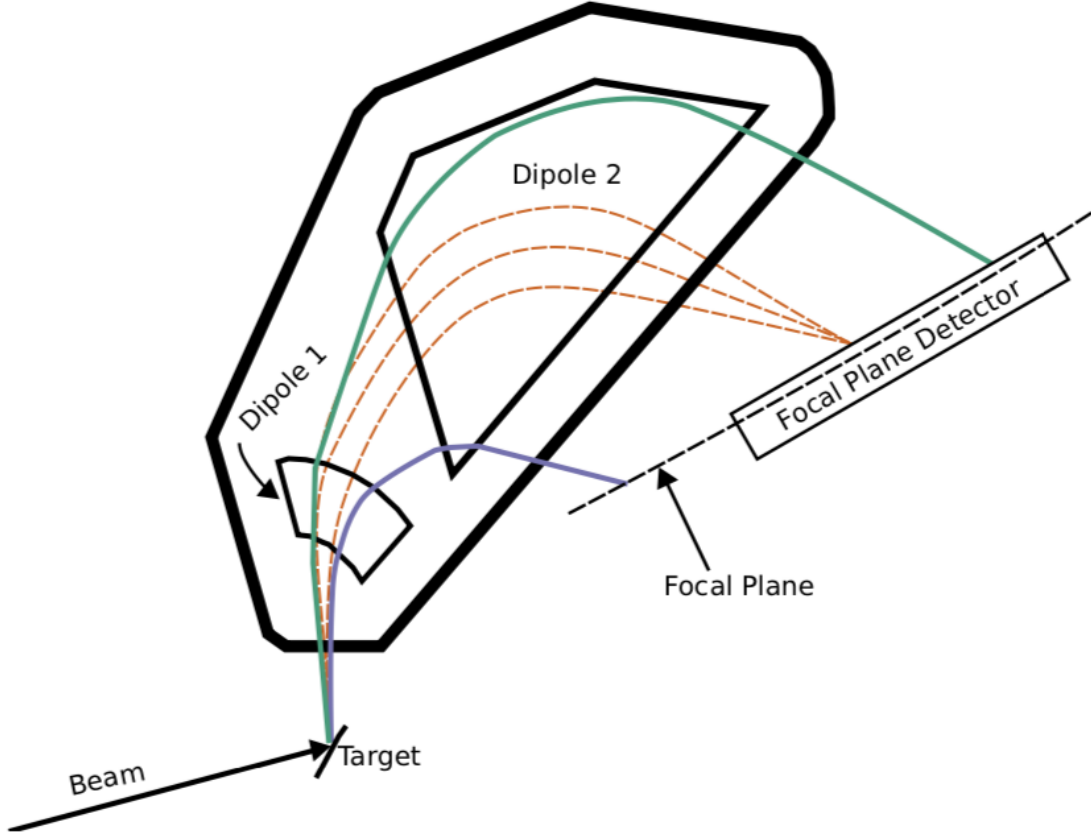


Figure 9.2: Schematic of trajectories through the split pole spectrograph from Marshall et al. [78].

The Enge split-pole allowed focusing of particles with the same mass/charge ratio and energy over the two dipoles [79, 78]. Particles arriving at the focal plane detector with the same positions are said to have had the same magnetic rigidity, described, for a non-relativistic system by eqn. 9.1. Magnetic rigidity is related to the gyroradius, defined in eqn. 10.3.

$$B\rho = \frac{mv_{\text{perp}}}{q} = \frac{\sqrt{2mE}}{q} \quad (9.1)$$

The Enge magnet allowed separation of beam particles from the reactant protons, some beam did however pass through the Enge magnet and arrive to the detector. The removal of the majority of this beam contamination or “leaky beam” took place when cutting the data

during the analysis process, seen in section 10.3.

9.3 Focal plane detector

The detector was orientated and located at the focal plane of the correct ion. We required the protons to fall onto the focal plane by the path described by the orange path in figure 9.2. It is important to note that if the detector was poorly positioned it would have caused a dramatic increase in recorded peak width and hence a reduction in resolution. With “correct” positioning the peak width was dominated by the actual detector resolution.

The detector consisted of two position sensitive detection components and a ΔE and E setup, the latter allowed for particle identification, this layout can be seen in figure 9.3.

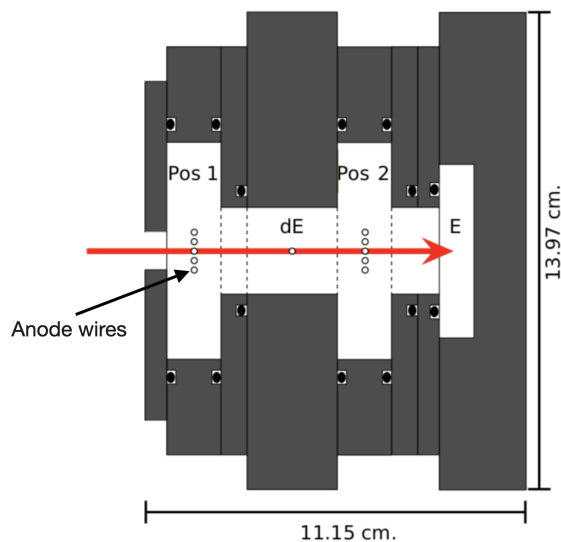


Figure 9.3: A cutaway perpendicular to the beam and looking down the anode wires. Figure from Marshall et al. [78] with minor adaptation. Red arrow represents reactant particle path, passing through 2 position sections.

The ΔE component of the detector consisted of one anode wire and two cathode planes forming a gas proportional counter. Particles deposited energy in the process creating charged pairs. The amount of charge arriving at the anode and cathode was proportional to the amount of energy deposited by a particle.

The E component of the detector consists of a plastic scintillator, the Saint-Gobain BC-404. This type has a fast response and hence was suitable to use to trigger the data acquisition system [78, 80]. As in Marshall et al. [78] the crystal was 28.25” by 2” by 0.25”, the size

was determined by ensuring full coverage of the detector and that all particles stop in the crystal.

The light produced in the BC-404 crystal was collected using a PMT, Photo-Multiplier Tube located on top of the detector. To transfer the light from the crystal to the PMT Bicon BCF-91A optical fibers joined the BC-404 crystal and linked to the PMT through a light tight tube. These fibers shifted the light produced by the crystal (380-495 nm, maximum emission at 408 nm) to green, with a range of 495-570 nm [78]. The photomultiplier tube was a Hamamatsu H6524 which has a range of 300-650 nm with peak detection sensitivity at 420 nm [81]. During the detector design this was chosen due to its high efficiency at the stated wavelengths [78].

Figure 9.4 shows the construction of the two position sensitive sections. These position sensitive sections were avalanche counters with anode wires, so the avalanche created was negatively charged. This negative charge induced charge at the copper pick-up strips where the location of the particle within the detector was found.

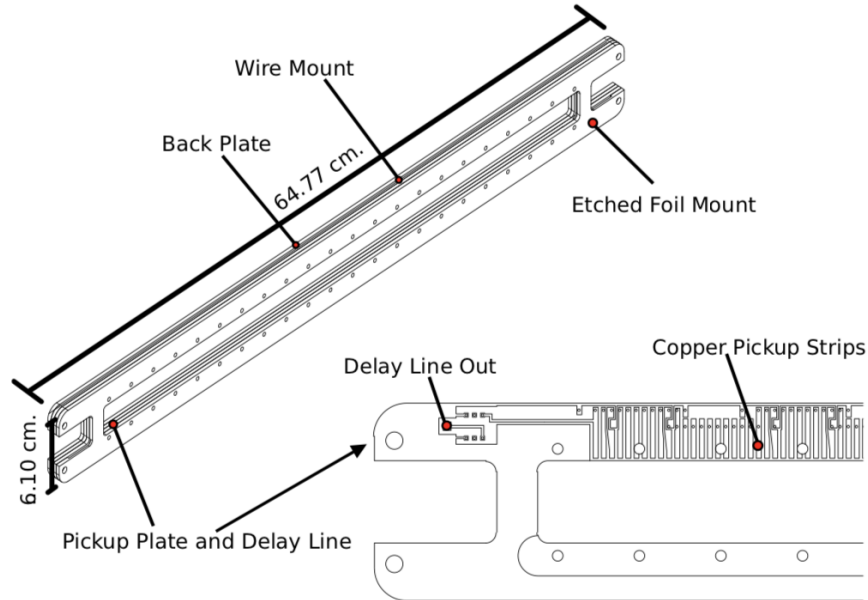


Figure 9.4: Schematic of one of the position section assemblies. Figure from Marshall et al. [78].

The Focal plane detector system had a solid angular acceptance of (0.54 ± 0.01) mSr and was movable in one plane. Measurements of $^{20}\text{Ne}(d,p)^{21}\text{Ne}$ took place at 5 different angles, which were 10° , 15° , 20° , 25° and 38° , equating to 10.6° , 15.9° , 21.2° , 26.4° and 40.1° in the centre of mass frame respectively. A conservative uncertainty was adopted of 0.2° in the lab

frame, equating to 0.21° in the centre of mass frame. This uncertainty accounted for the error in focal plane position and also the variation of differential cross-section across the 0.54 mSr aperture [82].

9.4 Target content

Prior to the commencement of the experiment RBS, Rutherford Back Scattering, was used to determine content of the target. The output from this was a plot of counts against energy for recoiling ions. SIMNRA [83] was used to simulate various target content fractions through various layers. The Neon content within layers, and layer thickness' were changed until the simulated fit replicated the RBS experimental data well. The initial content calculation had been done by collaborators at TUNL. Their values were inputted into SIMNRA and the ^{20}Ne content changed in increments to around 5% where the simulation could be perceived to no longer match the data. It was at this point the conservative uncertainty of 5% on the target content was adopted.

Between runs at every given angle an elastic scattering measurement was made at 25° . This allowed for target content monitoring and correction for target degradation when extracting differential cross-sections. Unfortunately this did not occur before the experiment commenced but after the first run. A method was developed to alleviate this and is discussed in section 10.2.

So far discussion has been about the ^{20}Ne target only. At each of the five measurement angles measurements were also taken of a carbon target. Theoretically identical in make-up to the implanted neon target, but without the implanted neon. This was for the investigation of a background subtraction method to remove any contaminants. Some measurements were also taken using SiO_2 and Aluminium, intended for calibration purposes. These proved to be too densely populated to reliably identify states.

Chapter 10

$^{20}\text{Ne}(\text{d},\text{p})^{21}\text{Ne}$ Data Analysis

10.1 Beam normalisation

Beam delivered onto the target was recorded by collecting the total charge over each run. Charge collected, noting the deuteron is singly charged, can be converted into beam particles for each run and grouped by measurement angle. An instantaneous reading of beam onto target was also taken for each run and a time weighted average taken for each group of runs, also grouped by measurement angle. The two methods were compared and were found to be in approximate agreement. It was deemed normal that the beam may fluctuate slightly in intensity during the experiment. The total beam on target by measurement angle can be seen below in table 10.1. Note the uncertainty was deemed to be 10% for each integrated beam reading, per run, due to the uncertainties on the electron suppression setup [82].

Angle COM ($^{\circ}$)	Beam particles onto target	Uncertainty of Beam particles onto target
10.6	1.90×10^{16}	6×10^{14}
15.9	5.98×10^{16}	2.3×10^{15}
21.2	9.62×10^{16}	3.4×10^{15}
26.4	7.70×10^{16}	5×10^{14}
40.1	1.21×10^{17}	4×10^{15}

Table 10.1: Number of beam particles onto the target at each angle.

10.2 Target content

Initial target content and uncertainty was extracted from Rutherford back scattering data collected before the experiment commenced by those at TUNL. The thickness of carbon was found to be $2.2 \pm 0.1 \times 10^{18}$ atoms cm^{-1} with an average neon thickness of $1.01 \pm 0.05 \times 10^{17}$ atoms cm^{-1} , hence yielding a target content of $4.3 \pm 0.3\%$. The RBS modelling using SIMNRA gave a higher surface content of ^{20}Ne , as expected due to the target being a natural carbon foil implanted with ^{20}Ne . The initial target content by modelled layers can be seen below in table 10.2.

Layer Number	Total Thickness (10^{15} atoms cm^{-1})	Neon Fraction
1	750	0.09
2	80	0.08
3	120	0.07
4	90	0.02
5	130	0.07
6	200	0.04
7	950	0

Table 10.2: Target neon content by layers and also the total thickness of each layer. No uncertainties are presented on these thicknesses, as they are a modelling construct only. The neon fraction errors are not presented as the errors on individual layers were not investigated, but the uncertainty on the total neon content was found.

During the experiment it was expected that the content of neon in the target would fall. To quantify the target degradation after each group of runs at an angle an elastic measurement was taken at 25° . Figure 10.1 shows this elastic spectra after 20° overlaid with the Focal Plane Plotter package calculation, showing the expected location of elastic peaks. The ^{12}C peak is easily identifiable, it has by far the greatest peak integral. This was expected as the target is mostly natural Carbon.

Natural carbon consists of ^{12}C and ^{13}C at 98.93(8)% and 1.07(8)% respectively [84]. Direct comparison of the natural carbon content and the areas under the two carbon peaks; left most peaks seen in figure 10.1; are in agreement. These carbon peaks can also be seen fitted in figure 10.2. Note that negligible differences exist between raw integration of bins and the fitted bins as the peaks are of typical Gaussian shape.

The ^{20}Ne elastic peak was fitted for each elastic measurement after each measurement angle. The ratio of this peak to the number of beam particles during the elastic scattering

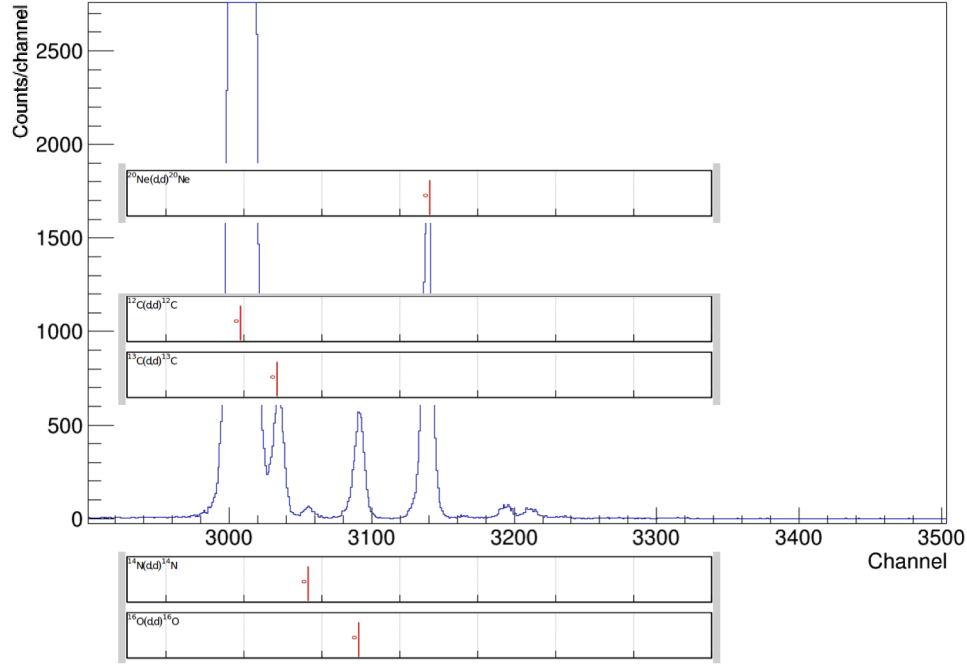


Figure 10.1: Elastic measurement spectra at 25° after the 20° measurement overlaid with Focal Plane Plotter calculation to identify peak species.

runs was taken and monitored. The elastic spectra, as fitted, for after the 38° runs can be seen fitted in figure 10.2.

The degradation of the target can be seen in figure 10.3 as the ratio of elastically backscattered particles from ^{20}Ne decreases per beam particle. The five data points were taken, each after a group of runs at one of the respective measurement angles. Note, as mentioned earlier, there was not however an equivalent run before beginning the first measurement at 25° . The five data points were fitted with a linear fit, resulting in a relationship as in eqn. 10.1.

$$\frac{I_{neon}}{N_{beam}} = 7.4 \times 10^{-12} - 5.082 \times 10^{-30} \times N_{CB} \quad (10.1)$$

where $\frac{I_{neon}}{N_{beam}}$ is the integral of the elastic neon peak per beam particle on target and N_{CB} the cumulative number of beam particles onto target.

The extrapolation of this fit back to when beam on target=0 gave an expected peak content per beam particle at the start of the experiment. The extracted elastic neon peak content at the start of the experiment was taken in ratio with the elastic neon peak content expected at a given beam on target point, extracted using eqn. 10.1 and eqn. 10.2.

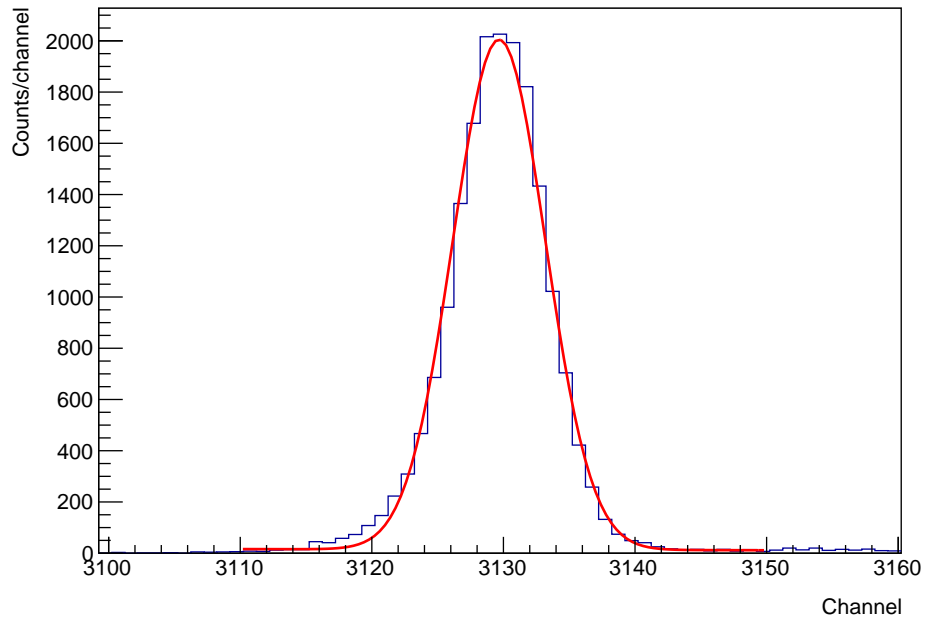


Figure 10.2: Elastic measurement ^{20}Ne peak at 25° after 38° measurement. Showing a fitted Gaussian peak.

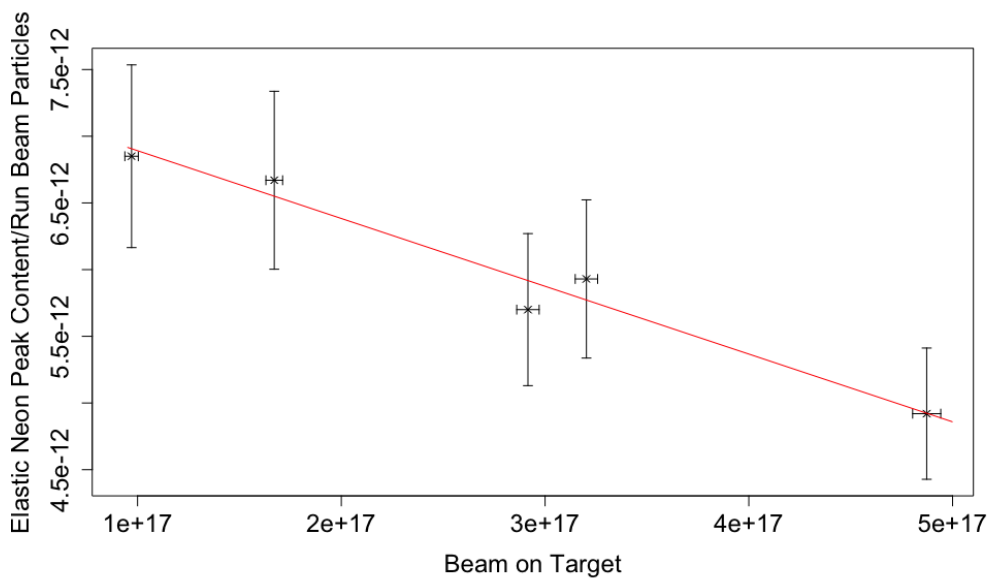


Figure 10.3: Counts in neon peak per unit beam particle during 25° elastic run against the total beam particles on target through whole experiment since initial RBS measurement of target.

$$N_{TNe} = N_{TNe0} \times \frac{\frac{I_{neon}}{N_{beam}}}{\frac{I_{neon0}}{N_{beam0}}} \quad (10.2)$$

where N_{TNe} is the target number of neon particles in the target at a given time, t ; N_{TNe0} is the target number of neon particles in the target at the beginning of the experiment, from the RBS; $\frac{I_{neon}}{N_{beam}}$ and $\frac{I_{neon0}}{N_{beam0}}$ the integral of the elastic neon peak per beam particle on target at a given time and at the experiment start respectively.

The uncertainty on this measurement was dominated by the uncertainty in the RBS, matching the profile of the elastic scattering beyond this 5% showed very significant deviation from the spectrum expected. The deviation between the third and fourth data point within figure 10.3 is expected to be due to striking a slightly different region in the target where the neon content was marginally higher.

The function of the fit in figure 10.3 and the output of the calculation in eqn. 10.2 was used to calculate the neon target content directly before a group of runs at an angle and directly after those runs. Due to the linear relationship seen in figure 10.3 it was expected that over a relatively small amount of beam on target so the degradation would be linear. Therefore a simple mean of the neon content before and after each measurement angle was taken as the neon content over the entire run. This method allows for degradation for all neon target exposure to beam since the Rutherford back scattering before the experiment began.

10.3 Contaminant removal

Before considering extracting neon peaks and fitting them, the removal of background contamination in the focal plane spectra took place. The dE-E make-up of the detector allowed particle identification and hence differentiation between the deuteron beam and the protons. For contaminant removal and peak fitment it should be noted that position 1 was used, ‘‘Pos 1’’ as labelled in figure 9.3. Gating occurred using a piece of software called Jam [85], it allows plotting of histograms and easy manipulation of gates. The energy deposited in the dE component of the detector plotted against the position on the focal plane detector for 40.1° yields figure 10.4.

There are four main features seen in figure 10.4. Firstly the deuteron loci at higher energy above the gated, shaded region, these are particles that deposited more energy when

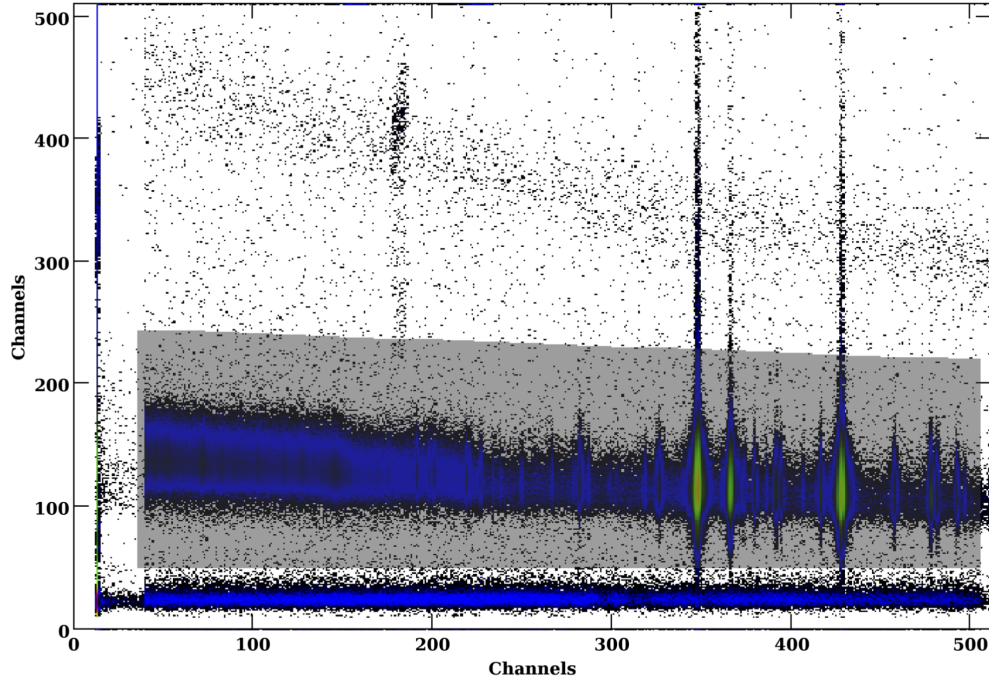


Figure 10.4: Energy deposited in the dE component of the detector against the focal plane position, both in an arbitrary channel number, for the 40.1° measurement. The shaded region represents the gated region. Figure extracted from Jam [85].

travelling through the dE region and as such these are identified as deuterons. Secondly the particles that deposited effectively no energy in the dE detector component seen at very low channel number in y . The counts with almost zero in the position, x axis, are simply discarded, these seem unlikely to be physical particles. The region gated can be seen to have structure and as such these are protons. Note how three states in ^{13}C can be seen originating from $^{12}\text{C}(d,p)$, the removal of the tails of these peaks in energy was deemed acceptable as; they are many standard deviations from the peak mean in energy, hence in reality minimal fractional count removal occurred. The integral of these $^{12}\text{C}(d,p)$ peaks was not used for analysis.

To further enhance the gating technique and background removal, the 2D histogram of the energy deposited in dE component of the detector and that energy deposited in the E component can be plotted. The gate from the respective dE against position plot, as in figure 10.4, was carried over to the dE against E plot for each angle as seen in figure 10.5 for 40.1° .

The region in figure 10.5 that is shaded represents the cut on the dE-E plot. Note those data points removed at low E, low channel number on the x axis, represents further background removal. These were particles with very low energy deposited in the E detector,

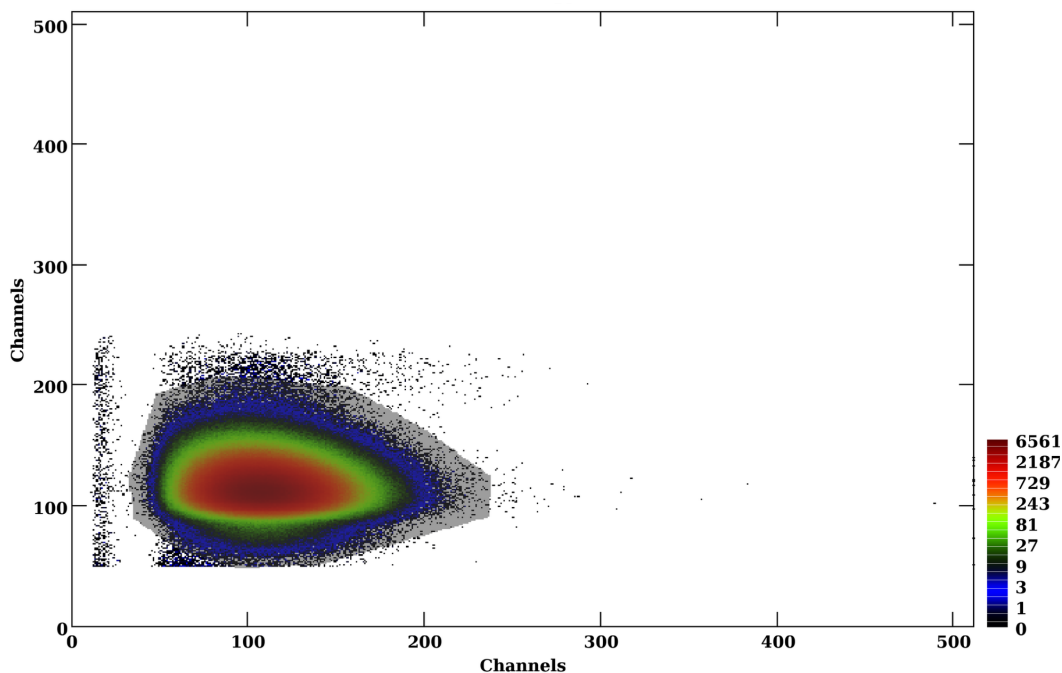


Figure 10.5: Energy deposited in the dE component of the detector against the remaining energy deposited in the E component of the detector. Both energies plotted in an arbitrary channel number, for the 40.1° measurement. The shaded region represents the dE-E gate region.

implying they had a relatively high stopping power through the dE detector when compared to the protons, these were deuterons. The position spectra was then plotted for the data points removed from the second cut, the dE-E cut as seen in figure 10.5 and can be seen in figure 10.6. Note the removal of some of the $^{12}\text{C}(d,p)$ protons. The spectra is at 8 channels per bin and despite this the region of interest, containing the Gamow window, ~ 800 to 1600 channels, shows little background removal and, more importantly, no structure. We can be confident that, relative to statistical uncertainty a negligible number of counts were removed from the region of interest, given the bin content is typically 1 or 2 counts despite being 8 channels per bin.

As an extra check of what particles were removed the anti-gate of both cuts can be seen in figure 10.7. The two loci of data around similar channel number to the protons seen in figure 10.5 are those removed from the first dE channel gate and are dominated by the $^{12}\text{C}(d,p)$ protons. These $^{12}\text{C}(d,p)$ can be seen to be of relatively high intensity to the neon peaks and the integral of these peaks are not used and as such the removal of these counts is deemed unimportant.

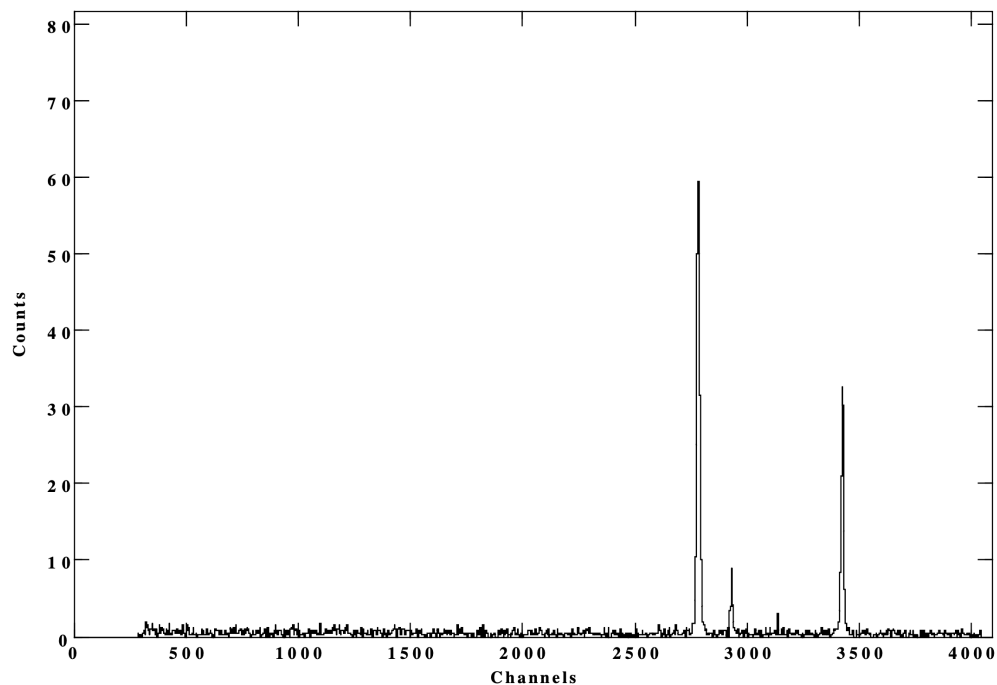


Figure 10.6: Position spectra for the anti-gated particles from the dE-E gate as seen in figure 10.5. Note the removal of what will later be shown as counts from the three carbon peaks formed through the $^{12}\text{C}(d,p)$ reaction.

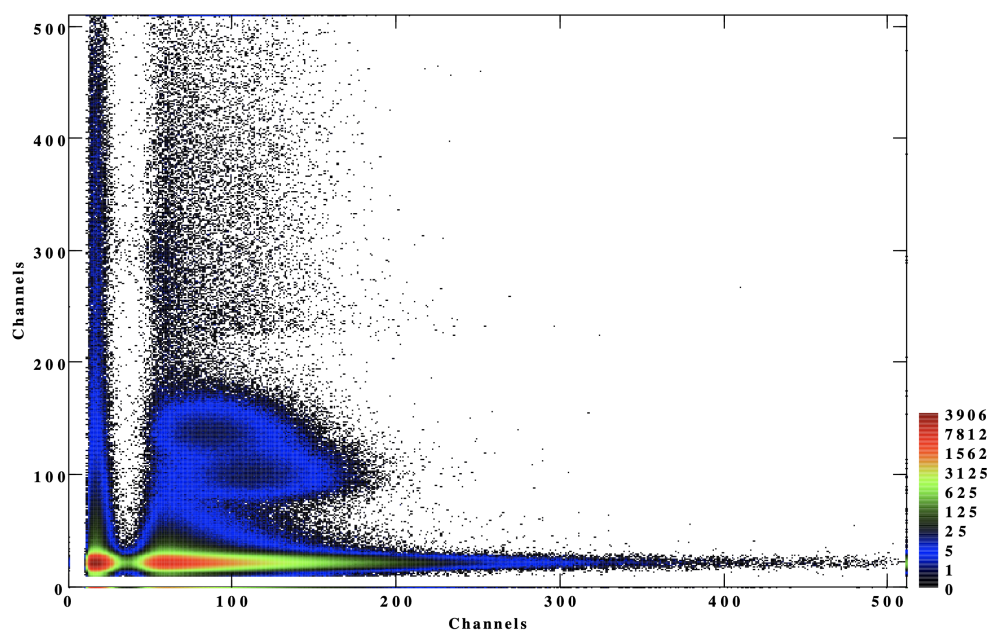


Figure 10.7: The particles present in the anti-gate of both the dE position gate and also the dE-E gate, displayed on a dE against E plot. Axis are in arbitrary channel numbers.

10.4 Narrow state width extraction

Due to the non-linear calibration function, as discussed later in section 10.6, the peak widths were not expected to remain perfectly constant across the focal plane. So, the assignment of a narrow peak width for the peaks within the region of interest was dictated by a peak within, or close to that region. The peak used for the narrow peak width was the 6.609 MeV energy state peak. The state was selected due to it being below the deuteron separation threshold and well separated but in relative close proximity to the Gamow window. A fitted example can be seen in figure 10.8 from the 21.2° runs.

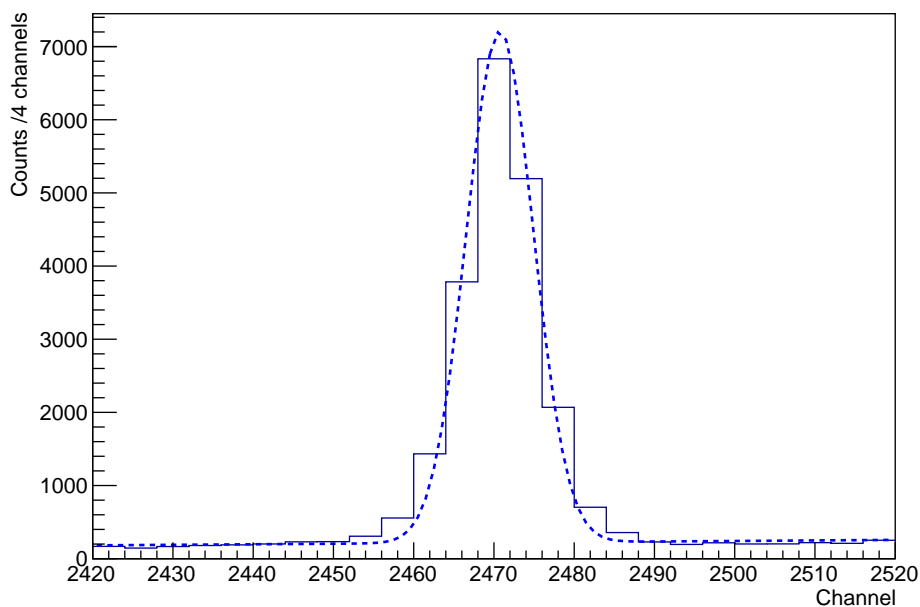


Figure 10.8: Fitted 6.609 MeV state at 21.2° showing good separation and flat, linear background.

The narrow widths at each angle were taken by fitting the 6.609 MeV energy state. The narrow widths were calculated by averaging across two different fits of 6.609 MeV for each angle, except at 40.1° where the 5.69 MeV energy state was also used as an extra reference point. The difference between these two fits was the binning, discussed and seen later in section 10.6. It must be noted that importantly all the narrow bin widths were within error of each other regardless of binning.

The 6.609 MeV energy state peak is normally well separated except at 40.1° . There is a peak of much smaller magnitude overlapping the 6.609 MeV energy state, this can be seen in figure 10.9.

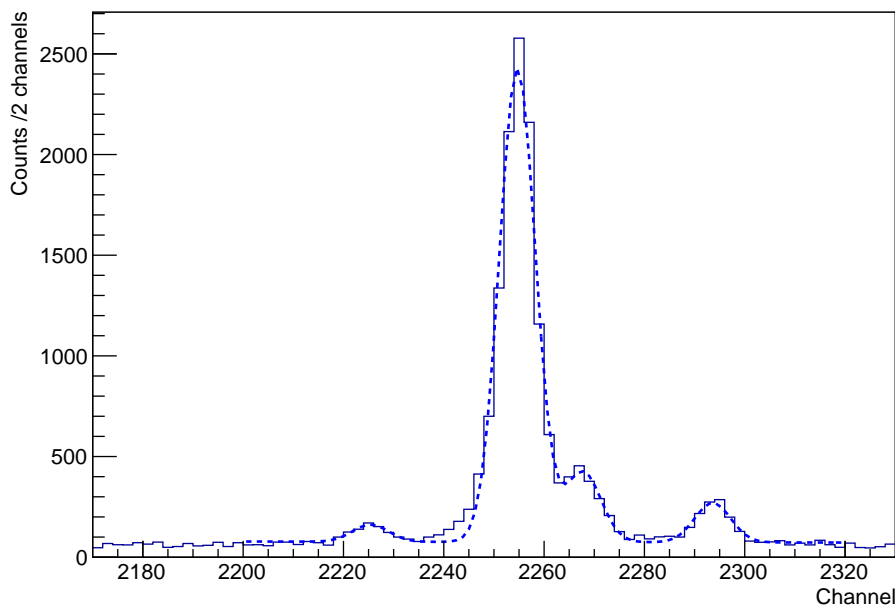


Figure 10.9: Fitted 6.609 MeV state at 40.1° showing composite fit with a linear background.

The value of 3.66 ± 0.09 ch for the 6.609 MeV energy state peak width is also in agreement with the fitted width of the 5.69 MeV state of 3.65 ± 0.04 channels, thus, 3.66 ± 0.09 channels was accepted as the narrow state peak width at 40.1° . When peak fitting in the Gamow window the width was constrained to this value where expected to be narrow. Where the state appeared narrow in the spectra the narrow width was limited to those values in table 10.3 at each respective angle. The final narrow state widths can be seen in table 10.3.

10.5 Peak fitting method development

There are several possible methods of removing further background after the cutting process described in section 10.3. The initial route of investigation was a fit using the natural carbon data followed by a composite fit to the neon data. This was quickly dropped in preference of a more reliable method of background subtraction. The method was more reliable due to the ability to check for a flat background, hence quantifying that the subtraction was not removing neon counts.

The first step of the background subtraction process was to effectively fit the carbon target spectra. The exact composite functions used to fit the spectra were unimportant, ultimately obtaining a representative function was of key importance. The function that

CoM Angle ($^{\circ}$)	Narrow peak width (channels)	Narrow peak width uncertainty (channels)
10.6	5.51	0.02
15.9	3.83	0.04
21.2	4.19	0.04
26.4	4.19	0.02
40.1	3.66	0.09

Table 10.3: Peak widths for narrow states, derived predominantly from the width of the 6.609 MeV peak.

best represented the carbon spectra was two gaussians and a cubic function; with one of the gaussians and the cubic forming the background and a gaussian fitting the majority of the oxygen peak, this fit can be seen in figure 10.10. The oxygen peak is the ^{17}O 5.084 MeV energy state, which was populated through the $^{16}\text{O}(d,p)^{17}\text{O}$ reaction.

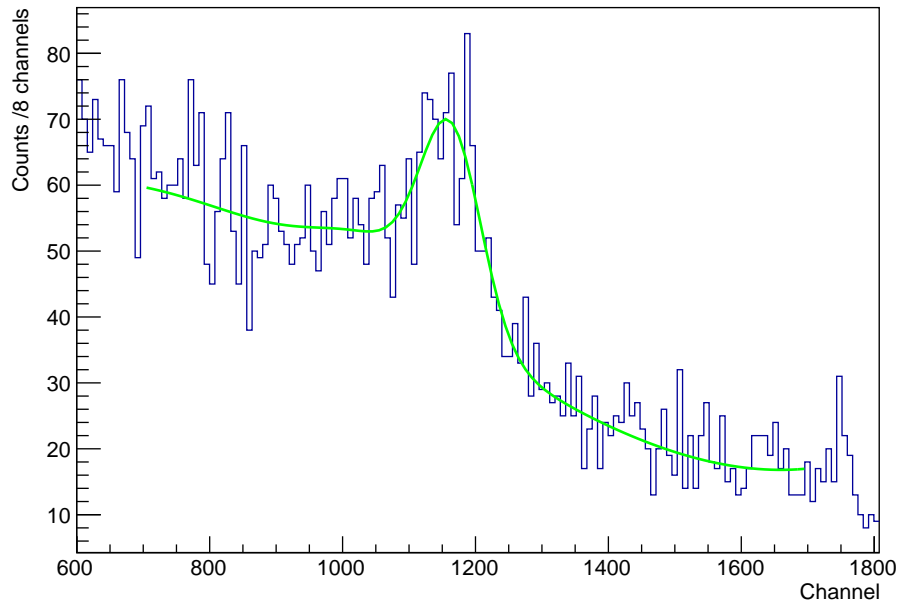


Figure 10.10: Carbon target 40.1° spectra fitted with a cubic function and two Gaussians, replicating the oxygen peak.

Having fitted the carbon spectra the next stage was to scale the fit to the neon spectra

background. The scaling was completed by fitting a range in both the carbon and neon spectra, the latter using a region with no peaks and both avoiding the oxygen peak. An example of the two regions for scaling can be seen in figure 10.11. These scaling fits are the yellow lines in the region of 900 channels and 1560 channels, these fits have a function of $y=c$. An average of the ratio of the c values between carbon and neon was used to scale the background carbon function. The fit region of the scaling function was made at the shown region in neon and an extended region in carbon; extended in carbon to avoid localised fluctuations, caused by greater statistical fluctuation from fewer counts.

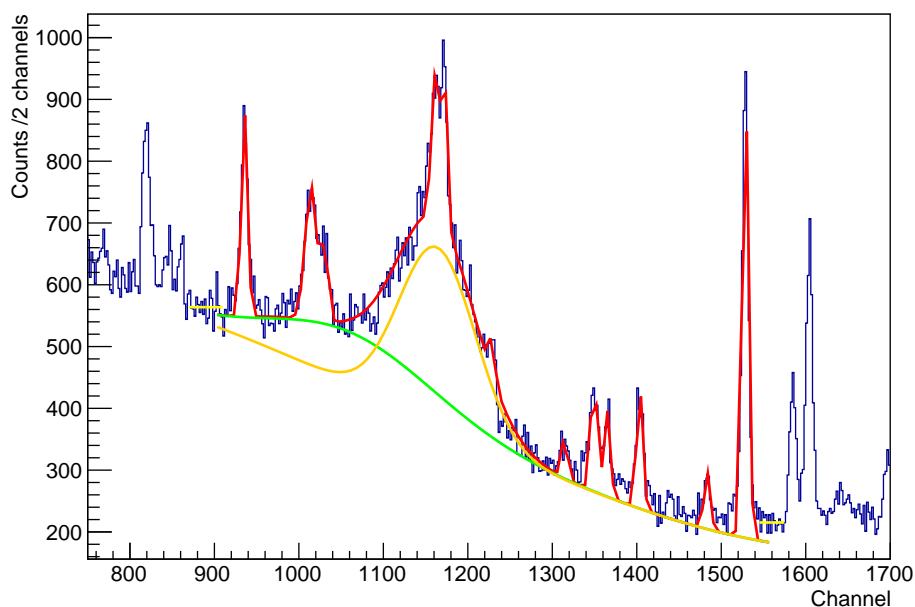


Figure 10.11: Neon spectra fitted (red) on scaled carbon background, comprised of a scaled version of the carbon fit, scaled gaussian and cubic function background (green) and cubic function and gaussian of oxygen (orange), 38° spectra shown.

The background was scaled from carbon and the individual neon peaks fitted as seen in red in figure 10.11. However the background subtraction allowed investigation of the effectiveness of the background fitting as seen in figure 10.12. Note the effective removal of the oxygen peak.

The scaled carbon background subtraction method was abandoned due to difficulty replicating the background due to the low statistics in the carbon spectra. Note the localised ill fitment of the background to the neon, as seen around channel 1400 in figure 10.11, seen also in figure 10.12. Note also around channel 1240 the background spectra falls below 0

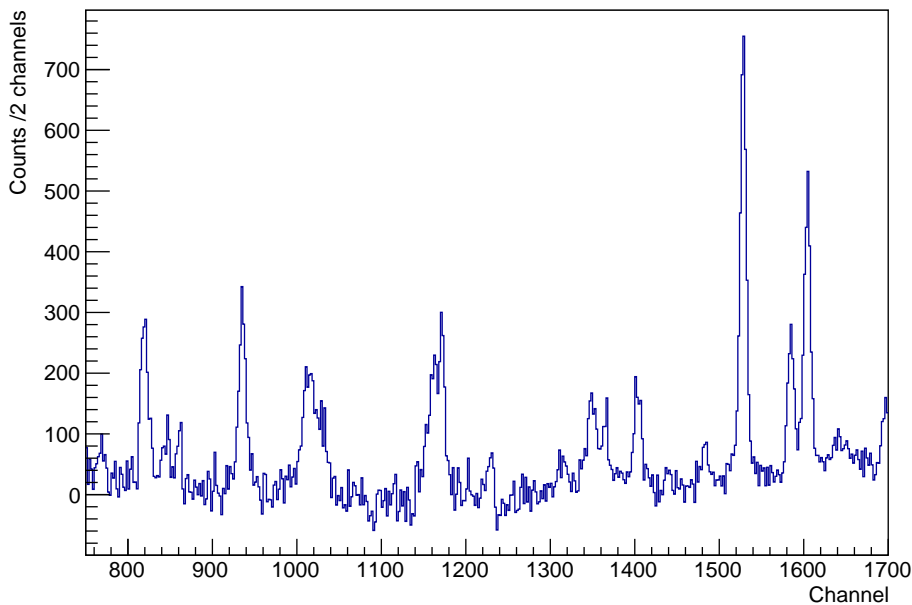


Figure 10.12: Neon background subtracted 38° neon spectra.

counts in figure 10.12. The difficulty in fitting the entire region makes justifying peak integral, especially around channel 1160 particularly difficult to justify without implementing exceptionally large uncertainties on the peak integrals.

Peak fit information used in the analysis was finally extracted by fitting the peaks individually or in small regions of the focal plane plotter including a local background fit. This final method reduced the dependence on a single accurate fit across the entire Gamow window and calibration states. It must be considered also that this oxygen state is likely off-focus and appears asymmetric. The gradually decreasing background seen in figures 10.11 and later in 10.13 can be seen to finish at channel 1900. This is thought to be due to protons from deuteron breakup. This can be replicated by scaling the the carbon background.

10.6 Calibration

Peaks were initially identified using a Focal Plane Plotter, FPPlotter, package. This allowed approximate channel correspondence to known state energies. The method of overlying spectra with the FPPlotter output has significant uncertainties, but does however allow identification of strongly populated and well separated states, such as those used for later calibration. In the FPPlotter package state energies from literature [30] were used for ^{21}Ne

states in the region of the focal plane, as well as, amongst others, ^2H for $^1\text{H}(d,p)$; ^{12}C for $^{12}\text{C}(d,d)$; ^{13}C for $^{12}\text{C}(d,p)$ and $^{13}\text{C}(d,d)$; ^{14}C for $^{13}\text{C}(d,p)$; ^{14}N for $^{14}\text{N}(d,d)$; ^{15}N for $^{14}\text{N}(d,p)$ and $^{15}\text{N}(d,d)$; ^{16}N for $^{15}\text{N}(d,p)$; ^{16}O for $^{16}\text{O}(d,d)$; ^{17}O for $^{16}\text{O}(d,p)$; ^{20}Ne for $^{20}\text{Ne}(d,d)$. A wide range of states from commonly found nuclei in nature were tested to gain awareness of potential contaminants, as above in the Gamow window. It must be noted that the $^{16}\text{O}(d,p)^{17}\text{O}$ neutron transfer reaction overlaps with the Gamow window and as such the minimisation of the contamination from the 5.0848(9) MeV ^{17}O state with width of 96 keV played a large part in the analysis.

Utilisation of the focal plane plotter package required identification of the location of the starting point of the focal plane plotter in channel number. The approximate setup of the focal plane plotter package was conducted from the estimated known ρ_{min} and ρ_{max} , the gyroradius, 68.2 cm and 84.3 cm respectively. The gyroradius is defined in eqn. 10.3, where m is the mass of a particle with charge q and v_{perp} its velocity perpendicular to the field of strength magnetic field of strength B .

$$\rho = \frac{mv_{perp}}{qB} = \frac{\sqrt{2mE}}{qB} \quad (10.3)$$

Having approximated ρ_{min} and ρ_{max} , the focal plane plotter locations of ^{13}C states 3.854 MeV, 3.685 MeV and 3.089 MeV were aligned with the three tallest peaks in the spectra. These peaks were strong as they originate from $^{12}\text{C}(d,p)^{13}\text{C}$. These were easily identifiable and due to target stoichiometry offer a reliable first reference when neon spectra were compared with the natural carbon target spectra. At this point a comparison with the spectra of Stanford and Quin [75] and Howard et al. [73] shows that we would expect to prominently see the 6.609 MeV state in ^{21}Ne . This allows further alignment of the focal plane plotter output with the spectra, at all measured angles. At this point the rough calibration is sufficient to identify the four calibration peaks, described in table 10.4 and seen in figure 10.13 with the Focal Plane Plotter output. Note the 5.334 MeV energy ^{21}Ne state was also used to confirm the focal plane plotter calculation alignment.

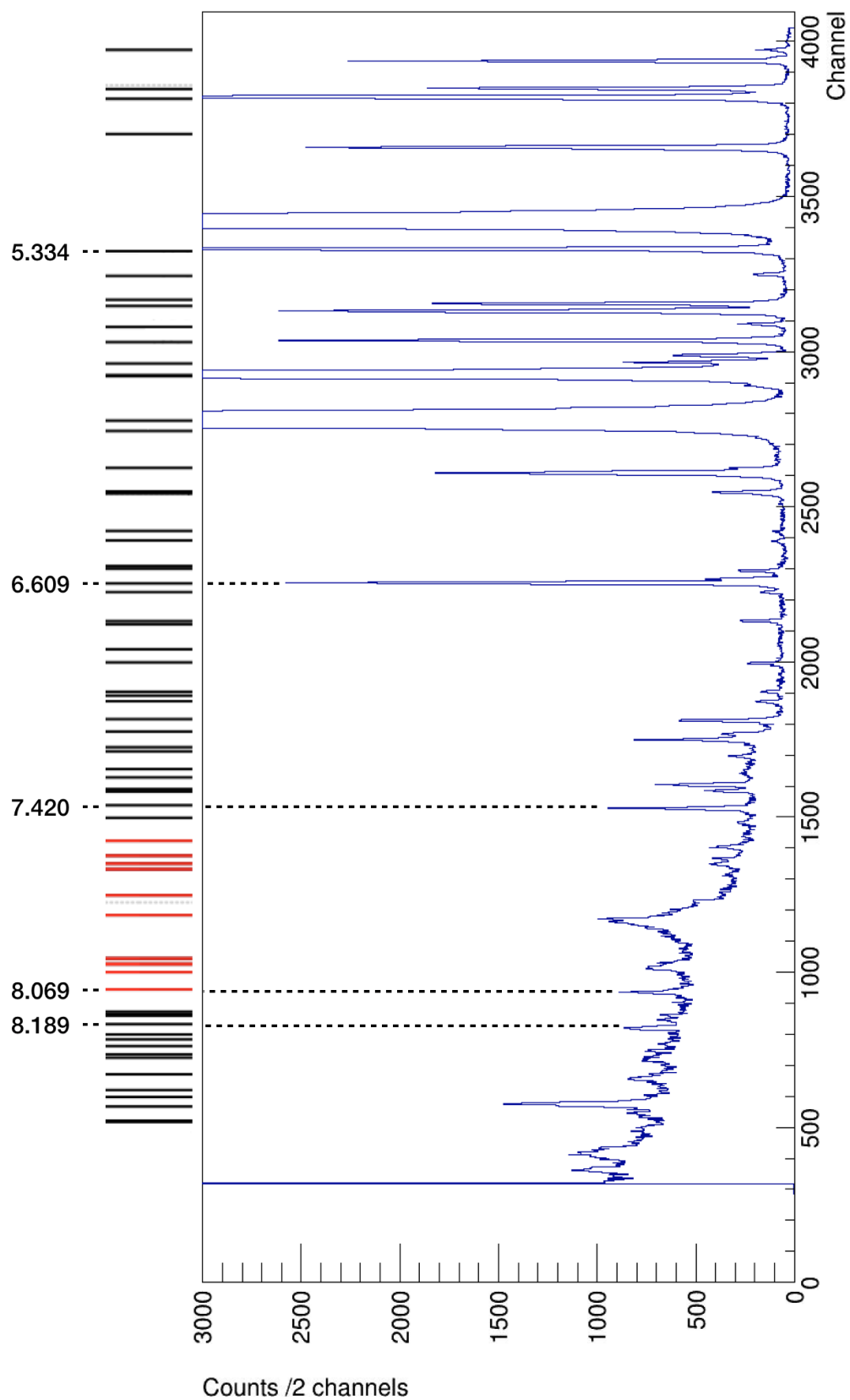


Figure 10.13: Rough calibration using the Focal Plane Plotter at 38° .

State energy (MeV)	State energy uncertainty (keV)
6.609	1
7.420	1
8.069	2
8.189	2

Table 10.4: The four calibration peaks, note their proximity to the Gamow window.

The four calibration peaks were chosen due to their separation at all angles and also their significant population. These were identified through the FPPlotter package rough calibration initially. Attempts were made to utilise both the SiO_2 and aluminium target data as an external calibration, however the region in both targets was heavily populated and as such individual states were exceptionally hard to identify. The internal calibration ^{21}Ne states were however unambiguously identified using the three ^{13}C states.

The 6.609(1) MeV energy ^{21}Ne state was measured by Rolfs et al. in 1972 [86] through $^{18}\text{O}(\alpha, n\gamma)$ as 6.6066(18) MeV, in 1975 Hallock et al. [87] found the state to be at 6.600(10) MeV, Stanford noted it to be at 6.605 MeV and measured it as 6.61 MeV in 1979 [75], by combining multiple measurements Endt in 1990 [88] concluded the state to be at 6.6081(9) MeV, this included the 6.6099(5) MeV measurement by Fortune et al. [89] in 1979, it is now accepted to be at 6.609(1) MeV [30]. Hallock measured the 7.420 MeV state at 7.413(10) MeV [87] using $^{12}\text{C}(^{13}\text{C}, ^4\text{He})^{21}\text{Ne}$ later in 2005 this same state was measured at 7.4198(6) MeV by Wheldon et al. [90].

In 2013 Best et al. [65] measured the energy of the 8.069 MeV and 8.189 MeV states with a 2 keV uncertainty. Both of which were in agreement with previous measurement of 8.065(10) MeV and 8.186(10) MeV respectively. The measurement of 8.186(10) MeV was conducted by Hinds and Middleton [91], where they found this state to be 8.174(10) MeV, later their values were found to have a systematic shift and corrected by Endt [88] to 8.186 MeV. Hinds and Middleton [91] had also measured the 8.069 MeV state to be at 8.058(10) MeV, later corrected by Endt [88] to be 8.065(10) MeV. Hence both these states have measurement history and so the value of Best is likely to be reliable.

Ultimately the ability to fit these states independent of other peaks or contamination played a key role in their selection as well as their significant history of being measured, giving confidence in the current accepted energies, hence improving confidence in the focal plane calibration.

The original calibration was conducted with 1 channel per bin for 40.1° and 2 channels per bin for all other measured angles. Initially the calibration was used as in table 10.5 using binning values of 1, 2, 2, 2 and 2 for 40.1° , 26.4° , 21.2° , 15.9° and 10.6° respectively. However as table 10.5 shows, the peak centroids are slightly dependant upon the binning. For achieving the maximum levels of reliability the calibration was repeated using the new binning of 2, 4, 4, 4, 4 channels per bin for 40.1° , 26.4° , 21.2° , 15.9° , 10.6° . This binning was chosen to mirror that of the final Gamow window fits.

CoM angle ($^\circ$)	Binning (channels /bin)	6.609MeV state peak centroid (channels)	Peak centroid uncertainty (channels)
10.6	2	2529.07	0.07
	4	2529.71	0.07
15.9	2	2509.01	0.03
	4	2509.60	0.03
21.2	2	2470.13	0.04
	4	2470.75	0.04
26.4	2	2422.53	0.04
	4	2423.13	0.04
40.1	1	2254.17	0.04
	2	2254.68	0.04

Table 10.5: Peak centroids at all angles for two selected chosen binning settings at each angle for the 6.609 MeV energy ^{21}Ne state.

The function, or form of calibration function was continuous and captured in a quadratic calibration fit. Earlier calibrations included the 5.334 MeV state. The inclusion of this state does however increase the χ^2 on the calibration fit dramatically, as seen in table 10.6. The 5.334 MeV state was removed from the calibration not only due to the effect on the χ^2 value but also the concern that this state, relative to the other calibration states is far from the Gamow Window.

The increase in the bin widths for calibration was so that the calibration binning matched that of the state fits in the Gamow window. Note the significant improvement of the χ^2 for the calibration fit at 26.4° with the final binning, suggesting that one of the calibration fits may have had a misleading centroid(s), caused by the binning. The improvement of the χ^2 suggests that poor selection of binning leads to a measurable level of fluctuation in peak centroid.

CoM Angle ($^{\circ}$)	χ^2 for fit with 5.334 MeV State	χ^2 for fit using narrower bins	χ^2 for final calibration
40.1	9.3	2.7	2.5
26.4	10.8	4.2	1.2
21.2	0.9	0.3	0.3
15.9	6.3	0.0	0.0
10.6	0.4	0.2	0.3

Table 10.6: χ^2 values for the key calibrations, note the particularly significant decrease in the quadratic calibration fit χ^2 with removal of 5.334 MeV state.

The final calibration was conducted using SPLITpole ANALYSIS Code, SPANC [92]. SPANC has the ability to calculate, given the calibration peak centroids and respective uncertainties to find the energy centroids of other fitted peaks and their associated uncertainties. SPANC also requires target stoichiometry by layers, allowing for variations in layer thickness and varying energy loss. The way that SPANC works does however imply that the peak fitting is conducted using plots in units of channel not a more conventional $\beta\rho$ for this type of data. Fitting spectra in channel requires careful consideration of each peaks identity. This method implied fitting of the spectra prior to the calibration, hence at this point the rough focal plane plotter calibration became important for peak identification only.

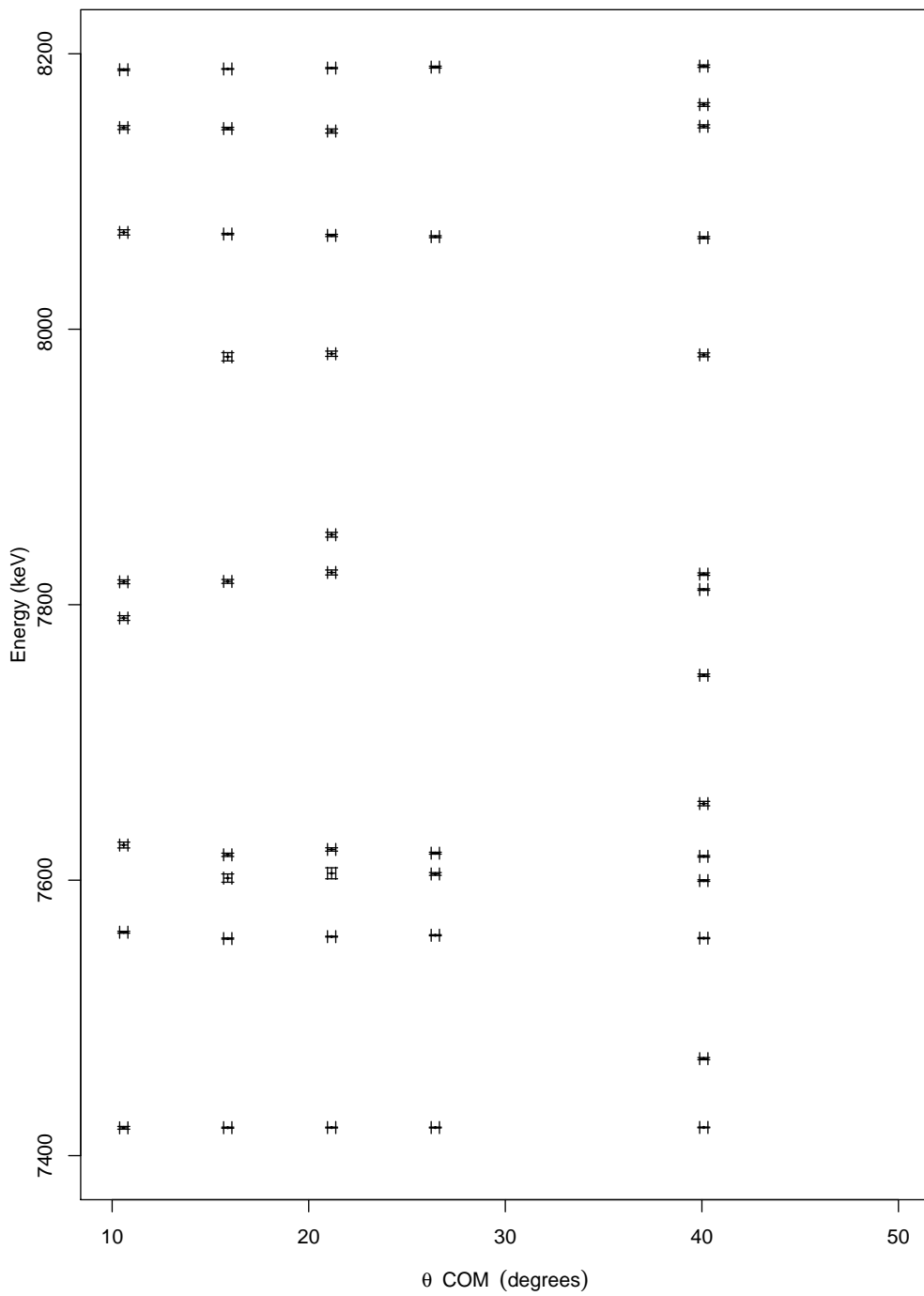
After SPANC had calculated the calibration and the fitting of the focal plane had been completed the states peak centroids were passed through SPANC. At this point the peak centroids and their associated uncertainties were extracted. A comparison of the energies of these states was then conducted across angles as seen in figure 10.14.

Where multiple peaks were close in energy the width of the state was compared with other angles in an attempt to identify the correct peak. If states had the same width so the state closest to the mean of the other 4 was selected as being a given state.

10.7 State fitting and parameter extraction

The states were fitted in groups or individually depending upon the form of the background. Whether peaks were included at a given angle depended upon whether the peak was visible beyond statistical fluctuations and whether fitting could be conducted such that the state could be separated from the background. After passing each peak centroid through SPANC [92] an energy uncertainty was extracted for each angle of each peak; where fitted.

The Gamow window fitted for 40.1° can be seen in figure 10.15. Note the varying colour

Figure 10.14: Energies for all fitted ^{21}Ne states except 6.609 MeV.

fits across the focal plane represent fitted groups. The fit regions at each angle were based on assessing the background and its complexity under the peak. Where background was less complex so the fit regions could be wider and around the oxygen contamination peak so the peak fitting was typically for a single ^{21}Ne state. The equivalent fits for the 26.4° , 21.2° , 15.9° and 10.6° can be seen in figures 10.16, 10.17, 10.18 and 10.19 respectively.

Due to the requirement of decreasing the beam intensity at 10.6° to avoid detector sparking so the quantity of protons from neon state population decreased, despite the increased run time. Hence the statistics were poorest for the 10.6° and the most challenging to fit, as seen in figure 10.19. Note also that it was required to increase the bin width to reduce statistical fluctuations relative to the peak heights.

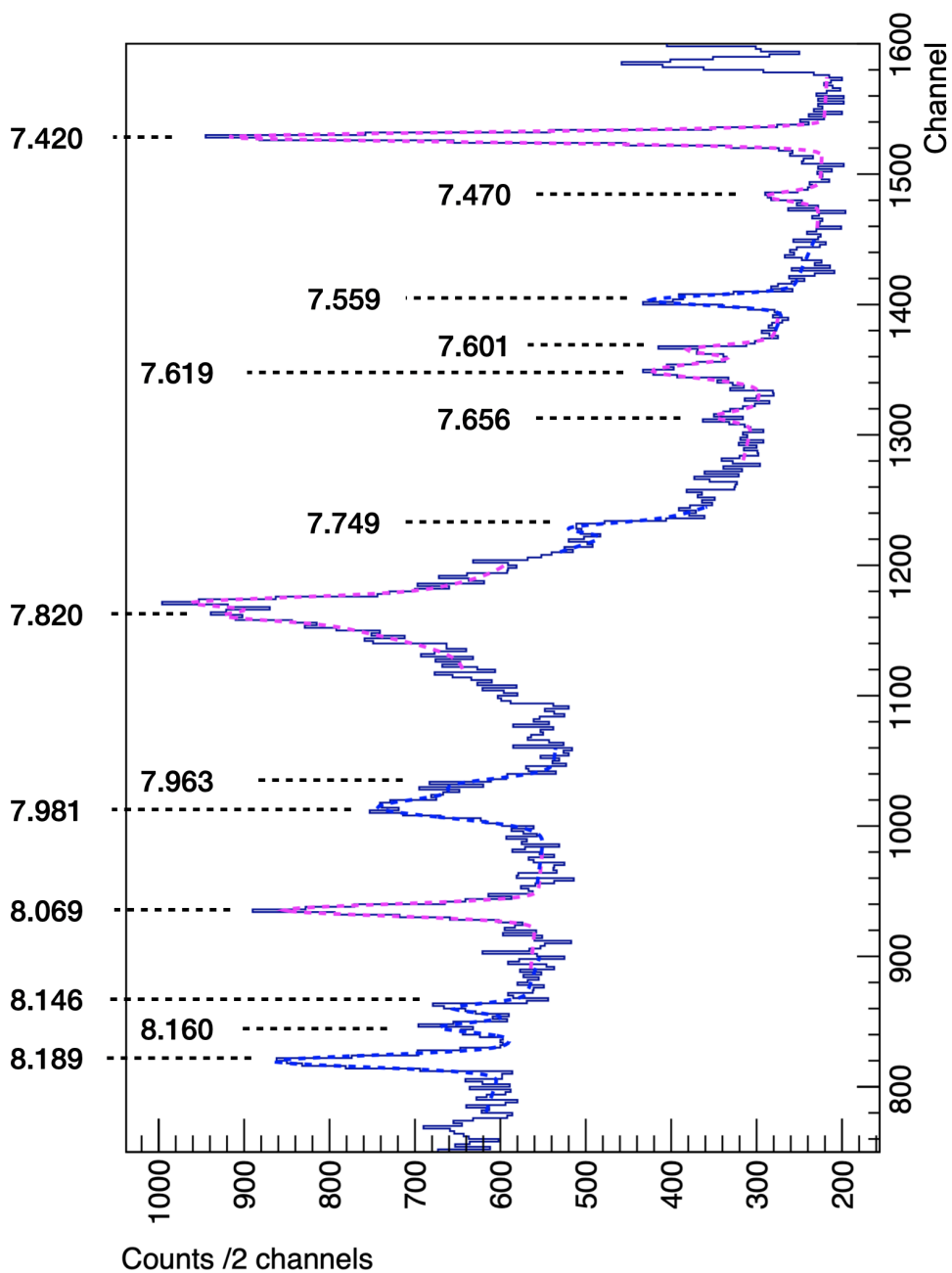


Figure 10.15: Fitting of ^{21}Ne states across the Gamow window for the 40.1° spectra. All state energies are in MeV and are those calculated across all angles using mean weighted average, where states were only seen at 40.1° the energies from the 40.1° spectra have been adopted.

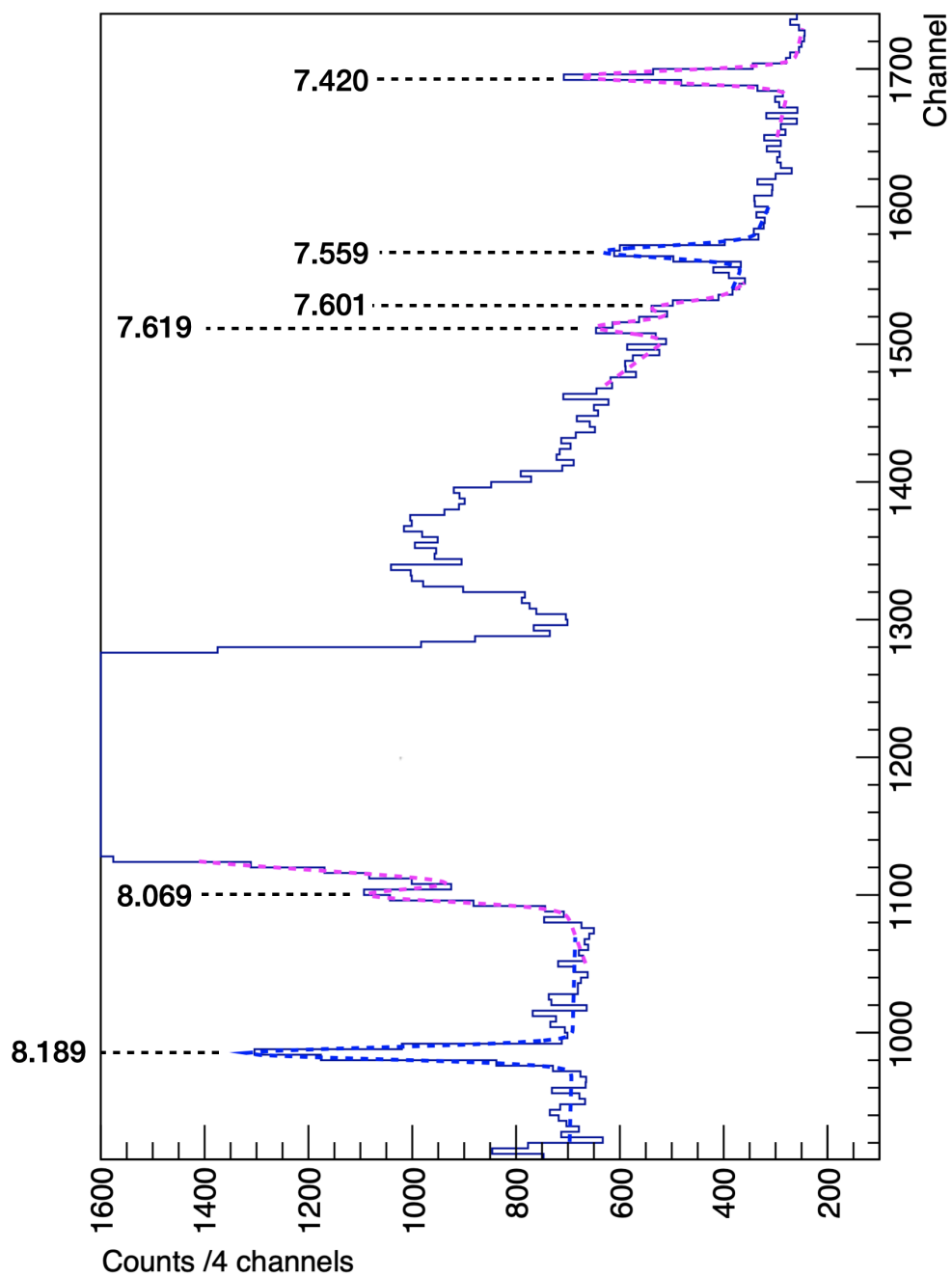


Figure 10.16: Fitting of ^{21}Ne states across the Gamow window for the 26.4° spectra. All state energies are in MeV and are those calculated across all angles using mean weighted average. Note the significant background centred around channel 1200 from the $p(d,p)d$ reaction.

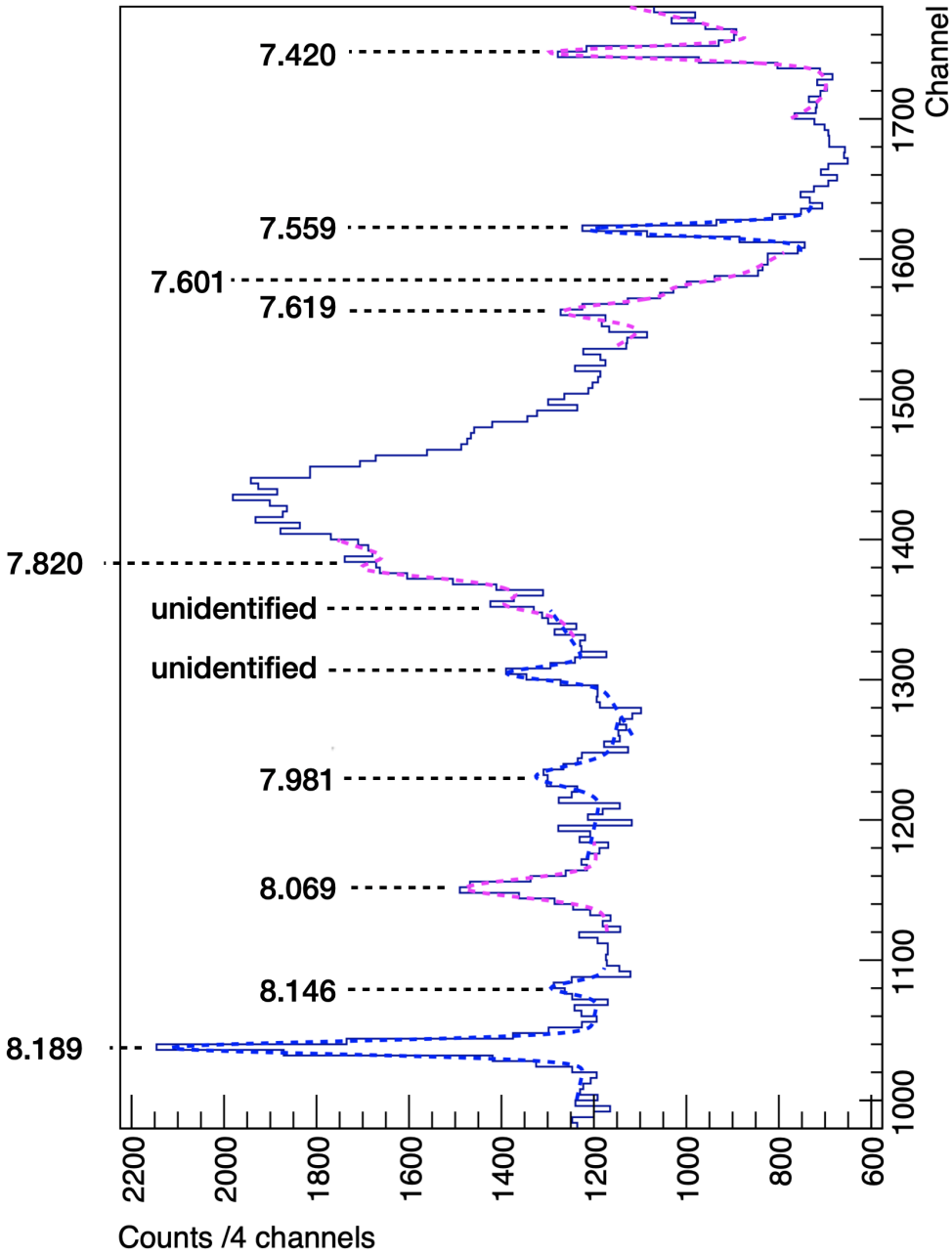


Figure 10.17: Fitting of ^{21}Ne states across the Gamow window for the 21.2° spectra. All state energies are in MeV and are those calculated across all angles using mean weighted average. Note the tail of the $p(d,p)d$ reaction tail around the 7.420 MeV energy state peak.

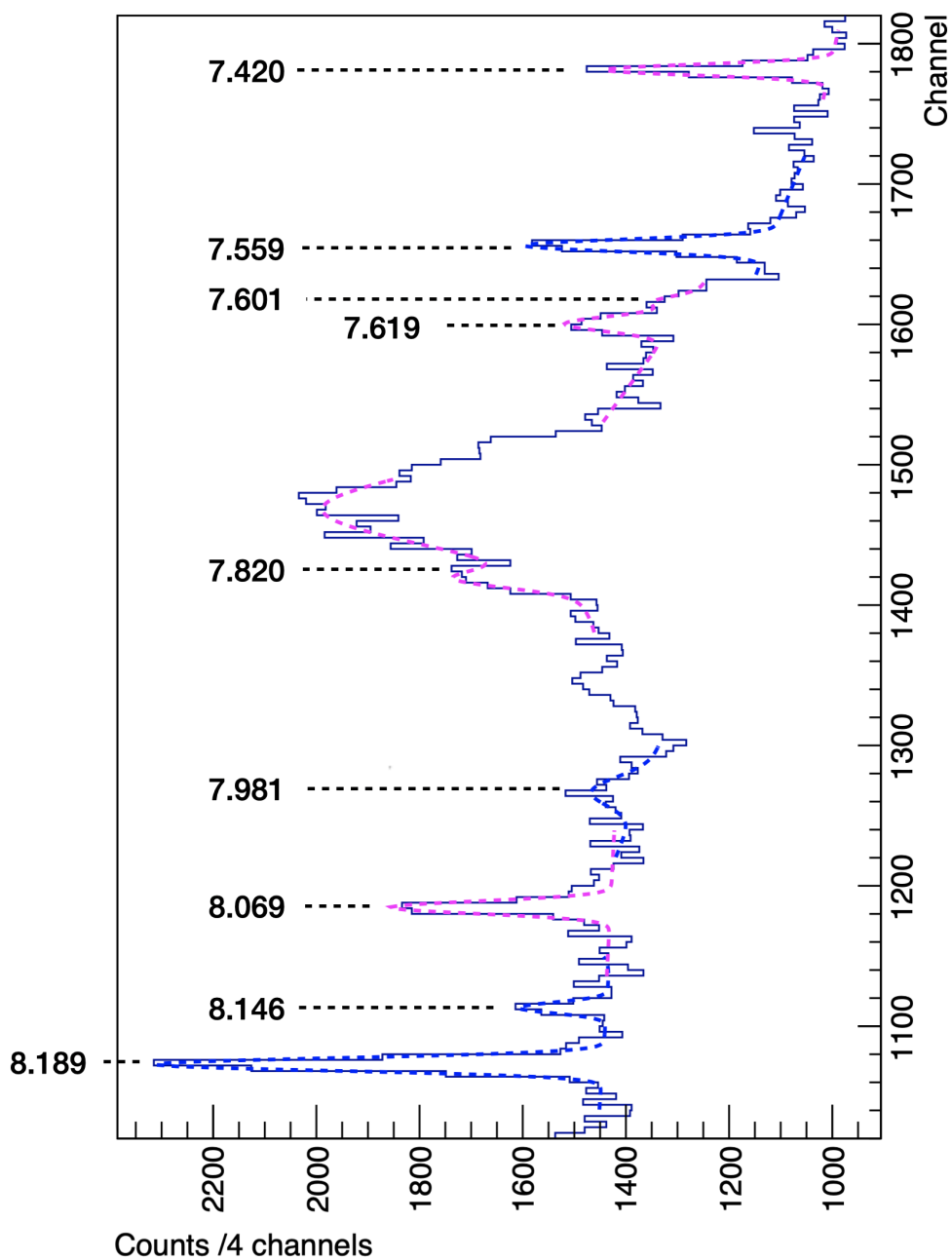


Figure 10.18: Fitting of ^{21}Ne states across the Gamow window for the 15.9° spectra. All state energies are in MeV and are those calculated across all angles using mean weighted average.

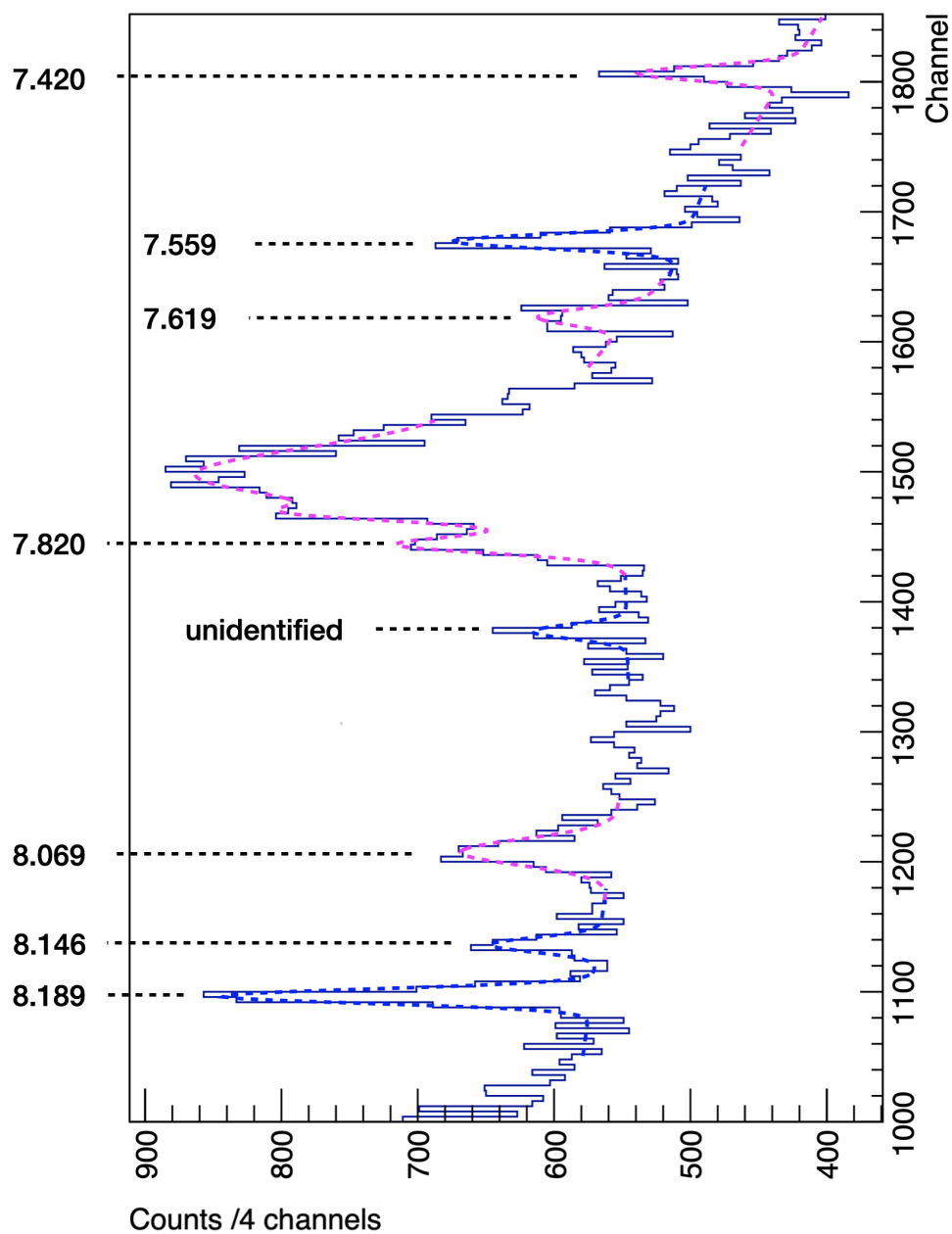


Figure 10.19: Fitting of ^{21}Ne states across the Gamow window for the 10.6° spectra. All state energies are in MeV and are those calculated across all angles using mean weighted average.

Note should also be taken of the heavy background contamination at 26.4° due to alignment of the Gamow window with hydrogen contamination and hence the detection of protons from $p(d,p)d$. This substantial contamination can be seen in figures 10.16 and 10.20, the former zoomed to view the ^{21}Ne fits that were still possible.

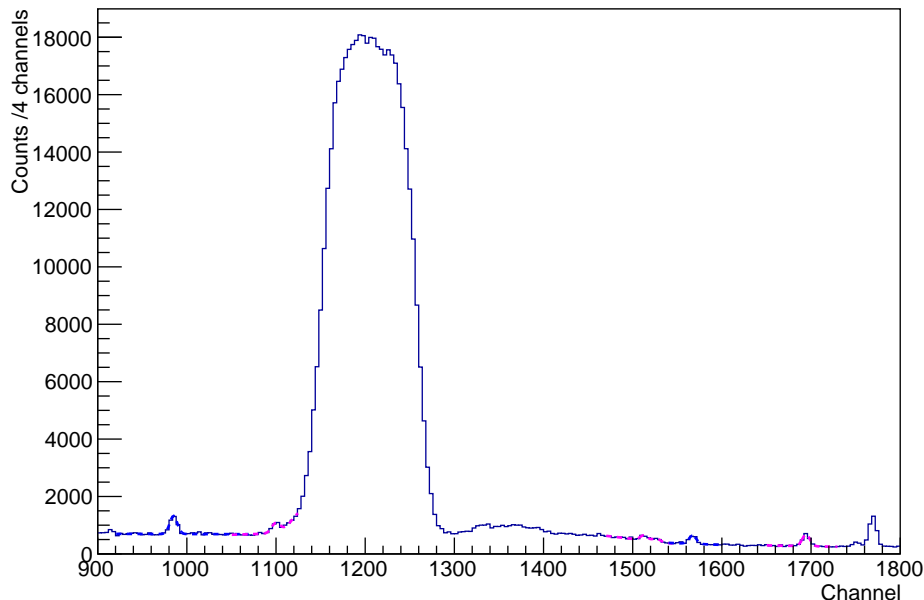


Figure 10.20: Fitting of ^{21}Ne states across the Gamow window for the 26.4° spectra. Note the distinct $p(d,p)d$ background.

10.8 State energies

After fitting and calibrating at all angles the state centroids in channel were passed through SPANC so the weighted average of state energies across all angles was found. The weighted average method seen in eqn. 10.4 was used. This method was used to weight the mean such that those energies with smaller uncertainty contribute more significantly to the mean than those energies with larger uncertainties. Hence should a fit have been of lower quality, with a centroid having a larger uncertainty this had less contribution to the weighted mean.

$$E_{average} = \frac{\sum_{i=1}^5 \frac{E_i}{\sigma_i^2}}{\sum_{i=1}^5 \frac{1}{\sigma_i^2}} \quad (10.4)$$

where i refers to the i -th angle at which a given state was measured. σ_i refers to the state energy uncertainty at the i -th angle. The uncertainty of the weighted average energy can be found using eqn. 10.5 or equivalently, eqn. 10.6.

$$\sigma_{E_{average}} = \sqrt{\frac{\sum_{i=1}^n \frac{E_i^2}{\sigma_i^2}}{\sum_{i=1}^n \frac{1}{\sigma_i^2}} - E_{average}^2} \quad (10.5)$$

$$\sigma_{E_{average}} = \sqrt{\overline{E^2} - E_{average}^2} \quad (10.6)$$

where $\overline{E^2}$ refers to the weighted mean of the squares. $\sigma_{E_{average}}$ includes both the experimental uncertainty and also accounts for a spread in the energy values at each angle. In the following subsections specifics relating to the analysis of each peak centroid fitted are considered.

7.420 MeV

Figure 10.21 shows the variation in energy of the 7.4203(10) MeV state of ^{21}Ne . The small energy deviations arise solely from the calibration fit as this was a calibration state. All fits are however within error and between angles have a range of 0.28 keV with a mean weighted average resulting in an energy of 7.4204(1) MeV, implying self-consistency of the calibration.

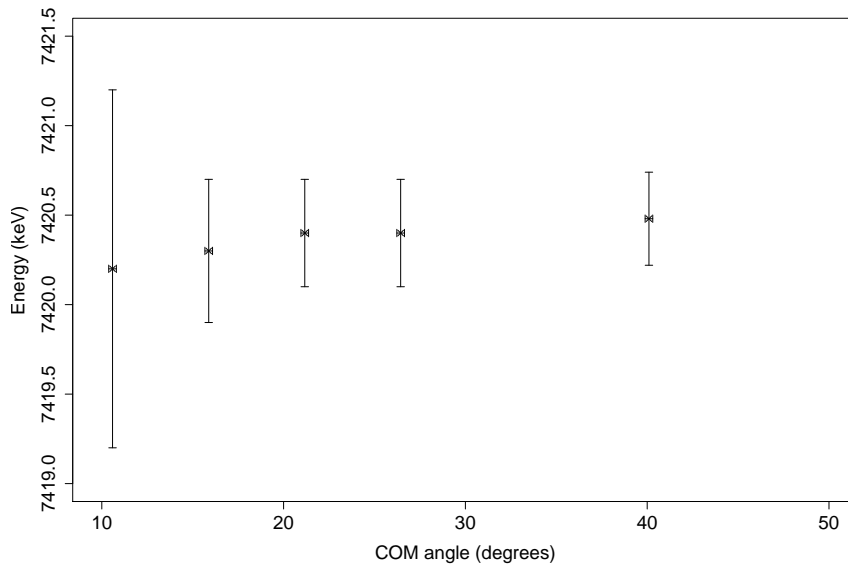


Figure 10.21: Energy with measurement angle, showing negligible fluctuation in state energy for the known 7.420 MeV calibration state of ^{21}Ne .

7.470 MeV

The 7.465(10) MeV energy state was thought to be measured at 7.470(1) MeV. It was only witnessed in the 40.1° spectrum where statistics were superior when compared to other measurement angles. The single fit can be seen in figure 10.15 which has a width of 3.60 channels, equal to the measured narrow width at 40.1°.

7.559 MeV

The 7.547(10) MeV energy state was measured at 7.559(1) MeV after taking the weighted mean. A state was not witnessed at 7.547 MeV at any angle and the observed peak was well separated at all angles. The uncertainty was calculated as the standard deviation of the weighted mean.

7.601 MeV and 7.619 MeV

The 7.601(2) MeV energy state peak was witnessed at all angles except the 10.6°. When it was compared with those states around it, especially the 7.619 MeV peak at other angles, it was expected to be seen at channel 1634 in the 10.6° spectrum. There was a small peak in that region of the 10.6° spectrum, however this peak had approximately the same magnitude as the background.

The 7.619(2) MeV state could be seen at all angles, with separation visible between the 7.601 MeV state at all angles except 21.2°. The fit of these two states can be seen in figure 10.22 and figure 10.23, representing the fits at 21.2° and 40.1° respectively. The centroid of the 7.601 MeV was constrained based on the difference in channels between the 7.619 MeV and 7.601 MeV energy states in each of the 15.9°, 21.2°, 26.4° and 40.1° spectra.

7.656 MeV

The 7.656(2) MeV energy peak seen here is believed to be the previously measured 7.648(2) MeV energy state. It must be noted that this measurement was only seen at 40.1° as in figure 10.15 and, relative to other states, had a low peak integral.

7.749 MeV

The 7.749(1) MeV energy peak seen in figures 10.24 and 10.15, was only seen at 40.1° with poor statistics, just above what would be considered background fluctuation when considering \sqrt{n} for bins in that region. Its location relative to the ^{17}O peak further makes fitting difficult.

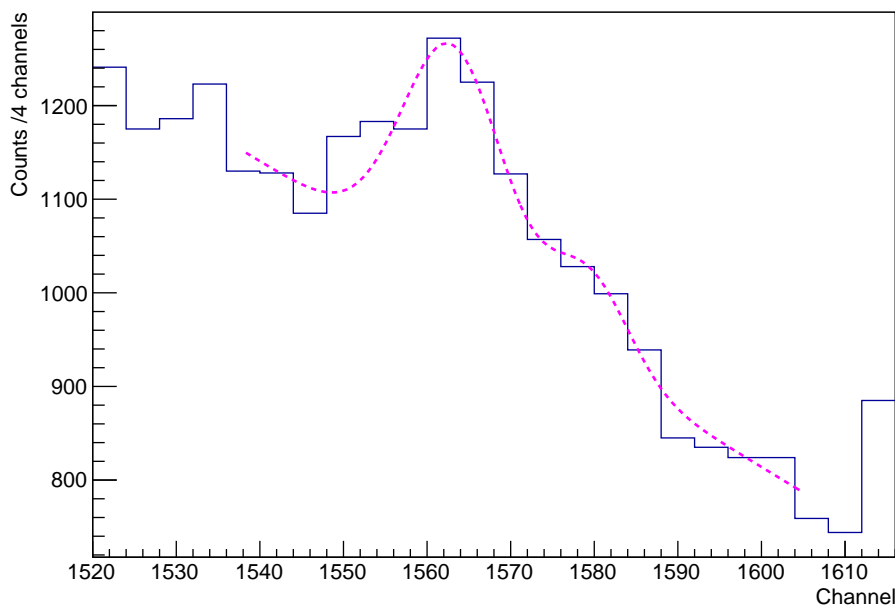


Figure 10.22: Extract of 21.2° spectra showing the 7.619 MeV and 7.601 MeV energy peak with centroids at 1563 ± 1 channels and 1579 ± 4 channels respectively.

Only the centroid was used for analysis to extract the state energy. The uncertainty of 1 keV arises from a combination of the peak centroid fit error and also the calibration error.

7.820 MeV

The initially identified centroids for the formerly designated 7.81 MeV state shows significant fluctuations between witnessed peak energies at different angles. The fact there are multiple peaks in the region seen at different angles and these peaks typically lie on the oxygen peak suggests the existence multiple states. The scale of the fluctuations confirms the presence of a second state that is not ^{21}Ne . Due to the energy of the states located at 10.6° , 15.9° and 21.2° the state at 40.1° was found to be the 7.820(3) MeV. The fluctuation between the other, non-neon state witnessed with dissimilar $\beta\rho$ is comparable in magnitude, when compared in figure 10.25.

7.961 MeV

What was initially believed to be the 7.961 MeV state yielded fluctuations in energy as seen in figure 10.26. In this particular case we can say with confidence these protons are not originating from ^{21}Ne due to the shift with angle. This further shows a non-constant $\beta\rho$ with

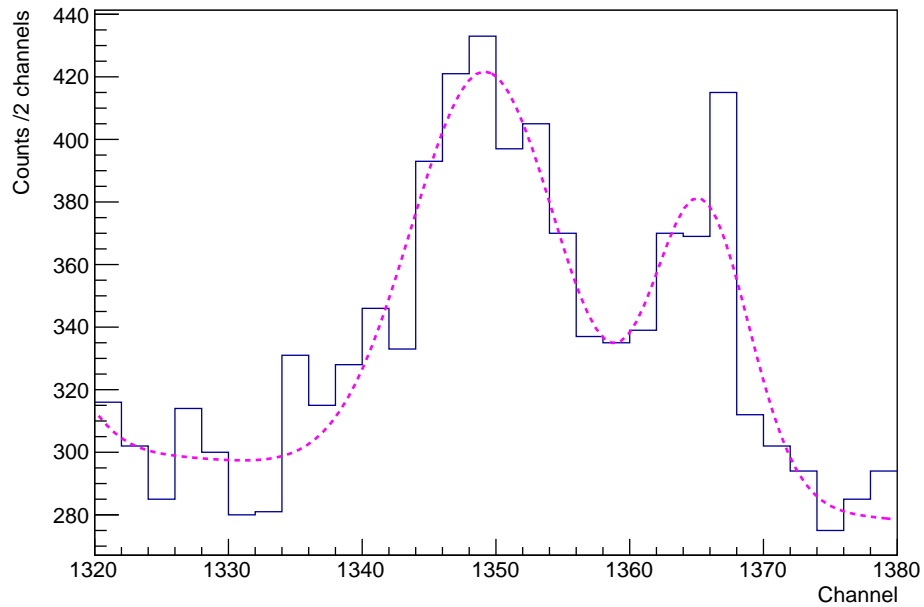


Figure 10.23: Extract of 40.1° spectra showing the 7.619 MeV and 7.601 MeV peak with centroids at 1349 ± 1 channels and 1365 ± 1 channels respectively, note the increased prominence when compared with the 21.2° of the 7.601 MeV energy state.

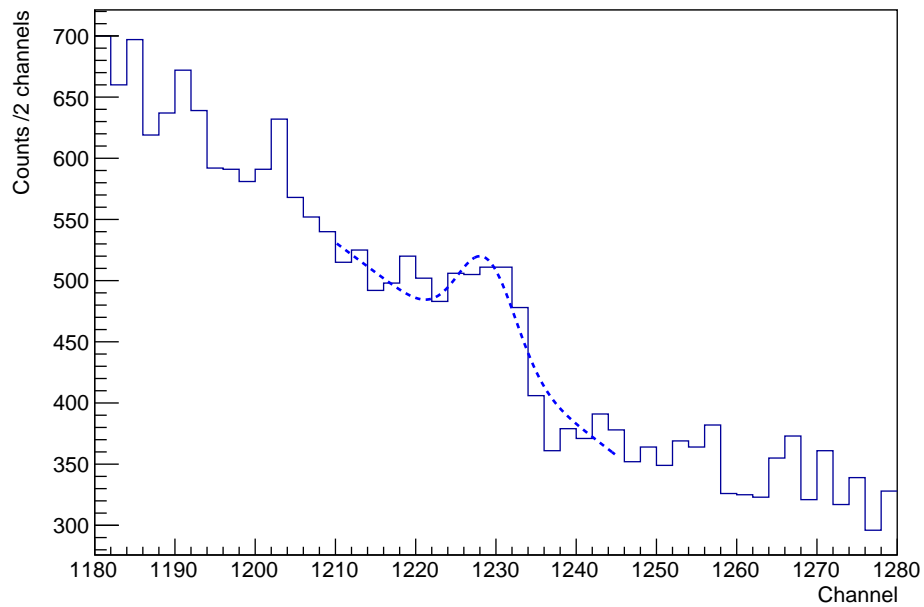


Figure 10.24: Extract of 40.1° spectra showing the fit of the 7.749 MeV energy state in ^{21}Ne .

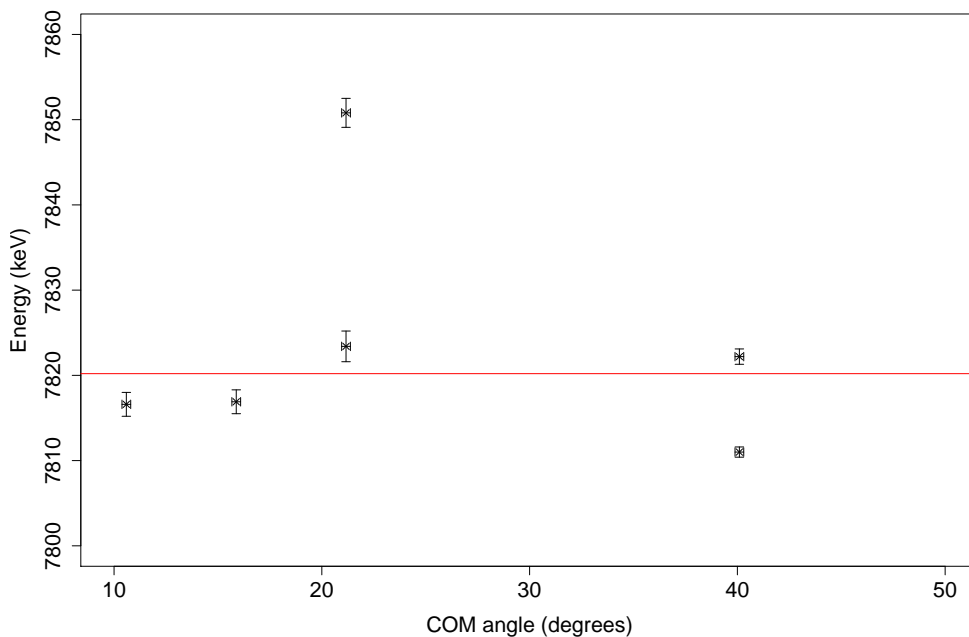


Figure 10.25: Fluctuations in energy and the originally suspected potential doublet witnessed at 40.1° . It seems however there is are contaminant state(s) in this region as well as the 7.820 MeV energy ^{21}Ne state.

angle. The uncertainties in energy are those calculated from SPANC. Note however at 40.1° the state fitted was measured to be at 7.963(2) MeV which may be the state in ^{21}Ne , but due to its proximity to an unknown source as seen in figure 10.26 it was discarded.

The inconsistency in energy in figure 10.26 led to the peaks being disregarded and assumed from a contaminant. This however did not correspond to a known contaminant centroid position, as calculated using the focal plane plotter. The origin of this peak is unknown.

7.981 MeV

The previously accepted state energy of 7.980(10) MeV has been measured here to be 7.981(1) MeV. It was seen and fitted at 15.9° , 21.2° and at 40.1° . In figure 10.15 it can be seen as a doublet with the 7.963 peak, with the latter, as discussed earlier, discarded due to reliability issues.

8.069 MeV

The 8.069(2) MeV energy state was used here as a calibration state, however here this states energy was measured as 8.068(1) MeV. The small drift with angle change of this calibration

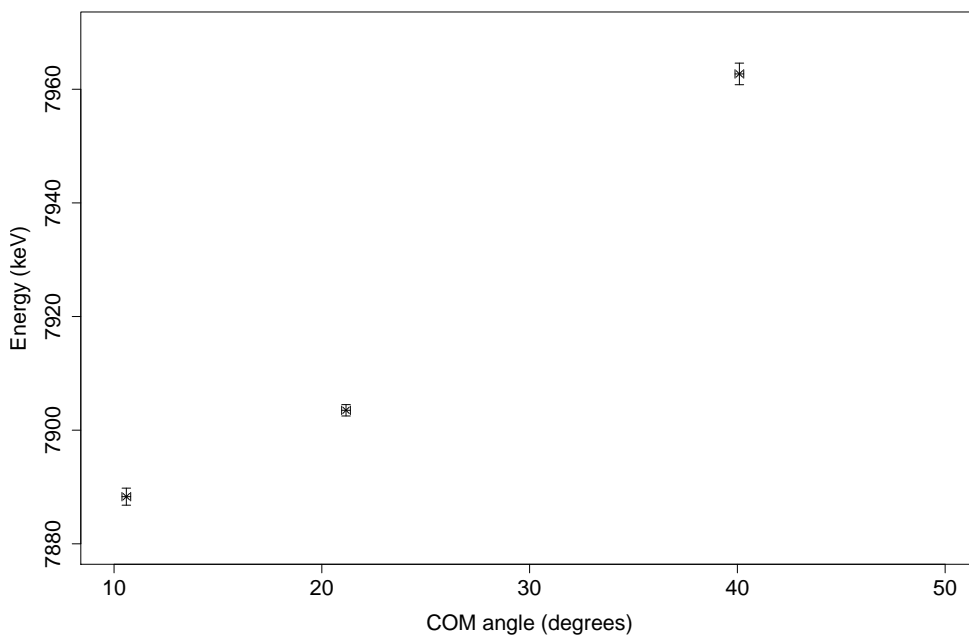


Figure 10.26: Energy drift with angle change of the 7.961 MeV energy state, implying these peaks are not from ^{21}Ne .

state is expected to be due to the fit in the calibration not being a perfect quadratic across the entire focal plane. Its proximity to the other 8.189 MeV calibration state will also account for much of the discrepancy. This alone is the reason sub-keV state energy extraction is not possible. Its width was extracted as 6(1) keV.

Investigations were made by tweaking the input calibration state energies into SPANC in an attempt to reproduce the literature value for this state and minimise drift. This involved changing energies of calibration states individually and in pairs. This was unsuccessful and hence it is believed this state energy is likely further constrained by this measurement.

8.146 MeV

The 8.146(2) MeV energy state was measured at 8.146(1) MeV, having been seen at all angles except 25° . At 25° this was likely due to the increased level of background from the p(d,p)d peak relative to the peak integral.

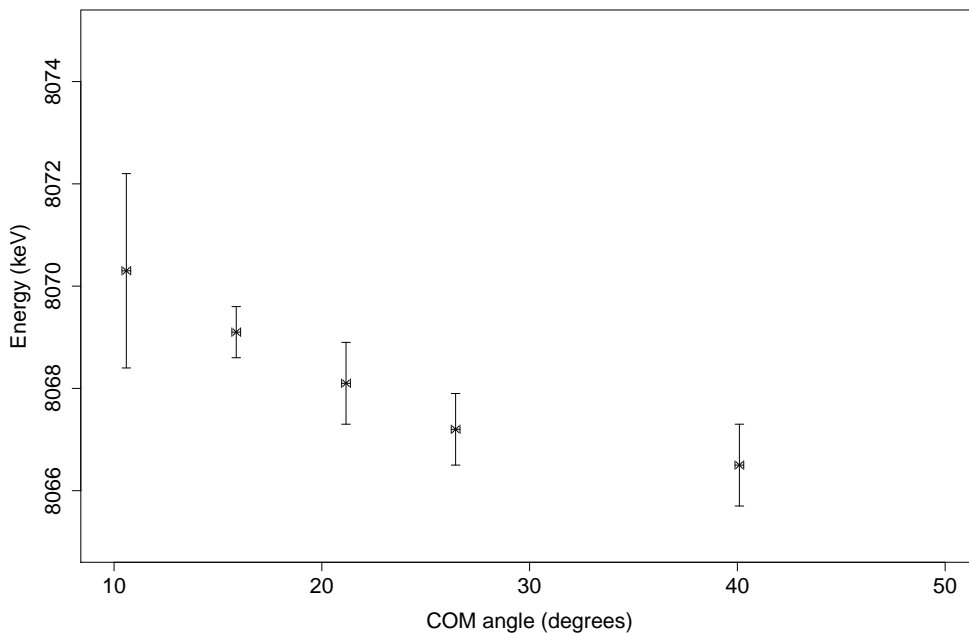


Figure 10.27: Minor energy drift with angle change of the 8.069 MeV energy calibration state.

8.163 MeV

The 8.160(2) MeV energy state has been measured as 8.163(1) MeV at 40.1° and can be seen in figure 10.15. The peak was of relatively low intensity and the energy could not be confirmed at another angle.

8.189 MeV

The 8.189(2) MeV energy state was used as a calibration state and measured as 8.189(1) MeV after combining the measurements at all angles. The energies across all angles can be seen in figure 10.28. As mentioned under the 8.068 MeV energy section significant attempts were made to reduce the drift, these were unsuccessful.

10.9 FRESCO

FRESCO [36] runs were conducted using optical model potentials from An and Cai [93], Varner et al. [35], Madland [94], Adsley [95] and Menet et al. [96] for the optical model potentials for the $^{20}\text{Ne} + d$, $^{21}\text{Ne} + p$, $^{20}\text{Ne} + n$, $n + p$ and the $^{20}\text{Ne} + p$ optical model potentials respectively. The potentials used can be seen in table 10.7.

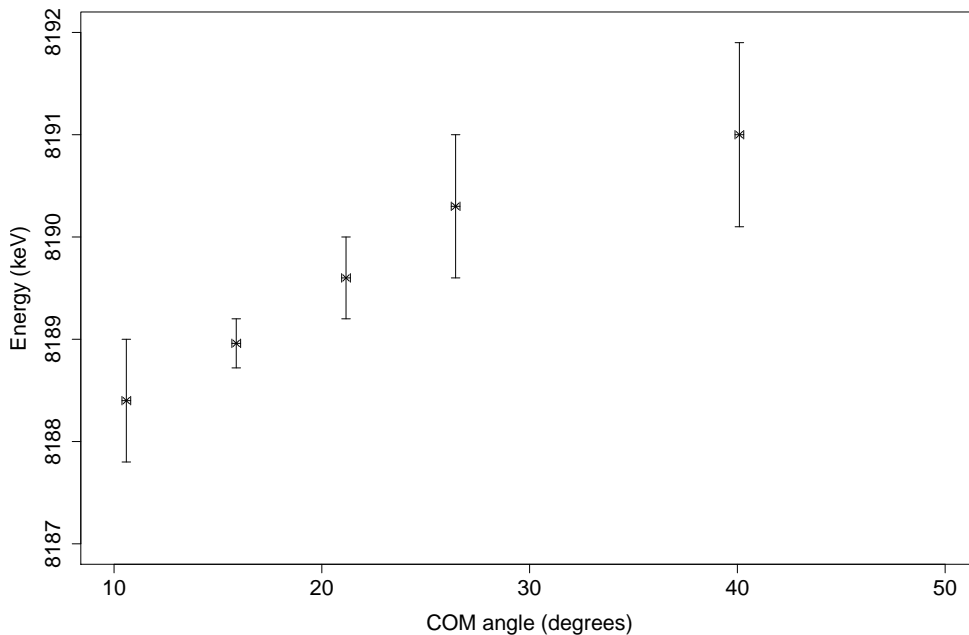


Figure 10.28: Minor energy drift with angle change of the 8.189 MeV energy calibration state.

Where v , r and a represent potential depth, radius and diffuseness respectively. The subscripts of these variables defined as: without i subscript representing the real volume potential; subscript i , the imaginary component; without s or so the volume potential; with s , the surface potential; with so , the spin orbit potential.

The $^{20}\text{Ne} + d$ potential was taken at the beam energy. The $^{21}\text{Ne} + p$ was taken at ~ 10.5 MeV, this is the maximum amount of energy available, calculated from $Q - E_x + E_{Beam}$ where Q is the q -value of the reaction and E_x is the energy of the excited state populated in ^{21}Ne . The $^{20}\text{Ne} + n$ potential was taken at 6 MeV, representing its share of the beam energy when incident on the ^{20}Ne . It must be noted that the depth of the $^{20}\text{Ne} + n$ potential was set within the code to be adjusted to reproduce the binding energy automatically. The core-core interaction of $^{20}\text{Ne} + p$ potential was taken at 7 MeV. It is hard to predict the exact energy of the proton at the moment of neutron transfer, as such this is an estimate.

It must be noted however that when running with $^{20}\text{Ne} + p$ and the $^{20}\text{Ne} + n$ potentials at 13 MeV minimal impact was seen on the fitted C^2S , of the order of a few % for the 7.601 MeV state. This minimal impact on the C^2S led to the small simplification that the optical potentials were extracted assuming an 8 MeV excitation energy of ^{21}Ne . Given the maximum difference in excitation values being 350 keV from this value inside the Gamow window it

Parameter	$^{20}\text{Ne} + d$	$^{21}\text{Ne} + p$	$^{20}\text{Ne} + n$	$n + p$	$^{20}\text{Ne} + p$
v	90.752	51.834	73.3	-	49.8
r_0	1.149	1.168	1.25	-	1.16
a	0.753	0.690	0.68	-	0.75
v_i	1.975	1.074	7.6	-	1.8
r_{i0}	1.342	1.178	1.17	-	1.37
a_i	0.584	0.690	0.57	-	0.68
v_s	-	-	-	72.15	-
r_{s0}	-	-	-	-	-
a_s	-	-	-	1.484	-
v_{si}	10.402	7.538	-	-	3.9
r_{si0}	1.390	1.178	-	-	1.37
a_{si}	0.699	0.690	-	-	0.68
v_{so}	3.557	5.900	13.3	-	6
r_{so0}	0.972	0.905	1.0	-	1.06
a_{so}	1.011	0.630	0.6	-	0.78
v_{soi}	-	-	4.2	-	-
r_{soi0}	-	-	0.97	-	-
a_{soi}	-	-	0.62	-	-
r_{c0}	1.303	1.283	-	-	1.25

Table 10.7: Optical model parameters used in FRESKO input. R-Match was assumed to be 11 fm, thought is given to the radius of the transfer in section 10.12.

represents a very small approximation, especially considering the significant uncertainties on optical model parameters.

For an $l=0$ transfer it is not likely the neutron enters the $n=0$ shell (where $n=0$ is the first principal quantum number), $l=0$ orbital as this is populated by two neutrons and so would require significant excitation of a $0S_{\frac{1}{2}}$ neutron. Instead it is more favourable that the $1S_{\frac{1}{2}}$ is populated as this shell is open, can be populated; and is empty. However considering the $\Delta l = 1$ transfer offers two options either the entrance can occur into the $0p_{\frac{1}{2}}$ or $0p_{\frac{3}{2}}$ which are both full or very significant energetic excitation into the $1p_{\frac{1}{2}}$ or $1p_{\frac{3}{2}}$. It is possible to excite a pair of neutrons out of the $0p$ shell and into an excited state. Ultimately this would arguably be more energetically favourable than populating the $1p$ shell, this was assumed to occur here. Given these ideas the principal quantum number and number of radial nodes can be found as in table 10.8.

FRESKO was run for each transferred angular momentum value calculated here, from 0 to 6 and for each state energy. It was expected that states with large angular momentum,

Δl	Principal Quantum Number	Number of Radial Nodes
0	2	2
1	1	1
2	1	1
3	1	1
4	1	1
5	1	1
6	1	1

Table 10.8: Transferred angular momentum, Δl , and the number of radial nodes.

j , requiring higher transferred l would be inhibited due to a larger angular momentum barrier. Note also the populated state energy, as measured here, was included in the DWBA calculations. The DWBA outputs are not sensitive to populated state energies varying a few keV, hence the assignments made here, where possible, are valid for both the literature and measured state energies.

Each transferred angular momentum value leads to the population of one of two states, through either aligning with the neutron spin or anti-aligning. During the FRESCO runs the value of j which minimised the transferred angular momentum in $^{17}\text{O}+\alpha$ was chosen.

10.10 Spin parity assignment and spectroscopic factors based on FRESCO

Experimental differential cross-sections were calculated from the measured data points using eqn. 2.3. Combining number of beam particles, number of target particles, extracted recoil protons and angular acceptance of the aperture. The following figures show the DWBA outputs, varying in transferred l , with the corresponding experimental differential cross-sections, where the latter could be extracted.

The FRESCO [36] outputs yielded much larger differential cross-sections as it assumes the ^{21}Ne wavefunction to be comprised purely of a ^{20}Ne and a neutron wavefunction. A factor of C^2S scaled the DWBA outputs to the experimental data and were fitted using this single, free scaling parameter. It must be noted the DWBA plots presented here are those where the neutron has an assumed binding energy of 0.1 MeV. This same process was repeated for 0.2 MeV, 0.5 MeV and 1 MeV neutron binding energy. The Gamow window lies above the

6.761 MeV neutron threshold. This discrepancy was corrected by extrapolating out to the correct unbound energy, this will be discussed further later. The C^2S factors presented here represent the extrapolated spectroscopic factors. The uncertainties are derived from the C^2S values for the bound energies at which the calculations were run, finding a minimum and maximum for the extrapolation function.

5.549 MeV

Channel numbers above 3000 were used with caution as there were concerns over the efficiency relative to the rest of the focal plane detector in that region of the detector. It was however expected that in a small enough region the number of counts would have been affected in a similar way such that a differential cross-section can be extracted as well as a transferred l , but the spectroscopic factor should be considered unreliable. The 5.549 MeV energy state was the only state in that region of the focal plane detector that was investigated. As can be seen in figure 10.29 an $l=2$ transfer was extracted, which is in direct agreement with literature, where the state is known to have a J^π of $\frac{3}{2}^+$ [30]. This implied the form of the FRESCO differential cross-section was comparable to what we extract experimentally, hence this increased confidence in the FRESCO output.

6.609 MeV

The experimental differential cross-sections and the FRESCO outputs for a 6.609 MeV energy state can be seen in figure 10.30. Note how the trend of the data points strongly suggests an $l=1$ transfer. The parity of this state is therefore a $\frac{1}{2}^-$ or $\frac{3}{2}^-$. The fits of the $l=3$, $l=4$, $l=5$, and $l=6$ transfers are poor it is clear that they do not have the same trend as the experimental data points. The C^2S for an angular momentum transfer of $l=1$ was found to be 0.093 ± 0.008 for this state. It should be noted where a partial width was extracted fitting occurred only between the first maxima and minima.

7.420 MeV

Figure 10.31 shows the scaled FRESCO outputs, assuming a 0.1 MeV neutron binding energy, for the 7.420 MeV energy state. The results here are somewhat inconclusive. Literature suggests it may be a $\frac{11}{2}^-$ state. The fit for all l transfers here is poor.

It must be noted that due to this inconclusive result the 40.1° data point was checked for 7.420 MeV energy state as the $l=2$ could potentially have been supported. The peak fit was checked, the 40.1° spectra compared to spectra at other angles to ensure the peak had

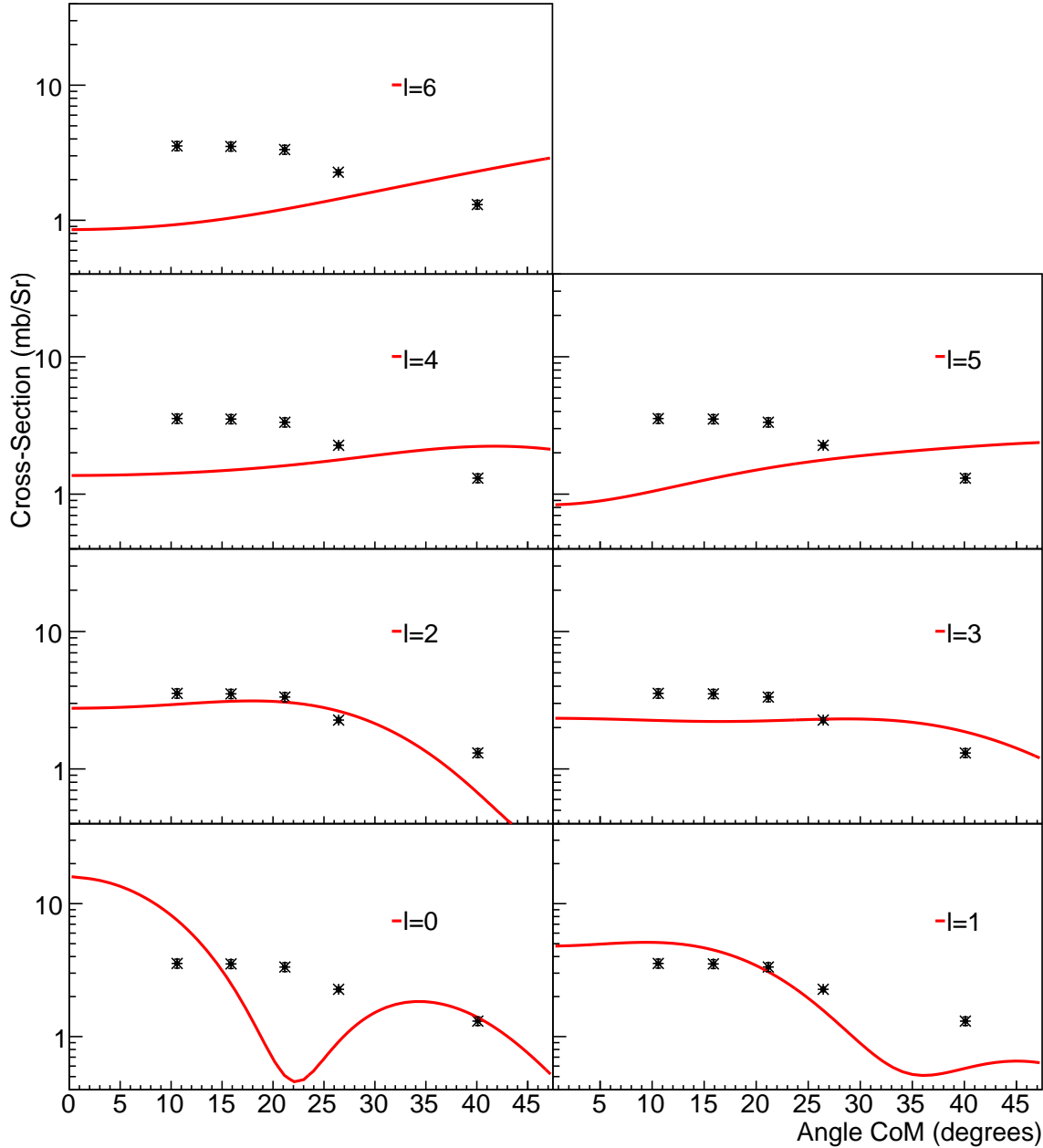


Figure 10.29: Experimental differential cross-sections for 5.549 MeV compared with FRESKO outputs. Each sub-plot has a different value of transferred angular momentum. It is clear the 5.549 MeV energy state was formed through an $l=2$ transfer.

not been misidentified and the focal plane plotter comparison rechecked, (this also occurred during calibration on several instances) it was re-confirmed this is the 7.420 MeV peak. It is unlikely, due to the first maxima in the FRESKO outputs increasing in angle with increasing transferred l , that the transferred l is higher than 6. The transfer could be speculated as

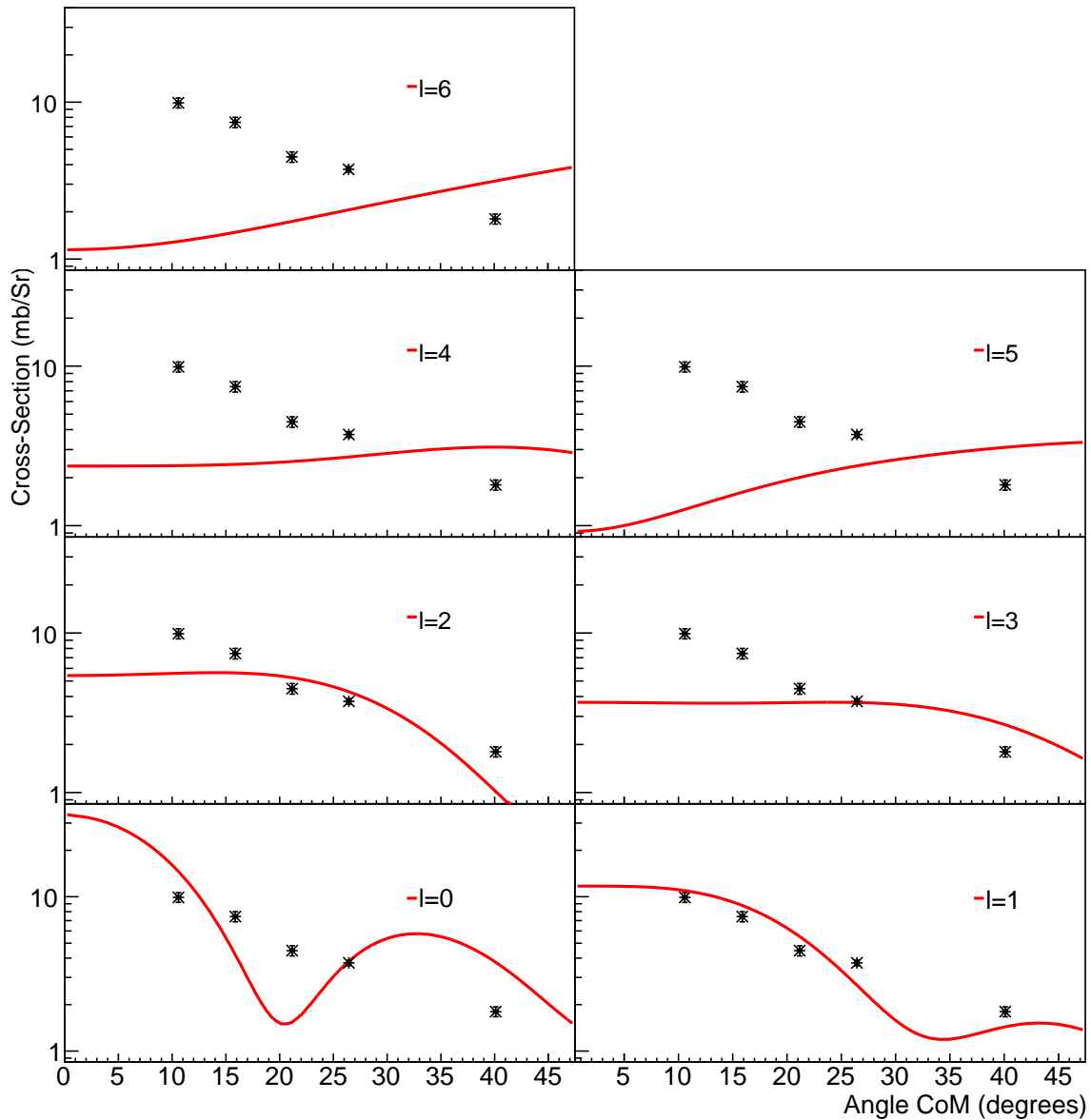


Figure 10.30: Experimental differential cross-sections for 6.609 MeV compared with FRESKO outputs. Each sub-plot has a different value of transferred angular momentum and different C^2S scaling factor.

an $l=4$ or $l=5$ transfer however this is unlikely due to its significant population in this (d,p) reaction.

It is proposed that there is some degree of compound reaction occurring and that this is likely not a pure transfer reaction. As such no l can be extracted here.

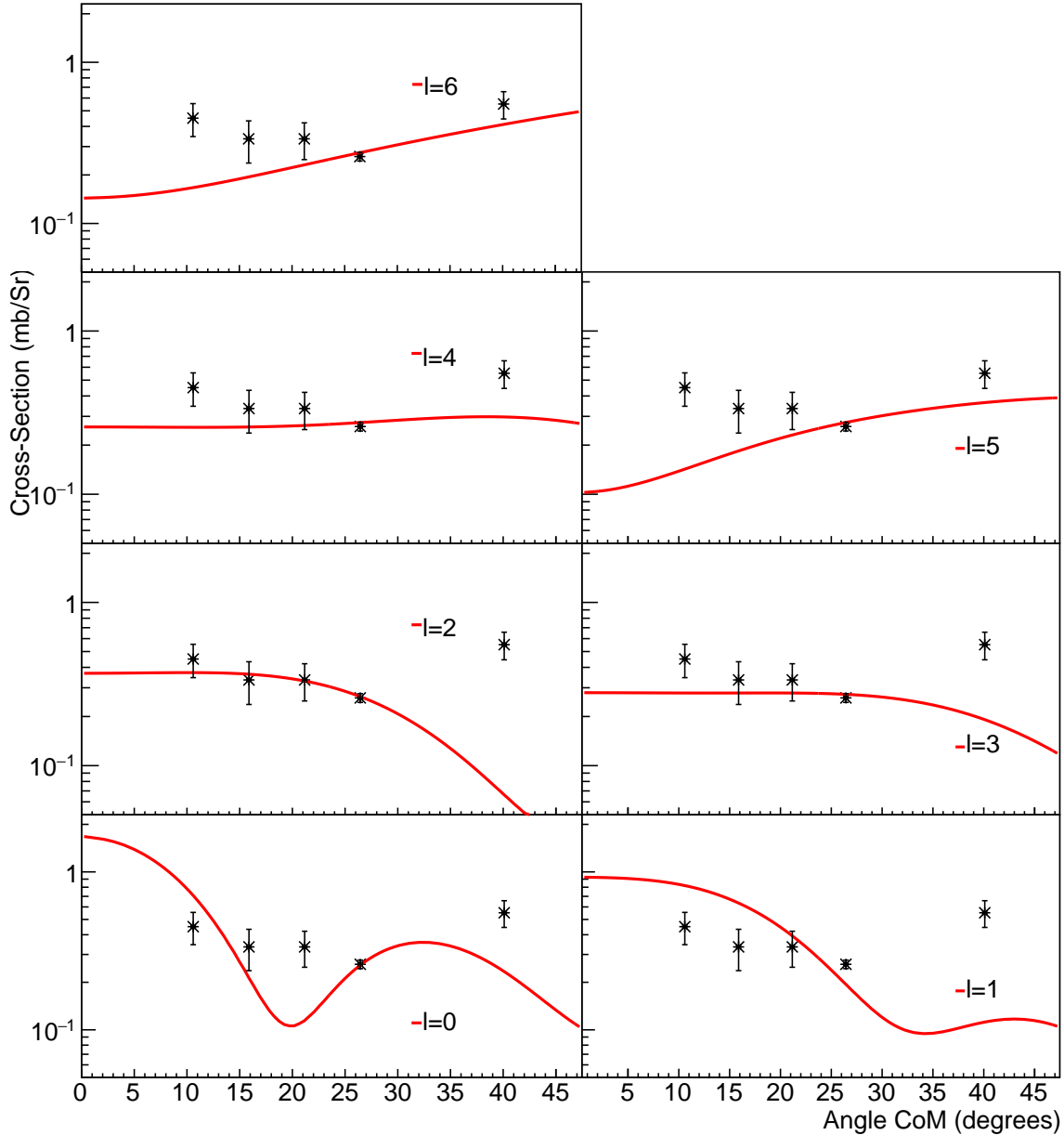


Figure 10.31: Experimental differential cross-sections for 7.420 MeV compared with FRESKO outputs. Each sub-plot has a different value of transferred angular momentum and different C^2S scaling factor.

7.559 MeV

The comparison of the experimental differential cross-section and the scaled and fitted DWBA outputs can be seen to be conclusive in figure 10.32 as an $l=1$ transfer. This implies that the 7.559 MeV state is either a $\frac{1}{2}^-$ or $\frac{3}{2}^-$ state. For an $l=1$ transfer the C^2S was found to be 0.0027 ± 0.0003 . As in figure 10.30 higher angular momenta transfers are of poor fit.

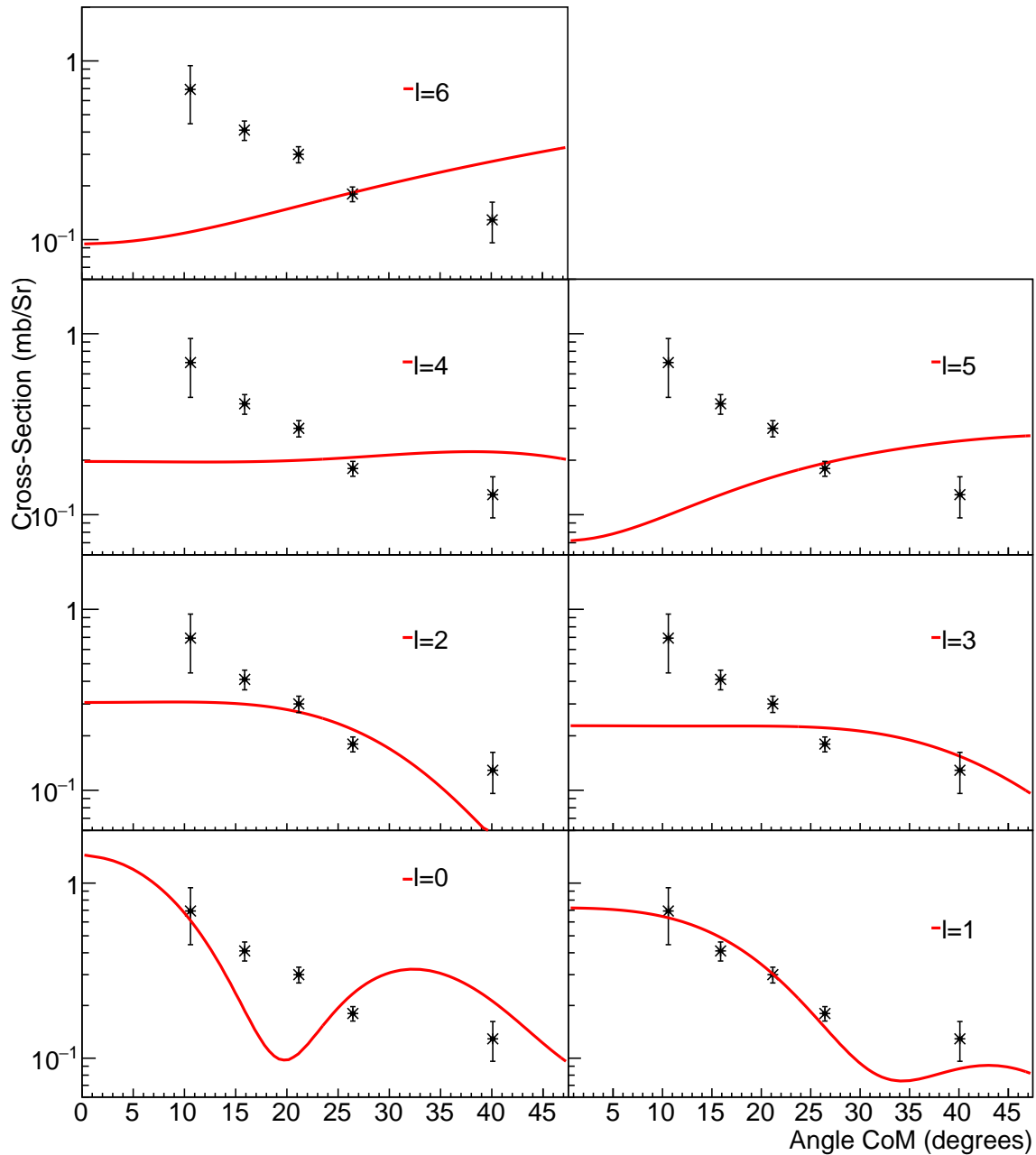


Figure 10.32: Experimental differential cross-sections for 7.559 MeV compared with FRESKO outputs. Each sub-plot has a different value of transferred angular momentum and different C^2S scaling factor.

7.601 MeV

Using figure 10.33 to compare the fitted DWBA outputs and the experimental differential cross-sections it becomes apparent that to populate the 7.601 MeV state a higher l transfer has likely taken place, or that this is a not a transfer. Assuming a transfer the fit is best for

an $l=4$ transfer and as such it is likely the 7.601 MeV state has a spin parity of $\frac{7}{2}^+$ or $\frac{9}{2}^+$. An $l=4$ transfer implied a C^2S of 0.0060 ± 0.0007 . This is consistent as the state was poorly populated.

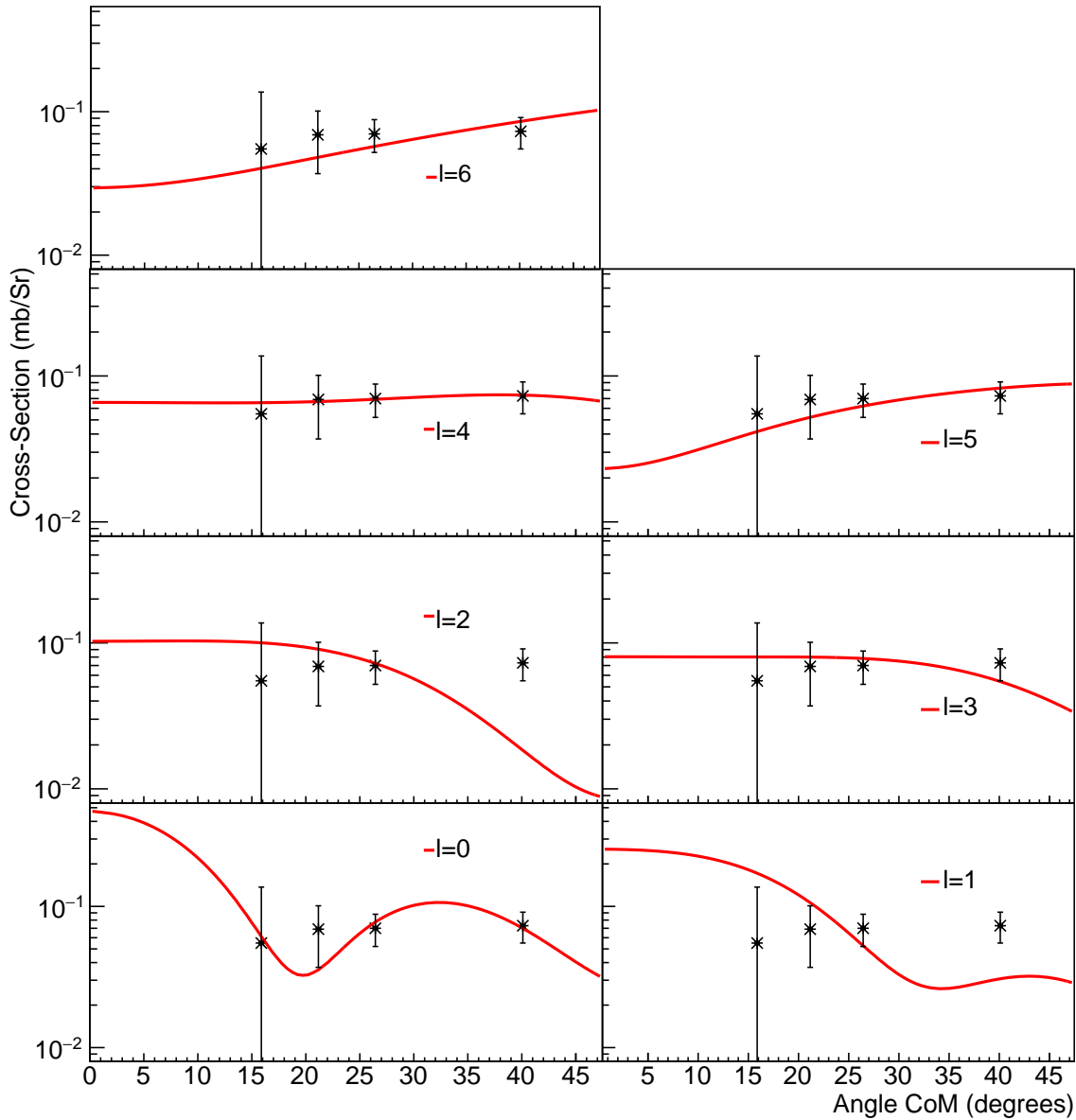


Figure 10.33: Experimental differential cross-sections for 7.601 MeV compared with the FRESCO outputs. Each sub-plot has a different value of transferred angular momentum.

Despite the scaled DWBA fit for $l=6$ being within error of the experimental data the second order derivative of the function in that region is positive, whereas for the experimental data points this is negative, hence $l=6$ was discounted.

7.619 MeV

The 7.619 MeV energy state DWBA outputs and experimental data can be seen in figure 10.34. The scaled DWBA plots suggest the transferred angular momentum was most likely a 1 or 3, given the previous literature [97] suggesting an $l=1$ transfer also, this transfer shall be adopted. The C^2S of this state was found to be 0.0018 ± 0.0004 .

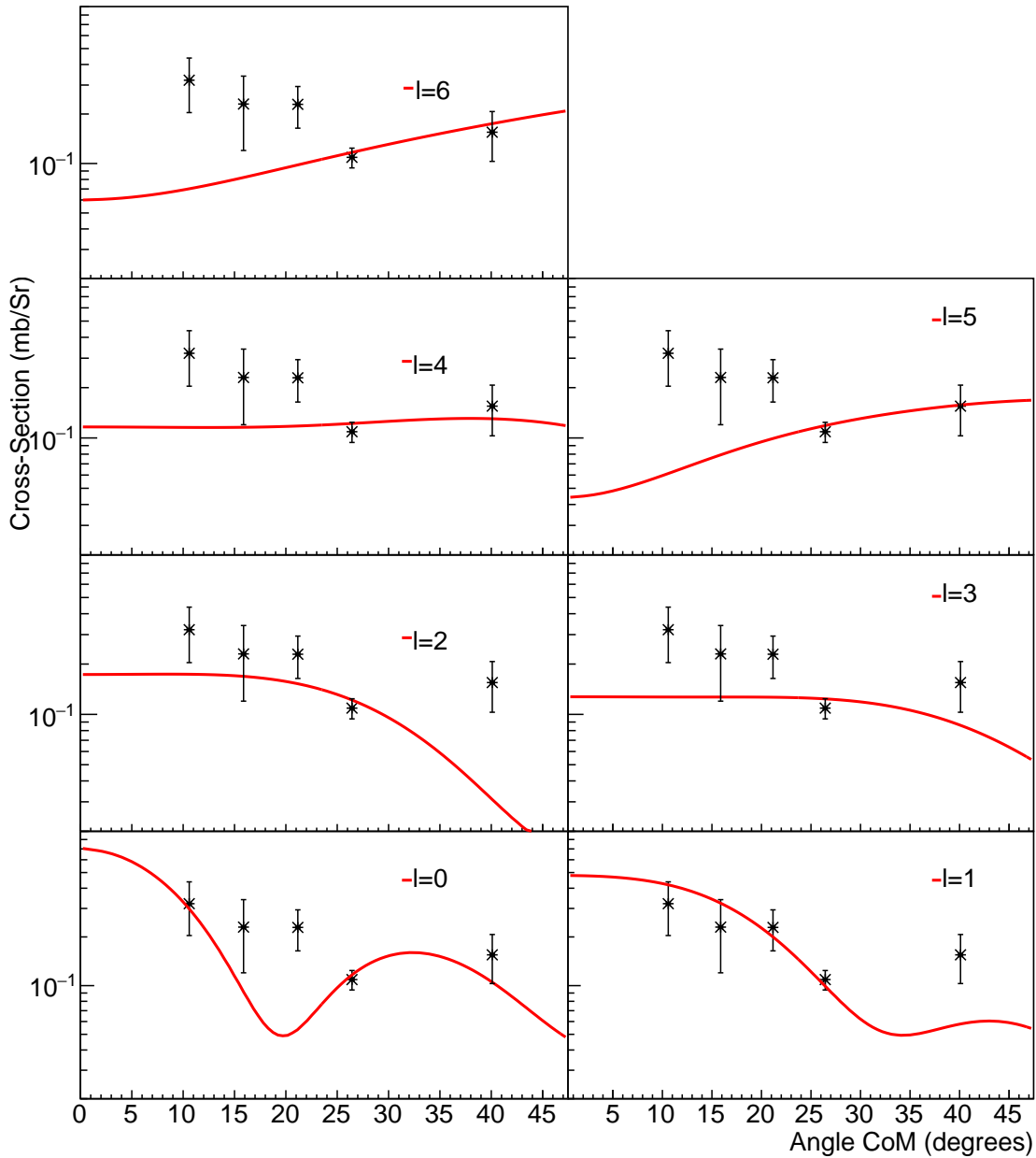


Figure 10.34: Experimental differential cross-sections for 7.619 MeV compared with FRESKO outputs. Each sub-plot has a different value of transferred angular momentum and different C^2S scaling factor.

7.820 MeV

Figure 10.35 shows the experimental cross sections and the scaled DWBA outputs for the 7.820 MeV energy state. The fits of the angular momentum transfers suggest an $l=0$ transfer, which yields a C^2S factor of 0.018 ± 0.003 . Consideration was also given to an $l=1$ transfer as $l=0$ transfers should be broad states, the C^2S found for an $l=1$ transfer was 0.0007 ± 0.0007 , giving an upper limit of 0.0014. For higher values of l transfer the first maxima in the DWBA calculations occur at larger angles. The $l=1$ transfer suggests the the 7.820 MeV state has a spin parity of $\frac{1}{2}^-$ or $\frac{3}{2}^-$.

7.981 MeV

It must be noted that the 7.981 MeV energy state discussed here will likely consist of contributions from the literature [30] accepted states of energy 7.9821(6) MeV and 7.980(10) MeV. The 7.981 MeV energy state was only measured at three angles. However when fitting the DWBA outputs to these three data points we see that three angular momentum transfers are possible: $l=0$, $l=5$ or $l=6$, higher transfers are however inhibited by the angular momentum barrier. The C^2S value for an $l=0$ transfer would be 0.002 ± 0.013 at a binding energy of 0.1 MeV, hence representing an upper limit and spin parity of $\frac{1}{2}^+$. Transferred l values of 4, 5 or 6 would suggest a spin parity of $\frac{1}{2}^+$ or $\frac{9}{2}^-$ or $\frac{11}{2}^-$ or $\frac{11}{2}^+$ or $\frac{13}{2}^+$.

Unfortunately the 7.981 MeV energy state could not be extracted at either 10.6° or 26.4° , the former due to insufficient statistics due to beam intensity reduction and the later due to the $p(d,p)$ peak. It must also be noted that while a transfer upto $l=6$ has been measured here the transfer could have been higher, but due to the increased angular momentum barrier this seems unlikely. Because this peak may be a doublet a transferred l and hence C^2S cannot be conclusively extracted.

8.068 MeV

The 8.068 MeV energy state experimentally extracted differential cross-sections can be seen with the fitted DWBA outputs in figure 10.37. l transfers greater than 3 can be discounted due to the experimental differential cross-sections general negative gradient with increasing angle, across those angles measured here. For $l=1$ the respective C^2S value extracted was -0.00018 ± 0.00163 , strictly non-physical, creating an upper limit of 0.0015.

Due to the differential cross-sections at 10.6° and 40.1° the $l=2$ transfer seems less likely than an $l=1$ transfer and due to the overall trend of data points the $l=1$ transfer seems most

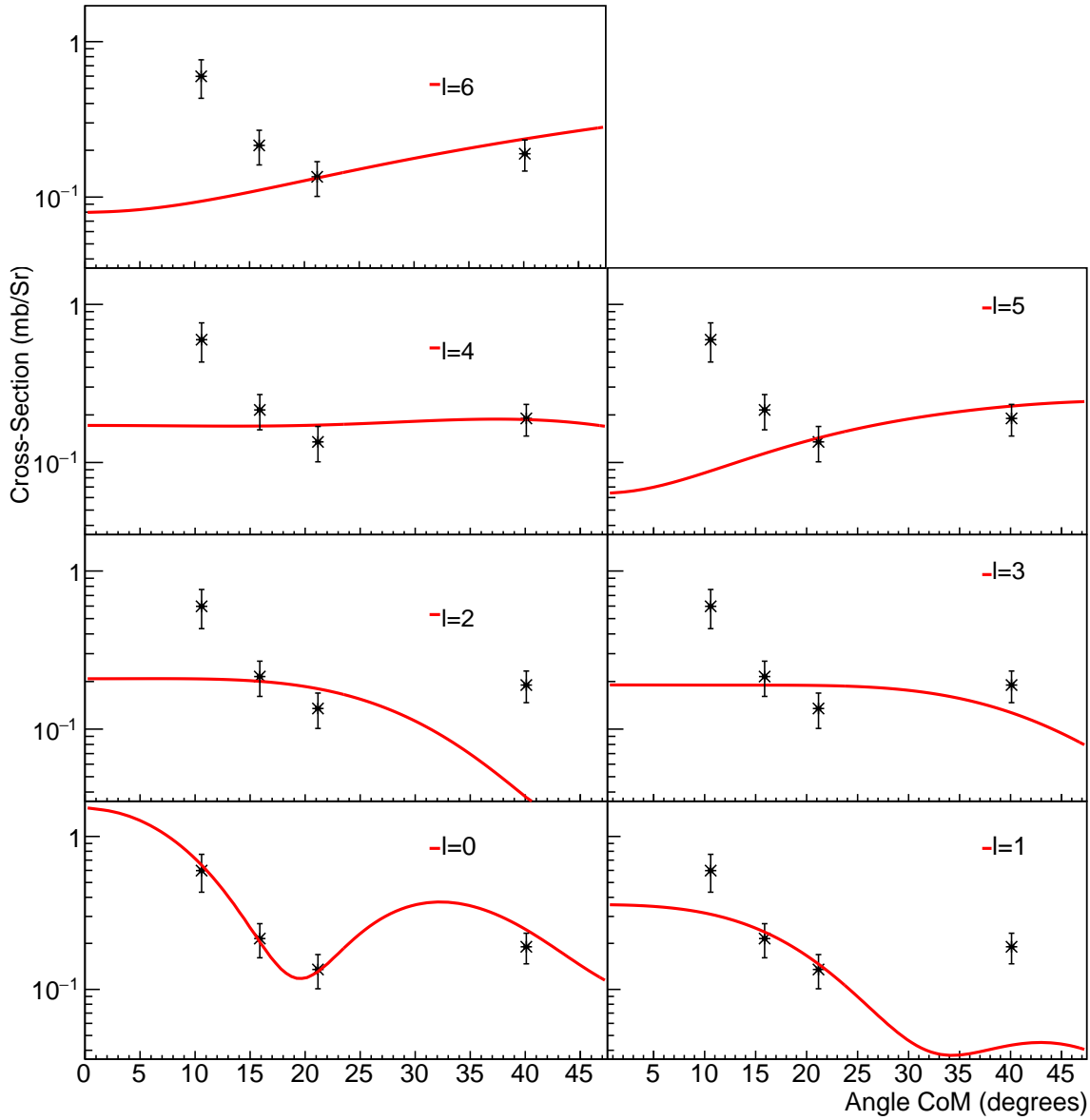


Figure 10.35: Experimental differential cross-sections for 7.820 MeV compared with FRESKO outputs. Each sub-plot has a different value of transferred angular momentum and different C^2S scaling factor.

likely when compared with an $l=0$ transfer also. This would yield a spin parity value of $\frac{1}{2}^-$ or $\frac{3}{2}^-$.

An $l=3$ transfer is represented within error of the differential cross-sections also. The C^2S for this transfer was found to be 0.0122 ± 0.0009 .

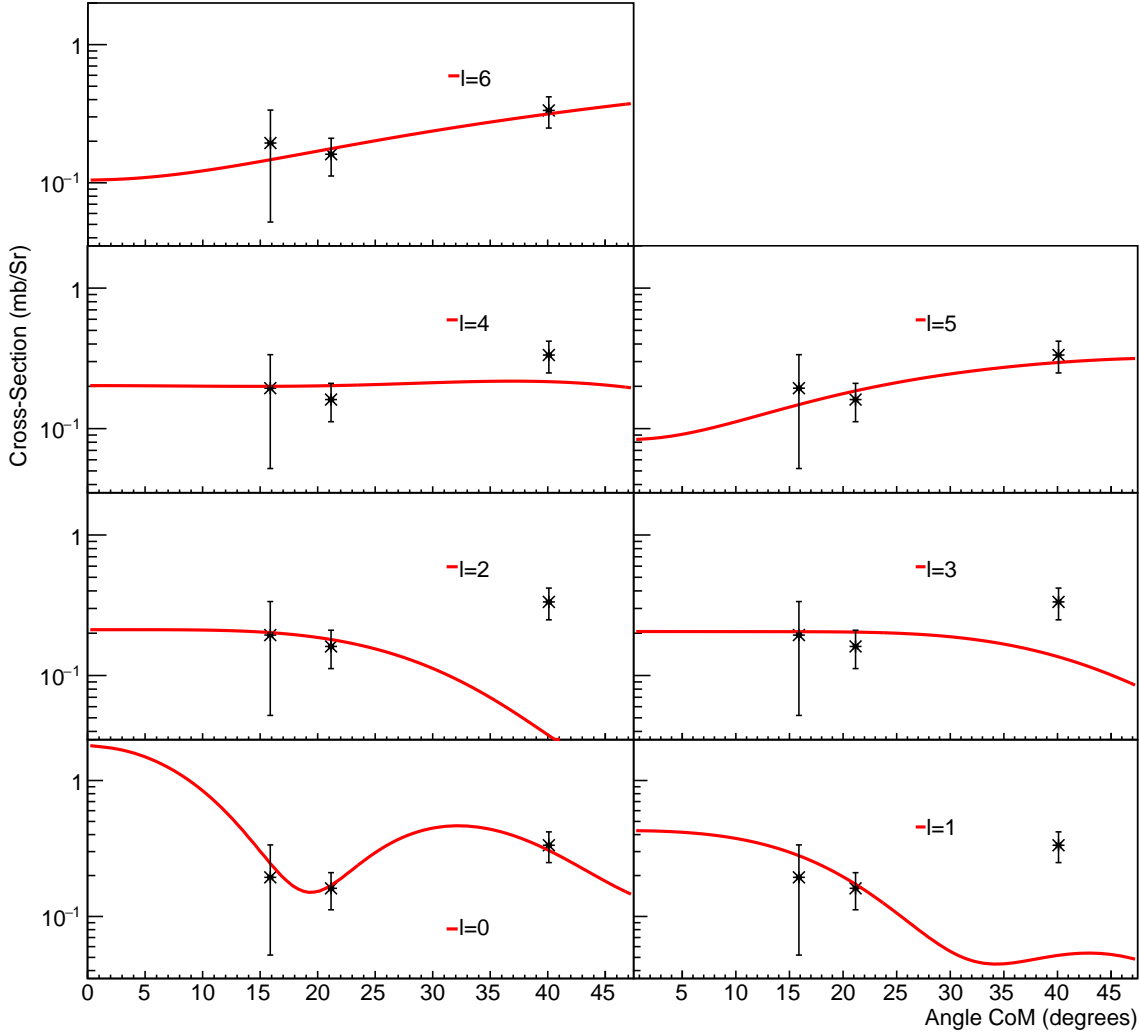


Figure 10.36: Experimental differential cross-sections for 7.981 MeV compared with FRESKO outputs. Each sub-plot has a different value of transferred angular momentum and different C^2S scaling factor.

8.146 MeV

Figure 10.38 shows the experimentally extracted differential cross-sections for the 8.146 MeV energy state as well as the scaled DWBA differential cross-sections for each transferred l value. It can be seen that all transferred l values above 1 fit poorly and so the angular momentum transferred is either an $l=0$ or $l=1$. Due to the DWBA calculation for $l=0$ at lower angles aligning more convincingly with the 10.6° and 15.9° data points, matching the magnitude of the gradient, it is likely, from this data alone an $l=0$ transfer. However considering that an $l=0$ transfer would be broad, so an $l=1$ state becomes arguably much more likely.

A transferred angular momentum value of $l=1$ resulted in a C^2S of 0.00009 ± 0.00110 ,

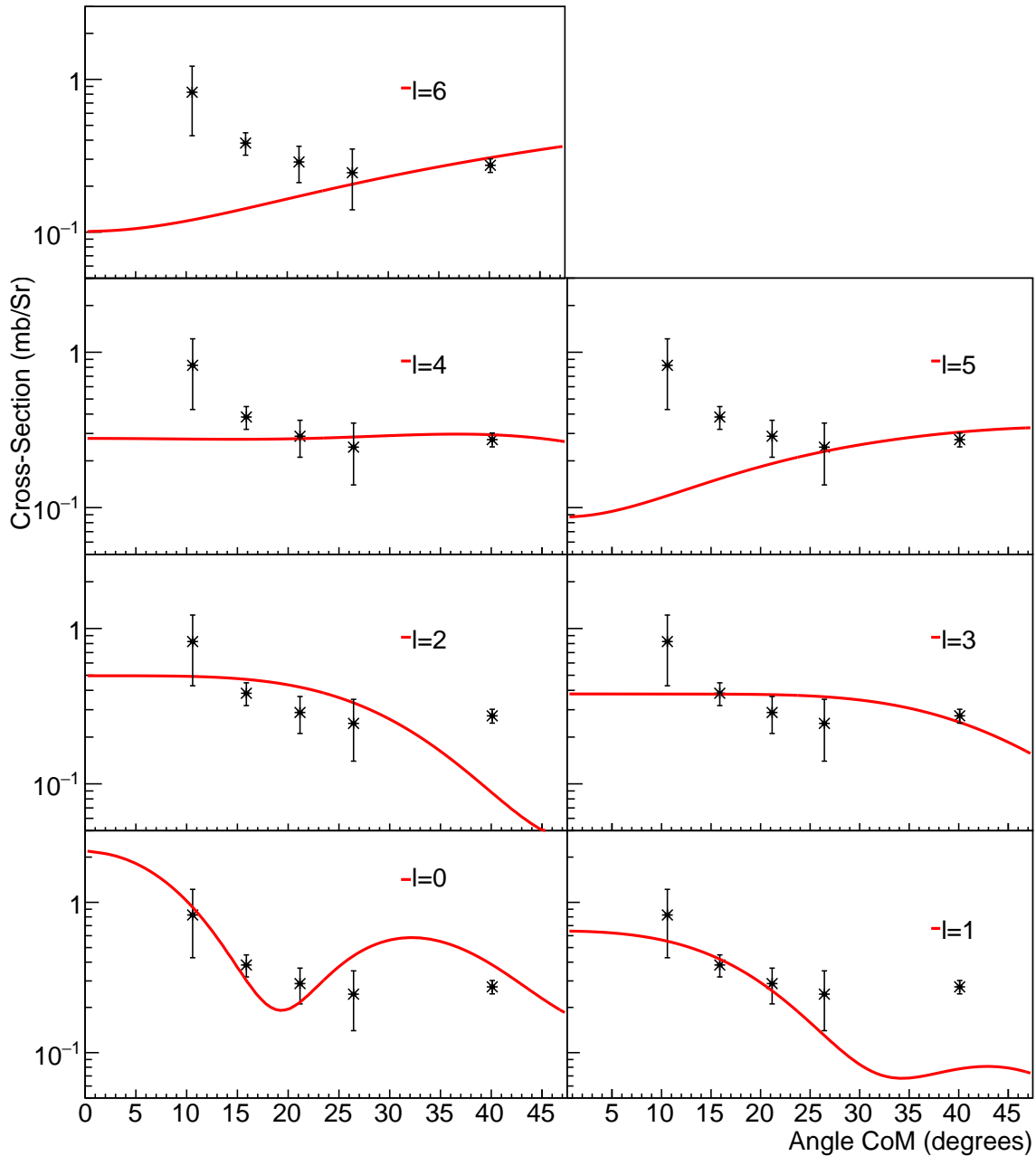


Figure 10.37: Experimental differential cross-sections for 8.068 MeV compared with FRESKO outputs. Each sub-plot has a different value of transferred angular momentum and different C^2S scaling factor.

an upper limit of 0.0012. An $l=1$ transfer would suggest a spin parity assignment for the 8.146 MeV energy state of $\frac{1}{2}^-$ or $\frac{3}{2}^-$.

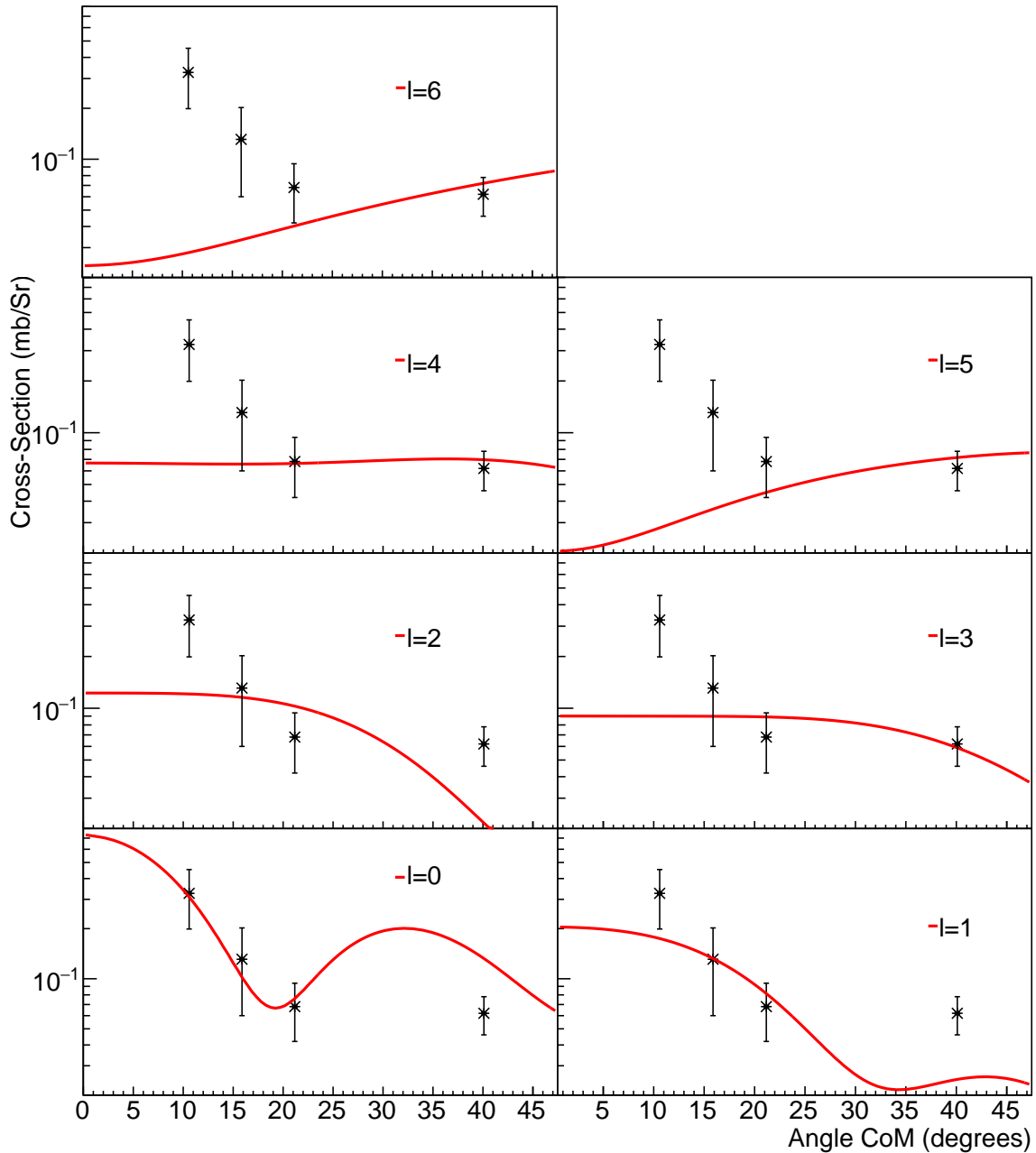


Figure 10.38: Experimental differential cross-sections for 8.146 MeV compared with FRESKO outputs. Each sub-plot has a different value of transferred angular momentum and different C^2S scaling factor.

8.189 MeV

The measured differential cross-sections and the scaled DWBA fits for different values of angular momentum transfer for the 8.189 MeV states can be seen in figure 10.39. It can be seen due to the function shape relative to the data points that an $l=1$ transfer is the

only appropriate transfer matching the experimental data. An $l=1$ transfer implies the spin-parity of this 8.189 MeV energy state is $\frac{1}{2}^-$ or $\frac{3}{2}^-$. This yielded a C^2S value of -0.0007 ± 0.0018 , clearly not physical but representing an upper limit of 0.0011.

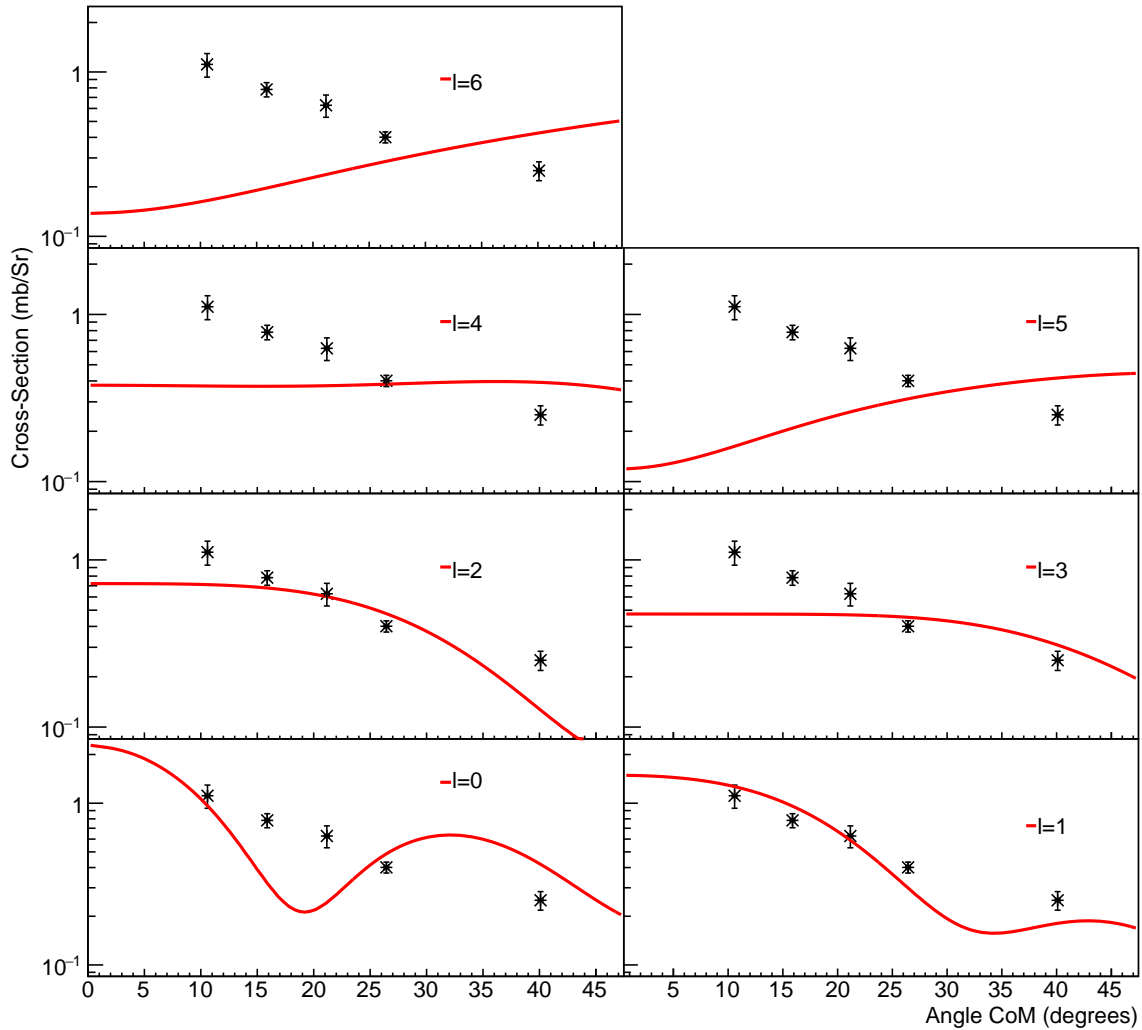


Figure 10.39: Experimental differential cross-sections for 8.189 MeV compared with FRESKO outputs. Each sub-plot has a different value of transferred angular momentum and different C^2S scaling factor.

10.11 Spin parity assignment using known states

Using the FRESCO calculation outputs as discussed in section 10.10 checks can be made to confirm whether the FRESCO calculations: firstly agree with expected l transfers from literature, and secondly whether the assignment of transferred l agrees with that previous literature.

Assuming the 7.619(2) MeV energy state, in literature [30] referred to as the 7.628(10) MeV energy state with an $l=1$ transfer in $^{20}\text{Ne}+n$, so the ratio of differential cross-sections for states that did not yield a flat differential cross-section can be scrutinised as in figure 10.40. An $l=1$ transfer should have had a consistent ratio, within error, across angles. It can be seen from figure 10.40 that the $l=1$ transfers of the 7.559 MeV, 8.068 MeV and 8.146 MeV can be confirmed using this method. The 6.609 MeV and 8.189 MeV energy states show deviation from a consistent ratio and cannot have their transferred angular momentum confirmed as $l=1$ using solely figure 10.40. Note must be made to figure 10.34 and the fluctuations around the FRESCO calculation for $l=1$. These fluctuations imply that solely using a ratio with the differential cross-sections of the 7.619 MeV energy state may not be conclusive.

FRESCO strongly suggested the 8.189 MeV energy state is formed via an $l=1$ transfer in $^{20}\text{Ne}(d,p)$ and as such the ratio process seen in figure 10.40 were repeated using the 8.189 MeV energy state differential cross-sections as a reference point as in figure 10.41. The 6.609 MeV and 7.559 MeV can be considered to be populated via the same l transfer as the 8.189 MeV. The 7.559 MeV can be seen in agreement using both the 8.189 MeV and 7.619 MeV plot.

This ratio process can be repeated for $l=2$ transfers, using the 5.549 MeV energy state as the reference point and taking the ratio of the states yields figure 10.42. Note none of the other states tested in figure 10.42 appear to be formed through an $l=2$ transfer.

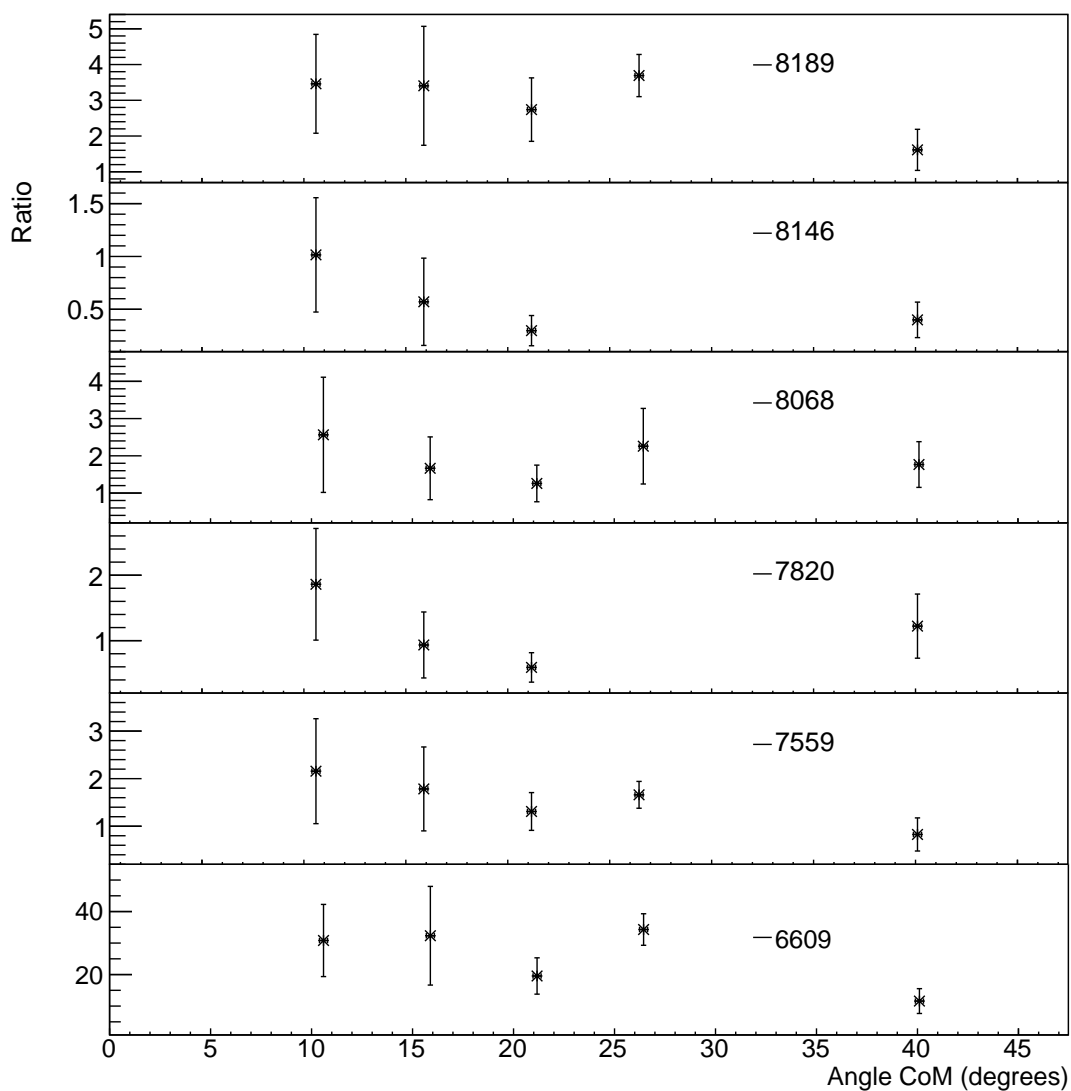


Figure 10.40: Experimental differential cross-sections for the 8.189 MeV, 8.146 MeV, 8.068 MeV, 7.820 MeV, 7.559 MeV and 6.609 MeV energy states taken in ratio with the differential cross-sections of the known $l=1$ transfer of the 7.619 MeV energy state.

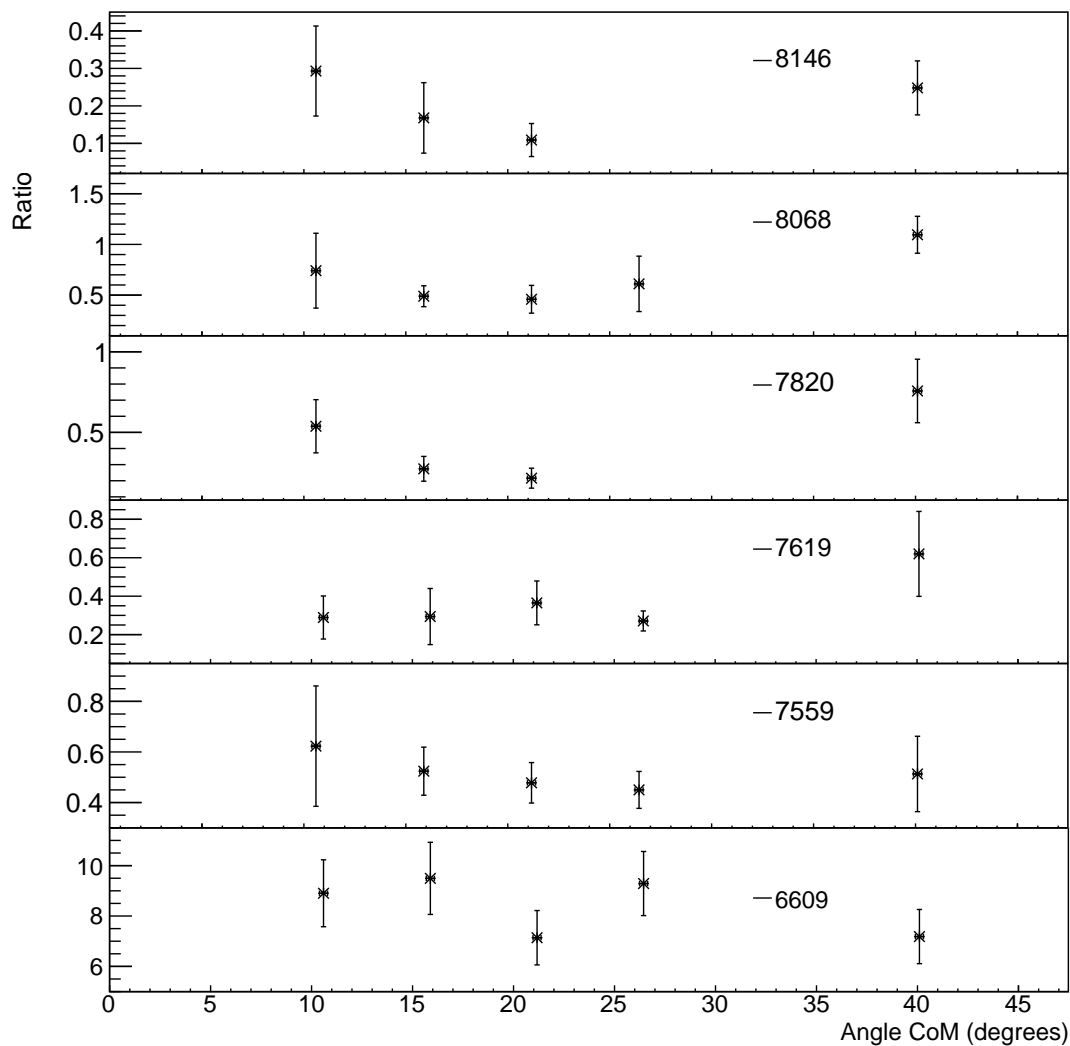


Figure 10.41: Experimental differential cross-sections for the 8.146 MeV, 8.068 MeV, 7.820 MeV, 7.619 MeV, 7.559 MeV and 6.609 MeV energy states taken in ratio with the differential cross-sections of the 8.189 MeV energy state.

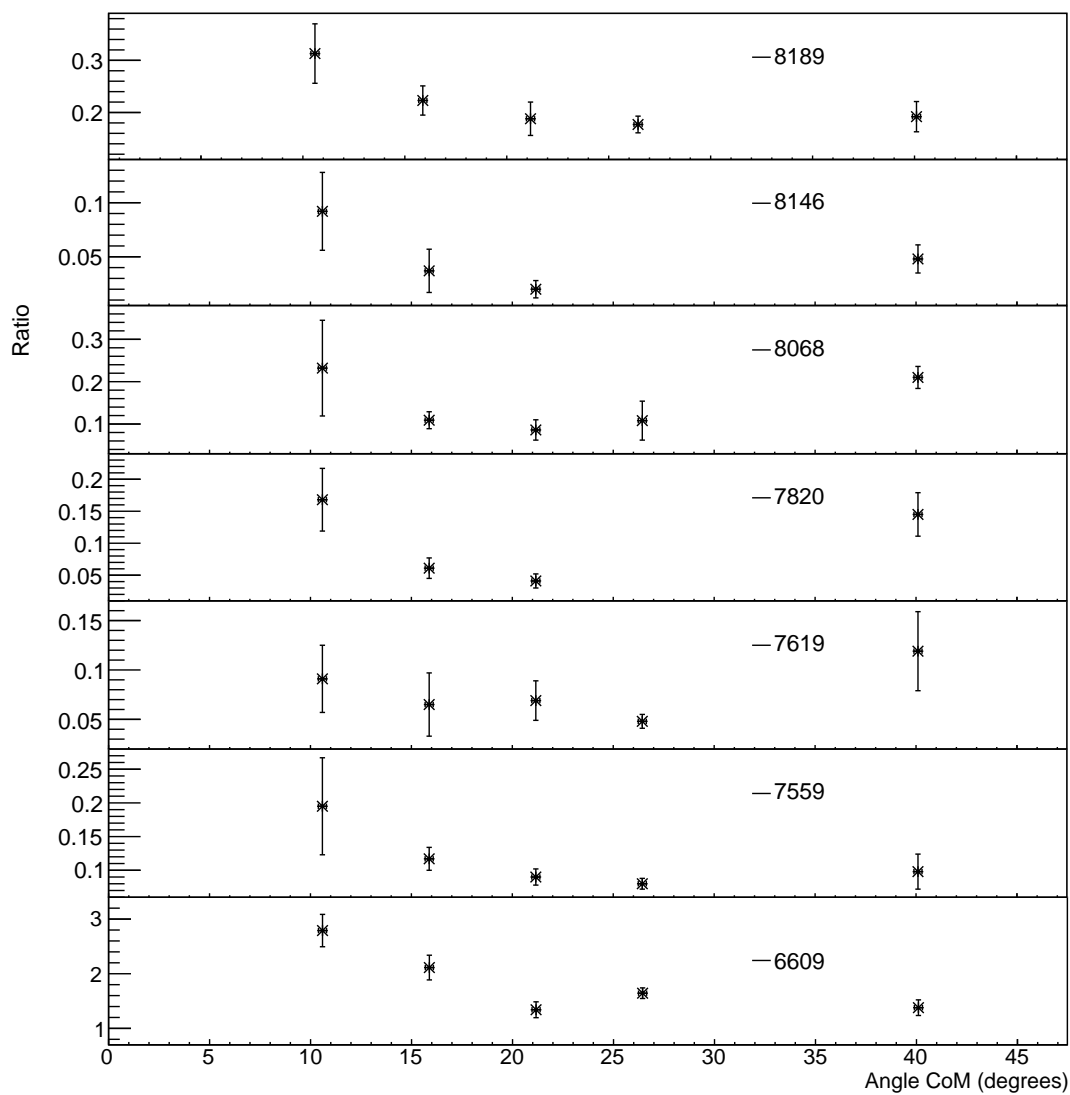


Figure 10.42: Experimental differential cross-sections for the 8.189 MeV, 8.146 MeV, 8.068 MeV, 7.820 MeV, 7.619 MeV, 7.559 MeV and 6.609 MeV energy states taken in ratio with the differential cross-sections of the 5.549 MeV energy state.

10.12 Neutron partial widths

Having scaled the FRESCO outputs the likely transferred angular momentum values in $^{20}\text{Ne}(d,p)$ were found as discussed earlier, along with the value of C²S. At this point the penetrability as in eqn. 2.20 for the calculation of the neutron partial width as in eqn. 2.19 was found. Values of spectroscopic factors at bound energies were used at the respective bound energies for the partial width calculations, not the extrapolated values. The calculated partial width with varying interaction radius can be seen in figure 10.43 which is for the 7.619 MeV energy state for $\Delta l=1$ in $^{20}\text{Ne}+n$, assuming a binding energy of 100 keV due to FRESCO's inability to calculate differential cross-sections for unbound states. Note how the partial width rapidly rises at low radius, inside the nucleus, and then begins to plateau.

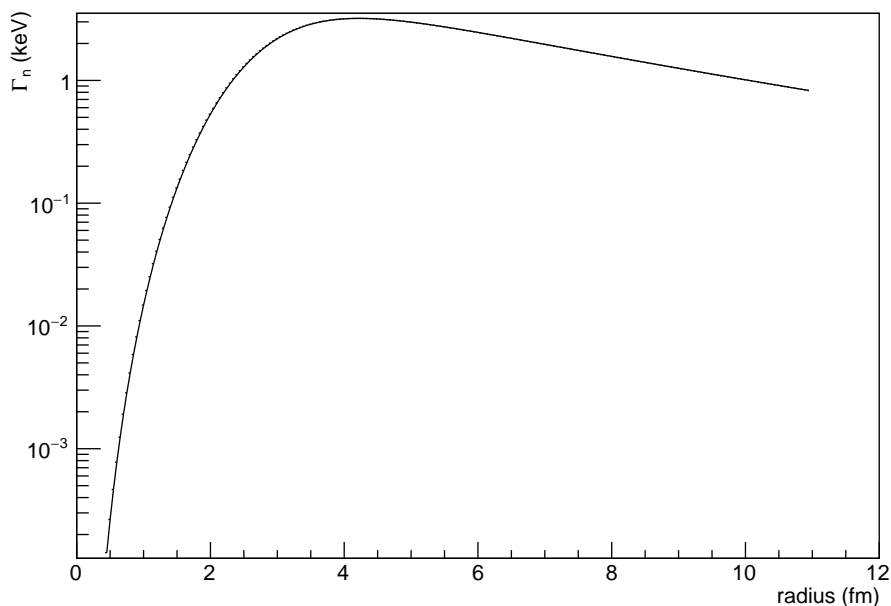


Figure 10.43: The partial width as a function of interaction radius for the 7.619 MeV energy state with a 100 keV binding energy for an $l=1$ transfer.

The final radius at which to extract the partial width was found where the asymptotic normalisation coefficient, ANC, became constant. In all cases this was larger than the nuclear radius and typically in the region of ~ 6 -7 fm. The choosing of the reaction radius resulted in significant uncertainty in the partial widths, as seen later in figure 10.45. A conservative 1.5 fm tolerance was given to the extraction of the reaction radius. The partial width at 1.5 fm larger was taken and the difference between this and the partial width adopted as the

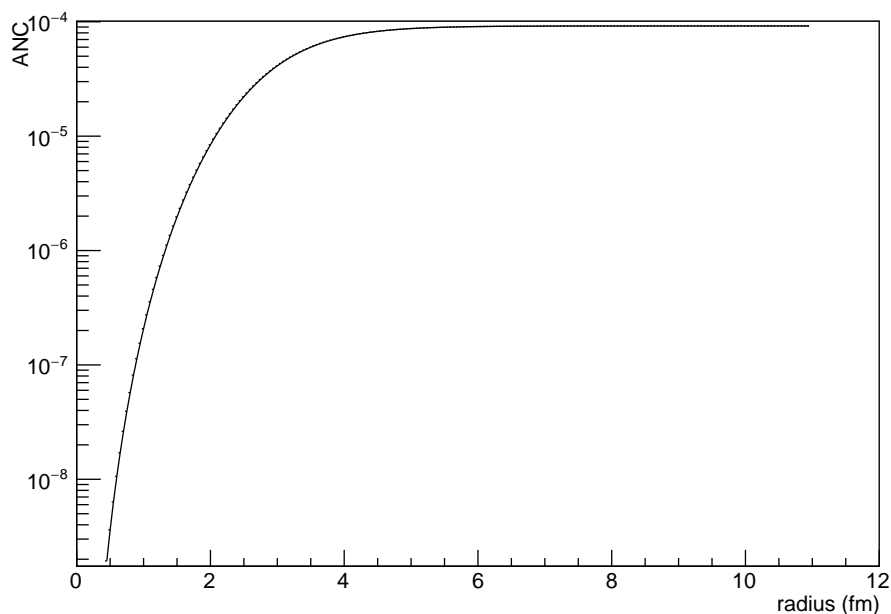


Figure 10.44: The Asymptotic Normalisation Coefficient as a function of interaction radius for the 7.619 MeV energy state with a 100 keV binding energy for an $l=1$ transfer in $^{20}\text{Ne}+n$.

uncertainty. This resulted in a significant uncertainty in the partial width. This highlights the significant partial width dependence on the interaction radius.

The penetrability for transfers of $l=0$ results in large partial widths, as neutrons face no Coulomb barrier and the significant penetrability at higher transferred l was that of the angular momentum barrier. For the states where the partial width was found it was calculated by extrapolating back from the four binding energies tested, 100 keV, 200 keV, 500 keV and 1000 keV up to the resonance energy. These binding energies were chosen as the extrapolation above the neutron threshold was typically 800-1300 keV for states inside the Gamow window. The data and fit used for the extrapolation for the 7.619 MeV $l=1$ transfer can be seen below in figure 10.45.

The extrapolation function used was linear in the case of each state, in part due to the conservative errors as seen in figure 10.45. The uncertainties on the final neutron partial widths are given by the extremes of this extrapolation fit, hence including the dominating uncertainty from the location of the reaction radius.

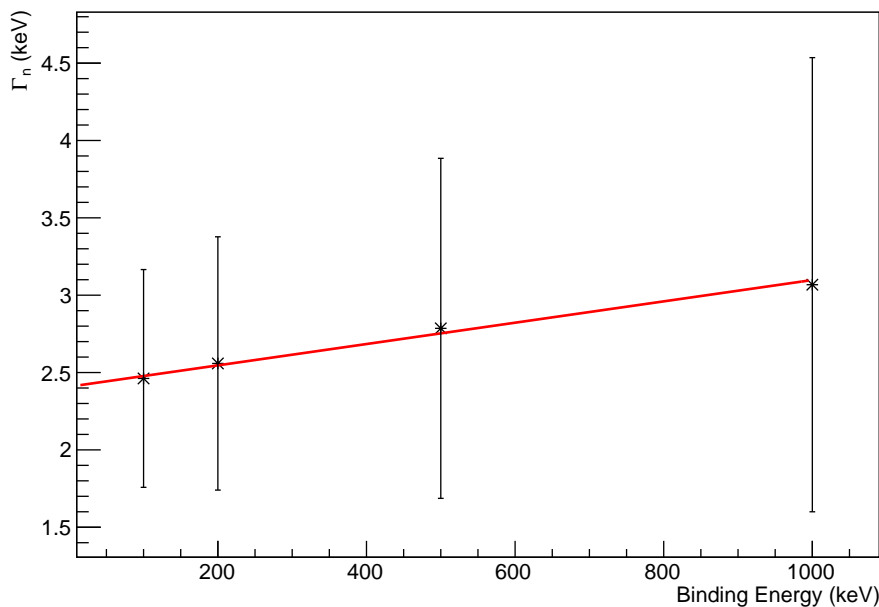


Figure 10.45: The partial width as a function of binding energy for the 7.619 MeV energy state for an $l=1$ transfer.

10.13 Reaction rate

The $^{17}\text{O}(\alpha,n)$ reaction rate was first calculated using the narrow resonance formula as seen in equation 2.16. This was a useful initial estimate for viewing the effect of each resonance on the total reaction rate and how these contributions vary with temperature.

The final $^{17}\text{O}(\alpha,n)$ reaction rate calculation was made using the Monte-Carlo RatesMC reaction rate code [98], utilising the partial widths, energies and in most cases their decreased energy uncertainties, and also the new transferred l values from the work conducted here. The input files were generated as part of this work and then the code was run by P.Adsley [95]. It offers a detailed error calculation using a Monte-Carlo simulation giving the confidence interval of the rate and the individual contributions [37].

The Monte Carlo code allows integration, and hence full treatment of the variation in reaction rate across the width, as seen in equation 2.15. A conservative approach of integrating over any state with a width of greater than 1 keV was taken. This only increased the computation time for states where arguably integration was not required.

The states where the transferred angular momentum in $^{20}\text{Ne}+n$ was found so the value of the state spin adopted for ^{21}Ne was that which minimised the transferred l in $^{17}\text{O}+\alpha$. This resulted in the lower of the penetrabilities possible and hence the higher rate possible, as

such the rates found here can be considered the upper of the possible rates.

The objective of this work was to measure the effect of ^{16}O as a neutron poison and as such the ratio of $^{17}\text{O}(\alpha,n)^{20}\text{Ne} / ^{17}\text{O}(\alpha,\gamma)^{21}\text{Ne}$ is required. The $^{17}\text{O}(\alpha,\gamma)^{21}\text{Ne}$ reaction rate was also calculated using the Monte Carlo code, including the updated parameters extracted here. Where the neutron channel is included as a spectator channel the new neutron partial widths were included.

The inputs for the Monte Carlo code can be seen in Appendix A.

Chapter 11

$^{20}\text{Ne}(\text{d,p})^{21}\text{Ne}$ Results

The extracted neutron partial widths, Γ_n and Γ_α can be seen in table 11.1. The Γ_α used here is the Wigner limit with a 0.01 overlap correction applied, unless otherwise stated. The Wigner limit [99] represents the maximum possible width as described by eqn. 2.21. The resultant resonance strength, $\omega\gamma_{(\alpha,n)}$ was calculated using equation 2.9, unless otherwise stated. The calculated resonance strengths are assumed to have an uncertainty of 50%, the uncertainty in the overlap assumption and the hence the Wigner limit of the α partial widths dominate the uncertainty.

Discussion and consideration to the 8.068 MeV states spin parity is given later in the context of its width, ultimately yielding the $\Delta l = 1$ assignment. Its Γ_α width was calculated from the $\omega\gamma_{(\alpha,\gamma)}$ of Taggart et al. [24], $(8.7_{-3.7}^{+7.0}) \times 10^{-6}$ eV, and the $\omega\gamma_{(\alpha,n)}$ of Denker [66] $(42 \pm 5) \times 10^{-3}$ eV. Taking these in ratio yields the ratio of Γ_n and Γ_γ , yielding a ratio of 4828 ± 3920 . Given that Γ_n was measured the Γ_γ was found to be 1.1 ± 1 eV. The Γ_α was extracted directly from the value of Denker to be $63(7) \times 10^{-3}$ eV as the neutron width is large.

Where an experimentally informed Γ_γ could not be extracted from literature it was assumed to be 3.0 ± 1.5 eV. The 631 keV and the 660 keV energy $^{17}\text{O} + \alpha$ resonance widths, corresponding to the lower energy state in the doublet of ^{21}Ne at 7.981(1) MeV and the 8.009(10) MeV energy state respectively, have been previously measured. The widths of the 7.981(1) MeV energy state has been measured by Cohn and Fowler [100] and the 8.009(10) MeV can be seen in Mughabghab [97]. The ratios from Best et al. [65] were adopted for the neutron and gamma widths, hence the Γ_γ widths can be calculated for these two states. The more broadly adopted value of 3.0 ± 1.5 eV for the other Γ_γ was reached based on work of Longland et al. [101]. These Γ_γ values do represent an approximation.

The $\omega\gamma_{(\alpha,\gamma)}$ of the 634 keV energy $^{17}\text{O} + \alpha$ resonance was taken from Taggart et al. [24].

Measured State Energy (MeV)	Energy in $^{17}\text{O}+\alpha$ (keV)	Δl in $^{20}\text{Ne}+n$	Γ_n (eV)	Γ_α (eV)	$\omega\gamma_{(\alpha,n)}$ (μeV)
7.559(2)	211(2)	1	$3.4(26)\times 10^3$	4.8×10^{-16}	3.2×10^{-10}
7.601(2)	253(2)	4	0.4(7)	2.0×10^{-14}	3.4×10^{-8}
7.619(2)	271(2)	1	$2(3)\times 10^3$	6.9×10^{-13}	4.6×10^{-7}
7.820(3)	472(3)	1	$2.3(7)\times 10^3$	3.5×10^{-7}	0.23
7.981(1)	633(1) ^{***}	1	$6(2)\times 10^3$ **	9.0×10^{-5}	60
8.068(2) ^c	720(2)	1	$5.4(16)\times 10^3$	6.3×10^{-2} ^T	4.2×10^4 ^D
8.068(2)	720(2)	3	$1.4(18)\times 10^2$	7.9×10^{-4}	-
8.146(2)	798(2)	1	$1.8(6)\times 10^3$	4×10^{-3}	2.7×10^3
8.189(1) ^c	841(1)	1	$7(32)\times 10^3$	8.8×10^{-2} *	5.9×10^4

Table 11.1: Δl along with the extracted partial widths for both the neutron channel and α channel. * Γ_α from Best et al. [65]. **Partial width assumed equal to the total width from Cohn and Fowler [100] as the neutron partial width expected to dominate. ***The resonance energy of this state is shown as 631 keV as the state energy extracted of 7.981(1) MeV cannot be confirmed to be solely from this state and not partly its higher in energy doublet counterpart. ^TThis alpha width is informed by Taggart et al. [24] and Denker et al. [66]. ^DResonance strength from the thesis of Denker [66]. ^cThe energy of these states is assumed from literature as these are calibration states.

The ratio and magnitude of the Γ_γ and Γ_n was adopted from Best et al. [65]. This allowed calculation of Γ_α for this resonance. The adopted 3 eV Γ_n informed by from Best et al. [65] and Longland et al. [37] seems plausible given the state was not witnessed.

The total reaction rate found using the narrow resonance formula, the values presented in table 11.1 and those discussed earlier, can be seen as a function of temperature in figure 11.1.

The fractional contribution to the reaction rate can be seen in figure 11.2. Note how at 0.2 GK three key states contribute towards the rate. These are the 7.749 MeV, 7.820 MeV and the 7.619 MeV energy ^{21}Ne states, corresponding to $^{17}\text{O}+\alpha$ resonance energies of 401 keV, 472 keV and 271 keV respectively. The later of which was measured here in $^{20}\text{Ne}(d,p)$ and found to have its width dominated by Γ_n , as such the resonance strength and by extension the reaction rate is known to be dominated by the Γ_α .

The 7.749 MeV energy state was only seen at 40.1° and so was populated. However, the oxygen contamination caused significant difficulty in extracting other angles and hence its transferred l or width. It was assumed the 7.749 MeV had an $l=2$ transfer in $^{20}\text{Ne}(d,p)$. Hence, as in Best et al. [65], it is assumed an $l=0$ transfer in $^{17}\text{O}+\alpha$ took place, representing

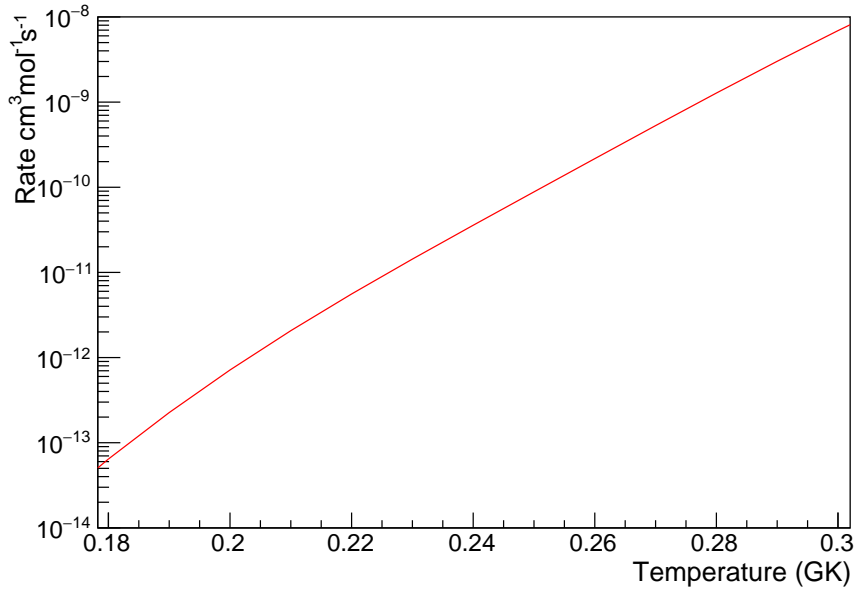


Figure 11.1: Total reaction rate from the narrow resonance equation as a function of temperature. At 0.2 GK the rate is $7(4) \times 10^{-13} \text{cm}^3 \text{s}^{-1} \text{mol}^{-1}$.

an upper limit on the Γ_α . As such it is expected the true contribution from the 7.749 MeV state will be equal to, or weaker than that presented here. The importance of this 401 keV resonance for the reaction rate of $^{17}\text{O}(\alpha, n)$ can be seen in figure 11.2.

Having approximated the individual resonance contributions to the reaction rate using the narrow resonance formula so the Monte Carlo reaction rate code [98] was run. The total reaction rate with temperature can be seen in table 11.2. Presented here are the medians as it suggests half of the simulated rates are lower and half higher. The mean rates are not presented as the Porter-Thomas distribution represents a skewed distribution and as such the median is a more representative measure.

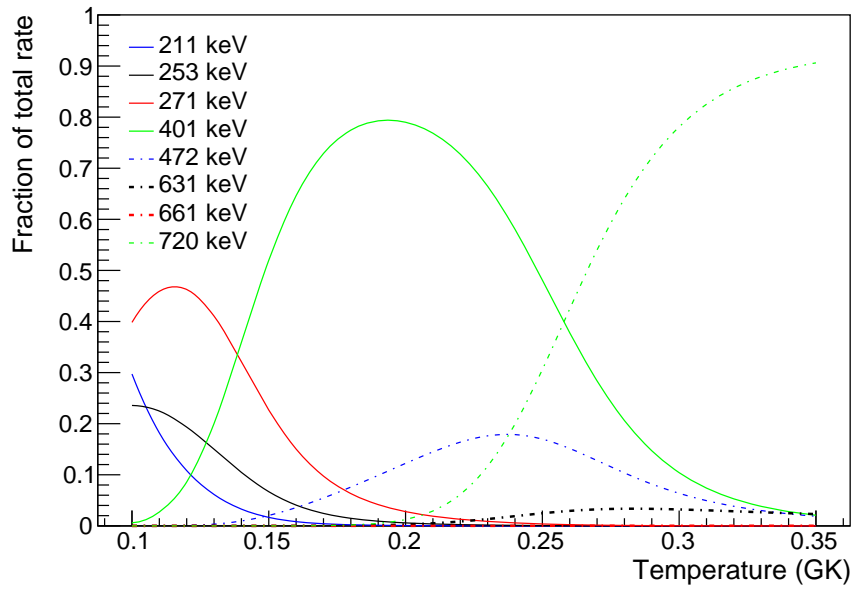


Figure 11.2: Fractional contribution to the reaction rate using the narrow resonance formula to calculate the rates. Note how at astrophysically important temperatures the 7.749 MeV dominates the rate. The fractional rate plot should only be considered complete up to 0.3 GK.

Temperature (GK)	Median reaction rate $\text{cm}^3\text{mol}^{-1}\text{s}^{-1}$	Lower limit reaction rate $\text{cm}^3\text{mol}^{-1}\text{s}^{-1}$	Upper limit reaction rate $\text{cm}^3\text{mol}^{-1}\text{s}^{-1}$
0.1	1.1×10^{-20}	3.8×10^{-21}	2.8×10^{-20}
0.125	4.1×10^{-18}	1.7×10^{-18}	9.4×10^{-18}
0.15	4.4×10^{-16}	1.7×10^{-16}	1.1×10^{-15}
0.175	1.8×10^{-14}	6.7×10^{-15}	5.6×10^{-14}
0.2	4.2×10^{-13}	1.5×10^{-13}	1.3×10^{-12}
0.225	6.1×10^{-12}	2.6×10^{-12}	1.6×10^{-11}
0.25	7.2×10^{-11}	4.4×10^{-11}	1.4×10^{-10}
0.275	6.1×10^{-12}	2.6×10^{-12}	1.6×10^{-11}
0.3	6.9×10^{-9}	5.9×10^{-9}	8.3×10^{-9}

Table 11.2: The total reaction rate for $^{17}\text{O}(\alpha,n)^{20}\text{Ne}$ extracted using the Monte Carlo reaction rate code [98].

Chapter 12

$^{20}\text{Ne}(\text{d,p})^{21}\text{Ne}$ Discussion

12.1 ^{21}Ne state properties

^{21}Ne state energies and spin parities measured here can be seen in table 12.1. Previous literature values used in this table were taken from NNDC [30] with individual states discussed in more detail through this section.

Table 12.2 shows the measured spin parities from $^{20}\text{Ne}(\text{d,p})$ and the equivalent transferred l in $^{17}\text{O}+\alpha$ alongside the values used by Best et al. [65] for their measurement and calculation of the $^{17}\text{O}(\alpha,\gamma)$ and $^{17}\text{O}(\alpha,\text{n})$ reaction rate ratio. Best noted that their J^π values measured may be contestable and that their results may be produced using other values of J^π .

Subtracting experimental ^{21}Ne state energies found in this work from those in the literature and combining both the experimental error and the error from literature results in the state energy residuals, which are seen in figure 12.1.

Figure 12.1 shows the experimental state energies found here are in good agreement with those values found in literature. Only significant disagreement is seen from the state at 7.648(2) MeV, which was measured here to be 7.656(2) MeV.

In general good agreement is made with previous literature. States of previous literature energy of 7.547(10) MeV, 7.648(2) MeV and 8.160(2) MeV can be seen to be in slight disagreement with the measurement carried out here.

6.609 MeV

The 6.609 MeV energy ^{21}Ne state was used as a calibration point due to its substantial measurement history and relatively high population in the focal plane spectra. In general it was also found to be well separated in the spectra. The final energy extracted for this state

Measured Energy (MeV)	Measured Spin Parity	Previous Energy (MeV) [30]	Previous Spin Parity [30]
-	$3/2^+, 5/2^+$	5.549(2)	$3/2^+$
6.609(1) ^c	$1/2^-, 3/2^-$	6.609(1)	-
7.4204(10) ^c	Inconclusive	7.4203(10)	($11/2^-$)
7.470(1)	-	7.465(10)	($1/2, 3/2$) ⁻
7.559(2)	$1/2^-, 3/2^-$	7.547(10)	-
7.601(2)	$7/2^+, 9/2^+$	7.600(5)	-
7.619(2)	$1/2^-, 3/2^-$	7.628(10)	$3/2^-$
7.656(2)	-	7.648(2)	($7/2^+$)
7.749(1)	-	7.750(10)	-
7.820(3)	$1/2^-, 3/2^-$	7.810(10)	-
7.981(1) [*]	-	7.980(10)	$3/2^-$
-	- or ≥ 5	7.9821(6)	($7/2, 11/2$) ⁺
8.068(2) ^c	$1/2^-, 3/2^-$	8.069(2)	($3/2^+$)
8.146(2)	$1/2^-, 3/2^-$	8.146(2)	($3/2^+$)
-	- or ≥ 5	8.155(1)	($9/2$) ⁺
8.163(2)	-	8.160(2)	($5/2^+$)
8.189(1) ^c	$1/2^-, 3/2^-$	8.189(2)	($3/2^-$)

Table 12.1: ^{21}Ne state energies, spins and parities measured here and those from previous accepted literature. ^{*}This state energy likely has contribution from peaks in an unresolvable doublet. ^cThe energy of these states is assumed from literature as these are calibration states, any difference in energy from literature is from the calibration fit.

from the calibration was 6609.0(4) keV. At the time of writing NNDC [30] shows no spin parity, however in 1979 Fortune et al. [89] refer to a private communication of Hoffmann, Betz and Röpke suggesting a $\frac{3}{2}^+$ or less likely a $\frac{5}{2}^+$. It must be noted in 1970 Howard et al. [73] measured the state to have a spin parity of $\frac{3}{2}^+$ or $\frac{5}{2}^+$, interestingly here however it was found to have a spin parity of either a $\frac{1}{2}^-$ or $\frac{3}{2}^-$ with confidence. The DWBA [36] calculation matched the experimental differential cross-section data points well. The difference in transferred l assignment is likely due to improved optical potentials and the use of a more modern code with an increased number of potentials, FRESKO [36]. The model described in Howard [73] suggests an optical model with two potentials, one each for the proton and deuteron. The model used in this work considers the $^{20}\text{Ne}+^2\text{H}$, $^{21}\text{Ne}+p$, $^{20}\text{Ne}+n$, $n+p$, $^{20}\text{Ne}+p$, potentials and it is expected that the calculated differential cross-sections here are more reliable.

Figure 12.2 shows the measured differential cross-sections from this work and that of Howard et al. [73] for the 6.609 MeV energy state. The difference in experimentally extracted

Measured Energy (MeV)	Measured Δl in $^{17}\text{O}+\alpha$	Measured Δl in $^{20}\text{Ne}+n$	Literature Δl used in $^{17}\text{O}+\alpha$ Best et al. [65]	Literature [65] Δl used in $^{20}\text{Ne}+n$ equivalent
7.4204(10) ^c	Inconclusive	Inconclusive	2	0, 4
7.470(1)	-	-	1	1, 3
7.559(2)	1	1	0	2
7.601(2)	2	4	0	2
7.619(2)	1	1	1	1, 3
7.656(2)	-	-	0	2
7.749(1)	-	-	0	2
7.820(3)	1	1	0	2
7.9609(13) ^a	-	-	3	5
7.981(1) ^b	-	-	1	1, 3
7.9821(6) ^b	-	-	2	0, 4
8.068(2) ^c	1	1	2*	2*
8.146(2)	1	1	2*	2*
8.163(2)	-	-	0, 2*	2*
8.189(1) ^c	1	1	1*	1*

Table 12.2: ^{21}Ne state energies, spins and parities measured here and those from previous accepted literature.

^aState measurement could not be confirmed as being measured here and this energy is from NNDC, [30] including the measurement of Thummerer et al.

^bIn literature these states are represented as the 7.980(10) MeV and the 7.9821(6) MeV states respectively [102], detector resolution here was insufficient to separate these peaks.

^cThe energy of these states is assumed from literature as these are calibration states, any difference in energy from literature is from the calibration fit.

*Measured by Best et al. [65], however their results could be reproduced by other transferred l values.

differential cross-sections between the data set is primarily due to the ~ 2.4 MeV difference in beam energy; confirmed using FRESKO, which at the Howard et al. energy is still suggestive of an $l=1$ transfer.

7.420 MeV

The 7.420 MeV energy state was a calibration state and so the energy was based on the previous literature value of 7.420.3(10) MeV [30]. The calibration yielded an energy of 7.4204(10) MeV showing self consistency. Previous literature suggests the spin parity of

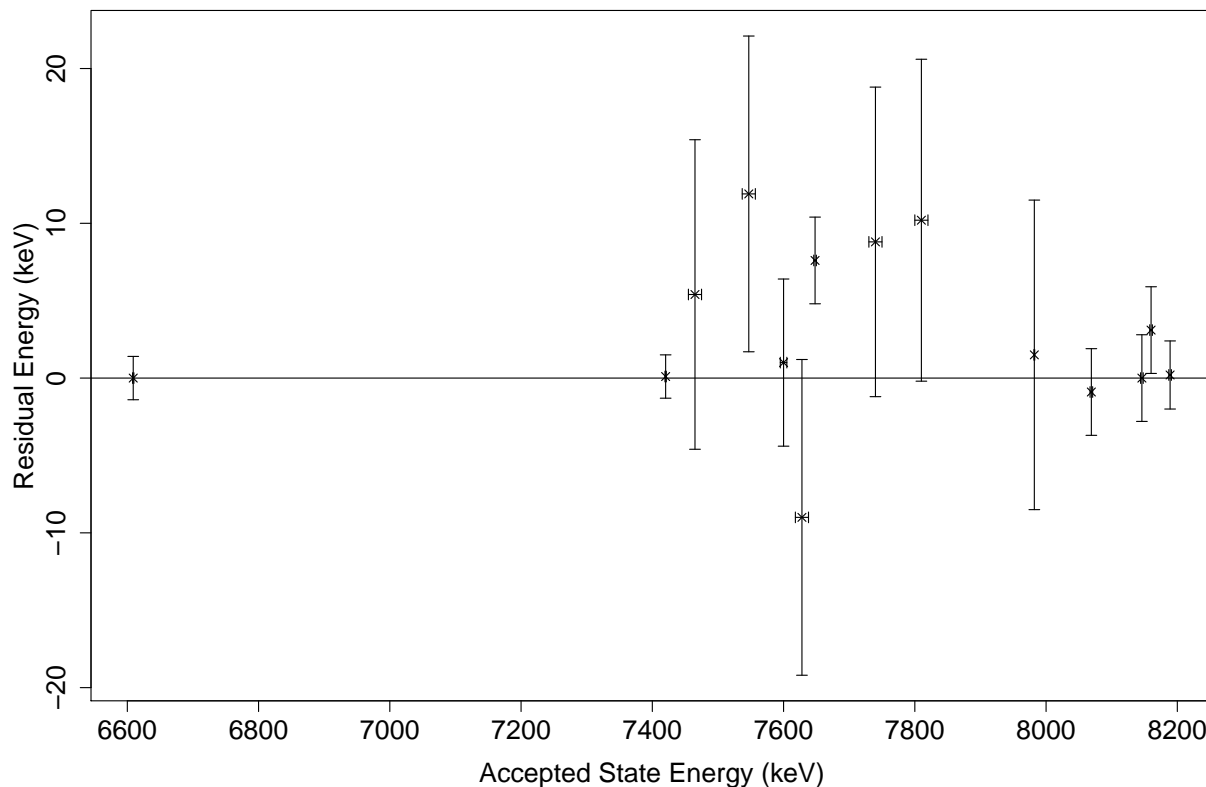


Figure 12.1: Residuals of energies for each measured state. Weighted average across all angles. Uncertainties represent the combination of uncertainties from this work and also the literature uncertainties.

this state may be $\frac{11}{2}^-$ [103] which was inferred by comparison with the $\frac{13}{2}^-$ 9.401 MeV energy ^{21}Ne state, studied through the detection of gammas from the $^{18}\text{O}(\alpha, n\gamma)$ reaction. No spin parity could be extracted here. Despite double checking both the identification of peaks and the quality of fits on numerous occasions, the differential cross-sections do not match those as calculated using the FRESKO [36] DWBA code. It is suggested that the population of this state was potentially through a compound reaction. The identity of this peak has been investigated as it would be unexpected that a higher spin state would be strongly populated in $^{20}\text{Ne}(d,p)$, this calls into question the suspected $\frac{7}{2}^+$ or $\frac{11}{2}^-$ spin parity assignment of the state. Or this is a state exhibiting a cluster like structure.

The confidence in the correct identification of this state arose from the alignment of the 3 strongly populated $^{12}\text{C}(d,p)$ peaks. The 6.609 MeV state is shown strongly populated in literature [91] including another $^{20}\text{Ne}(d,p)$ measurement [75]. The centroids of other states

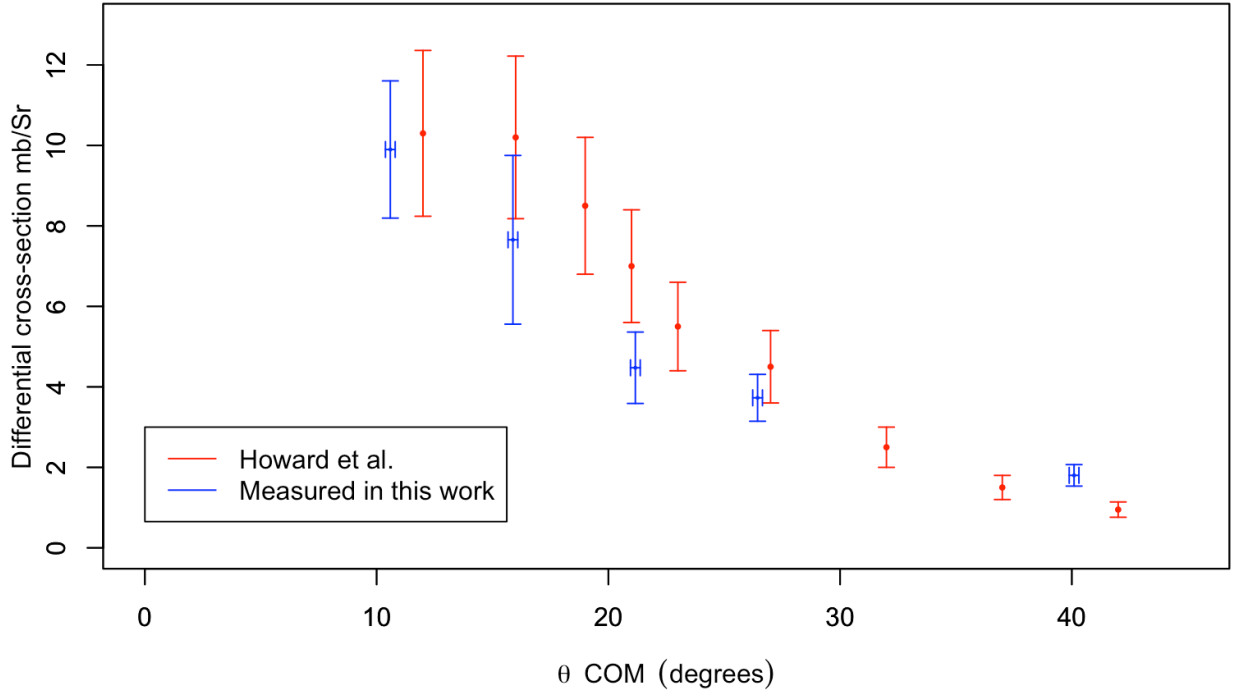


Figure 12.2: A comparison of the differential cross-section measurements for the 6.609 MeV energy state from Howard et al. [73] compared with those measured in this work. Note how the peak is at more forward angles in the data measured here. Hence the different assignment of transferred l from previous literature.

with matching characteristics to those seen in literature were correctly predicted by the focal plane plotter calculation, using the 7.420 MeV, 6.609 MeV ^{21}Ne states and the three ^{13}C states. This included the width of the 8.069 MeV with a width seen here of 6(1) keV compared to that of 8(3) keV in literature [30]. Furthermore the broad 5.084 MeV energy ^{17}O state is correctly predicted using the calibration including this 7.420 MeV state.

7.470 MeV

The measurement of the 7.470(1) MeV energy state shows agreement with the literature accepted energy of 7.465(10) [30]. The most recent measurement of Meirle et al. [104] in 1981 measured the state energy to be 7.47 MeV, with Hallock et al. [87] studying $^{12}\text{C}(^{13}\text{C}, ^{21}\text{Ne})^4\text{He}$ and finding the state to have an energy of 7.465(10) MeV and earlier Hinds and Middleton [91] found it to be at 7.461(10) MeV. This state was only measured at 40.1° as such there was no spin parity extracted for the state to confirm the suspected $\frac{1}{2}^-$ or $\frac{3}{2}^-$ spin parity of the state by Meirle et al. [104].

7.559 MeV

The previous 7.547(10) MeV energy state measurement is from Hinds and Middleton from 1959 [91]. The reaction used a solid, thin target of ^{19}F , performing the $^{19}\text{F}(^3\text{He},p)^{21}\text{Ne}$ reaction. The ^3He beam energy has a 10 keV uncertainty and all states had 10 keV or greater energy uncertainty. Here we measured a state of 7.559(2) MeV in energy and saw it at all 5 angles. The measurement has yielded a spin parity of this state of $\frac{1}{2}^-$ or $\frac{3}{2}^-$, which was previously unassigned by literature. The neutron partial width for this state extracted here was 3.4 ± 2.6 keV.

7.601 MeV and 7.619 MeV

In literature the width of the 7.628(10) MeV state has been concluded to have a width of 14 keV [97], here the state was measured as much narrower, just above the narrow resonance width at 2 ± 2 keV. It is hypothesised that the 14 keV width was a combination of both the 7.601(2) MeV and the 7.628 MeV states with a significant energy shift. Or alternatively, however very unlikely the 7.628 MeV measured elsewhere is a doublet and here only one of these peaks has been measured, at 7.619 MeV, due to its larger neutron partial width.

The total angular momentum of the 7.628 MeV state is currently accepted to be $\frac{3}{2}^-$. It is not possible here to conclusively confirm this, however the DWBA fits here as seen in figure 10.34 suggest the transferred l value could be 1 or 3, supporting most the former. The previously accepted spin parity for the 7.628(10) MeV state of $\frac{3}{2}^-$ [97] would not be contradicted by our DWBA measurements here and suggests an $l=1$ transfer in the $^{20}\text{Ne}(d,p)$ reaction. Assuming the previous spin-parity of $\frac{3}{2}^-$ so the neutron partial width is 1.8 ± 3.3 keV, hence an upper limit can be placed on the width of 5.1 keV using the neutron partial width alone.

The energy measured for the 7.601(2) MeV energy state was previously accepted in literature to be 7.600(5) MeV [30] and so our result is in agreement. In 1959 Hinds and Middleton [91] measured this state to be 7.597(10) MeV and Rolfs et al. [86] found it to have an energy of 7.600(5) MeV.

No spin-parity assignment currently exists for the 7.601(2) MeV energy state, however, during this measurement it can be concluded that the modulus of $j \geq 7/2$. No conclusive spin parity assignment can however occur due to agreement between several transferred l value DWBA calculations, but an $l=4$ transfer is suggested and assumed for the rate calculations. Representing a maximum contribution to the $^{17}\text{O}(\alpha,n)$ reaction rate compared to other matching transferred l values. With this transfer the partial width would be 0.43 ± 0.22 eV,

implying the state has minimal contribution in the $^{17}\text{O}(\alpha,n)$ reaction rate.

7.656 MeV

The most recent measurement of 7.648(2) MeV state was in 2010 by Freer et al. [105] using $^{12}\text{C}(^{13}\text{C},^{21}\text{Ne})^4\text{He}$ yielding an energy of 7.65(8) MeV. Prior to this the 7.648 MeV energy state was witnessed by Hinds and Middleton in 1959 [91] it was measured to be 7.644(10) MeV. Rolfs et al. [86] then measured this state to be 7.655(5) MeV which would be in agreement with the energy of 7.656(2) MeV here.

Whilst not in agreement with the value quoted on ENSDF [30] it can be seen multiple measurements are in agreement with our measurement of this states energy. The state was only witnessed at 40.1° , due to the significantly higher beam on target at this angle. Due to this single measurement no differential cross-section function was extracted.

7.749 MeV

In previous literature the 7.749(1) MeV state measured here is accepted to be 7.750(10) MeV [30], from Hinds and Middleton [91] and 7.750(10) MeV from Endt [88]. This state was only measured at 40.1° , but its energy however is in agreement with previous literature. The effect of this energy measurement on the reaction rate uncertainty can be seen in figure 12.3. Note the significant reduction in fractional uncertainty on the reaction rate. Due to the single measurement of this state no spin parity could be assigned here. The value estimated in literature [65] for the $^{20}\text{Ne}+n$ transferred l was adopted and assumed to be 2, hence in $^{17}\text{O}+\alpha$ an l transfer of 0.

7.820 MeV

The 7.820 MeV state was also seen by Hinds and Middleton where it was measured to be 7.805(10) MeV. The 7.810 MeV state was then measured by Hallock et al. in 1975 [87]. Their measurement used $^{12}\text{C}(^{13}\text{C},^{21}\text{Ne})^4\text{He}$ and yielded a state energy of 7.814(10) MeV which is in good agreement with this measurement. The measurement of this state at 4 angles gave a spin parity assignment of $\frac{1}{2}^-$ or $\frac{3}{2}^-$, which was previously unassigned. The neutron partial width was found to be 2.3 ± 0.7 keV. The $l=0$ transfer agreed with the FRESKO calculation, however it suggests a partial width of 28 ± 5 keV. Much broader than the width of the state seen in the spectra and as such not physical. An $l=1$ transfer has been adopted in the rate calculations for this reason.

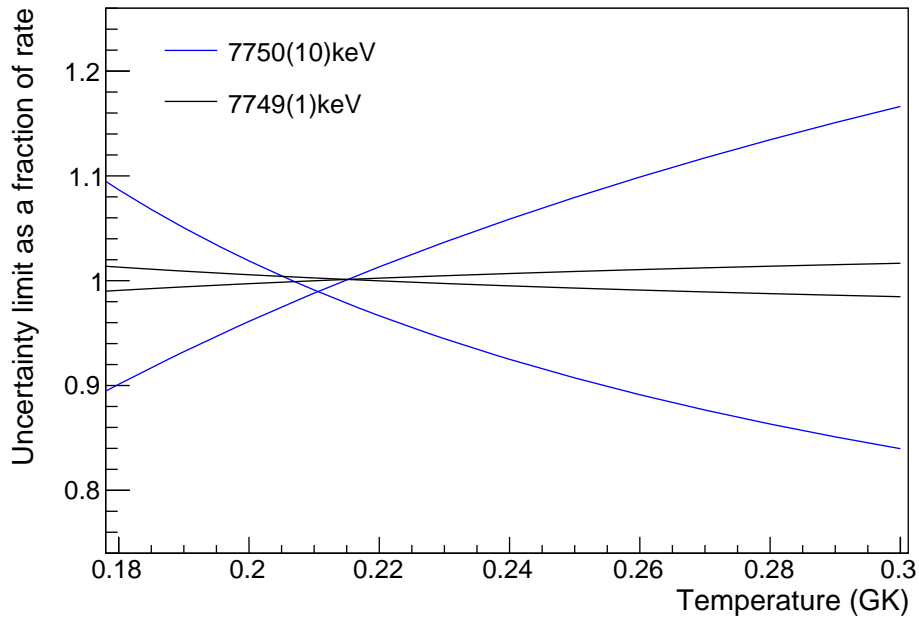


Figure 12.3: The effect on the reaction rate uncertainty of the 7.749 MeV energy state with its new reduced uncertainty. Black: the literature [88] rate at 7.750 MeV taken in ratio with the rates at ± 10 keV. Red: the reaction rate from the narrow resonance formula at 7.749 MeV taken in ratio with the rates at ± 1 keV. Where these curves cross is where the upper and lower limits have equal rate. Note the significant fractional uncertainty reduction in reaction rate achieved.

7.961 MeV

Due to the fluctuations in the centroid energy in the focal plane spectra what was initially believed to be the 7.961 MeV fits were discarded. Their drift in energy suggests that the peak fitted was not a ^{21}Ne peak. It should be noted that at 40.1° the peak centroid was located at 7.963(2) MeV and as such it is possible this was the 7.961 MeV state, however due to the peaks at 10.6° and 21.2° and the trend which contains the 40.1° measurement the energy measurement here was disregarded.

7.981 MeV

Measured at three angles here to be at 7.981(1) MeV in energy this measurement contains both the literature accepted energy states of 7.9821(6) MeV [30], with which the energy measurement here is in agreement and also with the 7.980(10) MeV state, also in agreement.

The 7.9821(6) MeV energy state has been measured multiple times including by Hallock

et al. [87] at 7.982(10) MeV, Andritsopoulos et al. [106] who measured the state to have an energy of 7.9830(28) MeV and Hoffmann et al. [103] who had it at an energy of 7.981 MeV. Hoffmann et al. found the state to have spin parity of $\frac{11}{2}^+$ or $\frac{7}{2}^+$. Given the identified possible angular momentum transfers using the three measurements of the state, if the measured state here is dominated by the 7.9821(6) MeV energy state then this is likely a $\frac{11}{2}^+$. The previous identified spin parity of $\frac{7}{2}^+$ would not align with the possible fitted DWBA calculations performed here. However, it cannot be concluded that this was a pure transfer reaction as the differential cross-section was flat and the high transfer of l required suggests the measurement here was not dominated by this state.

The 7.980(10) MeV state has a literature accepted spin parity from Cohn and Fowler [100] of $\frac{3}{2}^-$, implying an $l=1$ transfer. The measurement of Cohn and Fowler of 1958 [100] was a neutron measurement conducted by bombarding a neon gas target with a neutron beam, resulting in a spectra with a 10 keV resolution. The 7.980 MeV energy ^{21}Ne state represents 1.28 MeV neutron energy, which lies close to the 1.31 MeV energy neutron peak seen in their spectra. Whilst these two resonances appear well separated in their spectra it must be noted the four differential cross-section data points are not in perfect agreement with their model, neither is the data on-trend with the proposed fit.

Due to the decreased angular momentum barrier when compared with an $l=6$ transfer it is expected the state here is dominated by the 7.980(10) MeV energy state, assuming it is of lower spin and hence lower l transfer in $^{20}\text{Ne}+n$. It is therefore not possible to assume the angular distribution measured here is solely that of a single one of these two states but likely a product of the two and dominated by the 7.980(10) MeV. Figure 10.36 shows the form of the differential cross-sections and one could argue that the expected $l=1$ transfer required to form the $\frac{3}{2}^-$ of the 7.980(10) energy state we would expect a much lower 40.1° differential cross-section. Whilst an $l=0$ dominant transfer forming a $\frac{1}{2}^+$ state is much more likely and in perfect agreement with the FRESKO calculation data here, it would produce a broad state and the peaks fitted here are narrow. An $l=1$ transfer in $^{20}\text{Ne}+n$ was hence adopted with a neutron partial width of 6 ± 2 keV, assuming the total width from Cohn and Fowler [100].

8.068 MeV

In 2013 Best et al. [65] found this state to be at 8.069(2) MeV and the spin parity to be $\frac{3}{2}^+$. The measurement history of this state and its proximity to the Gamow window led to its use as a calibration state. Here its energy was found to be 8.068(1) MeV from the calibration. The difference is representative of both the peak uncertainty and the calibration uncertainty

combined. However, to have spin parity agreement with Best et al. the measurement here would require an l transfer of 2. It is found that an $l=1$ transfer DWBA calculation fits the data most effectively. A neutron partial width of 5.3 ± 1.6 keV was extracted.

Best et al. [65] does explain that some of their R-matrix fits can be reproduced using different spin-parities and that only the cross-sections and resonance energies should be considered definitive, hence the disagreement between the measurement conducted here is not of concern.

Agreement was seen between FRESKO and the differential cross-section plots for an $l=3$ transfer. This transfer gave a partial width upper limit of 0.32 keV. In $^{17}\text{O}+\alpha$ the transfer is the same, $l=1$, for a transfer of $l=1$ or 3 in $^{20}\text{Ne}+n$. An $l=1$ transfer in $^{20}\text{Ne}+n$ is adopted as the total width of literature [30] of 8(3) keV, also in agreement with the width measured here of 6(1) keV, suggests the transfer is lower to yield such a width. The extracted neutron width was 5.4(16) keV for an $l=1$ transfer in $^{20}\text{Ne}+n$, showing agreement with the focal plane width.

8.146 MeV

The 8.146(1) MeV energy as measured here is in agreement with the measurement of Best et al. [65] who measured this state at 8.146(2) MeV. As with the 8.068(1) MeV energy state Best et al. found the state to have a spin parity of $\frac{3}{2}^+$. The measurement here finds that it was likely an $l=1$ transfer has occurred, resulting in a partial width of 1.8 ± 0.6 keV and a spin parity of either $\frac{1}{2}^-$ or $\frac{3}{2}^-$. As the 8.146 MeV state was seen as narrow so the $l=0$ transfer, where the differential cross-section data was also in agreement with the FRESKO calculation, is not expected to have occurred.

8.163 MeV

Best et al. [65] measured this state at 8.160(2) MeV. Here we measured this state at a single angle to be 8.163(1) MeV, showing agreement within error. Due to the measurement only occurring at a single angle so it was not possible to extract a transferred l value for this state.

8.189 MeV

Best et al. [65] measured this state to be 8.189(2) MeV, with a previous literature value of 8.186(10) MeV [88]. Their spin parity assignment of $\frac{3}{2}^-$ must be noted as a possible value and unconfirmed, they state their results could potentially be reproduced with other J^π . Here we are able to confirm the transferred l in $^{20}\text{Ne}(d,p)$ was 1 and as such the state has a spin parity

of either $\frac{1}{2}^-$ or $\frac{3}{2}^-$. The neutron partial width extracted was an upper limit of 40 keV, which in reality is much larger than the focal plane width and therefore uninformative. Its location ~ 200 keV above the Gamow window and narrow total width from the focal plane detector implies it would have minimal impact on the rate and as such the neutron partial width is of little concern and is likely such a large upper limit due to significant extrapolation beyond the neutron threshold.

12.2 Reaction rate

The contribution to the total reaction rate was found using both the narrow resonance assumption for the rate, as in eqn. 2.16 and using a Monte Carlo simulation. The narrow resonance method appears to have predicted which states are important well when compared with the output of the Monte Carlo reaction code. The individual resonance contributions from the Monte Carlo reaction rate code can be seen in figure 12.4 for the $^{17}\text{O}(\alpha,n)$ reaction rate. Good agreement is seen between which states are of key importance between the Monte Carlo code reaction rate and the narrow resonance formula method. Note how at astrophysically important energies ~ 0.2 GK the same three states can be seen as important with large uncertainties. The uncertainties on the Monte Carlo reaction rate ratios originate from the use of the Wigner limits for the alpha partial widths.

Figure 12.5 shows the fractional contribution to the $^{17}\text{O}(\alpha,\gamma)$ reaction rate of each resonance with a significant contribution. Note the dominance of the 308 keV energy $^{17}\text{O}+\alpha$ resonance corresponding to the 7.656(2) MeV energy state in ^{21}Ne at 0.2 GK. The 253 keV resonance, corresponding to the 7.601(2) MeV ^{21}Ne state also contributes significantly and has been measured here in $^{20}\text{Ne}(d,p)$, extracting both a transferred l and a neutron partial width, which showed this state to have a narrower neutron partial width than initially anticipated by Best et al. [65]. This weakly populated state has an extracted neutron partial width with an upper limit of 1.1 eV with an expectation of 0.4 eV. Using the assumed 3 eV Γ_γ so the ratio of Γ_γ / Γ_n is significantly different to the 0.1 proposed by Best et al. [65]. This was found to be one of the contributors behind the change in the $^{17}\text{O}(\alpha,\gamma)$ reaction rate ratio.

The 810 keV resonance, corresponding to 8.158 MeV ^{21}Ne state as in Taggart et al. [24] is referred to on NNDC [30] as the 8.155(1) MeV energy ^{21}Ne state. This state is seen to dominate the $^{17}\text{O}(\alpha,\gamma)$ reaction rate at ~ 0.3 GK. The $\omega_{\gamma(\alpha,\gamma)}$ of this state is extracted from Taggart et al. [24] where it was measured to have a value of $5.4(8) \times 10^{-3}$ eV.

For the Monte Carlo code, where states had a width greater than 1 keV integration was

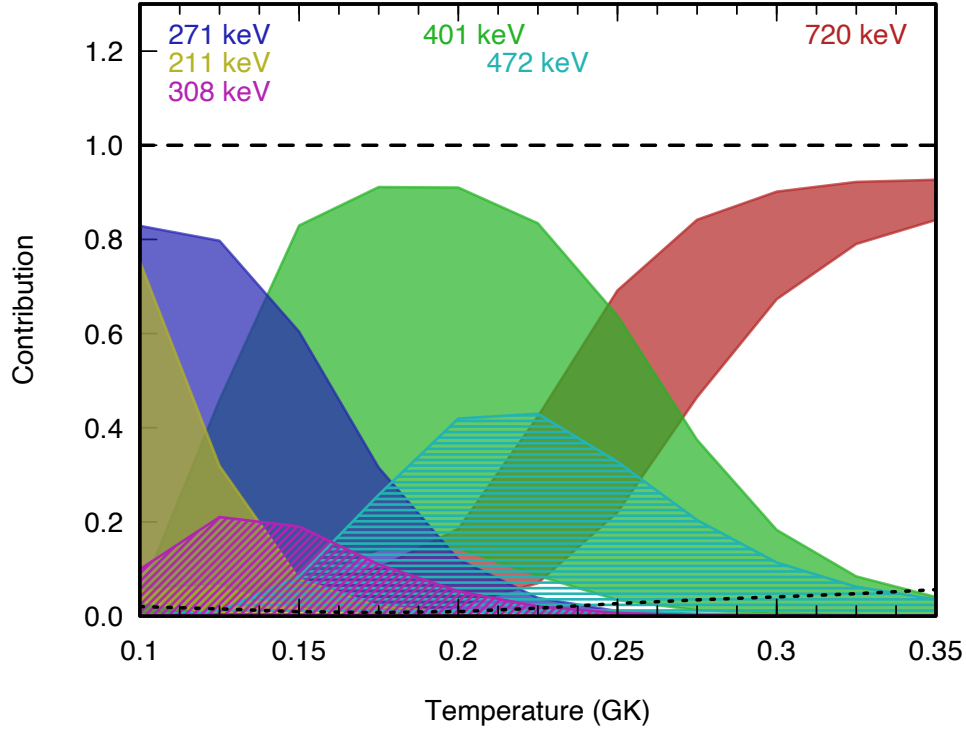


Figure 12.4: Fractional contribution of each state to the $^{17}\text{O}(\alpha,n)$ reaction rate, calculated using the Monte Carlo code. Note the agreement between this method and the narrow resonance assumption rate calculation. Higher energy resonances may not be included at higher temperatures above >0.3 GK, however from an astrophysics perspective at 0.2 GK all known states are accounted for.

conducted, this was likely the key source of difference between the Monte Carlo method and the narrow resonance formula method. The code also takes into account the other open channels, so the neutron and γ channels were considered simultaneously using the Monte Carlo method, allowing an extraction of a median. For these reasons and its ability to quantify uncertainties so the Monte Carlo code outputs were considered primarily when comparing to literature.

The $^{17}\text{O}(\alpha,n)$ rate can be seen in figure 12.6 to have, in general, a lower median than that predicted by Best et al. [65] at astrophysically important temperatures. However, at these temperatures 0.2-0.3 GK the rate is within agreement. This is not surprising given the rate is dominated by the $^{17}\text{O}+\alpha$ 401 keV energy resonance, corresponding to the 7.749 MeV energy ^{21}Ne state, for which only an energy has been extracted here. This rate does however represent a constrained value with uncertainties.

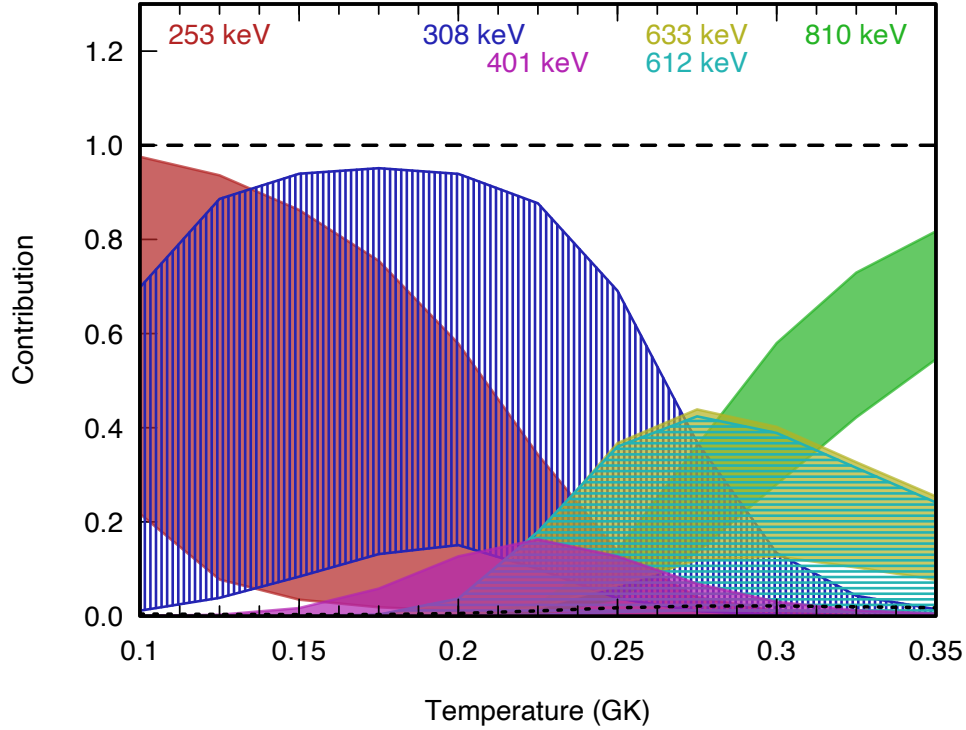


Figure 12.5: Fractional contribution to the $^{17}\text{O}(\alpha,\gamma)$ reaction rate, calculated using the Monte Carlo code. Higher energy resonances may not be included at temperatures above >0.3 GK, however from an astrophysics perspective, at 0.2 GK, all known states are accounted for.

The $^{17}\text{O}(\alpha,n)^{20}\text{Ne}/^{17}\text{O}(\alpha,\gamma)^{21}\text{Ne}$ reaction rate ratio measured here compared to that of Best et al. [65] can be seen in figure 12.7. Note how there is agreement within the extremity of the errors. A peak in reaction rate in both the upper uncertainty and the median can be seen at 0.2-0.25 GK. Figure 12.8 shows the ratio of reaction rates measured here divided by the same ratio of Best et al [65].

Comparison of figure 12.7 with figures 12.4 and 12.5 allows identification of the key contributing states at astrophysically relevant temperatures. Inspection of figure 12.6 suggests that the cause of this peak in reaction rate ratio is not the $^{17}\text{O}(\alpha,n)$ reaction rate, but the $^{17}\text{O}(\alpha,\gamma)$, due to a smooth consistent $^{17}\text{O}(\alpha,n)$ reaction rate. The significant difference in the $^{17}\text{O}(\alpha,\gamma)$ reaction rate relative to that of Best et al. [65] can be seen in figure 12.9. Further thought on the dominant resonances was therefore given.

Best et al. [65] assumed the 308 keV $^{17}\text{O}+\alpha$ resonance or equivalently the 7.656(2) MeV energy ^{21}Ne state has a spin parity of $\frac{5}{2}^+$. Literature [30] suggests a spin parity of $\frac{7}{2}^+$ may

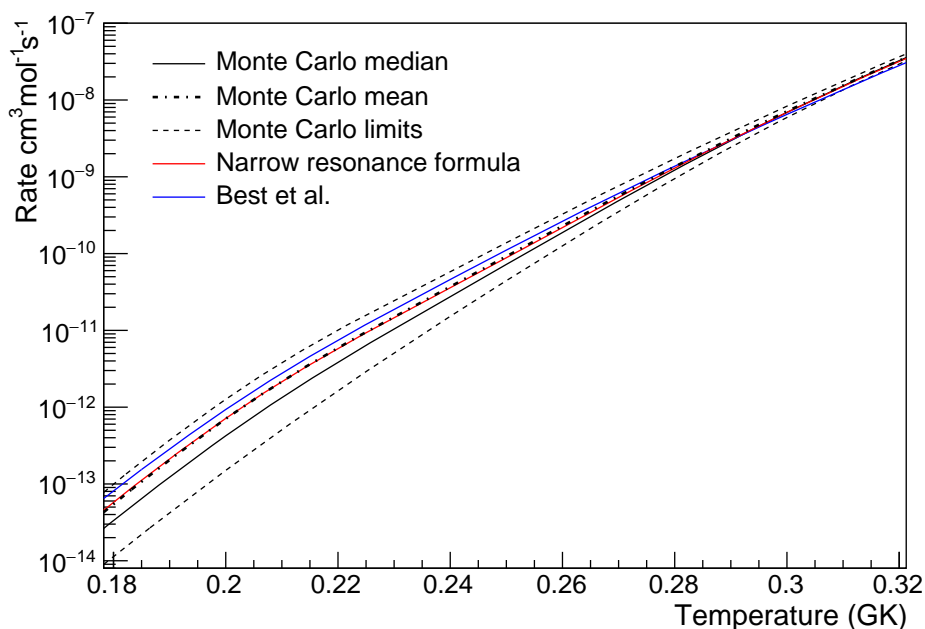


Figure 12.6: The effect of the measurement here on the $^{17}\text{O}(\alpha,n)$ total median reaction rate relative to Best et al. [65]. The dashed lines represent the upper and lower uncertainties on the rate extracted here. Note the good agreement between the Monte Carlo mean and the narrow resonance formula method.

be possible and not $\frac{5}{2}^+$. Best et al. [65] also confirm that the state is a $\frac{7}{2}^+$ and possibly a $\frac{5}{2}^+$ in their table where the values are extracted from Endt [88] and also Firestone [107]. Firestone later dropped the $\frac{5}{2}^+$ as a potential assignment [30]. In this work we assumed a $\frac{7}{2}^+$ assignment as in Firestone 2015 [30]. This assignment requires an $l=2$ transfer in $^{17}\text{O}+\alpha$. The effect on the $^{17}\text{O}(\alpha,n)^{20}\text{Ne}/^{17}\text{O}(\alpha,\gamma)^{21}\text{Ne}$ reaction rate ratio of this state being $\frac{5}{2}^+$ can be seen in figure 12.7. At 0.2 GK this yields a reduction in the $^{17}\text{O}(\alpha,n)^{20}\text{Ne}/^{17}\text{O}(\alpha,\gamma)^{21}\text{Ne}$ reaction rate ratio of a factor ~ 5 using the narrow resonance formula. This shows the rate is highly dependent upon the J^π of the 308 keV $^{17}\text{O}+\alpha$ resonance.

At 0.2 GK the reaction rate ratio of $^{17}\text{O}(\alpha,n)^{20}\text{Ne}/^{17}\text{O}(\alpha,\gamma)^{21}\text{Ne}$ measured by Best et al. [65] was 3.8, here we find a ratio of 31_{-28}^{+287} . This implies a significant decrease in the effectiveness of ^{16}O as a neutron poison, by a factor of 8_{-7}^{+76} when compared to the value of Best et al.. This would imply a significant increase in the neutrons available for the s-process. Hence the s-process would proceed at a greater rate and an increase in heavy element production is therefore expected.

The change suggested in Taggart et al. [24] from the Best et al. [65] was around a factor of 10 decrease in $^{17}\text{O}(\alpha,\gamma)^{21}\text{Ne}$. This would have implied a factor of 10 increase in

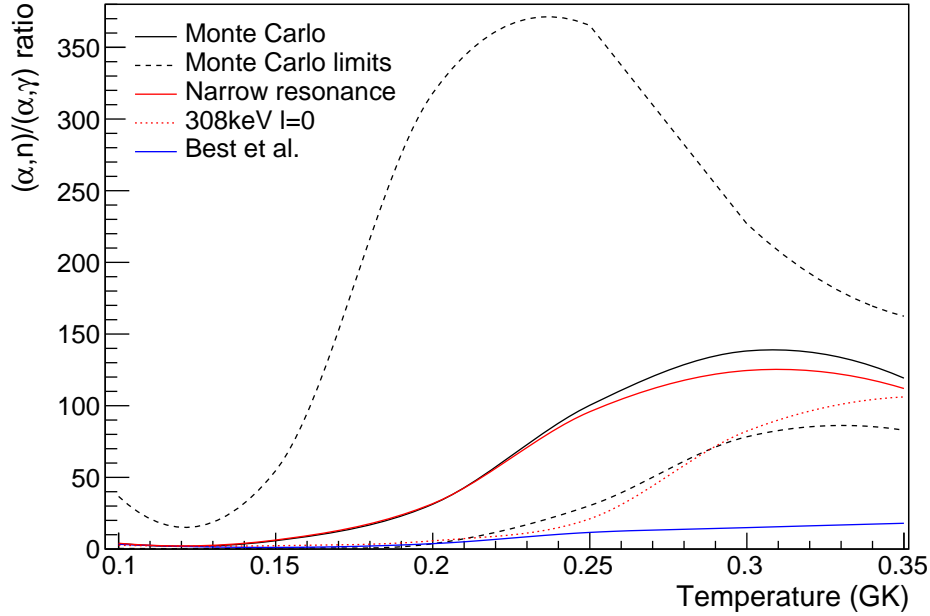


Figure 12.7: The ratio of the $^{17}\text{O}(\alpha, n)^{20}\text{Ne}/^{17}\text{O}(\alpha, \gamma)^{21}\text{Ne}$ as a function of temperature. The dashed lines represent the upper and lower uncertainties on the Monte Carlo rate ratio, the median of which is the solid black line, the red line represents the narrow resonance formula rate calculation, the blue line the ratio from Best et al. [65] and the finely dashed red line represents the narrow resonance ratio if the 308 keV resonance was a $5/2+$.

$^{17}\text{O}(\alpha, n)^{20}\text{Ne}/^{17}\text{O}(\alpha, \gamma)^{21}\text{Ne}$ reaction rate ratio, which aligns with the work completed here, where a factor of 8_{-7}^{+76} increase on the Best et al. [65] value is suggested. Figure 12.10, from Taggart et al. [24], shows the effect on heavy element production using the Best et al. rate compared to that of Taggart et al.. The production of s-process element given the results extracted here is a little lower than that of the red line, depicting the factor of 10 increase in the Best et al. [65] $^{17}\text{O}(\alpha, n)^{20}\text{Ne}/^{17}\text{O}(\alpha, \gamma)^{21}\text{Ne}$ reaction rate ratio. The difference between the ratio suggested by Taggart et al. [24] and the measurement here is the cumulative effect of the state properties measured here.

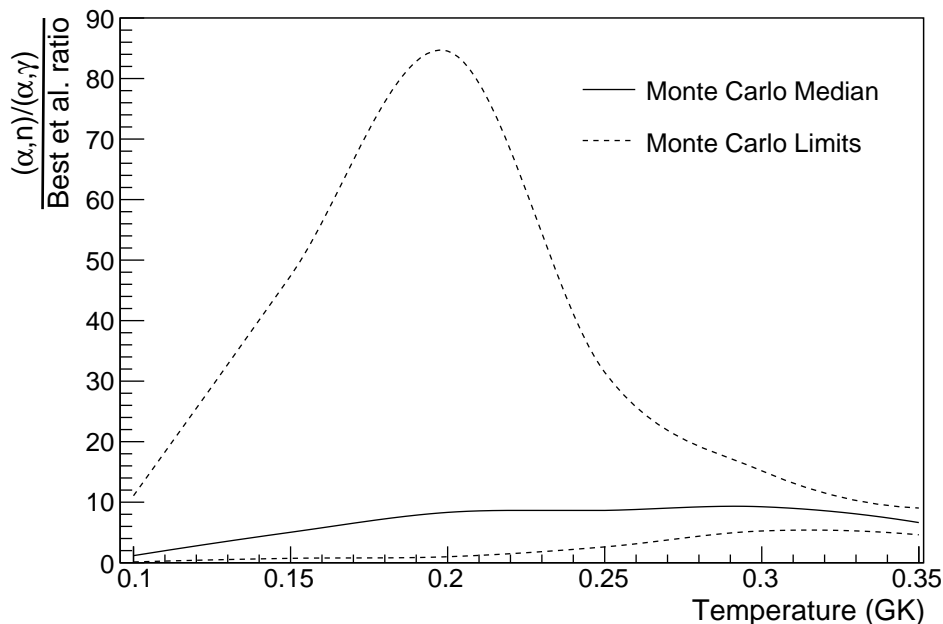


Figure 12.8: The Monte Carlo ratio of the $^{17}\text{O}(\alpha,n)^{20}\text{Ne}/^{17}\text{O}(\alpha,\gamma)^{21}\text{Ne}$ reaction rate as a ratio with $^{17}\text{O}(\alpha,n)^{20}\text{Ne}/^{17}\text{O}(\alpha,\gamma)^{21}\text{Ne}$ of Best et al. [65]. The dashed lines represent the upper and lower uncertainties on the ratio.

12.3 Further work

The $^{17}\text{O}(\alpha,\gamma)^{21}\text{Ne}$ has been shown to be heavily dependent upon the spin parity of the 7.656(2) MeV energy state in ^{21}Ne and such confirmation of this state's spin parity would yield a dramatic reduction in uncertainty in the $^{17}\text{O}(\alpha,\gamma)^{21}\text{Ne}$ reaction rate. It is in part because of this we see such a large difference between the $^{17}\text{O}(\alpha,n)^{20}\text{Ne}/^{17}\text{O}(\alpha,\gamma)^{21}\text{Ne}$ reaction rate ratio of Best et al. [65] and the measurement here.

The ^{21}Ne 7.749(1) MeV state, corresponding to an $^{17}\text{O}+\alpha$ resonance energy of 401(1) keV is expected to dominate the reaction rate. Effective measurement of this state would require removal of the broad oxygen state from the region. This would allow extraction of this states spin parity and as such reduce the uncertainty on this states reaction rate. A change in l transfer in $^{17}\text{O}+\alpha$ would have a dramatic effect on the reaction rate, as shown in figure 12.11 a 71% drop in the reaction rate for this state would occur at 0.2 GK.

Given the 401(1) keV $^{17}\text{O}+\alpha$ resonance accounts for $\sim 80\%$ of the $^{17}\text{O}(\alpha,n)^{20}\text{Ne}$ reaction rate at 0.2 GK it can be concluded that both the transferred l and both the Γ_α and Γ_n must be extracted via measurement for this state. The Γ_n must be measured to confirm the neutron width does dominate as predicted and expected, and if so the Γ_α to yield an experimentally

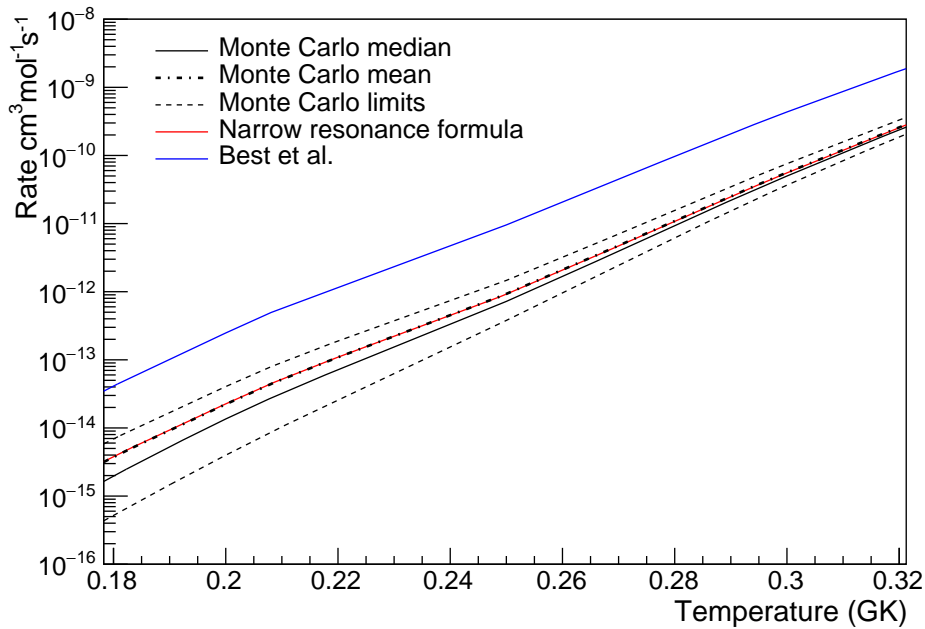


Figure 12.9: The effect of the measurement here on the $^{17}\text{O}(\alpha,\gamma)$ total median reaction rate relative to Best et al. [65]. The dashed lines represent the upper and lower uncertainties on the Monte Carlo method rate extracted here. Note the difference between the Monte Carlo method median and the rate of Best et al. [65].

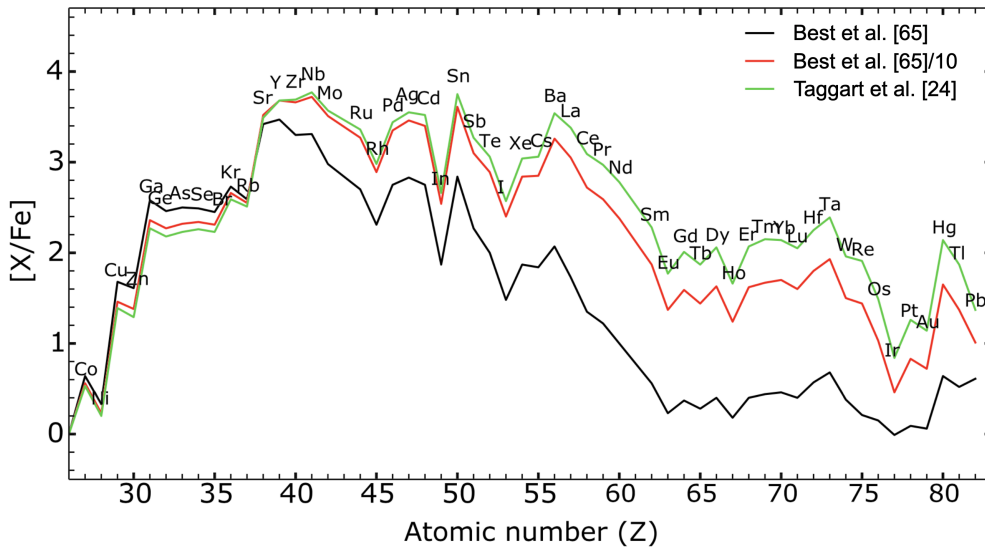


Figure 12.10: Yields from the s-process for a $25 M_{\text{sun}}$ star. Note the effect on reducing the $^{17}\text{O}(\alpha,\gamma)^{21}\text{Ne}$ by a factor of 10 (increasing the $^{17}\text{O}(\alpha,n)^{20}\text{Ne}/^{17}\text{O}(\alpha,\gamma)^{21}\text{Ne}$ ratio). Figure from Taggart et al. [24] with minor adaptation.

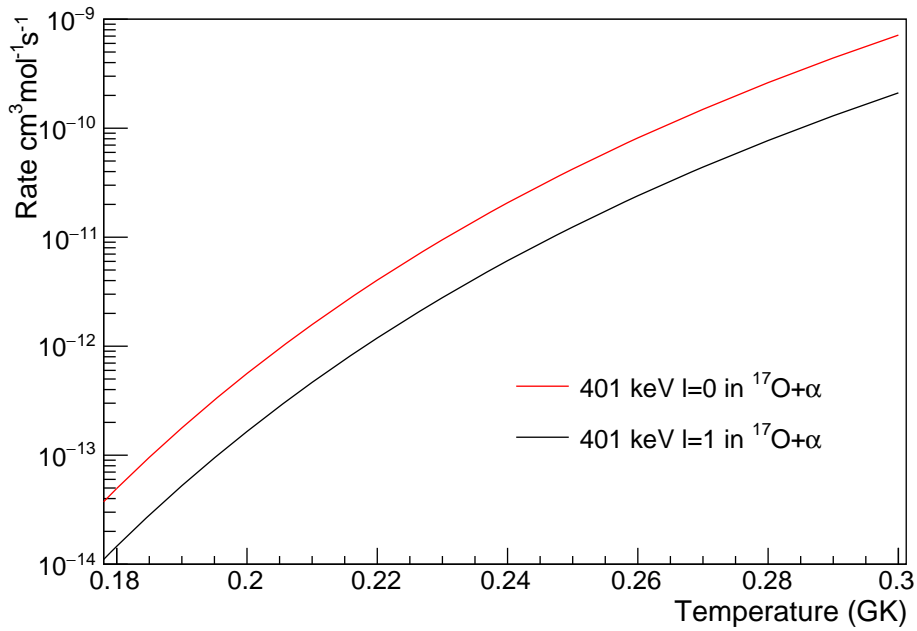


Figure 12.11: The effect on the reaction rate by changing the transferred l in $^{17}\text{O}+\alpha$ from 0 to 1. This results in a 71% decrease in reaction rate for this resonance at 0.2 GK.

determined resonance strength.

A team are currently re-measuring the 612 keV and 633 keV resonance at DRAGON with the aim of reducing the uncertainties on these states. Another measurement of $^{20}\text{Ne}(d,p)$ is currently taking place in inverse kinematics at HELIOS, HELical Orbit Spectrometer [108]. This will have significantly lower resolution than the data here, however it presents the opportunity to measure the Gamow window ^{21}Ne states without the broad 5.084 MeV energy ^{17}O state contamination. It is hoped the 7.749 MeV ^{21}Ne state will be measured.

Chapter 13

Conclusions

$^{15}\text{N}(\alpha,\gamma)^{19}\text{F}$ was directly measured using DRAGON. Utilising a windowless He gas target and ^{15}N beam, recoils were measured in coincidence for several direct capture energies and the 1.323 MeV resonance in $^{15}\text{N}+\alpha$.

The $^{15}\text{N}(\alpha,\gamma)^{19}\text{F}$ measurement resulted in the clarification of the recent discrepancy raised of the 1.323 MeV resonance beam energy. A measurement was conducted containing the resonance beam energy recently suggested by Di Leva et al. [27] of 1.3314(16) MeV and was proved by the wider DRAGON collaboration to not be at this new energy.

Analysis was conducted here to determine the 1.323 MeV resonance strength which was found to be 0.92 ± 0.11 eV. The discrepancy between this and the measurements of Aitken et al. [39] and another of Dixon and Storey [43] are explored and explained. The difference largely being due to unreliable reference resonances. A more recent measurement of the reference resonance [64] of $^{15}\text{N}+\text{p}$ brought the measurement into agreement with the DRAGON measurement here. They corrected their third absolute measurement to align with the values from relative measurements. The disagreement in resonance strength between the measurement presented in this thesis and that of Wilmes et al. [16] remains unexplained.

The direct capture beam energies in the centre-of-mass frame of 957.1(2) keV, 1202.5(3) keV, 1209.5(3) keV and 1720(9) keV yielded S-factors of $28.7_{-8.0}^{+9.6}$ MeVb, $108.9_{-25.2}^{+25.3}$ MeVb, $100.6_{-18.3}^{+18.7}$ MeVb and $24.3_{-3.8}^{+3.9}$ MeVb respectively. This is the first time direct capture has been measured directly for $^{15}\text{N}(\alpha,\gamma)^{19}\text{F}$.

The impact of ^{16}O as a neutron poison has been investigated through the study of the $^{17}\text{O}(\alpha,\text{n})^{20}\text{Ne}/^{17}\text{O}(\alpha,\gamma)^{21}\text{Ne}$ ratio. It has been investigated using the $^{20}\text{Ne}(\text{d},\text{p})^{21}\text{Ne}$ reaction. This populated states most important for the $^{17}\text{O}(\alpha,\text{n})^{20}\text{Ne}$ reaction.

State energies were measured and where possible their uncertainties reduced. Where states were seen at multiple angles so their differential cross-sections were plotted. The

differential cross-sections have been compared with FRESKO [36] calculations to extract transferred l in the $^{20}\text{Ne}(\text{d},\text{p})$ reaction. These assignments were also checked for consistency with the well described, by FRESKO, $l=1$ transfer to form the 8.189(1) MeV ^{21}Ne state, the known $l=1$ required to form the 7.619(2) MeV energy state and $l=2$ to form the 5.549(2) MeV energy state. These comparisons were made by taking the ratio of the experimental differential cross-sections.

The measurement has constrained the possible J^π values of some of the states in the Gamow window and reduced the reaction rate of $^{17}\text{O}(\alpha,\text{n})^{20}\text{Ne}$ and quantified its uncertainties. It must be emphasised that to obtain the value extracted here assumptions were made to minimise transferred l , i.e. an $l=1$ transfer in $^{20}\text{Ne}+\text{n}$ gave a J^π of $\frac{3}{2}^-$, hence minimising the angular momentum transfer in $^{17}\text{O}+\alpha$ to $l=1$. This could have resulted in an overestimation of the $^{17}\text{O}(\alpha,\text{n})$ median reaction rate. Without the measurement of state spins and parities improvement beyond this assumption appears difficult.

Where previous literature did not allow calculation of an alpha partial width they were calculated using the Wigner partial width limit with a 0.01 overlap factor applied. In the case of the 8.068 MeV energy ^{21}Ne state the transferred l value disagreed with Best et al. [65] and so the $\omega\gamma_{(\alpha,\gamma)}$ was taken from Taggart et al. [24] and $\omega\gamma_{(\alpha,\text{n})}$ from Denker [66] with the Γ_α extracted from the latter. Where no previous data was available assumptions informed by literature [37] were made that the $\Gamma_\gamma = 3(1.5)$ eV.

The 7.749(1) MeV energy state had the uncertainty on its energy reduced when compared to the previously accepted value of 7.750(10) MeV [88]. This state has been shown to be the dominant state at astrophysically relevant energies of around 0.2 GK for $^{17}\text{O}(\alpha,\text{n})^{20}\text{Ne}$. Whilst the transferred angular momentum in $^{20}\text{Ne}+\text{n}$ has not been measured and so the Best et al. [65] value of $l=0$ in $^{17}\text{O}+\alpha$ was adopted, the effect of a change in this transferred l value has been explored and found to be profound.

The new proposed rate for the $^{17}\text{O}(\alpha,\text{n})$ reaction rate was found to be lower but arguably within error of the values suggested by Best et al. [65]. Furthermore the new reaction rate has been constrained by uncertainties.

The $^{17}\text{O}(\alpha,\gamma)$ reaction rate was re-calculated including the data from Taggart et al. [24] and the new state parameters found here. The ratio of $^{17}\text{O}(\alpha,\text{n})/^{17}\text{O}(\alpha,\gamma)$ was found to be significantly higher than that of Best et al. [65] by a factor 8_{-7}^{+76} . So ^{16}O is expected to be less of a neutron poison in massive stars. This is inline with the ratio of values compared to Best et al. [65] presented in Taggart et al. [24]. It is found the s-process is therefore expected to be significantly less inhibited than expected by Best et al. [65]. Note must be made that the significant uncertainty in the ratio is driven largely by the uncertainty in the $^{17}\text{O}(\alpha,\gamma)$.

Appendix A

```

170(a,n)20Ne
*****
2          ! Zproj
8          ! Ztarget
0          ! Zexitparticle (=0 when only 2 channels open)
4.003     ! Aproj
16.999    ! Atarget
1.009     ! Aexitparticle (=0 when only 2 channels open)
0.0       ! Jproj
2.5       ! Jtarget
0.5       ! Jexitparticle (=0 when only 2 channels open)
7347.93   ! projectile separation energy (keV)
6761.16   ! exit particle separation energy (=0 when only 2 channels open)
1.25      ! Radius parameter R0 (fm)
3         ! Gamma-ray channel number (=2 if ejectile is a g-ray; =3 otherwise)
*****
1.0       ! Minimum energy for numerical integration (keV)
5000     ! Number of random samples (>5000 for better statistics)
17       ! =0 for rate output at all temperatures; =NT for rate output at selected temperatures
*****
Non-resonant contribution
S(keVb)  S'(b)          S''(b/keV)      fracErr  Cutoff Energy (keV)
0.0      0.0            0.0          0.0      0.0
0.0      0.0            0.0          0.0      0.0
*****
Resonant Contribution
Note: G1 = entrance channel, G2 = exit channel, G3 = spectator channel !! Ecm, Exf in (keV); wg, Gx in (eV) !!
Note: if Er<0, theta^2=C2S*theta_sp^2 must be entered instead of entrance channel partial width
Ecm  DEcm  Jr  G1  DG1  L1  PT  G2  DG2  L2  PT  G3  DG3  L3  PT  Exf  Int
720.2  2.0  0.0  0.0  1.5  63e-3  7e-3  1  5.4e+3  1.6e+3  1  1.1  1  1  0.0  1
815.1  2.0  0.0  0.0  2.5  16.0e-3  8.0e-3  0  23.0e+03  12.5e+03  2  3.0  1.5  1  0.0  1
841.1  1.0  0.0  0.0  1.5  88.4e-3  44.2e-3  1  3.32e+03  1.66e+03  1  3.0  1.5  1  0.0  1
916.0  2.0  0.0  0.0  2.5  54.4e-3  27.2e-3  1  3.3e+03  1.65e+03  3  3.0  1.5  1  0.0  1
944.0  2.0  0.0  0.0  1.5  559.e-3  279.5e-3  1  7.54e+3  3.77e+03  1  3.0  1.5  1  0.0  1
*****
Upper Limits of Resonances
Note: enter partial width upper limit by choosing non-zero value for PT, where PT=-theta^2 for particles and...
Note: ...PT<B> for g-rays [enter: "upper_limit 0.0"]; for each resonance: # upper limits < # open channels!
Ecm  DEcm  Jr  G1  DG1  L1  PT  G2  DG2  L2  PT  G3  DG3  L3  PT  Exf  Int
211.1  2.0  1.5  4.8e-14  0.0  1  0.01  3.4e+3  2.6e+3  1  0.0  3.0  1.5  1  0  0.0  1
253.1  2.0  4.5  2.0e-12  0.0  2  0.01  0.43  0.65  4  0.0  3.0  1.5  1  0  0.0  0
271.1  2.0  1.5  1.4e-11  0.0  1  0.01  1.8e+3  3.3e+3  1  0.0  3.0  1.5  1  0  0.0  1
472.1  3.0  1.5  3.5e-5  0.0  1  0.01  2.3e+3  0.7e+3  1  0.0  3.0  1.5  1  0  0.0  1
795.1  2.0  1.5  4.0e-1  0.0  1  0.01  1.8e+3  600  1  0.0  3.0  1.5  1  0  0.0  1
122.1  1.0  1.5  1.7e-22  0.0  1  0.01  3.0e+3  1.5e+3  1  0.0  3.0  1.5  1  0  0.0  1
308.1  2.0  3.5  4.0e-10  0.0  2  0.01  1.5  0.75  4  0.0  3.0  1.5  1  0  0.0  0
401.1  1.0  2.5  2.4e-6  0.0  0  0.01  3.0e+3  1.5e+3  2  0.0  3.0  1.5  1  0  0.0  1
612.0  13.0  5.5  1.2e-4  0.0  3  0.01  1.5  0.75  1  0.0  3.0  1.5  1  0  0.0  0
631.0  10.0  1.5  9.0e-3  0.0  1  0.01  6e+3  2e+3  1  0.0  0.06  0.02  1  0  0.0  1
633.0  1.0  3.5  6.0e-4  0.0  2  0.01  3.0  1.5  4  0.0  3.0  1.5  1  0  0.0  0
660.0  10.0  0.5  4.7e-4  0.0  3  0.01  3.2e+4  6.0e+3  1  0.0  0.32  0.06  1  0  0.0  1
*****
Interference between Resonances [numerical integration only]
Note: + for positive, - for negative interference; +- if interference sign is unknown
Ecm  DEcm  Jr  G1  DG1  L1  PT  G2  DG2  L2  PT  G3  DG3  L3  PT  Exf
!+-
0.0  0.0  0.0  0.0  0.0  0  0.0  0.0  0.0  0  0  0.0  0.0  0  0  0.0
0.0  0.0  0.0  0.0  0.0  0  0.0  0.0  0.0  0  0  0.0  0.0  0  0  0.0
*****
Reaction Rate and PDF at NT selected temperatures only
Note: default values are used for reaction rate range if Min=Max=0.0
T9      Min      Max
0.1
0.125
0.15
0.175
0.2
0.225
0.25
0.275
0.3
0.325
0.35
0.375
0.4
0.425
0.45
0.475
0.5
*****

```

Figure 13.1: RatesMC [98] input for $^{17}\text{O}(\alpha,n)$.

```

170(a,g)21Ne
*****
2          ! Zproj
8          ! Ztarget
0          ! Zexitparticle (=0 when only 2 channels open)
4.003     ! Aproj
16.999    ! Atarget
1.009     ! Aexitparticle (=0 when only 2 channels open)
0.0       ! Jproj
2.5       ! Jtarget
0.5       ! Jexitparticle (=0 when only 2 channels open)
7347.93   ! projectile separation energy (keV)
6761.16   ! exit particle separation energy (=0 when only 2 channels open)
1.25      ! Radius parameter R0 (fm)
2         ! Gamma-ray channel number (=2 if ejectile is a g-ray; =3 otherwise)
*****
1.0       ! Minimum energy for numerical integration (keV)
5000      ! Number of random samples (>5000 for better statistics)
17        ! =0 for rate output at all temperatures; =NT for rate output at selected temperatures
*****
Non-resonant contribution
S(keV) S'(b) S''(b/keV) fracErr Cutoff Energy (keV)
0.0 0.0 0.0 0.0 0.0
0.0 0.0 0.0 0.0 0.0
*****
Resonant Contribution
Notes: G1 = entrance channel, G2 = exit channel, G3 = spectator channel !! Ecm, Exf in (keV); wg, Gx in (eV) !!
Note: if Er<0, theta^2=C2S+theta_sp^2 must be entered instead of entrance channel partial width.
Ecm DEcm Jr G1 G2 G3 L1 L2 L3 L4 L5 L6 L7 L8 L9 L10 L11 L12 L13 L14 L15 L16 L17 L18 L19 L20 L21 L22 L23 L24 L25 L26 L27 L28 L29 L30 L31 L32 L33 L34 L35 L36 L37 L38 L39 L40 L41 L42 L43 L44 L45 L46 L47 L48 L49 L50 L51 L52 L53 L54 L55 L56 L57 L58 L59 L60 L61 L62 L63 L64 L65 L66 L67 L68 L69 L70 L71 L72 L73 L74 L75 L76 L77 L78 L79 L80 L81 L82 L83 L84 L85 L86 L87 L88 L89 L90 L91 L92 L93 L94 L95 L96 L97 L98 L99 L100 L101 L102 L103 L104 L105 L106 L107 L108 L109 L110 L111 L112 L113 L114 L115 L116 L117 L118 L119 L120 L121 L122 L123 L124 L125 L126 L127 L128 L129 L130 L131 L132 L133 L134 L135 L136 L137 L138 L139 L140 L141 L142 L143 L144 L145 L146 L147 L148 L149 L150 L151 L152 L153 L154 L155 L156 L157 L158 L159 L160 L161 L162 L163 L164 L165 L166 L167 L168 L169 L170 L171 L172 L173 L174 L175 L176 L177 L178 L179 L180 L181 L182 L183 L184 L185 L186 L187 L188 L189 L190 L191 L192 L193 L194 L195 L196 L197 L198 L199 L200 L201 L202 L203 L204 L205 L206 L207 L208 L209 L210 L211 L212 L213 L214 L215 L216 L217 L218 L219 L220 L221 L222 L223 L224 L225 L226 L227 L228 L229 L230 L231 L232 L233 L234 L235 L236 L237 L238 L239 L240 L241 L242 L243 L244 L245 L246 L247 L248 L249 L250 L251 L252 L253 L254 L255 L256 L257 L258 L259 L260 L261 L262 L263 L264 L265 L266 L267 L268 L269 L270 L271 L272 L273 L274 L275 L276 L277 L278 L279 L280 L281 L282 L283 L284 L285 L286 L287 L288 L289 L290 L291 L292 L293 L294 L295 L296 L297 L298 L299 L300 L301 L302 L303 L304 L305 L306 L307 L308 L309 L310 L311 L312 L313 L314 L315 L316 L317 L318 L319 L320 L321 L322 L323 L324 L325 L326 L327 L328 L329 L330 L331 L332 L333 L334 L335 L336 L337 L338 L339 L340 L341 L342 L343 L344 L345 L346 L347 L348 L349 L350 L351 L352 L353 L354 L355 L356 L357 L358 L359 L360 L361 L362 L363 L364 L365 L366 L367 L368 L369 L370 L371 L372 L373 L374 L375 L376 L377 L378 L379 L380 L381 L382 L383 L384 L385 L386 L387 L388 L389 L390 L391 L392 L393 L394 L395 L396 L397 L398 L399 L400 L401 L402 L403 L404 L405 L406 L407 L408 L409 L410 L411 L412 L413 L414 L415 L416 L417 L418 L419 L420 L421 L422 L423 L424 L425 L426 L427 L428 L429 L430 L431 L432 L433 L434 L435 L436 L437 L438 L439 L440 L441 L442 L443 L444 L445 L446 L447 L448 L449 L450 L451 L452 L453 L454 L455 L456 L457 L458 L459 L460 L461 L462 L463 L464 L465 L466 L467 L468 L469 L470 L471 L472 L473 L474 L475 L476 L477 L478 L479 L480 L481 L482 L483 L484 L485 L486 L487 L488 L489 L490 L491 L492 L493 L494 L495 L496 L497 L498 L499 L500 L501 L502 L503 L504 L505 L506 L507 L508 L509 L510 L511 L512 L513 L514 L515 L516 L517 L518 L519 L520 L521 L522 L523 L524 L525 L526 L527 L528 L529 L530 L531 L532 L533 L534 L535 L536 L537 L538 L539 L540 L541 L542 L543 L544 L545 L546 L547 L548 L549 L550 L551 L552 L553 L554 L555 L556 L557 L558 L559 L560 L561 L562 L563 L564 L565 L566 L567 L568 L569 L570 L571 L572 L573 L574 L575 L576 L577 L578 L579 L580 L581 L582 L583 L584 L585 L586 L587 L588 L589 L590 L591 L592 L593 L594 L595 L596 L597 L598 L599 L600 L601 L602 L603 L604 L605 L606 L607 L608 L609 L610 L611 L612 L613 L614 L615 L616 L617 L618 L619 L620 L621 L622 L623 L624 L625 L626 L627 L628 L629 L630 L631 L632 L633 L634 L635 L636 L637 L638 L639 L640 L641 L642 L643 L644 L645 L646 L647 L648 L649 L650 L651 L652 L653 L654 L655 L656 L657 L658 L659 L660 L661 L662 L663 L664 L665 L666 L667 L668 L669 L670 L671 L672 L673 L674 L675 L676 L677 L678 L679 L680 L681 L682 L683 L684 L685 L686 L687 L688 L689 L690 L691 L692 L693 L694 L695 L696 L697 L698 L699 L700 L701 L702 L703 L704 L705 L706 L707 L708 L709 L710 L711 L712 L713 L714 L715 L716 L717 L718 L719 L720 L721 L722 L723 L724 L725 L726 L727 L728 L729 L730 L731 L732 L733 L734 L735 L736 L737 L738 L739 L740 L741 L742 L743 L744 L745 L746 L747 L748 L749 L750 L751 L752 L753 L754 L755 L756 L757 L758 L759 L760 L761 L762 L763 L764 L765 L766 L767 L768 L769 L770 L771 L772 L773 L774 L775 L776 L777 L778 L779 L780 L781 L782 L783 L784 L785 L786 L787 L788 L789 L790 L791 L792 L793 L794 L795 L796 L797 L798 L799 L800 L801 L802 L803 L804 L805 L806 L807 L808 L809 L810 L811 L812 L813 L814 L815 L816 L817 L818 L819 L820 L821 L822 L823 L824 L825 L826 L827 L828 L829 L830 L831 L832 L833 L834 L835 L836 L837 L838 L839 L840 L841 L842 L843 L844 L845 L846 L847 L848 L849 L850 L851 L852 L853 L854 L855 L856 L857 L858 L859 L860 L861 L862 L863 L864 L865 L866 L867 L868 L869 L870 L871 L872 L873 L874 L875 L876 L877 L878 L879 L880 L881 L882 L883 L884 L885 L886 L887 L888 L889 L890 L891 L892 L893 L894 L895 L896 L897 L898 L899 L900 L901 L902 L903 L904 L905 L906 L907 L908 L909 L910 L911 L912 L913 L914 L915 L916 L917 L918 L919 L920 L921 L922 L923 L924 L925 L926 L927 L928 L929 L930 L931 L932 L933 L934 L935 L936 L937 L938 L939 L940 L941 L942 L943 L944 L945 L946 L947 L948 L949 L950 L951 L952 L953 L954 L955 L956 L957 L958 L959 L960 L961 L962 L963 L964 L965 L966 L967 L968 L969 L970 L971 L972 L973 L974 L975 L976 L977 L978 L979 L980 L981 L982 L983 L984 L985 L986 L987 L988 L989 L990 L991 L992 L993 L994 L995 L996 L997 L998 L999 L1000 L1001 L1002 L1003 L1004 L1005 L1006 L1007 L1008 L1009 L1010 L1011 L1012 L1013 L1014 L1015 L1016 L1017 L1018 L1019 L1020 L1021 L1022 L1023 L1024 L1025 L1026 L1027 L1028 L1029 L1030 L1031 L1032 L1033 L1034 L1035 L1036 L1037 L1038 L1039 L1040 L1041 L1042 L1043 L1044 L1045 L1046 L1047 L1048 L1049 L1050 L1051 L1052 L1053 L1054 L1055 L1056 L1057 L1058 L1059 L1060 L1061 L1062 L1063 L1064 L1065 L1066 L1067 L1068 L1069 L1070 L1071 L1072 L1073 L1074 L1075 L1076 L1077 L1078 L1079 L1080 L1081 L1082 L1083 L1084 L1085 L1086 L1087 L1088 L1089 L1090 L1091 L1092 L1093 L1094 L1095 L1096 L1097 L1098 L1099 L1100 L1101 L1102 L1103 L1104 L1105 L1106 L1107 L1108 L1109 L1110 L1111 L1112 L1113 L1114 L1115 L1116 L1117 L1118 L1119 L1120 L1121 L1122 L1123 L1124 L1125 L1126 L1127 L1128 L1129 L1130 L1131 L1132 L1133 L1134 L1135 L1136 L1137 L1138 L1139 L1140 L1141 L1142 L1143 L1144 L1145 L1146 L1147 L1148 L1149 L1150 L1151 L1152 L1153 L1154 L1155 L1156 L1157 L1158 L1159 L1160 L1161 L1162 L1163 L1164 L1165 L1166 L1167 L1168 L1169 L1170 L1171 L1172 L1173 L1174 L1175 L1176 L1177 L1178 L1179 L1180 L1181 L1182 L1183 L1184 L1185 L1186 L1187 L1188 L1189 L1190 L1191 L1192 L1193 L1194 L1195 L1196 L1197 L1198 L1199 L1200 L1201 L1202 L1203 L1204 L1205 L1206 L1207 L1208 L1209 L1210 L1211 L1212 L1213 L1214 L1215 L1216 L1217 L1218 L1219 L1220 L1221 L1222 L1223 L1224 L1225 L1226 L1227 L1228 L1229 L1230 L1231 L1232 L1233 L1234 L1235 L1236 L1237 L1238 L1239 L1240 L1241 L1242 L1243 L1244 L1245 L1246 L1247 L1248 L1249 L1250 L1251 L1252 L1253 L1254 L1255 L1256 L1257 L1258 L1259 L1260 L1261 L1262 L1263 L1264 L1265 L1266 L1267 L1268 L1269 L1270 L1271 L1272 L1273 L1274 L1275 L1276 L1277 L1278 L1279 L1280 L1281 L1282 L1283 L1284 L1285 L1286 L1287 L1288 L1289 L1290 L1291 L1292 L1293 L1294 L1295 L1296 L1297 L1298 L1299 L1300 L1301 L1302 L1303 L1304 L1305 L1306 L1307 L1308 L1309 L1310 L1311 L1312 L1313 L1314 L1315 L1316 L1317 L1318 L1319 L1320 L1321 L1322 L1323 L1324 L1325 L1326 L1327 L1328 L1329 L1330 L1331 L1332 L1333 L1334 L1335 L1336 L1337 L1338 L1339 L1340 L1341 L1342 L1343 L1344 L1345 L1346 L1347 L1348 L1349 L1350 L1351 L1352 L1353 L1354 L1355 L1356 L1357 L1358 L1359 L1360 L1361 L1362 L1363 L1364 L1365 L1366 L1367 L1368 L1369 L1370 L1371 L1372 L1373 L1374 L1375 L1376 L1377 L1378 L1379 L1380 L1381 L1382 L1383 L1384 L1385 L1386 L1387 L1388 L1389 L1390 L1391 L1392 L1393 L1394 L1395 L1396 L1397 L1398 L1399 L1400 L1401 L1402 L1403 L1404 L1405 L1406 L1407 L1408 L1409 L1410 L1411 L1412 L1413 L1414 L1415 L1416 L1417 L1418 L1419 L1420 L1421 L1422 L1423 L1424 L1425 L1426 L1427 L1428 L1429 L1430 L1431 L1432 L1433 L1434 L1435 L1436 L1437 L1438 L1439 L1440 L1441 L1442 L1443 L1444 L1445 L1446 L1447 L1448 L1449 L1450 L1451 L1452 L1453 L1454 L1455 L1456 L1457 L1458 L1459 L1460 L1461 L1462 L1463 L1464 L1465 L1466 L1467 L1468 L1469 L1470 L1471 L1472 L1473 L1474 L1475 L1476 L1477 L1478 L1479 L1480 L1481 L1482 L1483 L1484 L1485 L1486 L1487 L1488 L1489 L1490 L1491 L1492 L1493 L1494 L1495 L1496 L1497 L1498 L1499 L1500 L1501 L1502 L1503 L1504 L1505 L1506 L1507 L1508 L1509 L1510 L1511 L1512 L1513 L1514 L1515 L1516 L1517 L1518 L1519 L1520 L1521 L1522 L1523 L1524 L1525 L1526 L1527 L1528 L1529 L1530 L1531 L1532 L1533 L1534 L1535 L1536 L1537 L1538 L1539 L1540 L1541 L1542 L1543 L1544 L1545 L1546 L1547 L1548 L1549 L1550 L1551 L1552 L1553 L1554 L1555 L1556 L1557 L1558 L1559 L1560 L1561 L1562 L1563 L1564 L1565 L1566 L1567 L1568 L1569 L1570 L1571 L1572 L1573 L1574 L1575 L1576 L1577 L1578 L1579 L1580 L1581 L1582 L1583 L1584 L1585 L1586 L1587 L1588 L1589 L1590 L1591 L1592 L1593 L1594 L1595 L1596 L1597 L1598 L1599 L1600 L1601 L1602 L1603 L1604 L1605 L1606 L1607 L1608 L1609 L1610 L1611 L1612 L1613 L1614 L1615 L1616 L1617 L1618 L1619 L1620 L1621 L1622 L1623 L1624 L1625 L1626 L1627 L1628 L1629 L1630 L1631 L1632 L1633 L1634 L1635 L1636 L1637 L1638 L1639 L1640 L1641 L1642 L1643 L1644 L1645 L1646 L1647 L1648 L1649 L1650 L1651 L1652 L1653 L1654 L1655 L1656 L1657 L1658 L1659 L1660 L1661 L1662 L1663 L1664 L1665 L1666 L1667 L1668 L1669 L1670 L1671 L1672 L1673 L1674 L1675 L1676 L1677 L1678 L1679 L1680 L1681 L1682 L1683 L1684 L1685 L1686 L1687 L1688 L1689 L1690 L1691 L1692 L1693 L1694 L1695 L1696 L1697 L1698 L1699 L1700 L1701 L1702 L1703 L1704 L1705 L1706 L1707 L1708 L1709 L1710 L1711 L1712 L1713 L1714 L1715 L1716 L1717 L1718 L1719 L1720 L1721 L1722 L1723 L1724 L1725 L1726 L1727 L1728 L1729 L1730 L1731 L1732 L1733 L1734 L1735 L1736 L1737 L1738 L1739 L1740 L1741 L1742 L1743 L1744 L1745 L1746 L1747 L1748 L1749 L1750 L1751 L1752 L1753 L1754 L1755 L1756 L1757 L1758 L1759 L1760 L1761 L1762 L1763 L1764 L1765 L1766 L1767 L1768 L1769 L1770 L1771 L1772 L1773 L1774 L1775 L1776 L1777 L1778 L1779 L1780 L1781 L1782 L1783 L1784 L1785 L1786 L1787 L1788 L1789 L1790 L1791 L1792 L1793 L1794 L1795 L1796 L1797 L1798 L1799 L1800 L1801 L1802 L1803 L1804 L1805 L1806 L1807 L1808 L1809 L1810 L1811 L1812 L1813 L1814 L1815 L1816 L1817 L1818 L1819 L1820 L1821 L1822 L1823 L1824 L1825 L1826 L1827 L1828 L1829 L1830 L1831 L1832 L1833 L1834 L1835 L1836 L1837 L1838 L1839 L1840 L1841 L1842 L1843 L1844 L1845 L1846 L1847 L1848 L1849 L1850 L1851 L1852 L1853 L1854 L1855 L1856 L1857 L1858 L1859 L1860 L1861 L1862 L1863 L1864 L1865 L1866 L1867 L1868 L1869 L1870 L1871 L1872 L1873 L1874 L1875 L1876 L1877 L1878 L1879 L1880 L1881 L1882 L1883 L1884 L1885 L1886 L1887 L1888 L1889 L1890 L1891 L1892 L1893 L1894 L1895 L1896 L1897 L1898 L1899 L1900 L1901 L1902 L1903 L1904 L1905 L1906 L1907 L1908 L1909 L1910 L1911 L1912 L1913 L1914 L1915 L1916 L1917 L1918 L1919 L1920 L1921 L1922 L1923 L1924 L1925 L1926 L1927 L1928 L1929 L1930 L1931 L1932 L1933 L1934 L1935 L1936 L1937 L1938 L1939 L1940 L1941 L1942 L1943 L1944 L1945 L1946 L1947 L1948 L1949 L1950 L1951 L1952 L1953 L1954 L1955 L1956 L1957 L1958 L1959 L1960 L1961 L1962 L1963 L1964 L1965 L1966 L1967 L1968 L1969 L1970 L1971 L1972 L1973 L1974 L1975 L1976 L1977 L1978 L1979 L1980 L1981 L1982 L1983 L1984 L1985 L1986 L1987 L1988 L1989 L1990 L1991 L1992 L1993 L1994 L1995 L1996 L1997 L1998 L1999 L2000 L2001 L2002 L2003 L2004 L2005 L2006 L2007 L2008 L2009 L2010 L2011 L2012 L2013 L2014 L2015 L2016 L2017 L2018 L2019 L2020 L2021 L2022 L2023 L2024 L2025 L2026 L2027 L2028 L2029 L2030 L2031 L2032 L2033 L2034 L2035 L2036 L2037 L2038 L2039 L2040 L2041 L2042 L2043 L2044 L2045 L2046 L2047 L2048 L2049 L2050 L2051 L2052 L2053 L2054 L2055 L2056 L2057 L2058 L2059 L2060 L2061 L2062 L2063 L2064 L2065 L2066 L2067 L2068 L2069 L2070 L2071 L2072 L2073 L2074 L2075 L2076 L2077 L2078 L2079 L2080 L2081 L2082 L2083 L2084 L2085 L2086 L2087 L2088 L2089 L2090 L2091 L2092 L2093 L2094 L2095 L2096 L2097 L2098 L2099 L2100 L2101 L2102 L2103 L2104 L2105 L2106 L2107 L2108 L2109 L2110 L2111 L2112 L2113 L2114 L2115 L2116 L2117 L2118 L2119 L2120 L2121 L2122 L2123 L2124 L2125 L2126 L2127 L2128 L2129 L2130 L2131 L2132 L2133 L2134 L2135 L2136 L2137 L2138 L2139 L2140 L2141 L2142 L2143 L2144 L2145 L2146 L2147 L2148 L2149 L2150 L2151 L2152 L2153 L2154 L2155 L2156 L2157 L2158 L2159 L2160 L2161 L2162 L2163 L2164 L2165 L2166 L2167 L2168 L2169 L2170 L2171 L2172 L2173 L2174 L2175 L2176 L2177 L2178 L2179 L2180 L2181 L2182 L2183 L2184 L2185 L2186 L2187 L2188 L2189 L2190 L2191 L2192 L2193 L2194 L2195 L2196 L2197 L2198 L2199 L2200 L2201 L2202 L2203 L2204 L2205 L2206 L2207 L2208 L2209 L2210 L2211 L2212 L2213 L2214 L2215 L2216 L2217 L2218 L2219 L2220 L2221 L2222 L2223 L2224 L2225 L2226 L2227 L2228 L2229 L2230 L2231 L2232 L2233 L2234 L2235 L2236 L2237 L2238 L2239 L2240 L2241 L2242 L2243 L2244 L2245 L2246 L2247 L2248 L2249 L2250 L2251 L2252 L2253 L2254 L2255 L2256 L2257 L2258 L2259 L2260 L2261 L2262 L2263 L2264 L2265 L2266 L2267 L2268 L2269 L2270 L2271 L2272 L2273 L2274 L2275 L2276 L2277 L2278 L2279 L2280 L2281 L2282 L2283 L2284 L2285 L2286 L2287 L2288 L2289 L2290 L2291 L2292 L2293 L2294 L2295 L2296 L2297 L2298 L2299 L2300 L2301 L2302 L2303 L2304 L2305 L2306 L2307 L2308 L2309 L2310 L2311 L2312 L2313 L2314 L2315 L2316 L2317 L2318 L2319 L2320 L2321 L2322 L2323 L2324 L2325 L2326 L2327 L2328 L2329 L2330 L2331 L2332 L2333 L2334 L2335 L2336 L2337 L2338 L2339 L2340 L2341 L2342 L2343 L2344 L2345 L2346 L2347 L2348 L2349 L2350 L2351 L2352 L2353 L2354 L2355 L2356 L2357 L2358 L2359 L2360 L2361 L2362 L2363 L2364 L2365 L2366 L2367 L2368 L2369 L2370 L2371 L2372 L2373 L2374 L2375 L2376 L2377 L2378 L2379 L2380 L2381 L2382 L2383 L2384 L2385 L2386 L2387 L2388 L2389 L2390 L2391 L2392 L2393 L2394 L2395 L2396 L2397 L2398 L2399 L2400 L2401 L2402 L2403 L2404 L2405 L2406 L2407 L2408 L2409 L2410 L2411 L2412 L2413 L2414 L2415 L2416 L2417 L2418 L2419 L2420 L2421 L2422 L2423 L2424 L2425 L2426 L2427 L2428 L2429 L2430 L2431 L2432 L2433 L2434 L2435 L2436 L2437 L2438 L2439 L2440 L2441 L2442 L2443 L2444 L2445 L2446 L2447 L2448 L2449 L2450 L2451 L2452 L2453 L2454 L2455 L2456 L2457 L2458 L2459 L2460 L2461 L2462 L2463 L2464 L2465 L2466 L2467 L2468 L2469 L2470 L2471 L2472 L2473 L2474 L2475 L2476 L2477 L2478 L2479 L2480 L2481 L2482 L2483 L2484 L2485 L2486 L2487 L2488 L2489 L2490 L2491 L2492 L2493 L2494 L2495 L2496 L2497 L2498 L2499 L2500 L2501 L2502 L2503 L2504 L2505 L2506 L2507 L2508 L2509 L2510 L2511 L2512 L2513 L2514 L2515 L2516 L2517 L2518 L2519 L2520 L2521 L2522 L2523 L2524 L2525 L2526 L2527 L2528 L2529 L2530 L2531 L2532 L2533 L2534 L2535 L2536 L2537 L2538 L2539 L2540 L2541 L2542 L2543 L2544 L2545 L2546 L2547 L2548 L2549 L2550 L2551 L2552 L2553 L2554 L2555 L2556 L2557 L2558 L2559 L2560 L2561 L2562 L2563 L2564 L2565 L2566 L2567 L2568 L2569 L2570 L2571 L2572 L2573 L2574 L2575 L2576 L2577 L2578 L2579 L2580 L2581 L2582 L2583 L2584 L2585 L2586 L2587 L2588 L2589 L2590 L2591 L2592 L2593 L2594 L2595 L2596 L2597 L2598 L2599 L2600 L260
```

Bibliography

- [1] O. Neugebauer, *A history of ancient mathematical astronomy*, vol. 1. Springer Science & Business Media, 2012.
- [2] E. Rutherford, “Lxxxix. the scattering of α and β particles by matter and the structure of the atom,” *The London, Edinburgh, and Dublin Philosophical Magazine and Journal of Science*, vol. 21, no. 125, pp. 669–688, 1911.
- [3] C. Iliadis, *Nuclear Physics of Stars*. Physics textbook, Wiley, 2007.
- [4] F. Kappeler, H. Beer, and K. Wisshak, “S-process nucleosynthesis-nuclear physics and the classical model,” *Reports on progress in physics*, vol. 52, no. 8, p. 945, 1989.
- [5] M. Pignatari, R. Gallino, M. Heil, M. Wiescher, F. Käppeler, F. Herwig, and S. Bisterzo, “The weak s-process in massive stars and its dependence on the neutron capture cross sections,” *The Astrophysical Journal*, vol. 710, no. 2, p. 1557, 2010.
- [6] C. Abia, K. Cunha, S. Cristallo, and P. de Laverny, “The origin of fluorine: abundances in agb carbon stars revisited,” *Astronomy & Astrophysics*, vol. 581, p. A88, 2015.
- [7] S. Lucatello, T. Masseron, J. A. Johnson, M. Pignatari, and F. Herwig, “Fluorine and sodium in c-rich low-metallicity stars,” *The Astrophysical Journal*, vol. 729, no. 1, p. 40, 2011.
- [8] S. Federman, Y. Sheffer, D. L. Lambert, and V. Smith, “Far ultraviolet spectroscopic explorer measurements of interstellar fluorine,” *The Astrophysical Journal*, vol. 619, no. 2, p. 884, 2005.
- [9] G. D’Agata, R. Pizzone, C. Spitaleri, S. Blagus, P. Figuera, L. Grassi, G. Guardo, M. Gulino, S. Hayakawa, I. Indelicato, *et al.*, “Agb nucleosynthesis: The $^{19}\text{F}(\alpha, p)^{22}\text{Ne}$ reaction at astrophysical energies,” in *AIP Conference Proceedings*, vol. 1852, p. 080001, AIP Publishing, 2017.

-
- [10] C. Angulo, M. Arnould, M. Rayet, P. Descouvemont, D. Baye, C. Leclercq-Willain, A. Coc, S. Barhoumi, P. Aguer, C. Rolfs, *et al.*, “A compilation of charged-particle induced thermonuclear reaction rates,” *Nuclear Physics A*, vol. 656, no. 1, pp. 3–183, 1999.
- [11] P. A. Crowther, “Physical properties of wolf-rayet stars,” *Annu. Rev. Astron. Astrophys.*, vol. 45, pp. 177–219, 2007.
- [12] R. Longland, P. Lorén-Aguilar, J. José, E. García-Berro, L. G. Althaus, and J. Isern, “Nucleosynthesis during the merger of white dwarfs and the origin of r coronae borealis stars,” *The Astrophysical Journal Letters*, vol. 737, no. 2, p. L34, 2011.
- [13] S. Cristallo, A. Di Leva, G. Imbriani, L. Piersanti, C. Abia, L. Gialanella, and O. Straniero, “Effects of nuclear cross sections on ^{19}F nucleosynthesis at low metallicities,” *Astronomy & Astrophysics*, vol. 570, p. A46, 2014.
- [14] M. Lugaro, C. Ugalde, A. I. Karakas, J. Görres, M. Wiescher, J. C. Lattanzio, and R. C. Cannon, “Reaction rate uncertainties and the production of ^{19}F in asymptotic giant branch stars,” *The Astrophysical Journal*, vol. 615, no. 2, p. 934, 2004.
- [15] O. Straniero, S. Cristallo, and L. Piersanti, “Heavy elements in globular clusters: The role of asymptotic giant branch stars,” *The Astrophysical Journal*, vol. 785, no. 1, p. 77, 2014.
- [16] S. Wilmes, V. Wilmes, G. Staudt, P. Mohr, and J. Hammer, “The $^{15}\text{N}(\alpha, \gamma)^{19}\text{F}$ reaction and nucleosynthesis of ^{19}F ,” *Physical Review C*, vol. 66, no. 6, p. 065802, 2002.
- [17] A. Jorissen, V. Smith, and D. Lambert, “Fluorine in red giant stars-evidence for nucleosynthesis,” *Astronomy and Astrophysics*, vol. 261, pp. 164–187, 1992.
- [18] H. Zinnecker and H. W. Yorke, “Toward understanding massive star formation,” *Annual Review of Astronomy and Astrophysics*, vol. 45, 2007.
- [19] I. A. Bonnell, S. G. Vine, and M. R. Bate, “Massive star formation: nurture, not nature,” *Monthly Notices of the Royal Astronomical Society*, vol. 349, no. 2, pp. 735–741, 2004.
- [20] I. A. Bonnell, M. R. Bate, and H. Zinnecker, “On the formation of massive stars,” *Monthly Notices of the Royal Astronomical Society*, vol. 298, no. 1, pp. 93–102, 1998.

- [21] M. Limongi, O. Straniero, and A. Chieffi, “Massive stars in the range 13-25 m: Evolution and nucleosynthesis. ii. the solar metallicity models,” *The Astrophysical Journal Supplement Series*, vol. 129, no. 2, p. 625, 2000.
- [22] T. Rauscher, A. Heger, R. Hoffman, and S. Woosley, “Nucleosynthesis in massive stars with improved nuclear and stellar physics,” *The Astrophysical Journal*, vol. 576, no. 1, p. 323, 2002.
- [23] M. F. El Eid, B. S. Meyer, *et al.*, “s-process nucleosynthesis in advanced burning phases of massive stars,” *The Astrophysical Journal*, vol. 655, no. 2, p. 1058, 2007.
- [24] M. P. Taggart, C. Akers, A. M. Laird, U. Hager, C. Ruiz, D. Hutcheon, M. A. Bentley, J. R. Brown, L. Buchmann, A. Chen, *et al.*, “A direct measurement of the $^{17}\text{O}(\alpha, \gamma)^{21}\text{Ne}$ reaction in inverse kinematics and its impact on heavy element production,” *Physics Letters B*, vol. 798, p. 134894, 2019.
- [25] U. Frischknecht, R. Hirschi, and F.-K. Thielemann, “Non-standard s-process in low metallicity massive rotating stars,” *Astronomy & astrophysics*, vol. 538, p. L2, 2012.
- [26] M. Rayet and M.-a. Hashimoto, “The s-process efficiency in massive stars,” *Astronomy and Astrophysics*, vol. 354, pp. 740–748, 2000.
- [27] A. Di Leva, G. Imbriani, R. Buompane, L. Gialanella, A. Best, S. Cristallo, M. De Cesare, A. D’Onofrio, J. Duarte, L. Gasques, *et al.*, “Measurement of 1323 and 1487 keV resonances in $^{15}\text{N}(\alpha, \gamma)^{19}\text{F}$ with the recoil separator erna,” *Physical Review C*, vol. 95, no. 4, p. 045803, 2017.
- [28] K. S. Krane, *Introductory Nuclear Physics*. John Wiley and Sons, Inc., 1988.
- [29] J. J. van Zyl, *Two-nucleon transfer in the $^{58}\text{Ni}(p, ^3\text{He})^{56}\text{Co}$ reaction at incident energies of 80, 100 and 120 MeV*. PhD thesis, Stellenbosch University, 2012.
- [30] R. Firestone, “127, 1,” *Nucl. Data Sheets*, 2015.
- [31] J. Kelley, D. Tilley, H. Weller, and C. Chaves, “564, 1,” 1992.
- [32] C. Iliadis, “Proton single-particle reduced widths for unbound states,” *Nuclear Physics A*, vol. 618, no. 1-2, pp. 166–175, 1997.
- [33] C. B. Dover, C. Mahaux, and H. A. Weidenmüller, “The single-particle limit for partial widths,” *Nuclear Physics A*, vol. 139, no. 3, pp. 593–604, 1969.

-
- [34] A. Koning and J. Delaroche, “Local and global nucleon optical models from 1 keV to 200 MeV,” *Nuclear Physics A*, vol. 713, no. 3-4, pp. 231–310, 2003.
- [35] R. Varner, W. Thompson, T. McAbee, E. Ludwig, and T. Clegg, “A global nucleon optical model potential,” *Physics Reports*, vol. 201, no. 2, pp. 57–119, 1991.
- [36] I. Thompson, “Getting started with fresco,” *Comput. Phys. Rep*, vol. 7, pp. 167–212, 1988.
- [37] R. Longland, C. Iliadis, A. Champagne, J. R. Newton, C. Ugalde, A. Coc, and R. Fitzgerald, “Charged-particle thermonuclear reaction rates: I. monte carlo method and statistical distributions,” *Nuclear Physics A*, vol. 841, no. 1-4, pp. 1–30, 2010.
- [38] A. Lennarz, “Inverse kinematics study of the direct-capture contribution to the $^{15}\text{N}(\alpha, \gamma)^{19}\text{F}$ reaction rate relevant for the synthesis of ^{19}F in agb stars.” Experimental Proposal S1762 2017.
- [39] J. Aitken, R. Azuma, A. Litherland, A. Charlesworth, D. Rogers, and J. Simpson, “A survey of new resonances in the $^{15}\text{N}(\alpha, \gamma)^{19}\text{F}$ reaction,” *Canadian Journal of Physics*, vol. 48, no. 13, pp. 1617–1621, 1970.
- [40] P. C. Price *Proc. Phys. Soc. (London) Ser A*, 68, 553, 1955.
- [41] P. C. Price *Proc. Phys. Soc. (London) Ser. A*, 70, 661, 1957.
- [42] K. A. Snover. PhD thesis, Stanford University, Stanford, California, 1969.
- [43] W. Dixon and R. Storey, “Radiative yield of the $e\alpha = 1.68$ MeV resonance in the $^{15}\text{N}(\alpha, \gamma)^{19}\text{F}$ reaction,” *Canadian Journal of Physics*, vol. 49, no. 13, pp. 1714–1723, 1971.
- [44] W.-K. Chu and D. Powers, “Alpha-particle stopping cross section in solids from 400 keV to 2 MeV,” *Physical Review*, vol. 187, no. 2, p. 478, 1969.
- [45] P. Parker, “ $^{14}\text{N}(\alpha, \gamma)^{18}\text{F}$ reaction,” *Physical Review*, vol. 173, no. 4, p. 1021, 1968.
- [46] S. Gorodetzky, J. Adloff, F. Brochard, P. Chevallier, D. Dispier, P. Gorodetzky, R. Modjtahed-Zadeh, and F. Scheibling, “Cascades γ - γ de quatre résonances de la réaction $^{15}\text{N}(p, \gamma)^{16}\text{O}$,” *Nuclear Physics A*, vol. 113, no. 1, pp. 221–232, 1968.

-
- [47] F. De Oliveira, A. Coc, P. Aguer, C. Angulo, G. Bogaert, J. Kiener, A. Lefebvre, V. Tatischeff, J.-P. Thibaud, S. Fortier, *et al.*, “Determination of α -widths in ^{19}F relevant to fluorine nucleosynthesis,” *Nuclear Physics A*, vol. 597, no. 2, pp. 231–252, 1996.
- [48] T. Griegel, H. W. Drotleff, J. W. Hammer, H. Knee, and K. Petkau, “Physical properties of a heavy-ion-beam-excited supersonic jet gas target,” *Journal of applied physics*, vol. 69, no. 1, pp. 19–22, 1991.
- [49] D. Tilley, H. Weller, C. Cheves, and R. Chasteler, “Energy levels of light nuclei $A=18$ – 19 ,” *Nuclear Physics A*, vol. 595, no. 1, pp. 1–170, 1995.
- [50] K. Jayamanna, F. Ames, G. Cojocar, R. Baartman, P. Bricault, R. Dube, R. Laxdal, M. Marchetto, M. MacDonald, P. Schmor, *et al.*, “Off-line ion source terminal for isac at triumf,” *Review of Scientific Instruments*, vol. 79, no. 2, p. 02C711, 2008.
- [51] G. Ball, G. Hackman, and R. Krücken, “The triumf-isac facility: two decades of discovery with rare isotope beams,” *Physica Scripta*, vol. 91, no. 9, p. 093002, 2016.
- [52] S. Koscielniak, R. Laxdal, R. Lee, and L. Root, “Beam dynamics studies on the ISAC RFQ at TRIUMF,” in *Proceedings of the 1997 Particle Accelerator Conference (Cat. No. 97CH36167)*, vol. 1, pp. 1102–1104, IEEE, 1997.
- [53] R. Laxdal and M. Marchetto, “The ISAC post-accelerator,” *Hyperfine Interactions*, vol. 225, no. 1-3, pp. 79–97, 2014.
- [54] D. Hutcheon, S. Bishop, L. Buchmann, M. Chatterjee, A. Chen, J. D’Auria, S. Engel, D. Gigliotti, U. Greife, D. Hunter, *et al.*, “The DRAGON facility for nuclear astrophysics at TRIUMF-ISAC: design, construction and operation,” *Nuclear Instruments and Methods in Physics Research Section A: Accelerators, Spectrometers, Detectors and Associated Equipment*, vol. 498, no. 1-3, pp. 190–210, 2003.
- [55] D. Hutcheon, L. Buchmann, A. Chen, J. D’Auria, C. Davis, U. Greife, A. Hussein, D. Ottewell, C. Ouellet, A. Parikh, *et al.*, “Background suppression by the dragon radiative capture facility at triumf/isac,” *Nuclear Instruments and Methods in Physics Research Section B: Beam Interactions with Materials and Atoms*, vol. 266, no. 19-20, pp. 4171–4175, 2008.
- [56] W. Liu, “Charge state studies of heavy ions passing through gas,” Master’s thesis, Simon Fraser University, 2001.

-
- [57] D. Hutcheon, C. Ruiz, J. Fallis, J. D’Auria, B. Davids, U. Hager, L. Martin, D. Ottewell, S. Reeve, and A. Rojas, “Measurement of radiative capture resonance energies with an extended gas target,” *Nuclear Instruments and Methods in Physics Research Section A: Accelerators, Spectrometers, Detectors and Associated Equipment*, vol. 689, pp. 70–74, 2012.
- [58] O. Tengblad, U. Bergmann, L. Fraile, H. O. U. Fynbo, and S. Walsh, “Novel thin window design for a large-area silicon strip detector,” *Nuclear Instruments and Methods in Physics Research Section A: Accelerators, Spectrometers, Detectors and Associated Equipment*, vol. 525, no. 3, pp. 458–464, 2004.
- [59] J. Yorkston, A. Shotter, D. Syme, and G. Huxtable, “Interstrip surface effects in oxide passivated ion-implanted silicon strip detectors,” *Nuclear Instruments and Methods in Physics Research Section A: Accelerators, Spectrometers, Detectors and Associated Equipment*, vol. 262, no. 2-3, pp. 353–358, 1987.
- [60] G. J. Feldman and R. D. Cousins, “Unified approach to the classical statistical analysis of small signals,” *Physical Review D*, vol. 57, no. 7, p. 3873, 1998.
- [61] C. Wrede, A. Hussein, J. G. Rogers, and J. D’Auria, “A double sided silicon strip detector as a dragon end detector,” *Nuclear Instruments and Methods in Physics Research Section B: Beam Interactions with Materials and Atoms*, vol. 204, pp. 619–624, 2003.
- [62] M. A. Lovely, *Proton capture on ^{34}S in the astrophysical energy regime*. PhD thesis, Colorado School of Mines, 2020.
- [63] F. Zijderhand and C. Van der Leun, “Strong m_2 transitions,” *Nuclear Physics A*, vol. 460, no. 2, pp. 181–200, 1986.
- [64] M. Marta, E. Trompler, D. Bemmerer, R. Beyer, C. Broggini, A. Caciolli, M. Erhard, Z. Fülöp, E. Grosse, G. Gyürky, *et al.*, “Resonance strengths in the $^{14}\text{N}(p,\gamma)^{15}\text{O}$ and $^{15}\text{N}(p,\alpha\gamma)^{12}\text{C}$ reactions,” *Physical Review C*, vol. 81, no. 5, p. 055807, 2010.
- [65] A. Best, M. Beard, J. Görres, M. Couder, S. Falahat, R. Güray, A. Kontos, K.-L. Kratz, P. LeBlanc, Q. Li, *et al.*, “Measurement of the reaction $^{17}\text{O}(\alpha,n)^{20}\text{Ne}$ and its impact on the s process in massive stars,” *Physical Review C*, vol. 87, no. 4, p. 045805, 2013.
- [66] A. Denker. PhD thesis, Universität Stuttgart, 1994.

-
- [67] R. Azuma, E. Uberseder, E. C. Simpson, C. R. Brune, H. Costantini, R. J. de Boer, J. Görres, M. Heil, P. J. LeBlanc, C. Ugalde, and M. Wiescher, “Azure: An r-matrix code for nuclear astrophysics,” *Phys. Rev. C* **81**, 045805, 2010.
- [68] P. Kunz, “Distorted wave code dwuck4, university of colorado,”
- [69] A. Carmen and N. Collaboration, “Nacre: A european compilation of reaction rates for astrophysics,” in *AIP Conference Proceedings*, vol. 495, pp. 365–366, American Institute of Physics, 1999.
- [70] G. R. Caughlan and W. A. Fowler, “Thermonuclear reaction rates v,” *Atomic Data and Nuclear Data Tables*, vol. 40, no. 2, pp. 283 – 334, 1988.
- [71] P. Descouvemont, “Microscopic three-cluster study of 21-nucleon systems,” *Phys. Rev. C*, vol. 48, pp. 2746–2752, Dec 1993.
- [72] A. Best, J. Görres, M. Couder, R. DeBoer, S. Falahat, A. Kontos, P. LeBlanc, Q. Li, S. O’Brien, K. Sonnabend, *et al.*, “First direct measurement of resonance strengths in $^{17}\text{O}(\alpha,\gamma)^{21}\text{Ne}$,” *Physical Review C*, vol. 83, no. 5, p. 052802, 2011.
- [73] A. Howard, J. Pronko, and C. Whitten Jr, “Studies on ^{21}Ne and ^{23}Ne via the $^{20}\text{Ne}(\text{d,p})^{21}\text{Ne}$ and $^{22}\text{Ne}(\text{d,p})^{23}\text{Ne}$ reactions,” *Nuclear Physics A*, vol. 152, no. 2, pp. 317–336, 1970.
- [74] G. Satchler, “The distorted-waves theory of direct nuclear reactions with spin-orbit effects,” *Nuclear Physics*, vol. 55, pp. 1–33, 1964.
- [75] A. Stanford and P. Quin, “Study of stripping to levels of ^{21}Ne ,” *Nuclear Physics A*, vol. 342, no. 2, pp. 283–292, 1980.
- [76] *P. D. Kunz DWUCK 2.*
- [77] A. H. Couture, *Cross-Section Measurement of $^2\text{H}(n,np)n$ at 16 MeV in Symmetric Constant Relative Energy Configurations*. PhD thesis, Chapel Hill, 2011.
- [78] C. Marshall, K. Setoodehnia, K. Kowal, F. Portillo, A. E. Champagne, S. Hale, A. Dummer, and R. Longland, “The focal plane detector package on the tunl split-pole spectrograph,” *arXiv preprint arXiv:1806.02401*, 2018.
- [79] H. A. Enge, “Magnetic spectrographs for nuclear reaction studies,” *Nuclear Instruments and Methods*, vol. 162, no. 1-3, pp. 161–180, 1979.

-
- [80] “<https://www.crystals.saint-gobain.com/sites/imdf.crystals.com/files/documents/bc400-404-408-412-416-data-sheet.pdf>.” Accessed 05/01/2020.
- [81] “<https://www.hamamatsu.com/eu/en/product/type/h6524/index.html>.” Accessed 05/01/2020.
- [82] C. Marshall, “Private communication.”
- [83] M. Meyer, “Simnra user’s guide,” *Report IPP 9/113, Max-Planck-Institut fu r Plasma-physik, Garching, Germany*, 1997.
- [84] J. Coursey, D. Schwab, J. Tsai, and R. Dragoset, “Atomic weights and isotopic compositions with relative atomic masses,” *Atomic weights and isotopic compositions with relative atomic masses. Edited by Coursey, JS, Schwab, DJ, Tsai, JJ, Dragoset, RA, Physical measurement laboratory. https://www.nist.gov/pml/atomic-weights-and-isotopic-compositions-relativeatomic-masses*, 2015.
- [85] J. B. Ken Swartz, Dale Visser, “Jam v2.4.19,” <http://jam-daq.sourceforge.net/>.
- [86] C. Rolfs, H. Trautvetter, E. Kuhlmann, and F. Riess, “A study of excited states of ^{21}Ne ,” *Nuclear Physics A*, vol. 189, no. 3, pp. 641–664, 1972.
- [87] J. Hallock, H. Enge, J. Garrett, R. Middleton, and H. Fortune, “Study of the reaction $^{12}\text{C}+^{13}\text{C} \alpha+^{21}\text{Ne}$,” *Nuclear Physics A*, vol. 252, no. 1, pp. 141–151, 1975.
- [88] P. M. Endt, “Energy levels of A=21-44 nuclei (vii),” *Nuclear Physics A521 1-830*, 1990.
- [89] H. Fortune, J. Garrett, and R. Middleton, “Neutron pickup from ^{22}Ne ,” *Physical Review C*, vol. 19, no. 5, p. 1615, 1979.
- [90] C. Wheldon, T. Kokalova, W. Von Oertzen, S. Thummerer, H. Bohlen, B. Gebauer, A. Tumino, T. Massey, G. De Angelis, M. Axiotis, *et al.*, “Octupole-deformed molecular bands in ^{21}Ne ,” *The European Physical Journal A-Hadrons and Nuclei*, vol. 26, no. 3, pp. 321–326, 2005.
- [91] S. Hinds and R. Middleton, “The energy levels of ^{21}Ne ,” *Proceedings of the Physical Society*, vol. 74, no. 6, p. 779, 1959.
- [92] D. Visser, “SPANC - splitpole analysis code,” 2002.

-
- [93] H. An and C. Cai, “Global deuteron optical model potential for the energy range up to 183 MeV,” *Physical Review C*, vol. 73, no. 5, p. 054605, 2006.
- [94] D. G. Madland, “Spec. mtg. nucleon-nucleus opt.mod.to 200 MeV,” *OECD/NEA*, 1997.
- [95] P. Adsley, “Private communication.”
- [96] J. Menet, E. Gross, J. Malanify, and A. Zucker, “Total-reaction-cross-section measurements for 30-60 MeV protons and the imaginary optical potential,” *Physical Review C*, vol. 4, no. 4, p. 1114, 1971.
- [97] S. F. Mughabghab, *Atlas of Neutron Resonances, 5ed., Resonance Parameters and Thermal Cross Sections, Z = 1-100*. Elsevier, Amsterdam, 2006.
- [98] A. L. Sallaska, C. Iliadis, A. Champagne, S. Goriely, S. Starrfield, and F. Timmes, “Starlib: a next-generation reaction-rate library for nuclear astrophysics,” *The Astrophysical Journal Supplement Series*, vol. 207, no. 1, p. 18, 2013.
- [99] E. P. Wigner, “Lower limit for the energy derivative of the scattering phase shift,” *Physical Review*, vol. 98, no. 1, p. 145, 1955.
- [100] H. Cohn and J. Fowler, “Differential elastic scattering of neutrons from neon,” *Physical Review*, vol. 114, no. 1, p. 194, 1959.
- [101] R. Longland, C. Iliadis, and A. I. Karakas, “Reaction rates for the s-process neutron source $^{22}\text{Ne}+\alpha$,” *Physical Review C*, vol. 85, no. 6, p. 065809, 2012.
- [102] S. Thummerer, W. Von Oertzen, T. Kokalova, H. Bohlen, B. Gebauer, A. Tumino, T. Massey, G. De Angelis, M. Axiotis, A. Gadea, *et al.*, “A study of γ decays and octupole bands in ^{21}Ne and ^{21}Na ,” *Physics of Atomic Nuclei*, vol. 66, no. 8, pp. 1428–1433, 2003.
- [103] A. Hoffmann, P. Betz, H. Röpke, and B. Wildenthal, “Structure of the mirror nuclei ^{21}Ne and ^{21}Na ,” *Zeitschrift für Physik A Atomic Nuclei*, vol. 332, no. 3, pp. 289–304, 1989.
- [104] G. Mairle, L. K. Pao, G. Wagner, K. Knöpfle, and H. Riedesel, “A comparative spectroscopic investigation of ^{21}Ne and ^{21}F by pickup reactions,” *Zeitschrift für Physik A Atoms and Nuclei*, vol. 301, no. 2, pp. 157–163, 1981.

- [105] M. Freer, N. Ashwood, M. Barr, N. Curtis, J. Gibelin, F. Haas, J. Malcolm, T. Munoz-Britton, G. Randisi, N. Soić, *et al.*, “Neutron decay of excited states in ^{21}Ne populated in the $^{12}\text{C}(^{13}\text{C}, ^{21}\text{Ne})^4\text{He}$ reaction,” *Journal of Physics G: Nuclear and Particle Physics*, vol. 37, no. 12, p. 125102, 2010.
- [106] G. Andritsopoulos, W. Catford, E. Garman, D. Pringle, and L. Fifield, “States in ^{21}Ne via the $^{12}\text{C}(^{13}\text{C}, \alpha\gamma)^{21}\text{Ne}$ reaction,” *Nuclear physics A*, vol. 372, no. 1-2, pp. 281–300, 1981.
- [107] R. Firestone, “Nuclear data sheets for A= 21,” *Nuclear Data Sheets*, vol. 103, no. 2, pp. 269–324, 2004.
- [108] J. Lighthall, B. Back, S. Baker, S. Freeman, H. Lee, B. Kay, S. Marley, K. Rehm, J. Rohrer, J. Schiffer, *et al.*, “Commissioning of the helios spectrometer,” *Nuclear Instruments and Methods in Physics Research Section A: Accelerators, Spectrometers, Detectors and Associated Equipment*, vol. 622, no. 1, pp. 97–106, 2010.